

FINITE ELEMENT ANALYSIS OF STRESSES

AND CREEP IN TURBINE CASINGS

-by-

D.A.C. PARKES, B.Sc.

Thesis submitted to the University of Nottingham for the
degree of Doctor of Philosophy, May 1973.

IMAGING SERVICES NORTH

Boston Spa, Wetherby

West Yorkshire, LS23 7BQ

www.bl.uk

BEST COPY AVAILABLE.

VARIABLE PRINT QUALITY

57

BEST COPY AVAILABLE.

**TEXT IN ORIGINAL IS
CLOSE TO THE EDGE OF
THE PAGE**

**PAGE NUMBERS CLOSE TO
THE EDGE OF THE PAGE.
SOME ARE CUT OFF**

The finite element method has been used to calculate the stresses and creep deformations of flanged turbine casing models subjected to internal pressure and bolting forces. The finite element results have been compared with results from photoelastic and lead model turbine casings.

An axisymmetric thin shell of revolution ring finite element has been developed to analyse casings subjected to pressure, thermal and creep loads. The thin shell of revolution ring finite element is shown to be extremely powerful and has been used to investigate the shell portions of the turbine casing away from the flange. The three-dimensional isoparametric finite elements have been used for more accurate idealisations of the turbine casing. A thick shell isoparametric finite element has also been developed which can be used with the more common hexahedral isoparametric finite elements.

A solution algorithm based on a frontal technique has been developed to solve the large number of linear equations given by the finite element equations. This algorithm, which is fully automatic and uses fast access backing store, has a resolution facility which is used to recalculate subsequent creep solutions assuming that the stiffness of the structure remains constant. The creep algorithms are based on time marching techniques where the creep solutions are found for small time increments, the final solution being the sum of all the incremental solutions. During each time increment the stresses are assumed to remain constant and the change in stress between time increments is kept within a preset ratio. The creep algorithms have been used to predict the creep deformation of simple structures to compare with published results. The agreement between the finite element and lead model creep results is limited.

The finite element programs have been written to be compatible with the PAFEC suite of finite element programs.

Contents.

		Page
Chapter 1	Introduction	1
Chapter 2	Thin Shell of Revolution Finite Element	8
	Notation	8
2.1	Introduction	11
2.2.1	Analysis	12
2.2.2	Computation of Element Matrices	16
2.2.3	Solution Procedures	17
2.3.1.1	Static Loading	18
2.3.1.2	Numerical Examples (Static Loading)	18
2.3.2.1	Pressure Loading	19
2.3.2.2	Numerical Examples (Pressure Loading)	20
2.3.2.3	Torispherical Drumhead	21
2.3.2.4	3-Diameter Pressure Vessel	21
2.3.3.1	Thermal Loading	23
2.3.3.2	Numerical Examples (Thermal Loading)	25
	Standard Solutions for Cylindrical and Spherical Shells	
2.3.3.3	Semi-Infinite Cylinder subjected to a Varying Internal Wall Temperature	26
2.3.4.1	Creep Deformation	26
2.3.4.2	Numerical Examples (Creep Deformation)	29
	Simply Supported Cylinder subjected to Internal Pressure	
Chapter 3	The Parametric Family of Finite Elements	32
	Notation	32
3.1	Introduction	35

3.2.1	Isoparametric Finite Elements	37
3.2.2	Generation of Element Matrices	39
3.2.3	Numerical Integration	42
3.2.4	Generation of Thermal Loads	43
3.2.5	Pressure Loading	45
3.3.1	Thick Shell Parametric Finite Elements	47
3.3.2	Generation of Element Matrices	48
3.4.1	Transition Parametric Finite Element	51
3.4.2	Generation of Element Matrices	52
3.5.1	Programming Techniques	53
3.5.2	Programming Techniques (Thick Shell Parametric Element)	59
3.6	Numerical Examples	60
3.6.1	Isoparametric Finite Element	60
3.6.2	Thick Shell Parametric Finite Element	62
3.6.3	Transition Parametric Finite Element	62
3.6.4	Iso, Transition and Shell Parametric Finite Element Combination	63
Chapter 4	Frontal Solution	64
	Notation	64
4.1	Introduction	65
4.2	Numerical Analysis	67
4.3	Housekeeping	71
4.3.1	CPDDC Array	71
4.3.2	Merge Algorithm	73
4.3.3	Reduction Algorithm	76
4.3.4	Back Substitution Algorithm	78
4.3.5	Re-Solution Algorithm	79

4.3.6	Peripheral Handling	81
4.4	Data Generation	82
4.5	Error Diagnostics	82
4.6	Example Problem	83
Chapter 5	Creep Analysis	85
	Notation	85
5.1	Introduction	87
5.2	Creep Analysis	90
5.2.1	Solution Techniques	92
5.2.2	Multiaxial Stress-Strain Relationships	94
5.2.3	Uniaxial Stress-Strain-Time Relationships	96
5.3	Programming Techniques	97
5.4	Numerical Examples	103
5.4.1	Beam Subjected to a Constant Bending Moment	103
5.4.2	Effect of Initial Starting Time on Long Term Creep Analysis	105
5.4.3	Thick Ring Subjected to Internal Pressure	106
5.4.4	Thick Cylinder Subjected to Internal Pressure	107
Chapter 6	Stress Analysis of Turbine Casings	109
6.1	Introduction	109
6.2	2-Dimensional Analysis of the Cylindrical Portion of Split Turbine Casings	110
6.3	3-Dimensional Plane Strain Analysis of the Cylindrical Portion of Split Turbine Casings	113
6.4	Determination of Equivalent Bolt Loads	114

6.5	Stress Analysis of an Inner Turbine Casing subjected to an Axial Variation of Pressure	118
6.6	Finite Element Analysis of Split Turbine Casing	121
6.6.1	Turbine Casing subjected to Internal Pressure Loading	123
6.6.2	Turbine Casing subjected to Internal Pressure and Bolt Loading	127
6.7	Approximate Analysis of the Shell Portion of the Split Turbine Casing using the Thin Shell of Revolution Ring Finite Element	128
Chapter 7	Creep Deformation of a Turbine Casing Model	130
7.1	Introduction	130
7.2	Empirical Creep Law	130
7.3	Creep Deformation of 3-Dimensional Finite Element Idealisation of Lead Turbine Casing	131
7.3.1	Deformation of Lead Turbine Casing Model	132
7.3.2	Variation of Strain and Stress in the Model Turbine Casing due to Creep Deformation	133
7.4	Axisymmetric Approximation of the Creep Deformation of a Turbine Casing	138
7.5	Computation of Creep Deformation of a Turbine Casing	139
Chapter 8	Discussion	141
8.1	Introduction	141
8.2.1	Elastic Analysis	141

8.2.2	Creep Analysis	144
8.2.3	Economics of Solutions	146
8.3	Future Work	147
	Acknowledgements	149
Appendix 1	'A' Matrix for Thin Shell of Revolution Finite Element	151
Appendix 2	Stiffness Terms for Thin Shell of Revolution Finite Element	152
Appendix 3	Equivalent Nodal Force Terms for Axisymmetric Thin Shell of Revolution subjected to Thermal Strains	155
Appendix 4	Thermal Stresses in Cylinders subjected to Axisymmetric Temperature Distributions	156
Appendix 5	Equivalent Nodal Force Terms for Axisymmetric Thin Shell of Revolution subjected to Creep Deformation	159
Appendix 6	Transition Parametric Finite Element Constraints	160
Appendix 7	Decomposition of D matrices into $U^T U$ form	162
Appendix 8	Von Mises and Prandtl-Reuss Flow Rules	164
Appendix 9	Newton's Method for Solving Non-Linear Equations	168
Appendix 10	Creep Analysis applied to a Beam Finite Element	169
Appendix 11	Computation of Turbine Casing Finite Element Idealisations	171
	Tables	175

Figures	181
References	323

Chapter 1 Introduction

The basic prime mover used to generate the large quantities of power required by the Electricity Supply Industry and sometimes in large ocean going vessels is the high speed steam turbine. Modern steam turbines consist of a number of rotors spinning within cylindrical pressure vessels driving either an electrical alternator or propulsion device. Steam turbines are required to deliver anything from 15,000 to 900,000 shaft brake horse power with steam entry conditions varying from nearly saturated steam, delivered by water-cooled reactors, to superheated steam at supercritical pressure from the largest fossil fired boilers, (ref. 1). To obtain the highest efficiencies from the turbine plant it is necessary to extract all the useful energy in the steam between its entry condition and its exit at maximum vacuum conditions. The efficiency is further improved by introducing reheat cycles within the expansion cycle, usually restricted to one only by physical considerations, between the high pressure turbine exhaust and intermediate pressure turbine inlet belt. The reheat temperature is commonly identical to the initial steam entry temperature, and consequently the turbine casings of the first two rotors have to withstand the largest thermal gradients and also contain the highest pressures. Modern designs reduce the thermal and pressure stresses to which the casings are subjected by a multi-shell construction of inner and outer concentric casings.

The high temperature rotors are generally machined forgings to which blades have been attached, usually by a fir tree root fixing, supported by shrouds at the outer diameter, Each rotor contains a number of turbine stages and, unlike a gas turbine where each disc

can be removed from the rotor shaft, it is difficult to design annular continuous diaphragm stages. To facilitate erection and maintenance of the rotors and diaphragms the turbine casings are split horizontally into two halves along the shaft centre line. To maintain a pressure tight seal the two halves are mated together, metal to metal contact, and held by high tensile bolts through flanges running along the split. This greatly reduces the strength of the casing and consequently thicker shell structures are necessary. With increased steam entry conditions very thick flanges are necessary to maintain a pressure tight seal. Heavy bolted flanges give rise to large thermal stresses and some latter designs of high pressure cylinders incorporate an inner barrel casing to reduce these, (ref. 2). The majority of high pressure steam turbine casings comprise a flanged shell supporting a similar casing internally, labyrinth sealing gland housings, and numerous pipe and nozzle entries. Steam turbines used for electrical power generation are designed to operate at a set speed, 3000 rev/min. or 3,600 rev/min. governed by the electricity supply frequency, and set steam entry conditions. These have stabilised at 125-250 atm., 540°C-565°C with single boiler reheat to similar temperatures, (ref. 1). The very large amounts of power being generated by each machine, at present 500 MW, demand that the turbine be operated very close to the design condition to effect the greatest economy. The low nightly demand for electrical power, to be supplied by nuclear plants by 1975, means that a large number of steam turbines have to be shut down at night and run up again the next morning, being fully loaded within an hour of start up, (ref, 3). The planned life of the plant is 25-30 years, during which creep deformation or thermal fatigue

problems can become prominent and lead to premature damage (ref. 4). To transmit the large torques the shafts are rigidly coupled together resulting in a differential expansion between turbine casing and rotor of at least $\frac{1}{2}$ " at start up or load changing, (ref. 5). To maintain maximum interstage efficiency multiple radial seals are necessary and damage to these seals caused by rubbing or other uneven deformation can severely damage the turbine or, at best, impair the thermal efficiency. Costs caused by unplanned maintenance outages can be as high as £25,000 per day for a 500MW unit, (ref. 6) and more long term plant failure can be nationally disastrous.

The steam turbine designer is faced with larger power requirements while steam entry conditions, especially steam temperature, are limited by the metallurgical constraints imposed by the steels. Present 500 MW steam turbines comprise a high pressure, high temperature turbine, a double flow high temperature intermediate pressure turbine and usually three double flow low pressure turbines. These accommodate the large exhaust volume of steam at 28"-29" Hg vacuum, whilst keeping the final stage blading within acceptable physical dimensions. The designer cannot indefinitely upgrade existing well tried designs and increase thickness to maintain safety factors as the civil engineering demands made by the turbine-alternator complex become too great. To obtain the minimum cost requirements for a specified life a sound knowledge of the deformation and stresses of the turbine is necessary, together with the subsequent creep deformation and thermal fatigue cycles, at all times during the life of the turbine.

This thesis is based on one half of a joint research project into

the stresses and creep of split turbine casings, and concerns the theoretical computer model based on the Finite Element method of structural analysis. A need has long been felt by the CEGB and turbine manufacturers alike for a complete 3-dimensional analysis of a turbine casing to supplement the in-plane analysis of the cylindrical portion of the casing and flanges, interest being shown particularly in the toroidal and spherical end closures. The experimental part of this work involves photoelastic frozen stress model techniques for the stress analysis and constant temperature lead models for the creep deformation measurements. This work is reported elsewhere, (ref. 7).

The Finite Element method of structural analysis was chosen because of its flexibility in modelling and solving complex structures, and also because a large number of basic programs were already available. A very large number of programs were developed for this analysis, and these have been included in the PAFEC 70 (Program for Automatic Finite Element Calculation) (ref, 8) suite of structural analysis programs developed in the Department of Mechanical Engineering at Nottingham University.

Previously most methods of stress analysis of turbine casings have involved splitting the cylindrical part of the casing into two discrete parts, the designer using his experience to couple them together. Away from the flange area shell theory has been assumed, and the shell portion treated as an axisymmetric shell of revolution. The flanges have been analysed approximately, either by treating the flange as an eccentrically loaded column (ref, 9) or using a beam on elastic foundation analogy, (ref. 10). In both methods the flange is subjected to a compressive force

equivalent to the bolt loads and a tensile opening force due to the shell loads. A pressure tight seal is assumed to have been obtained when the inside compressive flange face stresses exceed the pressure within the casing.

With the more highly stressed modern steam turbines it is important to analyse the casings, as well as the rotors, more accurately, to design for the optimum efficiency and maximum power from the plant. The advent of the high speed digital computer has made more accurate analysis possible and manufacturers have made use of both in-plane finite difference and finite element programs to analyse turbine casing sections (ref. 11). These methods, although only approximate, do give a good indication of the stresses in the cylindrical portion of the casing, well away from the end closures. To achieve a more accurate solution, taking account of the end closures, a 3-dimensional analysis is imperative, particularly when determining creep deformations. The very complex shape of the steam turbine casing subjected to pressure and thermal loadings make exact computer modelling economically impossible.

The Finite Element method has been used to analyse the split turbine casing in two ways. First the shell portions of the casing were treated as an axisymmetric thin shell of revolution. It can be shown that this approximation is valid away from the flanges, provided that the thickness to radius ratio of the casing is within the limitations of the thin shell theory. An axisymmetric thin shell of revolution finite element of constant thickness and optional displacement order has been developed and proved very powerful. The stress analysis and creep deformation

of complex shells can be accurately predicted, with the number of equations to be solved small enough to enable very fast in-core solution algorithms to be used. The formulation assumes that the stresses normal to the shell surface, i.e. radial stresses, are negligible compared to the circumferential and meridional stresses. This element has been shown to be extremely efficient by a number of published results for shell elements, and has been used to analyse a number of pressure vessels subjected to static, pressure and thermal loadings. The creep deformation of a simply supported shell subjected to internal pressure has been obtained and compared with a published analytical solution.

To analyse a turbine casing and model it exactly, taking account of individual bolts, is beyond the scope of the present generation of computers. To assess the creep deformation of a turbine casing the flanges and shell portion of the casing are modelled, together with the end closures and sealing glands and subjected to approximate values of bolt loading. The isoparametric family of finite elements have been found to be the most efficient available for this purpose. Geometrically complex structures can be modelled using hexahedral blocks whose boundaries, edges, are defined in curvilinear co-ordinates, together with the displacements at these boundaries.

To model any structure sufficiently accurately requires a fine idealisation and, consequently, a very large number of linear equations have to be solved. Various methods of solution are available which either destroy part of the solution, or demand rigorous effort to keep the relationship between consecutive equations within a very narrow band. Non-linear problems, such as creep deformation, usually assume that the stiffness terms

remain constant with time and the equations have to be solved many times. If the problem is too large to retain the inverted stiffness matrix in the computer core then a solution algorithm has to be used which retains the initial stiffness terms. A frontal solution technique, using fast access backing store, usually in the form of temporary disc store to supplement the computer core store, has been used for the solution of these equations. The amount of core store required at any one time is determined by the number of active equations and consequently by careful element ordering very large idealisations can be solved. The initial equations are retained, and by modifying the loading terms the creep solution can be obtained.

The creep analysis used is based on a time-stepping process with constant stress states prevailing over each small time increment. Both time-hardening and strain-hardening solutions are obtainable and the empirical creep law contains both primary and secondary terms. The change in stress after each time increment is found before the next time increment is computed. The change in the stress over the time increment is checked and the increments are adjusted to give the most efficient solution within the limits set.

The stress analyses and creep deformations of turbine casing models have been found using these finite element programs. These models include a flanged inner turbine casing subjected to pressure loading only, a flanged closed turbine casing subjected to internal pressure and bolt loadings, and an axisymmetric approximation to the closed turbine casing. The results of these analyses are presented in the second part of this thesis.

Chapter 2. Thin Shell of Revolution Finite Element.

Notation.

E	Young's modulus
ipu	no. of terms in tangential displacement function
ipv	no. of terms in meridional displacement function
ipw	no. of terms in normal displacement function
l	meridional length of element
n	Fourier harmonic
p	pressure
r	radius from axis of symmetry
r_s	radius of curvature
s	distance along meridian
t	thickness
T	temperature at any point
T_0	temperature at mid-surface
\bar{T}	mean temperature
ΔT_0	temperature difference across shell thickness
u	tangential component of mid-surface displacement
v	meridional component of mid-surface displacement
w	normal component of mid-surface displacement
$\dot{u}, \dot{v}, \dot{w}, \dot{\theta}$	derivatives of mid-surface displacements with respect to meridional length
U	Potential Energy
V	Strain Energy
W.D.	Work Done
z	distance from mid-surface
α	coefficient of thermal expansion
ϵ	strain

σ	stress
λ	Poisson's ratio
ϕ	angle between normal and axis of symmetry
θ	circumferential co-ordinate

Suffices

C	creep	g	global axes
E	elastic	i	element
T	total	l	local axes
Therm	thermal	ϕ	meridional direction
e	equivalent	θ	circumferential direction

Matrices and Vectors

$\{ \}$	column vector
$[]$	matrix
$[]^T$	transpose of matrix
$[A]$	matrix linking nodal displacements to coefficients of generalised displacement functions
$[B]$	matrix linking generalised displacements to displacement function coefficients
$[D]$	stress/strain matrix
$[D']$	strain energy matrix in terms of generalised displacements
$\{DD'\}$	strain energy vector for thermal strains
$\{D_{creep}\}$	strain energy vector for creep strains
$\{F\}$	force vector
$[K]$	stiffness matrix
$\{p'\}$	pressure loading vector

$\{\delta\}$ list of nodal displacements
 $\{\bar{\delta}\} = \{u, v, w, \dot{u}, \dot{v}, \dot{w}, \ddot{u}, \ddot{v}, \ddot{w}\}^T$ generalised displacements (including derivatives)

2.1 Introduction

A shell of revolution may be idealised by a number of ring shell finite elements, each of which represents a portion of the total meridional length of the shell. Early researchers, Grafton and Strome (ref. 12), Pian et al (ref. 13) and Popov et al (ref. 14), used truncated conical frustra finite elements to model shells of revolution. Large numbers of these elements are required to give an accurate idealisation of the geometry of shells with meridional curvature. Jones and Strome (ref. 15) used doubly curved ring shell finite elements with co-ordinates and slope at the element ends matching those of the actual shell. The idealisation of these elements forms a smooth surface with continuity of curvature across element boundaries. The shell surface between the element ends is described by a polynomial function and the surface modelled by these elements may depart from the true shell surface. Navaratna (ref. 16) used ring finite elements which satisfied displacement and slope continuity at the common nodal circles for the analysis of deep spherical shells. In this type of idealisation it has been usual to represent the meridional variation of the normal mid-surface displacement within each element by a cubic function, and the variation of the meridional and tangential displacements by linear functions of the meridional co-ordinate. To converge to the exact solution of many problems large numbers of these elements are necessary. Webster (ref. 17) has used ring elements with higher order polynomial displacement functions for the solution of dynamic problems for shells of revolution. These results together with those given later by Webster (ref. 18), indicate that accurate solutions are obtained more efficiently with a few higher order displacement function ring elements than by many more

simpler displacement function ring elements.

A general thin shell of revolution ring finite element of constant meridional curvature and constant thickness using the higher order displacement functions in the meridional co-ordinate has been developed. Results are given for the analysis of shells subjected to static, pressure and thermal loadings as well as creep deformations and are compared with published results. The approximate axisymmetric analysis of the shell portions of turbine casings away from the flange is given in Chapter 6.

2.2.1 Analysis

Fig. 2.1 shows a thin shell of revolution ring finite element with constant meridional radius of curvature and shell thickness. The displacement functions used to represent the tangential, meridional and radial components of the mid-surface displacement are given in terms of the meridional co-ordinate.

$$u = \sum_{m=1}^{ipu} U_m (s/l)^{m-1} (1 \text{ or } \sin n\Theta) \quad 2.1(a)$$

$$v = \sum_{m=1}^{ipv} V_m (s/l)^{m-1} (1 \text{ or } \cos n\Theta) \quad 2.1(b)$$

$$w = \sum_{m=1}^{ipw} W_m (s/l)^{m-1} (1 \text{ or } \cos n\Theta) \quad 2.1(c)$$

The meridional arc length s is measured in the direction of increasing angle ϕ . The terms $(1 \text{ or } \sin n\Theta)$ and $(1 \text{ or } \cos n\Theta)$ allow either an axisymmetric load or the n^{th} Fourier harmonic component of a non-symmetric load to be considered. For non-torsional

axisymmetric loadings only the meridional and normal displacements need be considered.

The nodes, defined on the shell mid-surface at the element ends, take the form of nodal circles. The displacements at the nodes of any element may be expressed in terms of the displacement function coefficients U_m, V_m, W_m . The generalised displacements of an element are the nodal displacements and sufficient of the displacement coefficients to complete the definition of the element displacement function. These generalised displacements at the nodes $\{\delta_i\}$ can be expressed in terms of the displacement function coefficients $\{U_m, V_m, W_m\}^T$ by

$$\{\delta_i\} = [A] \{U_m, V_m, W_m\}^T \quad 2.2$$

The $[A]$ matrix, see Appendix 1, includes the transform of the meridional and normal mid-surface shell displacements at the nodes into the global x and y co-ordinates.

The displacements at any node are

$$u_g = u \quad 2.3(a)$$

$$v_g = v \sin\phi - w \cos\phi \quad 2.3(b)$$

$$w_g = v \cos\phi + w \sin\phi \quad 2.3(c)$$

$$\theta_g = \frac{\partial w}{\partial s} - \frac{v}{r_s} \quad 2.3(d)$$

The generalised displacements and derivatives of these displacements with respect to the meridional co-ordinate at any point are related to the coefficients of the displacement function by the matrix $[B]$

$$\{\bar{\delta}\} = [B] \{U_m, V_m, W_m\}^T \quad 2.4(a)$$

where $\{\bar{\delta}\}^T = \{u, v, w, \dot{u}, \dot{v}, \dot{w}, \dot{w}\}^T$ 2.4(b)

and $\dot{u} = \frac{\partial u}{\partial s}$ etc.

The strain displacement relationships are given by Flügge (ref. 19) and neglecting the terms associated with change in meridional curvature, give, when referred to Fig. 2.1

$$\epsilon_\phi = \frac{\partial v}{\partial s} + \frac{w}{r_s+z} - \left(\frac{z r_s}{r_s+z}\right) \frac{\partial^2 w}{\partial s^2} \quad 2.5(a)$$

$$\epsilon_\theta = \frac{1}{r} \frac{\partial u}{\partial \theta} + \frac{v \cos \phi (r_s+z)}{r_s (r+z \sin \phi)} + \frac{w \sin \phi}{(r+z \sin \phi)} - \frac{z}{(r+z \sin \phi)} \left(\frac{1}{r} \frac{\partial^2 w}{\partial \theta^2} + \cos \phi \frac{\partial w}{\partial s} \right) \quad 2.5(b)$$

$$\begin{aligned} \gamma_{\phi\theta} = & \frac{(r+z \sin \phi)}{(r_s+z)} \left(\frac{r_s}{r} \frac{\partial u}{\partial s} - \frac{r_s}{r^2} \cos \phi u \right) + \frac{(r_s+z)}{(r+z \sin \phi)} \cdot \frac{1}{r_s} \frac{\partial v}{\partial \theta} \\ & - \left(\frac{1}{(r+z \sin \phi)} + \frac{r_s}{r(r_s+z)} \right) \left(\frac{\partial^2 w}{\partial s \partial \theta} - \frac{\cos \phi}{r} \frac{\partial w}{\partial \theta} \right) \end{aligned} \quad 2.5(c)$$

The strain energy for a thin shell of revolution is given by

$$V = \frac{1}{2} \int_{Vol} \{ \epsilon_E \}^T \{ \sigma \} dVol \quad 2.6$$

where the elastic strain vector is given by

$$\{ \epsilon_E \} = \left\{ \begin{array}{l} \epsilon_{E\phi} \\ \epsilon_{E\theta} \\ \gamma_{E\phi\theta} \end{array} \right\} \quad 2.7(a)$$

and the stress vector is given by

$$\{ \sigma \} = \left\{ \begin{array}{l} \sigma_\phi \\ \sigma_\theta \\ \tau_{\phi\theta} \end{array} \right\} \quad 2.7(b)$$

The usual thin shell theory assumptions are that the normal direct and transverse shear stresses are negligible and their contribution to the strain energy is neglected.

The stress/strain relationship for thin shells is given by

$$\{\sigma\} = \frac{E}{(1-\nu^2)} \begin{bmatrix} 1 & \nu & 0 \\ \nu & 1 & 0 \\ 0 & 0 & \frac{(1-\nu)}{2} \end{bmatrix} \{e_E\} \quad 2.8$$

Hence the strain energy for a thin shell of revolution (Fig. 1)

is given by

$$V = \frac{E}{2(1-\nu^2)} \int_0^1 \int_0^{2\pi} \int_{-t/2}^{t/2} (\epsilon_\phi^2 + \epsilon_\theta^2 + 2\nu\epsilon_\phi\epsilon_\theta + \frac{(1-\nu)}{2}\gamma_{\phi\theta}^2) \left(\frac{r_s+z}{r_s}\right)(r+z.\sin\phi) dsd\theta dz \quad 2.9$$

The strain energy is found by substituting for the strains in equation 2.9 from Flügge's relationships, equations 2.5. This gives the strain energy in terms of generalised displacements and derivatives $\{\bar{\delta}\}$. The strain energy expression is integrated in the normal and tangential directions algebraically. The Flügge thin shell equations are given for small shell thickness to radius ratios. Terms of order $(t/r)^3$ are neglected in the algebraic integration. The partially integrated strain energy matrix $[D']$ after the algebraic integration is given in Appendix 2.

The strain energy for each element is then given by

$$V = \frac{1}{2} \int_0^1 \{\bar{\delta}\}^T [D'] \{\bar{\delta}\} ds \quad 2.10$$

which gives on substitution for the generalised displacements and derivatives

$$V = \frac{1}{2} \{\delta_1\}^T [A^{-1}]^T \int_0^1 [B]^T [D'] [B] ds [A^{-1}] \{\delta_1\} \quad 2.11$$

i.e. $V = \frac{1}{2} \{\delta_1\}^T [K_1] \{\delta_1\}$

in terms of the generalised nodal displacements.

The total strain energy of the structure is found by summing the individual contributions of each element. The solution of the structure subjected to an applied loading is found by the variational principle of the minimisation of the potential energy of the structure. The potential energy is given in terms of the strain energy and work done expressions.

$$U = V - W.D. \quad 2.12$$

where the work done expression for a static loading case is given by

$$W.D. = \{\delta\}^T \{F\} \quad 2.12(a)$$

where $\{F\}$ is a list of forces associated with the generalised displacements $\{\delta\}$ at all nodes.

The potential energy expression is minimised with respect to the nodal displacements to give the usual finite element equations (ref. 20).

$$0 = [K] \{\delta\} - \{F\} \quad 2.13$$

where $[K]$, the stiffness matrix of the complete shell, is found by summing the stiffness matrices for each element.

$$[K] = [A^{-1}]^T \int_0^1 [B]^T [D'] [B] ds [A^{-1}] \quad 2.13(a)$$

2.2.2 Computation of Element Matrices

The flow diagram for the algorithm to generate the Thin Shell of Revolution Finite Element stiffness and loading matrices is shown in Fig. 2.2. Gaussian quadrature (ref. 21) has been used for the numerical integration along the meridian of the shell to give

accurate strain energy terms. The integration points always yield a positive value of r , thus overcoming the singularity at the pole when $r=0$. Webster's second element (ref. 17) for generation of strain energy terms at the pole is not needed.

The terms associated with the displacement coefficients in excess of those sufficient to satisfy the generalised nodal displacements are termed "extra degrees of freedom". The extra degrees of freedom are associated individually with one element and the strain energy terms associated with them are placed in the lower portion of the element stiffness matrix. This position is dictated by the way in which the $[A]$ matrix is formed, Appendix 1.

The extra degrees of freedom are allocated positions in the combined strain energy matrix. By careful ordering of these positions the stiffness terms can be concentrated about the leading diagonal. Arbitrary ordering, see Fig. 2.3, places the stiffness terms associated with the extra degrees of freedom remote from the leading diagonal.

2.2.3 Solution Procedures

The total number of degrees of freedom needed to accurately model complex axisymmetric shells of revolution using the higher order ring finite elements is reasonably small. The full or banded stiffness matrix can then be retained in the core store of a medium sized computer.

Standard matrix inversion procedures or Cholesky algorithms for the symmetric decomposition of positive definite full and band matrices, see Wilkinson (refs. 22 & 23), are used for all examples

given. The Cholesky algorithms have been used for creep problems where the equivalent inverted stiffness matrices are used in subsequent re-solution stages.

2.3.1.1 Static Loading

The static loads contribute to the work done in the potential energy expression as

$$W.D. = \{\delta\}^T \{F\}$$

When the potential energy is minimised with respect to the nodal displacements the list of loads $\{F\}$ associated with each nodal displacement is left in the finite element equation 2.13.

2.3.1.2 Numerical Examples. (Static Loading)

Cylinder Clamped at One End and Loaded Radially at the Free End.

Pian (ref. 13) investigated the effect of using elements with different displacement functions by comparing solutions for a cylinder clamped at one end and loaded radially at the other. Pian's solutions, together with those for two idealisations using various orders of the higher order displacement function element, for the displacement under the load are shown in Fig. 2.4. The numbers of terms in the displacement functions and the degrees of freedom of the different idealisations are given in Fig. 2.4. These solutions are compared to solutions using 1 and 3 element idealisations of the higher order thin shell of revolution finite element.

The single element solution to this problem converges rapidly with increasing numbers of terms in the displacement functions, but even with 10 terms in the normal and meridional displacement functions

the solution is still 9% low. Numerical difficulties are likely to occur if more than about 10 terms are used in the displacement functions of a single element due to ill-conditioning of the equations. The 3 element solution with equal numbers of terms in the normal and meridional displacement functions converges well.

Comparison of the 3 element solution, with equal numbers of terms in each displacement function, with Pian's 3 element solution, with fewer terms in the meridional displacement function, illustrates the necessity of adequately representing both components of displacement, even though the meridional component is much smaller than the normal component.

2.3.2.1 Pressure Loading

The loading vector for pressure loads is determined by integrating the product of pressure and normal displacement over the area of the shell. This integration process is identical to that used in generating the stiffness terms. The integration in the tangential direction is algebraic and Gaussian quadrature is used in the meridional direction. The work done is given by

$$W.D. = \int_{Area} p w \, dArea \quad 2.14$$

where p , the applied surface pressure, is defined as $p(1 \text{ or } \cos n\theta)$ for axisymmetric or n^{th} harmonic Fourier loading and w is the generalised normal displacement.

$$W.D. = \int_0^1 \int_0^{2\pi} \{\bar{\delta}\}^T \{p\} \frac{(r_s + t/2)}{r_s} \, ds \, (r_s + t/2 \cdot \sin\phi) \, d\theta \quad 2.14(a)$$

The terms $\frac{(r_s+t/2)}{r_s}$ and $(\frac{r+t}{2} \cdot \sin\phi)$ depend on the shell surface to which the pressure is applied.

$$W.D. = \{\delta_i\}^T [A^{-1}]^T \int_0^1 [B]^T \{p'\} (\frac{r+t}{2} \cdot \sin\phi) ds \quad 2.14(b)$$

where $\{p'\}$ is the algebraic integrand in the tangential direction.

The minimisation of the potential energy gives the loading vector $\{F\}$ for the pressure loading as

$$\{F\} = \sum [A^{-1}]^T \int_0^1 [B]^T \{p'\} (\frac{r+t}{2} \cdot \sin\phi) ds \quad 2.15$$

The ring finite element of revolution is programmed to accept a linear variation of pressure in the meridional direction.

2.3.2.2 Numerical Examples, (Pressure Loading)

Pressurised Spherical Cap.

Pian (ref. 13) investigated the problem of a spherical cap subjected to external pressure, whose exact solution is given by Timoshenko and Woinowsky-Krieger (ref. 24). Pian's idealisation used 35 of the simplest conical frustra elements to approach the exact solution. A number of different idealisations were made with simple spherical elements as well as the higher order ones. The plots of Meridional Bending Moment and Circumferential Stress Resultant for single element idealisations with meridional and normal displacement functions of order 4, 6 and 8 are shown in Fig. 2.5(a). Results for 5 and 10 element idealisations of the shell, using elements with the simplest displacement functions, are shown in Figs. 2.5(b) and 2.5(c). The Meridional Bending Moments and Circumferential Stress Resultants when using 5 or 10

of the simplest elements give exact answers near the pole where the variation in the displacements is changing less rapidly. These results illustrate that large numbers of elements with the simplest displacement function are required to give accurate values for the stresses, whereas the solution for the single element idealisation with 8 terms in each displacement function is indistinguishable from the exact solution.

2.3.2.3 Torispherical Drumhead

The torispherical drumhead, Fig. 2.6(a), analysed experimentally by Findley, Moffat and Stanley (ref. 25) has been idealised using 6 axisymmetric thin shell of revolution finite elements. The prototype pressure vessel is No. 31 in (ref. 25).

The finite element analysis for the elastic stresses is shown in Fig. 2.6(b) compared with the experimental results. The discontinuities of the stresses between adjacent elements are so small that they are not apparent in Fig. 2.6(b) and a check on the discontinuities in the meridional bending moment and circumferential stress resultants confirmed this. The agreement between the two sets of results is excellent and shows the great power of the higher order element in idealising thin shells of revolution with complex stress functions.

2.3.2.4 3-Diameter Pressure Vessel

A stepped cylindrical pressure vessel was analysed originally as a grossly simplified vessel, Fig. 2.7(a), and as a more realistic idealisation, Fig. 2.7(b), to compare with the results of Bellamy and Fessler (ref. 26). A classical solution of the simple idealisation

of the 3-diameter pressure vessel given by Bellamy and Fessler was compared with a finite element solution. In the original analysis each half of the vessel was treated as two semi-infinite cylinders connected by a flexible annular diaphragm, whereas in the finite element solution the vessel was treated as a complete body. The agreement between the two solutions, Fig 2.7(a), is very satisfactory.

The second and more exact idealisation was limited by the constant thickness property of the elements which necessitated the omission of part of the knuckles from the internal corners as shown in Fig. 2.7(b). Further the analysis for the element is based on thin shell theory, and thus it was not expected that the element would be adequate to model the sections of the shell with large thickness to radius ratios.

Two finite element solutions for the inside and outside surface meridional stresses are compared with photoelastic results for the 3-diameter vessel in Fig. 2.7(c) and 2.7(d). In view of the assumptions associated with these finite element solutions, (i.e. thin shell theory and constant thickness elements) the agreement between the experimental and finite element solutions is very good. The large discontinuities in the stresses at the element junctions are due to thin shell approximation. The meridional bending moment and direct stress resultant gave only small discontinuities in these quantities at the element junctions. The difference in the photoelastic and finite element solutions for the meridional stresses at the inside surface between points B-C and G-H is due to the omission of the knuckles in the finite element solution.

2.3.3.1 Thermal Loading

Thermal loading is treated as an initial strain problem in developing the strain energy terms for the potential energy expression. The total strain is the sum of elastic and thermal strains and the strain energy is found by substituting for elastic strains in terms of total and thermal strains.

$$\begin{aligned}
 V &= \frac{1}{2} \int_{Vol} \{\epsilon_T - \epsilon_{Therm}\}^T [D] \{\epsilon_T - \epsilon_{Therm}\} dVol \quad (\text{see ref. 71}) \\
 V &= \frac{1}{2} \int_{Vol} \{\epsilon_T\}^T [D] \{\epsilon_T\} dVol - \int_{Vol} \{\epsilon_T\}^T [D] \{\epsilon_{Therm}\} dVol \\
 &\quad + \frac{1}{2} \int_{Vol} \{\epsilon_{Therm}\}^T [D] \{\epsilon_{Therm}\} dVol \quad 2.16
 \end{aligned}$$

The substitution of these terms in the potential energy equation together with those relating nodal displacements to total strains, equations 2.4, gives the potential energy in terms of the total nodal displacements. When the potential energy is minimised with respect to the nodal displacements the third term of equation 2.16 disappears, the first term giving the stiffness expression and the second term the equivalent nodal forces due to the thermal loadings.

$$\{F_e\} = [A^{-1}]^T \int_{Vol} [B]^T [DD]^T [D] \{\epsilon_{Therm}\} dVol \quad 2.17$$

where $\{\epsilon_T\} = [DD] \{\bar{\delta}\}$ 2.17(a)

The strain energy terms for the thermal deformation are found in the same way as the stiffness terms are generated. Algebraic integration in the radial and circumferential directions, terms of order greater than t^3 being neglected, and Gaussian numerical integration in the meridional direction is used.

The strain energy expression to be integrated is given by

$$V' = - \int_0^{2\pi} \int_{-t/2}^{t/2} \int_0^1 \frac{E}{(1-\nu^2)} \left(\epsilon_{\phi T} (\epsilon_{\phi Therm} + \nu \epsilon_{\theta Therm}) + \epsilon_{\theta T} (\epsilon_{\phi Therm} + \nu \epsilon_{\theta Therm}) \right) \frac{(r_s+z)}{r_s} ds (r+z \cdot \sin \phi) d\theta dz \quad 2.18$$

The Flügge shell theory used assumes that all strains are based on the mid-surface displacements. A more realistic value for the elastic strain at any point in the shell is found by modifying the radial displacement relative to its position to the mid-surface in the strain equations.

The temperature T at any point distance z away from the mid-surface is given by

$$T = T_0 + \frac{z}{t} \Delta T_0 \quad 2.19(a)$$

The mean temperature \bar{T} between this point and the mid-surface is given by

$$\bar{T} = T_0 + \frac{z}{2t} \Delta T_0 \quad 2.19(b)$$

The radial displacement w' at a point distance z from the mid-surface is given by

$$w' = w + z \alpha \bar{T} \quad 2.20$$

The elastic meridional strain is given by

$$\epsilon_{\phi E} = \frac{\partial v}{\partial s} - \frac{z r_s}{(r_s+z)} \frac{\partial^2 w}{\partial s^2} + \frac{(w' + \alpha z \bar{T})}{(r_s+z)} - \alpha T \quad 2.21(a)$$

$$\epsilon_{\phi E} = \epsilon_{\phi T} - \alpha \left(T - \frac{z}{(r_s+z)} \bar{T} \right) \quad 2.21(b)$$

and the equivalent thermal strain is therefore given by

$$\epsilon_{\phi Therm} = \alpha \left(T - \frac{z}{(r_s+z)} \bar{T} \right) \quad 2.21(c)$$

Similarly the elastic circumferential strain is given by

$$\epsilon_{\theta_E} = \frac{1}{r} \frac{\partial u}{\partial \theta} + \frac{v \cos \phi (r_s + z)}{r_s (r + z \sin \phi)} - \frac{z}{(r + z \sin \phi)} \left(\frac{1}{r} \frac{\partial^2 w}{\partial \theta^2} + \cos \phi \frac{\partial w}{\partial s} \right) + \frac{\sin \phi (w + z \alpha \bar{T})}{(r + z \sin \phi)} - \alpha T \quad 2.22(a)$$

$$\epsilon_{\theta_E} = \epsilon_{\theta_T} - \alpha \left(T - \frac{z \sin \phi \bar{T}}{(r + z \sin \phi)} \right) \quad 2.22(b)$$

and the equivalent thermal strain is therefore

$$\epsilon_{\theta_{Therm}} = \alpha \left(T - \frac{z \sin \phi \bar{T}}{(r + z \sin \phi)} \right) \quad 2.22(c)$$

The equations 2.21(c) and 2.22(c) are substituted into equation 2.18 in terms of T_0 and ΔT_0 which are functions of meridional length. The terms resulting after the algebraic integration in the radial and circumferential directions are given in Appendix 3 as a vector $\{DD'\}$. The equivalent nodal forces for each element are then given by

$$\{F_e\} = [A^{-1}]^T \int_0^1 [B]^T \{DD'\} ds \quad 2.23$$

2.3.3.2 Numerical Examples. (Thermal Loading)

Standard Solutions for Cylindrical and Spherical Shells

The thermal stresses for a cylindrical shell and a spherical shell when subjected to an overall temperature rise and a through thickness temperature gradient have been found.

When the shells are subjected to a uniform temperature rise significant stresses are given without equation 2.20 being used. By adjusting the thermal strains by equations 2.21 and 2.22 the stresses given for a uniform temperature rise are negligible.

The results for a mean temperature rise and through thickness

temperature gradient are given in Table 2.1 and are compared to the well known solutions given by Roark (ref. 27). The slight deviation is caused by the Roark solutions making no allowance for variation of the radial displacement through the shell thickness. This gives a difference of approximately 1% maximum for a shell with r/t of 10:1.

2.3.3.3 Semi-Infinite Cylinder Subjected to a Varying Internal Wall Temperature

A semi-infinite cylinder subjected to an exponentially decreasing temperature on the inside surface and a constant outside surface temperature was considered. The temperature variation is given by

$$T = \frac{T^*}{2} \left(1 - \frac{2z}{h}\right) e^{-x/r}$$

The following two sets of boundary conditions at the end of the cylinder were considered,

- (i) No constraints
- (ii) Unrestrained radial displacement but with zero slope.

The finite element idealisation of the cylinder and the inside wall temperature distribution are shown in Fig. 2.8(a). The finite element solutions for the radial displacement and the hoop stress distributions, shown in Fig. 2.8(b), agree well with the exact thin cylinder solutions given by Yang and Lee (ref. 28) and developed in Appendix 4.

2.3.4.1 Creep Deformation

The method of finite element analysis applied to creep deformation

is outlined fully in Chapter 5. The general method however is briefly explained here with its application to the thin shell of revolution finite element.

To generate the equivalent nodal forces the creep strains are treated as initial strains in the same manner as the thermal strains described previously. The creep deformation occurring during a small time increment is assumed to take place under a state of constant stress. The equivalent nodal forces due to these creep strain increments are found from

$$\{F_e\} = [A^{-1}]^T \int_{Vol} [B]^T [DD]^T [D] \{\epsilon_{creep}\} dVol \quad 2.24$$

The changes in elastic strains are found from the change in total strains caused by this loading and the change in creep strain from which this loading has been calculated

$$\{\Delta \epsilon_E\} = \{\Delta \epsilon_T\} - \{\Delta \epsilon_C\} \quad 2.25$$

The change in stress over the time increment is calculated from these strains and provided this change is within set limits the calculation proceeds.

The equivalent nodal forces to the creep strains after algebraic integration in the radial and circumferential directions are given as

$$\{\Delta F_e\} = [A^{-1}]^T \int_0^1 [B]^T \{D_{creep}\} ds \quad 2.26$$

where the vector $\{D_{creep}\}$ is given in Appendix 5.

The flow diagram for the algorithm to calculate creep deformations for the thin shell finite element is given in Fig. 2.9. The

philosophy behind this algorithm is different from the creep analyses described in Chapter 5. After the initial solution all creep deformations are calculated from creep and total strain information held in the matrix AKREAP at each Gaussian integration point. For each strain component, meridional, circumferential and shear, six terms are retained to enable the creep calculations to proceed. These are

1. last correct stress
2. change in stress
3. total creep strain
4. change in creep strain
5. total strain
6. change in total strain.

These eighteen items together with the last correct equivalent strain and change in equivalent strain at each integration point are held in AKREAP.

For the initial pass through the algorithm the total strains and stresses at time $t=0$ are found from the nodal displacements. The equivalent uniaxial stress is found so that the multiaxial creep strains over a small time increment Δt can be calculated from the uniaxial creep law. From these creep strains a set of equivalent nodal forces are calculated, which on solution give a set of nodal displacements equivalent to these creep strains.

A checking pass is made through the algorithm where the change in elastic stress over the time increment is found from equations 2.25 and 2.8. This stress change is compared to the initial equivalent uniaxial stress at the integration point and if greater than the ratio specified a new set of creep strains are computed

with a reduced time increment. Subsequent creep strain calculations are made using the information stored in AKREAP, one pass generating the creep strain increments, the next checking the previous creep strain increments.

2.3.4.2 Numerical Examples, (Creep Deformation)

Simply Supported Cylinder Subjected to Internal Pressure.

A simply supported thin shell of revolution subjected to internal pressure has been analysed by Murakami and Iwatsuki (ref. 29) and compared to the analytical solution of a long thin cylinder without end supports subjected to internal pressure. A thin shell of revolution finite element idealisation has been used to analyse both the above loading conditions. The exact analytical solution for a long thin cylindrical shell without end supports subjected to internal pressure assumes no variation of meridional or circumferential stress through the shell thickness. In this case there is no stress relaxation as the creep deformation proceeds, and the non-dimensional radial displacement is given as a function of the elapsed time.

$$\frac{Ehw}{pa^2} = \frac{(1-\nu)}{2} + \left(\frac{3}{4}\right)^{\frac{n+1}{2}} EA \left(\frac{pa}{h}\right)^{n-1} t^m \quad 2.27$$

where the empirical creep law is

$$e_C = A \sigma^n t^m \quad 2.28$$

Finite element solutions and solutions given by equation 2.27 for the non-dimensional radial deformation of the cylindrical shell at various times are given in Table 2.2. Values obtained from equation 2.27 are given for both zero starting time and

for a starting time of 10^{-5} hrs. Finite element solutions and the percentage differences between these and the values given by equation 2.27 are given only for the latter case.

The derivation of equation 2,27 is based on the assumption that the pressure load is applied on the mid-surface and that the meridional and circumferential stresses do not vary through the shell thickness. In the finite element analysis the pressure is applied on the inside surface and the circumferential strain varies inversely with the radius. Thus, in the finite element analysis there is a slight redistribution of stress as the creep proceeds and, for a given pressure load, the average equivalent uniaxial stress is about $2\frac{1}{2}\%$ lower than in the analysis for equation 2.27. This reduction of stress would reduce the radial displacement by about 9% and, if the stresses were constant, the reduction would be independent of time. It may be seen from Table 2.2 that the differences between the finite element results and those from equation 2.27 are somewhat greater than 9%. The percentage difference is tending to approximately 9% with increasing time and it would appear that the discrepancy is due to the slight stress redistribution which occurs in the finite element solution.

For the simply supported cylinder (Fig. 2.10(a)) a single thin shell of revolution finite element was used for the idealisation with the radial and meridional displacements represented by 8 term displacement functions. The finite element solutions for the non-dimensional radial displacement, for both time hardening and strain hardening creep laws, are compared with results given by Murakami and Iwatsuki (ref. 29) in Fig. 2.10(b). The latter results were obtained by numerical integration with respect to time, of the

finite difference forms of the cylindrical shell differential equations. Again the finite element solutions for the non-dimensional radial displacement are smaller than Murakami and Iwatsuki's results, (ref. 29). The differences are again due to the pressure load being applied at the inside surface for the finite element analysis rather than at the mid-surface in the published results. This has been confirmed by applying an internal pressure to the finite element model with a mean hoop stress identical to that found from simple thin shell theory with the original internal pressure applied at the shell mid-surface. The radial creep deformation of the simply supported cylinder under this new internal pressure agrees closely with the results of Murakami and Iwatsuki.

Chapter 3

The Parametric Family of Finite Elements

Notation

a	Gaussian integration point
n	Gaussian integration order
p	pressure
u,v,w	displacements in cartesian co-ordinates
x,y,z	cartesian co-ordinates
x',y',z'	local cartesian co-ordinates
E	Young's modulus
H	Gaussian weighting factor
K	shear strain factor
P	polynomial function
T	temperature
V	strain energy
W.D.	work done
α	coefficient of thermal expansion
δ	displacement normal to shell surface
ϵ	direct strain
γ	shear strain
ν	Poisson's ratio

Subscripts

e	element axes
i	nodal quantities
j,k,l	Gauss integration points
m,n,p	Gauss order
E	elastic strains

L	local axes
O	thermal strains
T	total strains

Matrices and Vectors

$\{ \}$	column vector
$[\]$	matrix
$[\]^T$	transpose of matrix
$[\bar{A}]$	matrix relating nodal values to coefficients of functions
$[A]$	partition of \bar{A} matrix
$[AA]$	matrix relating nodal pressures to pressure function coefficients
$[B]$	matrix relating strains to displacement function coefficients
$[D]$	stress/strain matrix
$[D']$	stress/strain matrix for thick shell
$\{ F \}$	force vector
$[J]$	Jacobian matrix
$\{ P(\xi, \eta, \zeta) \}$	polynomial function for displacements and geometry
$\{ P_p(\xi, \eta) \}$	polynomial function for pressure loads
$[U]$	upper triangular matrix
$[\alpha_u, \alpha_v, \alpha_w]$	displacement function coefficients
$[\alpha_x, \alpha_y, \alpha_z]$	geometric function coefficients
$\{ \sigma \}$	stress vector
$\{ e \}$	strain vector
$\{ e' \}$	strain vector for thick shell
$\{ \delta \}$	displacement vector
$[\theta]$	direction cosine array

$\hat{v}_\xi, \hat{v}_\eta, \hat{v}_\zeta$

vectors in ξ, η, ζ directions

$\hat{v}_x', \hat{v}_y', \hat{v}_z'$

normalised vectors in shell axes x', y', z'

3.1 Introduction

Large numbers of elements with simple geometric shapes e.g. triangles, parallelograms, tetrahedra, parallelepipeds etc. are required to give an accurate idealisation of the geometry of complex structures. The advantage of using sophisticated elements with large numbers of degrees of freedom may not be fully realised if large numbers of elements are required to idealise the geometry of the structure. These difficulties are overcome when curvilinear elements with curved boundaries are mapped into simple geometric shapes by suitable co-ordinate transformations. For each element functions which define the geometry of the element and functions which define the displacement variation over the element are required. Ergatoudis, Irons and Zienkiewicz (ref. 30) developed a set of "isoparametric" elements in which the functions used to define the geometry and the variation of displacements are identical. Structures can be accurately modelled with a few of these elements compared with the large numbers of the simple type of elements required to give equivalent accuracy. These elements have been used to analyse a number of complex structures, Zienkiewicz (ref. 31), Ergatoudis et al (ref. 32), Hellen (ref. 33), and offer the best general family of finite elements for the analysis of large in-plane and 3-dimensional structures.

Application of standard 3-dimensional isoparametric elements to thick shell problems lead to some difficulties because of the large stiffness coefficients associated with the relative displacements normal to the shell. Further, large numbers of degrees of freedom are associated with the displacements through

the shell thickness and by using the usual shell assumptions, that the normals to the middle surface remain straight after deformation, a large economy on the total number of degrees of freedom can be made. A development of the parametric family of elements was made by Ahmad (ref. 34) who proposed a thick shell "super-parametric" finite element. The term "super-parametric" means that the function defining the geometry of the element is more general than the displacement function (ref. 31). The Ahmad element has been modified to be more useful when using an idealisation which contains other parametric elements. The original Ahmad element was defined entirely by a series of nodes at the mid-surfaces of the element. The degrees of freedom at each node are 3 translations and 2 rotations of the shell normal. However it is difficult to join these elements to the isoparametric elements which have 3 translations at each of the nodes.

A thick shell isoparametric element, based on the proposals of Ahmad, which has nodes on the surface edges of the element rather than the mid-surface has been developed. Each single node of the Ahmad element is replaced by a pair of nodes in the new element. The number of degrees of freedom of each element is identical as each pair of nodes in the modified element is constrained such that straining of the mid-surface normal is neglected.

This element can be used to model the shell portion of a turbine casing together with the standard isoparametric element which models the flange section. The elements are connected by a transition parametric element based on the isoparametric element which has modified stiffness terms associated with the displacements

of the face joined to the thick shell element. These elements are shown in Fig. 3.1.

Standard tests have been performed for pressure loadings and the convergence to the exact solutions with each type of element is shown.

3.2.1 Isoparametric Finite Elements

The basic concept of the isoparametric finite element is that the polynomial functions used to describe the geometric shape of the element are identical to those used to describe the variation of the displacements over the element. To describe the element geometry in cartesian space a set of curvilinear co-ordinates (ξ, η, ζ) are used. These co-ordinates map a cube into a distorted form, as shown in Fig. 3.2. The curvilinear co-ordinates vary within the bounds $-1 \leq \xi \leq +1$ etc.

The co-ordinate transformations and variation of displacements are defined by polynomial functions in the curvilinear co-ordinates.

$$[x, y, z] = \{P(\xi, \eta, \zeta)\}^T [\alpha_x \alpha_y \alpha_z] \quad 3.1(a)$$

$$[u, v, w] = \{P(\xi, \eta, \zeta)\}^T [\alpha_u \alpha_v \alpha_w] \quad 3.2$$

where $\{P(\xi, \eta, \zeta)\}^T$ is a vector of functions of the curvilinear co-ordinates ξ, η, ζ and their coefficients are α_x, α_u , etc. The coefficients α_x, α_u , etc. can be defined in terms of the nodal co-ordinates x_i, y_i, z_i and the nodal displacements u_i, v_i, w_i by substituting the nodal curvilinear co-ordinates in equations 3.1 and 3.2

$$\{x_i\} = [A] \{\alpha_x\} \text{ etc.} \quad 3.3(a)$$

and $\{u_i\} = [A] \{\alpha_u\} \text{ etc.} \quad 3.4(a)$

Consequently $\{\alpha_x\} = [A]^{-1} \{x_i\}$ etc. 3.3(b)

and $\{\alpha_u\} = [A]^{-1} \{u_i\}$ etc. 3.4(b)

The displacements and geometry of the element are given in terms of the nodal values as

$$x = \{P(\xi, \eta, \zeta)\}^T [A]^{-1} \{x_i\} \text{ etc.} \quad 3.1(b)$$

i.e. $x = \{N_1(\xi, \eta, \zeta)\}^T \{x_i\}$

where $\{N_1(\xi, \eta, \zeta)\}^T = \{P(\xi, \eta, \zeta)\}^T [A]^{-1}$

is termed the shape function.

Zienkiewicz (ref. 31) discourages use of this method of defining the shape functions as there is a possibility that the inverse of $[A]$ may not exist. This method however is much simpler and more economical than defining shape functions. The $[A]$ matrix is non-singular for all the types of parametric element used.

The order of the polynomial function is dependent on the number of mid-side nodes. The total number of terms in the function is identical to the number of nodes in the element, as the nodal values determine uniquely the variation of the function. The choice of the polynomial function is made by retaining the lowest possible terms compatible with the order of the displacement functions required. The polynomial function used for the 20 node isoparametric element of Fig. 3.1, which has 1 mid-side node on all edges, has a parabolic variation in ξ, η and ζ and is given by

$$\{P(\xi, \eta, \zeta)\}^T = \{1, \xi, \eta, \zeta, \xi\eta, \eta\zeta, \xi\zeta, \xi^2, \eta^2, \zeta^2, \xi^2\eta, \eta^2\zeta, \xi\zeta^2, \xi^2\zeta, \xi\eta^2, \eta^2\zeta^2, \xi\eta\zeta^2, \xi^2\zeta^2, \xi\eta^2\zeta^2, \xi^2\eta\zeta^2, \xi\eta^2\zeta^2\}^T \quad 3.5$$

The element is conforming because the displacements on any surface

are uniquely defined by the nodal displacements of that surface. The polynomial function also satisfies the usual convergence criteria of rigid body modes and constant first derivative, Zienkiewicz (ref. 31).

3.2.2 Generation of Element Matrices

The finite element equations are obtained from the minimisation of the total potential energy of a structure, given in terms of the strain energy and the work done, with respect to the variation of the nodal displacements of the structure,

$$\text{i.e. } \frac{\partial}{\partial \delta} \left(\frac{1}{2} \int_{\text{Vol}} \{\epsilon\}^T \{\sigma\} \, d\text{Vol} - \{\delta\}^T \{F\} \right) = 0 \quad 3.6$$

for all nodal displacements.

The strain energy can be calculated individually for each element and the terms summed for the complete structure. The strain energy for each element is

$$U = \frac{1}{2} \int_{\text{Vol}} \{\epsilon\}^T \{\sigma\} \, d\text{Vol} \quad 3.7$$

The stress is related to the strain by the $[D]$ matrix

$$\{\sigma\} = [D] \{\epsilon\}$$

$$\text{where } \{\sigma\} = \begin{Bmatrix} \sigma_x \\ \sigma_y \\ \sigma_z \\ \tau_{xy} \\ \tau_{yz} \\ \tau_{zx} \end{Bmatrix} \quad \text{and} \quad \{\epsilon\} = \begin{Bmatrix} \epsilon_x \\ \epsilon_y \\ \epsilon_z \\ \delta_{xy} \\ \delta_{yz} \\ \delta_{zx} \end{Bmatrix}$$

and $[D] = \frac{E}{(1+\nu)(1-2\nu)}$

$$\begin{bmatrix} 1-\nu & \nu & \nu & 0 & 0 & 0 \\ & 1-\nu & \nu & 0 & 0 & 0 \\ & & 1-\nu & 0 & 0 & 0 \\ & & & \frac{1-2\nu}{2} & 0 & 0 \\ \text{sym} & & & & \frac{1-2\nu}{2} & 0 \\ & & & & & \frac{1-2\nu}{2} \end{bmatrix} \quad 3.8$$

The strains are defined in terms of the displacement function coefficients as

$$\{\epsilon\} = \begin{Bmatrix} \frac{\partial u}{\partial x} \\ \frac{\partial v}{\partial y} \\ \frac{\partial w}{\partial z} \\ \frac{\partial u}{\partial y} + \frac{\partial v}{\partial x} \\ \frac{\partial v}{\partial z} + \frac{\partial w}{\partial y} \\ \frac{\partial w}{\partial x} + \frac{\partial u}{\partial z} \end{Bmatrix} = \begin{bmatrix} \frac{\partial p}{\partial x}, 0, 0 \\ 0, \frac{\partial p}{\partial y}, 0 \\ 0, 0, \frac{\partial p}{\partial z} \\ \frac{\partial p}{\partial y}, \frac{\partial p}{\partial x}, 0 \\ 0, \frac{\partial p}{\partial z}, \frac{\partial p}{\partial y} \\ \frac{\partial p}{\partial z}, 0, \frac{\partial p}{\partial x} \end{bmatrix} \begin{Bmatrix} \alpha_u \\ \alpha_v \\ \alpha_w \end{Bmatrix} \quad 3.9$$

i.e. $\{\epsilon\} = [B] \{\alpha\}$ 3.9(a)

The displacement coefficients are defined in terms of the nodal displacements from equation 3.4(b)

$$\{\alpha\} = [\bar{A}]^{-1} \{\delta_1\} \quad 3.10$$

where $[\bar{A}]^{-1} = \begin{bmatrix} [A]^{-1} & 0 & 0 \\ & [A]^{-1} & 0 \\ \text{sym} & & [A]^{-1} \end{bmatrix}$ 3.10(a)

This gives the strain energy, equation 3.7 as

$$V = \frac{1}{2} \{ \delta_i \}^T [\bar{A}]^T \int_{Vol} [B]^T [D] [B] dVol [\bar{A}]^{-1} \{ \delta_i \} \quad 3.7(a)$$

The derivatives of the polynomial function $P(\xi, \eta, \zeta)$ with respect to the cartesian co-ordinates x, y, z in the $[B]$ matrix are given by

$$\begin{Bmatrix} \frac{\partial P}{\partial \xi} \\ \frac{\partial P}{\partial \eta} \\ \frac{\partial P}{\partial \zeta} \end{Bmatrix} = \begin{bmatrix} \frac{\partial x}{\partial \xi} & \frac{\partial y}{\partial \xi} & \frac{\partial z}{\partial \xi} \\ \frac{\partial x}{\partial \eta} & \frac{\partial y}{\partial \eta} & \frac{\partial z}{\partial \eta} \\ \frac{\partial x}{\partial \zeta} & \frac{\partial y}{\partial \zeta} & \frac{\partial z}{\partial \zeta} \end{bmatrix} \begin{Bmatrix} \frac{\partial P}{\partial x} \\ \frac{\partial P}{\partial y} \\ \frac{\partial P}{\partial z} \end{Bmatrix} = [J] \begin{Bmatrix} \frac{\partial P}{\partial x} \\ \frac{\partial P}{\partial y} \\ \frac{\partial P}{\partial z} \end{Bmatrix} \quad 3.11$$

The value of the Jacobian matrix $[J]$ can be found as the functions x, y, z are explicitly defined in terms of the curvilinear co-ordinates ξ, η, ζ from equation 3.1. Further the left hand vector can be evaluated directly as the polynomial expression is defined in terms of the curvilinear co-ordinates. The Jacobian matrix is inverted to give the derivatives of the polynomial function with respect to the cartesian co-ordinates.

$$\begin{Bmatrix} \frac{\partial P}{\partial x} \\ \frac{\partial P}{\partial y} \\ \frac{\partial P}{\partial z} \end{Bmatrix} = [J]^{-1} \begin{Bmatrix} \frac{\partial P}{\partial \xi} \\ \frac{\partial P}{\partial \eta} \\ \frac{\partial P}{\partial \zeta} \end{Bmatrix} \quad 3.12$$

These values are substituted in the strain/polynomial coefficient matrix of equation 3.9. The matrices in equation 3.7(a) are now defined in terms of curvilinear co-ordinates and the limits of the integration must be similarly modified. The transformation

of the variables is made using the determinant of the Jacobian matrix (ref. 35)

$$dx dy dz = \det [J] d\xi d\eta d\zeta \quad 3.13$$

3.2.3 Numerical Integration

The limits of integration are over a cube, not the distorted shape of the element, and are within the limits -1 to +1 for each co-ordinate direction.

We now have

$$\sum \left([A]^{-T} \int_{-1}^{+1} \int_{-1}^{+1} \int_{-1}^{+1} [B]^T [D] [B] \det [J] d\xi d\eta d\zeta [A]^{-T} \{ \delta_i \} \right) - \{ F \} = 0 \quad 3.14$$

It is impossible to perform this integration explicitly and numerical integration has been used. The process employed is that of Gaussian quadrature (ref. 21) where the integral of a function $f(x)$ is given by the summation

$$\int_{-1}^{+1} f(x) dx = \sum_{j=1}^n H_j f(a_j) \quad 3.15$$

where n is the number of summation points and H_j the weighting factor for the function when $x=a_j$. Table 3.1 gives values of H and a for Gauss values up to $n=6$. For n sampling points a polynomial of degree $2n-1$ can be integrated exactly.

To evaluate the triple integral of equation 3.14

$$[A^{-1}]^T \int_{-1}^{+1} \int_{-1}^{+1} \int_{-1}^{+1} f(\xi, \eta, \zeta) d\xi d\eta d\zeta [A^{-1}] \quad 3.14(a)$$

it is necessary to do the triple summation

$$\int_{-1}^1 \int_{-1}^1 \int_{-1}^1 f(\xi, \eta, \zeta) d\xi d\eta d\zeta = \sum_{j=1}^m \sum_{k=1}^n \sum_{l=1}^p H_j H_k H_l f(\xi_j, \eta_k, \zeta_l) \quad 3.16$$

The term $f(\xi_j, \eta_k, \zeta_l)$ can be directly found for all elements and the stiffness expression in the general equation can be calculated. It should be noted that the Gauss order, although usually the same in each curvilinear direction, may differ to suit the order of the polynomial functions in those directions.

3.2.4 Generation of Thermal Loads

The strain energy is given by the stresses and elastic strains which are a function of the total strains less any initial strains due to thermal expansion. In equation 3.6 the strain expressions are identical to the elastic strains. These have to be modified by

$$\{\epsilon_E\} = \{\epsilon_T\} - \{\epsilon_0\} \quad 3.17$$

where $\{\epsilon_0\}$ are the thermal strains. For each element the strain energy term in the potential energy expression is (ref. 71)

$$V = \frac{1}{2} \int_{Vol} \{\epsilon_E\}^T \{\sigma\} dVol = \frac{1}{2} \int_{Vol} \{\epsilon_T - \epsilon_0\}^T [D] \{\epsilon_T - \epsilon_0\} dVol$$

which reduces to

$$V = \frac{1}{2} \int_{Vol} \{\epsilon_T\}^T [D] \{\epsilon_T\} dVol - \int_{Vol} \{\epsilon_T\}^T [D] \{\epsilon_0\} dVol - \frac{1}{2} \int_{Vol} \{\epsilon_0\}^T [D] \{\epsilon_0\} dVol \quad 3.18$$

Defining the total strains $\{\epsilon_T\}$ in terms of the nodal displacements gives the strain energy as

$$V = \frac{1}{2} \{\delta_1\}^T [\bar{A}]^{-T} \int_{Vol} [B]^T [D] [B] dVol [\bar{A}]^{-1} \{\delta_1\} - \{\delta_1\}^T [\bar{A}]^{-T} \int_{Vol} [B]^T [D] \{\epsilon_0\} dVol - \frac{1}{2} \int_{Vol} \{\epsilon_0\}^T [D] \{\epsilon_0\} dVol \quad 3.19$$

When these terms are summed for all the elements and the potential energy is minimised with respect to the nodal displacements the finite element equations for each element are given as

$$\underbrace{[\bar{A}]^{-T} \int_{Vol} [B]^T [D] [B] dVol [\bar{A}]^{-1} \{\delta_1\}}_{\text{Stiffness Terms}} - \underbrace{[\bar{A}]^{-T} \int_{Vol} [B]^T [D] \{\epsilon_0\} dVol}_{\text{Equivalent Nodal Forces}} \quad 3.20$$

The equivalent nodal forces to the thermal strains are given

by

$$\{F_e\} = [\bar{A}]^{-T} \int_{Vol} [B]^T [D] \{\epsilon_0\} dVol \quad 3.21$$

To determine the forces due to the thermal strains the numerical integration is performed identically to equation 3.16. The values of the thermal strains are given by the coefficient of linear expansion α and the temperature T at the Gaussian integration point.

$$\{\epsilon_0\} = \begin{Bmatrix} \alpha T \\ \alpha T \\ \alpha T \\ 0 \\ 0 \\ 0 \end{Bmatrix} \quad 3.22$$

3.2.5 Pressure Loading

The Work Done by the pressure p over the face of an element is given by

$$W.D. = \int_{Area} p \delta \, dArea \quad 3.23$$

Here δ is defined as the displacement normal to the surface of the elements. The normal displacement is expressed in terms of the cartesian displacements u, v and w as follows.

The vectors \hat{V}_ξ and \hat{V}_η are tangent to the surfaces when $\zeta = -1$ or $\zeta = +1$ and are given by

$$\hat{V}_\xi = \frac{\partial x}{\partial \xi} \hat{i} + \frac{\partial y}{\partial \xi} \hat{j} + \frac{\partial z}{\partial \xi} \hat{k} \quad 3.24(a)$$

$$\hat{V}_\eta = \frac{\partial x}{\partial \eta} \hat{i} + \frac{\partial y}{\partial \eta} \hat{j} + \frac{\partial z}{\partial \eta} \hat{k} \quad 3.24(b)$$

where x, y, z are defined by equation 3.1.

The vector \hat{V} normal to the surface is normal to both \hat{V}_ξ and \hat{V}_η and is given by their cross product

$$\hat{V} = \hat{V}_\xi \times \hat{V}_\eta \quad 3.25(a)$$

which gives

$$\hat{V} = \left(\frac{\partial y}{\partial \xi} \frac{\partial z}{\partial \eta} - \frac{\partial y}{\partial \eta} \frac{\partial z}{\partial \xi} \right) \hat{i} + \left(\frac{\partial x}{\partial \eta} \frac{\partial z}{\partial \xi} - \frac{\partial x}{\partial \xi} \frac{\partial z}{\partial \eta} \right) \hat{j} + \left(\frac{\partial x}{\partial \xi} \frac{\partial y}{\partial \eta} - \frac{\partial x}{\partial \eta} \frac{\partial y}{\partial \xi} \right) \hat{k} \quad 3.25(b)$$

This vector when normalised gives the direction cosines of the normal to the $\zeta = -1$ or $+1$ surfaces relative to the element axes

$$\hat{v} = \Theta_1 \hat{i} + \Theta_2 \hat{j} + \Theta_3 \hat{k} = \{ \Theta \}^T \left\{ \begin{matrix} \hat{i} \\ \hat{j} \\ \hat{k} \end{matrix} \right\} \quad 3.25(c)$$

Hence the Work Done by the pressure load on each element is given by

$$W.D. = \int_{Area} p \{u, v, w\}^T \{ \Theta \} \, dArea \quad 3.26$$

Defining the cartesian displacements in terms of the nodal displacements gives the Work Done as

$$W.D. = \left\{ \delta_1 \right\}^T \left[\bar{A} \right]^{-T} \int_{Area} \left\{ \begin{array}{l} \theta_1 P(\xi, \eta, \zeta) \\ \theta_2 P(\xi, \eta, \zeta) \\ \theta_3 P(\xi, \eta, \zeta) \end{array} \right\} p \, dArea \quad 3.27(a)$$

A set of equivalent nodal forces is evaluated when the total work done expression is differentiated with respect to the nodal displacements in the minimisation of the total potential energy expression. This gives the equivalent nodal forces for each element as

$$\left\{ F_e \right\} = \left[\bar{A} \right]^{-T} \int_{Area} \left\{ \begin{array}{l} \theta_1 P(\xi, \eta, \zeta) \\ \theta_2 P(\xi, \eta, \zeta) \\ \theta_3 P(\xi, \eta, \zeta) \end{array} \right\} p \, dArea \quad 3.27(b)$$

The face being subjected to the pressure forces is described in a set of curvilinear co-ordinates and it is convenient to use the same numerical integration process used in the generation of the element stiffness matrices. Only two of the summations are needed when the value of the third co-ordinate ζ is -1 or +1. These two values allow internal and external pressure forces to be applied although when external pressure forces are applied $\zeta = +1$ the integral has to be multiplied by -1 as the normal defined by the tangents is outwards from the element. The scaling factor for integration in the curvilinear co-ordinates is introduced by not normalising the normal vector \hat{V} as the magnitude of this vector is equal to the ratios of the areas of the transformation. The equivalent nodal forces for pressure loading are given by

$$\left\{ F_e \right\} = \left[A^{-1} \right]^T \sum_{j=1}^n \sum_{k=1}^n H_j H_k \left\{ F(\xi_j, \eta_k, \zeta) \right\} \quad 3.28(a)$$

where $\zeta = -1$ or $+1$ and

$$\{F(\xi_j, \eta_k, \zeta)\} = \begin{Bmatrix} P(\xi_j, \eta_k, \zeta) \\ P(\xi_j, \eta_k, \zeta) \\ P(\xi_j, \eta_k, \zeta) \end{Bmatrix}^T \begin{Bmatrix} \frac{\partial y}{\partial \xi_j} \frac{\partial z}{\partial \eta_k} & \frac{\partial y}{\partial \eta_k} \frac{\partial z}{\partial \xi_j} \\ \frac{\partial x}{\partial \eta_k} \frac{\partial z}{\partial \xi_j} & \frac{\partial x}{\partial \xi_j} \frac{\partial z}{\partial \eta_k} \\ \frac{\partial x}{\partial \xi_j} \frac{\partial y}{\partial \eta_k} & \frac{\partial x}{\partial \eta_k} \frac{\partial y}{\partial \xi_j} \end{Bmatrix} p_{jk}$$

where the pressure p varies across the element surface.

3.3.1 Thick Shell Parametric Finite Elements

The element formulation for the thick shell finite element is based on the usual shell assumption of negligible through thickness direct stresses. These stresses are assumed to contribute nothing to the strain energy. The element is different to that proposed by Ahmad (ref. 34) in that the quadratic element is defined by 16 nodes each with 3 translations, compared with 8 nodes each with 3 translations and 2 rotations. Each node on the mid-surface of the "Ahmad" element is replaced by a pair of nodes on the outside surfaces of the shell. The difference in the total number of degrees of freedom is eliminated by constraining the shell thickness to remain constant. The degrees of freedom normal to the shell surface at each pair of nodes are made identical.

The co-ordinate transformations and displacements are again defined by polynomial functions, the coefficients of which are defined by the nodal values. The polynomial function for the 16 node thick shell parametric element with mid-side nodes on the top and bottom faces is

$$P(\xi, \eta, \zeta)^T = \left\{ 1, \xi, \eta, \zeta, \xi\eta, \eta\zeta, \xi\zeta, \xi^2, \eta^2, \xi^2\eta, \eta^2\zeta, \xi^2\zeta, \xi\eta^2, \xi^2\eta\zeta, \xi\eta^2\zeta \right\}$$

This element is also conforming because it is an isoparametric element.

3.3.2 Generation of Element Matrices

In order to eliminate the normal direct stress term from the strain energy expression it is convenient to set up local cartesian axes which include the normal to the shell. The orthogonal axes which define the local strain components are found from the variation of the functions defining the element geometry. The vectors in the ξ direction \hat{V}_ξ and η direction \hat{V}_η for any $\zeta = \text{constant}$ surface give the vector \hat{V}_z' normal to this surface as their cross product

$$\hat{V}_z' = \hat{V}_\xi \times \hat{V}_\eta \quad 3.30(a)$$

where $\hat{V}_\xi \times \hat{V}_\eta$ are given in equations 3.24 and

$$\hat{V}_z' = \left(\frac{\partial y}{\partial \xi} \frac{\partial z}{\partial \eta} - \frac{\partial y}{\partial \eta} \frac{\partial z}{\partial \xi} \right) \hat{i} + \left(\frac{\partial x}{\partial \eta} \frac{\partial z}{\partial \xi} - \frac{\partial x}{\partial \xi} \frac{\partial z}{\partial \eta} \right) \hat{j} + \left(\frac{\partial x}{\partial \xi} \frac{\partial y}{\partial \eta} - \frac{\partial x}{\partial \eta} \frac{\partial y}{\partial \xi} \right) \hat{k} \quad 3.30(b)$$

It is possible to define an infinite number of orthogonal axes one axis of which is defined by the vector \hat{V}_z' . However a unique set of axes is defined by noting that both the vectors \hat{V}_ξ and \hat{V}_η used to form the vector \hat{V}_z' are normal to \hat{V}_z' . Hence by defining the x' direction to be identical to the ξ direction then a unique set of axes is formed by the cross product of the vectors \hat{V}_z' and \hat{V}_x' where \hat{V}_x' is identical to \hat{V}_ξ .

$$\hat{V}_y' = \hat{V}_z' \times \hat{V}_x' \quad 3.31$$

These vectors are normalised to give the direction cosines of a set of local orthogonal axes in terms of the element axes

$$[\theta] = [\hat{v}_x', \hat{v}_y', \hat{v}_z'] \quad 3.32$$

The derivatives of u, v and w in the element axes are transformed into the local orthogonal axes to give the strain components as

$$\begin{bmatrix} \frac{\partial u'}{\partial x'} & \frac{\partial v'}{\partial x'} & \frac{\partial w'}{\partial x'} \\ \frac{\partial u'}{\partial y'} & \frac{\partial v'}{\partial y'} & \frac{\partial w'}{\partial y'} \\ \frac{\partial u'}{\partial z'} & \frac{\partial v'}{\partial z'} & \frac{\partial w'}{\partial z'} \end{bmatrix} = [\Theta]^T \begin{bmatrix} \frac{\partial u}{\partial x} & \frac{\partial v}{\partial x} & \frac{\partial w}{\partial x} \\ \frac{\partial u}{\partial y} & \frac{\partial v}{\partial y} & \frac{\partial w}{\partial y} \\ \frac{\partial u}{\partial z} & \frac{\partial v}{\partial z} & \frac{\partial w}{\partial z} \end{bmatrix} [\Theta] \quad 3.33$$

where

$$\begin{bmatrix} \frac{\partial u}{\partial x} & \frac{\partial v}{\partial x} & \frac{\partial w}{\partial x} \\ \frac{\partial u}{\partial y} & \frac{\partial v}{\partial y} & \frac{\partial w}{\partial y} \\ \frac{\partial u}{\partial z} & \frac{\partial v}{\partial z} & \frac{\partial w}{\partial z} \end{bmatrix} = \begin{Bmatrix} \frac{\partial P}{\partial x} \\ \frac{\partial P}{\partial y} \\ \frac{\partial P}{\partial z} \end{Bmatrix} [\alpha_u, \alpha_v, \alpha_w] \quad 3.34$$

The strain energy is evaluated in terms of the strains and stresses defined in a set of axes normal to the shell surface at each numerical integration point.

$$V = \frac{1}{2} \int_{Vol} \{\epsilon'\}^T \{\sigma'\} dVol \quad 3.35(a)$$

where

$$\{\sigma'\} = \begin{Bmatrix} \sigma_{x'} \\ \sigma_{y'} \\ \tau_{x',y'} \\ \tau_{y',z'} \\ \tau_{z',x'} \end{Bmatrix} \quad \text{and} \quad \{\epsilon'\} = \begin{Bmatrix} \epsilon_{x'} \\ \epsilon_{y'} \\ \delta_{x',y'} \\ \delta_{y',z'} \\ \delta_{z',x'} \end{Bmatrix}$$

This gives the usual finite element stiffness expression as

$$[K_e] = [\bar{A}]^{-T} \int_{Vol} [B']^T [D'] [B'] dVol [\bar{A}]^{-1} \quad 3.35(b)$$

where $[D']$, the stress/strain matrix, is based on zero normal

direct stress.

$$[D'] = \frac{E}{(1-\nu^2)} \begin{bmatrix} 1 & \nu & 0 & 0 & 0 \\ & 1 & 0 & 0 & 0 \\ & & \frac{1-\nu}{2} & 0 & 0 \\ & & & \frac{1-\nu}{2K} & 0 \\ \text{sym} & & & & \frac{1-\nu}{2K} \end{bmatrix}$$

The $[B']$ matrix relates the local components of strain to the displacement function coefficients as

$$\{\epsilon'\} = [B'] \begin{Bmatrix} \alpha_u \\ \alpha_v \\ \alpha_w \end{Bmatrix}$$

where

$$\{\epsilon'\} = \begin{Bmatrix} \epsilon_{x'} \\ \epsilon_{y'} \\ \gamma_{x'y'} \\ \gamma_{y'z'} \\ \gamma_{x'z'} \end{Bmatrix} = \begin{Bmatrix} \partial u' / \partial x' \\ \partial v' / \partial y' \\ \partial u' / \partial y' + \partial v' / \partial x' \\ \partial v' / \partial z' + \partial w' / \partial y' \\ \partial u' / \partial z' + \partial w' / \partial x' \end{Bmatrix} \quad 3.36$$

and $[B']$ relates the strains in a set of axes normal to the shell surface to the coefficients of the displacement functions. The factor K is introduced into the $[D']$ matrix to account more accurately for the shear strain energy. The usual value for K is 1.2.

The normal direct strain is constrained to be zero by defining the degrees of freedom for each node pair in a set of local axes whose x axis is normal to the shell surface. The degrees of freedom in the x direction at each node pair are constrained to be identical but the other degrees of freedom are independent to allow for shear

deformation (see Fig. 3.3).

The displacements are found by the summation over the total structure of equation 3.35 and solving for $\{\delta_i\}$. The equivalent nodal forces are found in the same way as those for the isoparametric elements, sections 3.2.3 and 3.2.4. The stresses are found in a set of local axes normal to the shell surface. In the formulation of the stiffness matrices it has been assumed that the normal direct stresses are zero, but when the stresses are evaluated for a shell subjected to pressure loading it is assumed that the normal stress varies linearly through the thickness.

3.4.1 Transition Parametric Finite Element

The idealisation of turbine casings is made using a combination of thick shell parametric finite elements to model the shell portion and isoparametric finite elements to model the flange and fillet portions of the casing. One method of joining these elements, see Fig. 3.4, constrains the displacements at the outside nodes of each element to be identical but imposes no coupling between the elements for the mid-side node(s). The result is that after deformation the normals to the shell surface remain straight, whereas the mating face of the isoparametric element becomes distorted leaving a gap or penetration between element faces. A possible method of combining such elements is to use a parametric transition element which is explicitly written to overcome these difficulties.

The transition parametric finite element is basically an isoparametric finite element with degrees of freedom on an end face constrained such that the normal to the surfaces before

deformation remains straight after deformation.

3.4.2 Generation of Element Matrices

The stiffness and loading matrices for the transition parametric finite element are generated in an identical manner to those for the equivalent isoparametric finite element. The mid-surface nodes on the face adjoining a shell element are constrained such that the normals remain straight after deformation. The displacements are transformed into the local set of axes whose x axis is normal to the shell surface from the element cartesian axes.

$$\{\delta_L\} = [DCA_L]^T [DCA_e] \{\delta_e\} \quad 3.37$$

The element illustrated in Fig. 3.5 is to be joined to a shell element on the surface 1-10-3-15-7-18-5-13-1. Node 13 is constrained to remain on the line joining nodes 1 and 5 and node 15 on the line joining nodes 3 and 7. The displacements in the local y and z directions at the mid-side nodes must be a linear function of the displacements at the corner nodes.

$$v_{L13} = \frac{1}{2}(v_{L1} + v_{L5}) \quad 3.38(a)$$

$$w_{L13} = \frac{1}{2}(w_{L1} + w_{L5}) \quad 3.38(b)$$

The u displacement is allowed to move, dependent on the coupling terms associated with these implicitly imposed constraints, and those associated with the other element degrees of freedom. By substituting equations 3.38 for the through thickness mid-side nodes on the junction face in the strain energy equations the the stiffness and loading matrices are modified, Appendix 6. The terms directly associated with the displacements constrained so that the nodes remain on a straight line are removed from the

stiffness and loading matrices. There are no longer any degrees of freedom associated with these terms in the structure.

The stiffness and loading terms are transformed back from the local or global axes to the element axes ready for summation with the other terms for the structure. This is necessary as the merge algorithm, being of the most general nature, has to have the element terms presented to it defined relative to a set of axes dependent on element topology.

To determine the stresses the values of the constrained displacements must be calculated from equations 3.38 before the coefficients of the displacement polynomials can be found.

3.5.1 Programming Techniques (Isoparametric Finite Element)

The programs to generate element stiffness and loading matrices for the parametric family of elements are very similar, the isoparametric and transition parametric element algorithms being combined. The basic modification for the shell element is the inclusion of the transformation steps to modify the element stiffness terms into axes normal to the element surfaces.

The flow diagram for the 20 node isoparametric element is shown in Fig. 3.6(a). The element nodes are defined in terms of the curvilinear co-ordinates to enable the $[\bar{A}]$ matrix to be calculated from the polynomial function $\{P(\xi, \eta, \zeta)\}$. The $[\bar{A}]$ matrix is partitioned into three portions to enable economy of store and central processor time to be achieved. These partitions are identical by definition of the parametric formulation. Taking equations 3.3(a) and 3.4(a) and by partitioning the $[\bar{A}]$ matrix

$$\{\delta_i\} = \begin{Bmatrix} u_i \\ v_i \\ w_i \end{Bmatrix} = \begin{bmatrix} [A] & 0 & 0 \\ 0 & [A] & 0 \\ 0 & 0 & [A] \end{bmatrix} \begin{Bmatrix} \alpha_u \\ \alpha_v \\ \alpha_w \end{Bmatrix} \quad 3.39(a)$$

and

$$\{X_i\} = \begin{Bmatrix} x_i \\ y_i \\ z_i \end{Bmatrix} = \begin{bmatrix} [A] & 0 & 0 \\ 0 & [A] & 0 \\ 0 & 0 & [A] \end{bmatrix} \begin{Bmatrix} \alpha_x \\ \alpha_y \\ \alpha_z \end{Bmatrix} \quad 3.40(a)$$

and typically

$$\{u_i\} = [A] \{\alpha_u\} \quad 3.39(c)$$

$$\{x_i\} = [A] \{\alpha_x\} \quad 3.40(c)$$

This partition reduces the size of the $[\bar{A}]$ matrix from the square of the number of degrees of freedom for the element to the square of the number of nodes of the element $[A]$. For the 20 node isoparametric element this reduces from 60 x 60 to 20 x 20, a reduction to 11% of the original store requirements. Similarly computation time is saved as a very much smaller matrix is now inverted.

$$\begin{Bmatrix} \alpha_u \\ \alpha_v \\ \alpha_w \end{Bmatrix} = \begin{bmatrix} [A]^{-1} & 0 & 0 \\ 0 & [A]^{-1} & 0 \\ 0 & 0 & [A]^{-1} \end{bmatrix} \begin{Bmatrix} u_i \\ v_i \\ w_i \end{Bmatrix} \quad 3.39(b)$$

and

$$\begin{Bmatrix} \alpha_x \\ \alpha_y \\ \alpha_z \end{Bmatrix} = \begin{bmatrix} [A]^{-1} & 0 & 0 \\ 0 & [A]^{-1} & 0 \\ 0 & 0 & [A]^{-1} \end{bmatrix} \begin{Bmatrix} x_i \\ y_i \\ z_i \end{Bmatrix} \quad 3.40(b)$$

and typically

$$\{\alpha_u\} = [A]^{-1} \{u_1\} \quad 3.39(d)$$

$$\{\alpha_x\} = [A]^{-1} \{x_1\} \quad 3.40(d)$$

The PAFEC suite of finite element programs has provision for the use of more than one element type in any structure. The number of elements of any one type for which the stiffness and loading terms are generated is read within the element algorithm. The algorithm loops through this number of elements to generate and merge the stiffness and loading terms.

Within each loop the element topology is defined by ordering the nodal points in the same way as the nodal points were defined when calculating the $[A]$ matrix, Fig. 3.7. The value of the density of the element is used as a control which saves recomputing the $[D]$ matrix or equivalent. This also saves data preparation in redefining the material properties should they be the same as the previous element. The nodal co-ordinates are listed to enable the element geometry to be calculated in terms of the co-ordinates of node 1, Fig. 3.7. The stiffness and loading terms are evaluated in terms of the element axes which are defined as the x_e direction being along the line joining nodes 1 and 2, the $x_e y_e$ plane containing the nodes 1, 2 and 3 and the z_e direction being normal to this plane. This enables large economies of computing to be achieved when elements have identical properties and geometry but are displaced and orientated relative to each other. Once the stiffness and loading terms have been calculated for the first element they can be used within the merge algorithm using the new

direction cosine array of the element axes and relevant nodal ordering information. The control for this step is that the material density has a value of -1.0 and the element is identical in every respect, including pressure and thermal loading if used, except position.

For elements which are not identical the stiffness and loading terms are found by numerical integration in curvilinear co-ordinates. The coefficients of the polynomial functions defining the element geometry in element axes are found from equations 3.40(d). Gaussian quadrature, Table 3.1, of order 3 is used for the numerical integration in all three co-ordinate directions. At each Gauss integration point, defined by the curvilinear co-ordinates ξ , η and ζ , the polynomial functions and derivatives with respect to the curvilinear co-ordinates are found.

$$\left\{ P(\xi, \eta, \zeta) \right\}^T, \left\{ \frac{\partial P(\xi, \eta, \zeta)}{\partial \xi} \right\}^T, \left\{ \frac{\partial P(\xi, \eta, \zeta)}{\partial \eta} \right\}^T, \left\{ \frac{\partial P(\xi, \eta, \zeta)}{\partial \zeta} \right\}^T \quad 3.41$$

The Jacobian matrix $[J]$ is found from the coefficients of the functions defining the element geometry, $\{\alpha_x\}$, $\{\alpha_y\}$, $\{\alpha_z\}$ and the derivatives of the polynomial functions, equation 3.41.

$$[J]_{3 \times 3} = \begin{bmatrix} \left\{ \frac{\partial P}{\partial \xi} \right\}^T \{\alpha_x\}, \left\{ \frac{\partial P}{\partial \xi} \right\}^T \{\alpha_y\}, \left\{ \frac{\partial P}{\partial \xi} \right\}^T \{\alpha_z\} \\ \left\{ \frac{\partial P}{\partial \eta} \right\}^T \{\alpha_x\}, \left\{ \frac{\partial P}{\partial \eta} \right\}^T \{\alpha_y\}, \left\{ \frac{\partial P}{\partial \eta} \right\}^T \{\alpha_z\} \\ \left\{ \frac{\partial P}{\partial \zeta} \right\}^T \{\alpha_x\}, \left\{ \frac{\partial P}{\partial \zeta} \right\}^T \{\alpha_y\}, \left\{ \frac{\partial P}{\partial \zeta} \right\}^T \{\alpha_z\} \end{bmatrix} \quad 3.42$$

The polynomial functions differentiated with respect to the element co-ordinates, $\frac{\partial P}{\partial x}$, $\frac{\partial P}{\partial y}$, $\frac{\partial P}{\partial z}$ are found by dividing the polynomial functions differentiated with respect to the curvilinear co-ordinates by the Jacobian matrix $[J]$,

equation 3.12. A by-product of this division process is the determinant of the Jacobian needed to scale the integration from curvilinear co-ordinates to element co-ordinates, equation 3.13.

The product $[B]^T [D] [B]$ can be found directly by matrix multiplication, $[B]$ and $[D]$ being defined by equations 3.8 and 3.10. This is a very large multiplication because $[B]$ is declared $6 \times IDE$, where IDE is the total number of degrees of freedom associated with the element, and $[D]$ is 6×6 . A more economic method of finding the product $[B]^T [D] [B]$ proposed by Irons (ref. 36) has been found to reduce the element generation time to at most 40% of the time required when using the direct multiplication method. The $[D]$ matrix being symmetric is easily converted to a lower and an upper matrix where the lower matrix is the transpose of the upper matrix.

$$[D] = [U]^T [U] \quad 3.43$$

The value of the upper matrix is given in Appendix 7.

The product $[B]^T [U]^T [U] [B]$ can be found more economically by forming $[U] [B]$ directly and noting that $[B]^T [U]^T$ is the transpose of $[U] [B]$. It is then only necessary to form the terms in the lower triangle of the stiffness matrix as the product $[B]^T [U]^T [U] [B]$ is symmetric.

Similarly for initial strain problems such as thermal loadings the product $[B]^T [D] \{\epsilon_0\}$ can be modified to $[B]^T [U]^T [U] \{\epsilon_0\}$ to make use of the previously calculated $[B]^T [U]^T$. These products are summed together with the weighting factors for each Gauss point, equation 3.16 and Table 3.1.

For pressure loadings the numerical integration has only to be applied in the ξ and η curvilinear directions. A linear pressure variation is defined by the pressure at the corner nodes of the $\zeta = \pm 1$ face. For internal pressure $\zeta = -1$ and the pressure is positive and for external pressure $\zeta = +1$ and the pressure is negative.

The pressure variation is defined by

$$p = \{P_p(\xi, \eta)\}^T \{\alpha_p\} \quad 3.44$$

where

$$\{\alpha_p\} = [AA]^{-1} \{p_i\} \quad 3.45$$

are the coefficients of the polynomial function

$$\{P_p(\xi, \eta)\}^T = \{1, \xi, \eta, \xi\eta\}^T \quad 3.46$$

The vectors \hat{v}_ξ and \hat{v}_η at the surface integration points are found from the differentials of polynomial functions with respect to the curvilinear axes and the coefficients of the functions defining the geometry. The equivalent nodal forces can then be found directly from equation 3.28.

After the numerical integration the product $\sum [B^T][D][B]$ has to be pre and post multiplied by the inverse of the $[\bar{A}]$ matrix to give the matrices in terms of the nodal displacements. This is achieved economically by the partitioned $[\bar{A}]$ matrix as

$$\begin{matrix} \text{IDE x IDE} \\ \left[\begin{array}{ccc} [A]^{-1} & 0 & 0 \\ 0 & [A]^{-1} & 0 \\ 0 & 0 & [A]^{-1} \end{array} \right]^T \end{matrix} [B]^T [D] [B] \begin{matrix} \text{IDE x IDE} \\ \left[\begin{array}{ccc} [A]^{-1} & 0 & 0 \\ 0 & [A]^{-1} & 0 \\ 0 & 0 & [A]^{-1} \end{array} \right] \end{matrix} \quad 3.43$$

These matrices are then summed into the total structure stiffness and loading matrices using the direction cosine array to transform the element terms to global axes.

3.5.2 Programming Techniques (Thick Shell Parametric Element)

The thick shell finite element is programmed in an identical manner to the isoparametric finite element taking account of the different number of nodes and change in polynomial functions but has an extra section in the numerical integration section. This calculates the stiffness terms in a set of orthogonal axes normal to the shell surface at each integration point. The point where the insertion of the extra program is made is shown in Fig. 3.6(a) and is given in Fig. 3.6(b). The set of orthogonal axes is found from the terms used to generate the Jacobian matrix, equations 3.32 and 3.33. The $[B]$ matrix is transformed by individually transforming the derivatives of the polynomial functions for each position in the $[B]$ matrix. The $[D]$ matrix given in equation 3.30 can be similarly operated on to give the upper and lower matrix type of formulation for economy of computation, Appendix 7.

3.5.3 Programming Techniques (Transition Parametric Element)

The generation of the element stiffness and loading terms is identical to the isoparametric element, Fig. 3.6(a), except for a portion immediately preceding the merge algorithm, Fig. 3.6(c). The terms associated with the nodes constrained to remain in a straight line, Fig. 3.5, are transformed from element axes to local axes through global axes. The terms are then adjusted by

substituting equations 3.38 in the strain energy equation. A simple example of this modification is given in Appendix 6. The stiffness and loading terms which have been eliminated are nulled before the terms are transformed back into element axes. The PAFEC merge algorithm will sum the stiffness and loading terms for this constraint correctly provided that no degree of freedom has been assigned to the v and w directions in the local axes at the nodes concerned.

3.6 Numerical Examples

The parametric family of finite elements has been shown to give good results for a number of problems for which exact solutions are known as well as more complex engineering structures (refs. 31, 32 and 33). A number of solutions using the parametric elements to idealise a cylinder subjected to internal pressure are compared with the exact Lamé solutions. These solutions give an indication of the usefulness of each element and provide information on the maximum arc length which the elements can idealise.

3.6.1 Isoparametric Finite Element

The results of 3 different isoparametric finite elements used to idealise a thick cylinder subjected to internal pressure are given in Table 3.2. The elements all have quadratic displacement and co-ordinate transformation functions in ξ and η but have linear (R37130), quadratic (R37110) and cubic (R37160) functions in the ζ direction normal to the shell surface.

The exact solution is known to have a quadratic radial strain

function through the thickness of the shell. This can only be represented exactly by the cubic ξ displacement function of the element R37160. The simpler quadratic element has a linear radial strain distribution and the linear element a constant radial strain through the thickness. The radial and hoop stresses for each of these solutions are compared with the Lamé solutions in Fig. 3.8(a). It can be seen on examination of the strain components which produce these stresses, Table 3.2, that the difference in the stresses is due to inaccuracies in the radial strain component. Because of the Poisson effect the stresses in all three directions are affected. The isoparametric element with only a linear polynomial function in the radial ξ direction is unacceptable even though the hoop stresses are approximated reasonably well. The cubic element gives exact answers at the cost of increased numbers of nodes, whereas the quadratic 20 node isoparametric element gives reasonable results for the radial stresses and good results for the hoop stresses. The variation of the stresses with angular position for the thick cylinder idealised by quadratic isoparametric finite elements across 30° arcs is given in Fig. 3.9(a). The small variation from the exact solutions shows that quite large arcs can be idealised by these elements without poor stresses resulting. The parabolic "looping" of the stress variation for each element is due to the inability of the parabolic co-ordinate transformation functions to define the shape of the cylinder exactly. When bending begins to be significant only small arcs can be modelled as the "looping" becomes large.

3.6.2 Thick Shell Parametric Finite Element

The thick shell parametric element overcomes the difficulties caused by inaccurate representation of the radial displacement of the linear and quadratic isoparametric elements. By neglecting the radial stress in the evaluation of the strain energy the meridional and hoop stresses are found in terms of the meridional and hoop strains.

The idealisation used in section 3.6.1 has been used to test the 16 node thick shell parametric element, with quadratic polynomial functions in ξ and η , when subjected to internal pressure. The results for this element are compared with the exact Lamé solution and the results for the 20 node isoparametric element, Table 3.3. The radial stresses for the thick shell element are calculated from the value of the internal pressure. It can be seen from Fig. 3.8(b) that the stresses for the thick shell element are as good as those given by the equivalent isoparametric element. However only 40 degrees of freedom are necessary to describe the displacements of the thick shell element compared with the 60 needed by the isoparametric element.

Similarly large arcs can be idealised by single elements when the thick shell element is used to idealise pressure vessels. The "looping" due to the inaccuracies in the function defining the cartesian co-ordinates is only just apparent in the hoop stresses. The radial stresses show no such "looping" as their values are directly set by the value of the internal pressure.

3.6.3 Transition Parametric Finite Element

The transition element which joins the thick shell element to

the isoparametric element is based on the latter element. When this element is used to model a thick cylinder subjected to internal pressure the results are identical to those given by the isoparametric element.

3.6.4 Iso, Transition and Shell Parametric Finite Element Combination

The three types of parametric element have been combined to model the thick cylinder subjected to internal pressure, see Fig. 3.10. This element combination is used when the "Thick Shell" parametric element is to be used to model the shell portions of turbine casings. It can be seen that the "Transition" parametric element joins the shell and isoparametric elements with good continuity of stresses. The shell element however shows a large "looping" effect in the stresses due probably to the constraints applied by the transition element. However the mean stresses are close to the exact solution and it would appear that the shell and transition elements on either side of the junction face should have as small an arc length as possible.

Chapter 4.

Frontal Solution.

Notation

i	position of "redundant" degree of freedom
id	maximum instantaneous size
idf	degree of freedom label
ilo	number of loading cases
x	unknown variable
F	loading term
F'	modified loading term
K	stiffness term
K'	modified stiffness term

Suffices

e	element axes
g	global axes
i,j,k	positions in matrices
l	local axes

Matrices and Vectors

[DAC]	direction cosine array, local to global axes
[DCA]	direction cosine array, element to global axes
{ F }	loading vector
[K]	stiffness matrix

4.1 Introduction

The variational principle of minimum potential energy of a structure from which the finite element equations are formulated gives a set of linear simultaneous equations for the nodal displacements. The solution of these usually large sets of equations can be simply obtained if the matrix containing the coefficients of the equation can be held within the computer core store. The majority of computer software systems have an efficient matrix handling pack and the solution of the finite element equations is found by a matrix inversion algorithm operating on a vector or vectors of constant right hand side terms. Efficient methods of inverting and storing this matrix are available and when the inverse is required for subsequent solutions the Cholesky decomposition algorithm given by Wilkinson (ref. 22) has been used.

When the size of the coefficient matrix to be stored exceeds the limits of the computer store economies can be made by reclaiming the areas of the matrix of zero coefficients. These are usually abundant in finite element analyses where many elements are used in an idealisation as coupling of stiffness terms only span adjacent elements. By suitable ordering of the degrees of freedom the non-zero coefficients are concentrated in a narrow band about the leading diagonal terms. The coefficient matrix is then declared in rectangular form, being only as wide as the bandwidth, thus enabling much larger idealisations to be used and still retain the coefficient matrix in core store. A banded Cholesky decomposition algorithm, again given by Wilkinson (ref. 23) has been found to be extremely efficient for this type of problem. Great care has to be exercised in the ordering of the nodes as this can significantly increase the semi-bandwidth of the coefficient matrix.

When the structure becomes so large that it is impossible to retain all the non-zero terms of the coefficient matrix in the computer core, methods which either destroy part of the coefficient matrix or transfer the coefficients to backing store have to be used. The methods are usually direct or iterative, the direct methods usually being based on Gaussian elimination and limited by the instantaneous semi-bandwidth of the structural equations. By only retaining the coefficient terms of equations giving the degrees of freedom of interest, the equations associated with the other degrees of freedom can be eliminated from the coefficient matrix when all the terms associated with them have been calculated. This is the standard "reduction" algorithm for analysing small areas of very large idealisations.

For very large idealisations it is better to use a few high order displacement function finite elements in place of very many simple elements. This reduces the total number of coefficients necessary for a solution, but is usually outside the bounds of the computer store. Irons (ref.37) has proposed a "Frontal Solution" to be used with these high order displacement function finite elements which retains all the terms eliminated from the coefficient matrix in fast access backing store and enables the displacements for the total structure to be calculated. Further the algorithm reduces the size of the "active" coefficient matrix by using empty rows and columns as they become available, thus eliminating a large amount of unnecessary store requirements. The algorithm also has a re-resolution facility by making use of the terms, in backing store, of the eliminated equations.

A block elimination algorithm based on Gaussian elimination which uses fast access backing store to retain the square submatrices of

the coefficients has been proposed by Cantin (ref.38). This method which is similar to Irons "Frontal Solution" can solve very much larger problems but is very heavy on peripheral traffic.

Iterative methods have been used extensively for the solution of linear equations, many methods of solution being given by Westlake (ref.39). Of these the Gauss-Seidal method, which always converges for positive definite matrices, if slowly, has been extensively used. For iterative solutions all the terms of the coefficient matrix have to be retained, even if backing store has to be used. An alternating component block iterative solution for very large finite element idealisations of simple tetrahedron elements has been proposed by Rashid (ref. 40).

A comparison of direct and iterative solution methods for finite element equations has been made by Irons and Kan (ref.41). They conclude that iterative methods are more inefficient than "frontal" methods when very large idealisations are to be solved, and that the Rashid approach is the only iterative method worthy of consideration.

The most attractive solution technique for finite element idealisations which cannot be contained in the computer core, either directly or in banded form, is the "Frontal Solution" of Irons. This not only offers complete solution but has the added advantage of ease of re-solution of subsequent right hand sides of the linear equations. The "Frontal Solution" algorithm written for these programs is compatible with the PAFEC suite of finite element programs and the housekeeping techniques used are completely new.

4.2 Numerical Analysis

The "Frontal Solution" method of solving a large set of linear

equations for the displacements of a finite element idealisation depends on a limited number of those equations becoming "redundant" as the formulation proceeds. A displacement or degree of freedom becomes and remains "active" when the stiffness and loading terms of the first element containing the degree of freedom are being generated, and while other stiffness and loading terms associated with elements having common boundary with this degree of freedom are still to be generated. The degree of freedom becomes "redundant" when the last stiffness and loading terms associated with it have been generated and summed with other terms in the overall stiffness matrix. When a degree of freedom has become "redundant" the stiffness and loading terms directly associated with it can be eliminated by Gaussian Reduction to reduce the storage requirements of "active" stiffness and loading matrices.

The maximum amount of core storage required is determined by the maximum number of degrees of freedom "active" over the duration of the program, termed the "maximum instantaneous size". The maximum instantaneous size of the "active" degrees of freedom is independent of nodal or degree of freedom ordering and is solely determined by careful choice of element ordering. The degree of freedom numbers are merely labels and are no longer used to determine the relative positions of terms in the stiffness and loading matrices. By making use of empty rows and columns in the "active" matrices the bandwidth is greatly reduced.

When a degree of freedom becomes "redundant" it is eliminated from the stiffness and loading matrices by reducing out all the terms associated with it. The set of linear equations for the total structure is given by

$$\sum_{j=1}^{idt} K_{ij} x_j = F_i \quad i=1, idt \quad 4.1$$

where idt is the total number of degrees of freedom in the structure.

This gives the "redundant" degrees of freedom as

$$x_i = \frac{F_i}{K_{ii}} - \sum_{j=1}^{i-1} \frac{K_{ij}}{K_{ii}} x_j - \sum_{j=i+1}^{idt} \frac{K_{ij}}{K_{ii}} x_j \quad 4.2$$

For large structures the majority of the K_{ij} terms are zero and the equation can be reduced to give the "redundant" degree of freedom in terms of the "active" degrees of freedom. Similarly because the stiffness matrix is symmetric an equal number of K_{ji} stiffness terms are zero. When this "redundant" degree of freedom is substituted into the equations with zero K_{ij} terms the equations remain unchanged and consequently the reduction equations can be written in terms of the maximum instantaneous size id .

$$x_i = \frac{F_i}{K_{ii}} - \sum_{j=1}^{i-1} \frac{K_{ij}}{K_{ii}} x_j - \sum_{j=i+1}^{id} \frac{K_{ij}}{K_{ii}} x_j \quad 4.3$$

Substituting equation 4.3 for the "redundant" degree of freedom in all the "active" equations

$$j \neq i \sum_{k=1}^{id} K_{kj} x_k = F_j \quad k=1, i-1, i+1, id \quad 4.4$$

gives a modified set of "active" linear equations as

$$j \neq i \sum_{k=1}^{id} K'_{kj} x_k = F'_j \quad k=1, i-1, i+1, id \quad 4.5$$

where the modified stiffness terms are given by

$$K'_{kj} = K_{kj} - \frac{K_{ki} K_{ij}}{K_{ii}} \quad 4.6$$

and the modified loading terms are given by

$$F'_k = F_k - \frac{K_{ki} F_i}{K_{ii}} \quad 4.7$$

The "redundant" equation, equation 4.3, is stored in fast access backing store for solution when the x_j terms have been determined. The rows and columns made available after the "redundant" degrees of freedom have been reduced out are filled with newly "active" equations as the formulation proceeds. After the stiffness and loading terms have been generated and summed for the last element in the structure all remaining degrees of freedom become "redundant", except for eigenvalue problems, mentioned later, and can all be reduced out. This leaves the last degree of freedom to be reduced out as

$$x_i = \frac{F_i}{K_{ii}} \quad 4.8$$

The solution for this degree of freedom can be found directly and by a process of back-substitution, calling down each reduction equation in reverse order to which the equations were sent to backing store, the solution of all the degrees of freedom can be found.

Re-resolution of subsequent right hand sides of the finite element equations is available by using the reduction equations written to fast access backing store. This means that the stiffness terms remain unaltered and non-linear problems using re-resolution have to be based on constant stiffness criteria. The loading terms are summed in the same manner as the stiffness terms were generated during the element formulation and are modified by equation 4.7 during the reduction process. The coefficients of equation 4.3, obtained from backing store, are identical to the terms required

by equation 4.7. The loading term in equation 4.3 is modified to the loading term given by the "redundant" degree of freedom. The coefficients and modified loading terms of equation 4.3 are then rewritten to backing store. The re-resolution by back substitution is obtained after the loading terms of all the reduction equations have been modified.

4.3 Housekeeping

The PAFEC suite of finite element programs comprise many types of element families, all of which can have up to three displacements and three rotations in orthogonal axes at each node. Information on the global position and allocated degrees of freedom at each node is held by the CPDDC array (Coefficients of Position, Displacements and Direction Cosines). Each degree of freedom is allocated a number within the limits 1-idt, where idt is the total number of degrees of freedom. For simple matrix inversion or banded solutions these numbers allocated to each degree of freedom determine the relative position of terms in the stiffness and loading matrices. In the frontal solution these numbers act merely as labels for storing loadings and displacements when calculated, as the position taken in the stiffness matrix is dependent on the empty rows and columns when the degree of freedom becomes "active".

A simple example with data prepared for the "frontal solution" is given in section 4.6 to describe the housekeeping algorithms.

4.3.1 CPDDC Array

The CPDDC array used by all types of finite element is the most convenient item for containing the reduction information for each

degree of freedom. The degrees of freedom associated with each node are stored in one row of the CPDDC array, together with the nodal co-ordinate data, and consequently the degrees of freedom although integer numbers are held as real variables. The reduction information associated with each degree of freedom is held in the decimal portion of this real variable in the form of a tag.

The tag which controls the reduction and elimination process has to accomodate solutions which may require master degrees of freedom, found in large eigenvalue problems, repeated degrees of freedom, where two or more degrees of freedom are rigidly coupled to move together, as well as the more normal solutions. An example of rigid coupling is in constraining a face to remain plane to calculate generalised plane strain solutions.

The displacements at a particular node cannot be eliminated until the matrices for all elements which contain the node have been merged into the system matrices. A count on the number of elements associated with each node has to be made as each element is merged. The tag 0.01 is added to the degrees of freedom at each node for each element which that node is common to. Hence a node common to 4 finite elements has degrees of freedom with tags of 0.04 associated with it. As the element stiffness and loading generation proceeds the tags on the degrees of freedom at each node associated with the element are reduced by 0.01 for each element appearance. When the tag finally disappears the degree of freedom has become "redundant" and the stiffness and loading terms associated with it can be reduced out.

Master degrees of freedom always have an extra 0.01 added to the tag, so that the tag never finally disappears and the terms are not

reduced out. Repeated degrees of freedom are treated in a similar manner by adding 0.01 to all the tags on the degree of freedom except for the node in the last element to be summed. This ensures that the degree of freedom remains "active" until all terms associated with it have been summed.

4.3.2 Merge Algorithm

The stiffness and loading matrices associated with each finite element are summed into the total structure stiffness and loading matrices element by element. A flow diagram for the Merge Algorithm is given in Fig. 4.1. The element stiffness terms are generated in a set of orthogonal axes whose direction cosines relative to the global orthogonal axes are dependent on the element geometry and are given in a direction cosine array $[DCA]$. To sum the element stiffness and loading matrices into the total structure matrices the terms are transformed from element to global axes.

$$[K_g] = [DCA]^T [K_e] [DCA] \quad 4.9(a)$$

$$\{F_g\} = [DCA]^T \{F_e\} \quad 4.9(b)$$

It may be required to constrain the degrees of freedom at any node in a set of orthogonal axes local to the node and different from the global axes. The local axes can vary from node to node and the direction cosines of the local axes relative to the global axes are held in the CPDDC array. When the terms associated with the degrees of freedom defined in the local axes are summed the direction cosines of the local axes are formed in the direction cosine array $[DAC]$. The stiffness and loading terms are transformed from global to local axes by

$$[K_1] = [DAC] [K_g] [DAC]^T \quad 4.10(a)$$

$$\{F_1\} = [DAC] \{F_g\} \quad 4.10(b)$$

The stiffness and loading terms after transformation can now be summed in the "active" matrices.

The frontal solution uses the vacant rows and columns left by "redundant" degrees of freedom to add in the stiffness and loading terms associated with degrees of freedom which have just become "active". A simple record has to be retained to allow easy determination of empty rows and columns of the matrices as well as the "active" degrees of freedom associated with them. The record of these positions is made in an extra row added to the stiffness matrix, which contains the number of the degree of freedom associated with that column and, as the stiffness matrix is symmetric, the equivalent row. When the row and column is empty the column of the extra row is empty. To determine the address of each stiffness term as it is summed into the stiffness matrix the extra row containing the positions of each "active" degree of freedom is searched. If the degree of freedom has only just become "active" the first vacant row and column is taken and the degree of freedom is placed in the relevant column of the extra row.

Other methods of allocating the position that each degree of freedom takes in the stiffness matrix have been used. A second tag is added to the degrees of freedom in the CPDDC array in the decimal part of the real variable after the tag which controls the elimination and reduction algorithms. This tag contains a pointer to the row and column with which this degree of freedom is associated. This reduces the number of searches of the extra row for the degree

of freedom position in the stiffness and loading matrices from $ide^2 + ide$ to ide for each element, where ide is the total number of degrees of freedom for the element. This can only be used with computers with at least a 48 bit word length as the sixth decimal place has to be determined accurately. A second and more economical method at run time is to use a destination vector for the positions of the degrees of freedom in the matrices. The destination vector holds pointers for each degree of freedom giving the position that the stiffness and loading terms are to take in the matrices. This vector is generated as a by-product of the data generation pre-program (see section 4.4) and changes the search process for the positions of the degrees of freedom in the matrices to one of direct addressing from the destination vector.

As the stiffness and loading matrices for each element are summed into the "active" matrices some of the degrees of freedom may have only just become "active". The back-substitution algorithm requires the knowledge of when degrees of freedom become "active" so a record of new activity has to be compiled. The transfer vector ATRANS (see section 4.3.3) is filled with the degrees of freedom newly "active" in a row one greater than the position taken in the matrices. This leaves the first row of the vector empty and serves as identification to differentiate this activity information from reduction information commonly held in ATRANS. This information is written to fast access backing store before the elimination process for the "redundant" degrees of freedom for the element is carried out.

The tags associated with all the degrees of freedom for the element whose terms have been summed into the "active" matrices are modified by reducing them by 0.01. The "redundant" degrees of freedom in the

"active" matrices will be indicated by the tags having become zero in the CPDDC array. The Gaussian reduction and elimination algorithm is called from the merge algorithm.

4.3.3 Reduction Algorithm

The reduction and elimination algorithm searches through the CPDDC array to find which degrees of freedom are now "redundant". These are only associated with the element whose stiffness and loading matrices have just been summed into the "active" matrices. For each "redundant" degree of freedom the stiffness and loading terms of equation 4.3 are eliminated from the matrices by modifying the remaining terms by equations 4.6 and 4.7. The coefficients of equation 4.3 are stored in the transfer vector ATRANS and written to backing store after each reduction.

Before the coefficients of the "redundant" equation are transferred to backing store the vector ATRANS is used as a workspace to modify the stiffness and loading terms remaining in the "active" matrices. Before the terms in the "active" matrices are modified a search is made for empty rows and columns to reduce the number of computations required. A check is made to ensure that the leading diagonal stiffness term of the reduction equation remains positive. The vector ATRANS is used for the modification of the stiffness terms in a slightly corrupt form as it is more convenient to use the terms $K_{ij}/\sqrt{K_{ii}}$, $K_{ik}/\sqrt{K_{ii}}$, and $F_i/\sqrt{K_{ii}}$ etc. when computing the reduction equations 4.6 and 4.7. It is more efficient to obtain the modified terms 4.6 and 4.7 as

$$K'_{kj} = K_{kj} - \frac{K_{ki}}{\sqrt{K_{ii}}} \cdot \frac{K_{ij}}{\sqrt{K_{ii}}} \quad 4.11$$

and
$$F'_k = F_k - \frac{K_{ki}}{\sqrt{K_{ii}}} \cdot \frac{F_i}{\sqrt{K_{ii}}} \tag{4.12}$$

Because the stiffness matrix is symmetric the terms K_{ki}/K_{ii} are stored in the vector ATRANS as K_{ik}/K_{ii} and all terms required for the modification of the stiffness and loading terms are obtained as a direct product of two terms temporarily held in the transfer vector ATRANS.

After the modification the terms in ATRANS are changed back into the correct form for the back substitution algorithm, i.e. K_{ij}/K_{ii} , K_{ik}/K_{ii} etc. and K_i/K_{ii} .

The transfer vector ATRANS is then filled with the following information

1st element, i= position of "redundant" degree of freedom in the "active" matrices.

Next (i-1) elements, the first i-1 coefficients of the reduction equations, K_{ij}/K_{ii} j=1, (i-1).

(i+1)th element, the degree of freedom which has become "redundant".

Next (id-i) elements, the remaining coefficients of the reduction equations K_{ij}/K_{ii} j=(i+1), id.

Next ilo elements, the F_i/K_{ii} terms for each loading condition.

Final (id+ilo+2)nd element, the leading diagonal stiffness term K_{ii} .

This information is sufficient for the back substitution algorithm together with the K_{ii} term which is needed for re-resolution problems. The vector ATRANS is written to fast access backing store and the rows and columns associated with the degree of freedom that has been eliminated are set to zero. This is repeated for all the "redundant" degrees of freedom in each element except for the last reduction equation. To give the re-resolution algorithm information on the number

of reductions in each element a tag is added to the last reduction equation written to backing store. This decimal tag is added to the integer value in the first element of the vector as identification of the last reduction in each element.

A flow diagram for the reduction algorithm is shown in Fig. 4.2. The algorithm does not shuffle the "active" equations into one corner of the "active" matrices as this adds complications to this algorithm and the back substitution. The reduction algorithm has been written for two cases, the first a very fast and economical version for static displacement problems by storing the lower half of the stiffness matrix in vector form. The second case stores the mass matrix in the top half of the stiffness matrix for the solution of dynamic problems by retaining master degrees of freedom.

4.3.4 Back-Substitution Algorithm

When the last "redundant" degree of freedom for the complete structure has been eliminated the stiffness matrix is empty or contains terms associated with master degrees of freedom for dynamic problems. The back substitution proceeds in the same way for either solution after the eigenvalues have been found for the dynamic case. The last reduction equation for normal displacement calculations, where the stiffness matrix is empty, contains a solution as all the K_{ij} terms of equation 4.3 are zero, and is given directly by equation 4.8. The solutions of the other degrees of freedom are found by proceeding back through the elimination equations but in reverse order to that in which they were formed. By keeping a record of every displacement associated with each degree of freedom and by keeping a running record of "active" degrees of freedom as they are calculated,

in the identical position which they were summed in the stiffness matrix, it is possible to calculate subsequent degrees of freedom. The vector ATRANS is again used as work space as a direct vector multiplication of the terms brought down from backing store by the "active" displacements give the "redundant" displacement by equation 4.3. This new displacement is added to the "active" displacement vector as well as being retained in the total record. The "redundant" degrees of freedom are found for each element and the transfer vector containing the information on degree of freedom activity is brought down. Degrees of freedom which became "active" at the equivalent point in the reduction process are removed from the "active" displacement vector using the information in this transfer vector. The solution proceeds until all displacements have been found and a final check is made on the number of solutions to ensure that the algorithm does not remain in a closed loop.

The flow diagram for this algorithm is shown in Fig. 4.3. The displacement vectors are printed at the end of this algorithm.

4.3.5 Re-Solution Algorithm

The Re-solution algorithm is very similar to the merge and reduction algorithms and is therefore included within them. Because of the constant stiffness criteria it is only necessary to modify the loading matrices and the appropriate loading terms in the transfer vector ATRANS. For non-linear problems where a set of equivalent nodal forces are calculated from the previous solutions it is imperative that they are generated in an identical order to the finite element stiffness equations.

The loading terms are summed in a manner identical to that used to

sum the stiffness terms in the merge algorithm, but very much faster as only one of the loops through the element nodes is needed. When these new loading terms have been summed the "redundant" degrees of freedom have to be reduced out. The reduction information is no longer held in the CPDDC array as this was destroyed in the original reduction algorithm. This information is obtained from the transfer vectors written to backing store and read back to find the first solution.

As the new loading terms are summed in an identical order to which the previous stiffness and loading terms were summed, the correct terms are in the "active" loading vector when each transfer vector ATRANS is found from backing store. This vector is read sequentially forward in the same way as the backing store was set up and is used to modify the loading terms by equation 4.7. The term F_i/K_{ii} is changed in the transfer vector ATRANS by the new loading term using the leading diagonal stiffness term stored in ATRANS. The transfer vector ATRANS is then rewritten to its old position in the backing store and the loading terms associated with the next "redundant" degree of freedom are modified. When the last degree of freedom to be eliminated in each element has been found, indicated by the tag in the first row of the transfer vector ATRANS, the equivalent nodal forces for the next element are summed.

The back-substitution algorithm is identical to that for the initial solution and gives a set of displacements equivalent to the new loading vector.

The re-resolution algorithms are within the merge and reduction algorithms, the flow diagrams of which are given in Figs. 4.1 and 4.2.

4.3.6 Peripheral Handling

The transfer of the vector ATRANS to and from fast access backing store is the only part of the Frontal Solution algorithm which is machine dependent. A very general algorithm based on sequential addressing has been found successful for initial solutions but cannot be used for the re-solution algorithm.

Direct transfer of the vector ATRANS to and from the backing store is inefficient and a transfer buffer is used to improve the time in peripheral transfers. Direct access devices are used to block address the buffer when reading or writing to backing store.

A flow diagram for the peripheral handling algorithm is given in Fig. 4.4.

Three processes have to be performed by this algorithm

- 1) Writing the vector ATRANS to the buffer and if necessary emptying the buffer into fast access backing store by a forward stepping process.
- 2) Reading the vector ATRANS from the buffer in a backward stepping process and refilling the buffer by a backward stepping process when it has been fully accessed.
- 3) Reading the vector ATRANS from the buffer in a forward stepping process for re-solution and refilling the buffer from the backing store in a forward direction when the buffer has been completely read.

These processes are governed by a control integer associated with a read/write control and can be at random. For problems requiring re-solution the buffer has to be emptied into backing store before the back-substitution begins as the last buffer is normally lost.

4.4 Data Generation

To enable the "Frontal Solution" to be completely automatic a pre-program is used to prepare the extra data necessary for the algorithms. The element ordering and topology to be used in the solution is defined in this pre-program together with the nodal co-ordinates. The element topology is scanned and a tag, O.C1, is added to each degree of freedom allocated to each node defined by the topology. Extra tags are added for master degrees of freedom and repeated displacements by simple control integers. A pack of data cards for the modified CPDDC array with the addition of the tags is punched by the program.

The "maximum instantaneous size" of the "active" stiffness matrix is determined using processes identical to those used in the merge and reduction algorithms. The destination vector of positions taken by each degree of freedom is formed to check the tags attached to the CPDDC array and to ensure that all the degrees of freedom are reduced out.

4.5 Error Diagnostics

Failure in the "Frontal Solution" usually occurs when the stiffness matrix becomes badly conditioned. The positive values of the leading diagonal terms in the stiffness matrix are reduced by each reduction equation with coupling terms associated with the leading diagonal term. When these terms become extremely small in comparison with the initial stiffness terms the equations are extremely ill-conditioned and the solutions to the equations become suspect.

Irons (ref.42) uses methods which diagnose ill-conditioning as a measure of the reduced stiffness term to the original stiffness term.

Bond (ref. 43) has shown that the linear equations can easily become ill-conditioned when a finite element with mid-side nodes, whose co-ordinates define a node displaced from the mid-side position, is used.

When the equations become drastically ill-conditioned the leading diagonal terms become negative as the reduction proceeds. The present algorithm stops when a negative leading diagonal term is found, usually indicating an error in input data of wrong element topology or nodal co-ordinates. These errors however can usually be found using data checking schemes based on graphical plotter output.

Other checks are made in the reduction algorithm to ensure that the correct terms are in the appropriate rows and columns for the re-resolution, as the reduction terms retrieved from backing store require the new loading terms in the appropriate positions. Failure usually occurs when the store becomes accidentally overwritten or errors in peripheral transfer have occurred.

4.6 Example Problem

A simple example of a curved cantilever idealised by 6 in-plane 4 noded isoparametric elements is given in Fig. 4.5. The cantilever is built in at one end and the free end constrained to move in a horizontal direction and assumed infinitely rigid so that the displacements at nodes 10, 11, and 12 are identical. The normal solution when core store is available is to form the total stiffness and loading matrices and solve for the displacements by inverting the stiffness matrix, Fig. 4.5(a). The data necessary for automatic solution by the "Frontal Solution" is given in Fig. 4.5(b) for the same example. The tags added to the degrees of freedom in the CPDDC

array is the only extra data required. The tags attached to the degrees of freedom for nodes 1-9 are identical to the number of elements each node appears in, but the tags added to the degree of freedom 13 are increased at nodes 10 and 11 so that degree of freedom 13 does not become "redundant" until the stiffness and loading terms associated with element 6 are summed.

The activity of the degrees of freedom is given by Fig. 4.5(c) together with a listing of the degrees of freedom as they become "redundant". The "maximum instantaneous size" is reached after the terms for the third element are summed. The terms stored in the transfer vector ATRANS are given in Fig. 4.5(c) for the newly "active" degrees of freedom as each element is summed and for the reduction equation coefficients and housekeeping information as "redundant" degrees of freedom are eliminated.

It is interesting to note that the "maximum instantaneous size" for this simple problem is reduced from 10 to 9 if the element ordering is varied in generating the stiffness and loading matrices as shown in Fig. 4.5(d).

Degrees of freedom are reduced out as soon as they have become "redundant" and after the last element terms have been summed the remaining degrees of freedom are "redundant" and can be reduced out.

Chapter 5 Creep Analysis

Notation

t	time
H	Gaussian weighting factor
S.E.	Strain Energy
T	temperature
U	Potential Energy
ϵ	strain
σ	stress
Δ	change during a time increment

Subscripts

e	equivalent uniaxial/effective
j,k,l	Gaussian integration points
x,y,z	co-ordinate axes
1,2,3	principal axes
c	creep
E	elastic
\emptyset	initial
T	total
Therm	thermal

Matrices and Vectors

$\{ \}$	column vector
$[]$	matrix
$[]^T$	transpose of matrix
$[A]$	matrix relating displacement function coefficients to nodal displacements

[B] matrix relating strains to displacement function coefficients
[D] stress/strain matrix
[J] Jacobian matrix
{ δ_i } vector of nodal displacements
{ ϵ } strain vector
{ σ } stress vector

5.1 Introduction

The efficiency of thermodynamic cycles increases as the maximum cycle temperature increases and thus there is a continuing pressure to develop plant capable of operating at higher temperatures. This has led to the development of materials capable of sustaining reasonable stress levels at high temperatures. In order to obtain the most economic use of these expensive materials the designer must design components which will withstand a specified life at the temperatures and stress levels at which creep occurs. The amount of creep design information available is very small and usually only in the form of uniaxial test data for each material. A number of methods for determining the creep deformation of structures are available. A full size prototype of the design which can be loaded in the same way as the structure will be loaded operationally can be used. However as the designer must work within reasonable safety margins it will probably be many years before any noticeable creep occurs. This method is both very expensive and time consuming and new designs are usually required before results are available from the prototype. A second method of determining the creep behaviour is to produce models made of materials which creep at a much faster rate than the high temperature materials. The model is then loaded in an equivalent way to the actual operational loadings and the accelerated creep deformations are found. There is then a large amount of extrapolation necessary from model to full size design, allowances being made for material differences, loadings etc. This method is still very expensive in model manufacture and extrapolation time. With the advent of larger digital computers a third method of

numerical analysis is becoming available for the creep analysis of complex structures. The numerical techniques involved require the generation of a computer model of the structure and the analysis of its creep deformation from experimental material test data. This method is still very expensive but is likely to increase in popularity as larger and faster digital computers become available.

The analysis of split turbine casings has been made using a computer model of the casing, basing the creep deformation on the uniaxial creep test data. This creep data has been used to produce an empirical uniaxial creep law for the casing material. The variation of the uniaxial creep strain with time comprises three distinct stages; a primary region with decreasing creep strain rate with time; a secondary steady-state of constant creep strain rate; a tertiary stage of increasing creep strain rate with time to failure. Approximate creep analyses have been based on steady-state solutions for simple structures where no stress redistribution takes place with time. Odqvist (ref. 44) in describing metallic creep uses steady-state solutions for a beam and a membrane, whilst Finnie (refs. 45 and 46) uses similar solutions for tubes and cylinders. Other analyses by Smith (ref. 47) and Fairburn and Mackie (ref. 48) have used steady-state creep analyses of pressure vessels and spinning discs.

Penny (ref. 49) has stated that neglecting the primary creep strain is unimportant for structures subjected to steady loading for long periods, but should be included where load changes in times shorter than the time to reach the stationary creep rates are experienced. Mendelson, Hirschberg and Manson (ref. 50) have shown that the transient conditions prior to the establishment of

a steady-state distribution have an appreciable effect on the total creep strains. Zienkiewicz et al (ref. 51) and Penny (refs. 52 and 53) have used similar methods to find the creep deformations with time by calculating creep strain rates over small time intervals. In the earlier papers the stress was assumed constant over very short time intervals, whereas in the more recent paper Penny uses stress rates to calculate the stress redistributions over each time increment. The solutions to the equations for each time increment are of an iterative nature to calculate the average creep strain dependent on the average stress over the interval.

The prediction of creep deformation for structures subjected to a complex stress system is dependent on experimental creep test data. This usually takes the form of uniaxial tensile creep tests but is sometimes given by biaxial stress fields. The creep flow rules adopted to predict creep deformations are in general those used to analyse plastic deformations. These include the Von Mises equivalent stress and Prandtl-Reuss flow rules. Johnson (ref. 54) has shown the validity of using the Von Mises equivalent stress rules from tension and torsion tests. Under a changing stress system and assuming constant stress during each time interval a cumulative law must be used. This can be of a number of forms, the time-hardening and strain-hardening laws being the most common. Johnson and Kahn (ref. 55) showed that for copper the time-hardening law predicted the stress levels most accurately, whereas Odqvist (ref. 56) has shown that the strain-hardening law predicts creep for stable materials at high stress levels most accurately. Smith (ref. 57) has used a life-hardening law based on

a locus of rupture to predict creep rates in changing uniaxial stress systems.

Very little work has been published on the creep analysis of geometrically complex structures. The finite element method is well suited to the analysis of complex structures due to the computer modelling of the structures with large numbers of distorted finite elements. This method of creep analysis has been used by Greenbaum and Rubinstein (ref. 58) to analyse general axisymmetric pressure vessels. Schultz and Van Fossen (ref. 59) have extended this to incorporate plastic and creep analysis of 2-dimensional bodies subjected to thermal loadings.

The creep analysis of 1, 2 and 3-dimensional structures is given using the initial strain technique in the finite element method. The multiaxial stresses are reduced to an equivalent uniaxial stress using the Von Mises equivalent stress rules and the multiaxial creep strains given by Prandtl-Reuss plastic flow rules. The programs are written for both time-hardening and strain-hardening laws, the creep strain increments being found from the empirical creep laws. Checks are incorporated to ensure that the stress remains reasonably constant during each time interval.

The creep analysis of a simply supported beam subjected to a constant bending moment, a thin shell subjected to internal pressure and a thick ring subjected to internal pressure are given. The analysis of turbine casings subjected to creep deformation is given in Chapter 7.

5.2 Creep Analysis

The analysis of structures having non-linear material properties

by the finite element method can be treated in a number of ways, Zienkiewicz (ref. 31). Creep deformation is a particular case of a material property with a stress-strain-time relationship. A solution for the stresses in a structure at a particular time can be obtained from an elastic analysis if the cumulative creep strain distribution throughout the structure at the time is known. The cumulative creep strains ϵ_c are a function of the previous stress-strain history.

The stress-strain relationship is given by

$$\{\sigma\} = [D] (\{\epsilon_T\} - \{\epsilon_0\}) \quad 5.1$$

where $[D]$ is the stress/strain matrix, $\{\epsilon_T\}$ are the total strains and $\{\epsilon_0\}$ are the initial creep, plastic and thermal strains.

The empirical creep law, usually formulated from uniaxial constant stress creep test data, gives the creep strain as a function of stress, time and temperature.

$$\epsilon_c = f(\sigma, t, T) \quad 5.2$$

It is most convenient to use the "initial strain" method of finite element analysis with the creep data presented in this form. The "initial strain" method obtains a solution to the finite element equations by adjustment of $\{\epsilon_0\}$ in equation 5.1 to yield the same stress and strain values in equations 5.1 and 5.2. A major advantage of the initial strain method is that the $[D]$ matrix remains unaltered and it is unnecessary to recalculate the stiffness expression for the structure.

The computation for non-linear creep deformation with time proceeds in an incremental manner considering small time steps.

During each time interval the stress levels in the structure are assumed to remain constant. The increments of creep strain during each time increment are calculated from the stress levels, the previous strain history if using a strain-hardening law, and the time increment in the empirical creep law. These creep strain increments, when treated as "initial strains" in the strain energy expressions, give a set of equivalent nodal forces which together with the inverted stiffness matrix give the changes in the nodal displacements equivalent to the creep strain increments. From these displacements and the creep strain increments the change in the stress levels during the time increment are calculated. Provided that these changes in the stress levels are small enough not to invalidate the constant stress criteria the solution is valid, The analysis assumes that creep deformation is a small strain process and that the strain-displacement relationships remain linear.

5.2.1 Solution Techniques

The solution of creep problems in finite element analysis is based on the "initial strain" method. Considering the strains in terms of the strain increments during any time interval the total strain increment is given as

$$\{\Delta\epsilon_T\} = \{\Delta\epsilon_E\} + \{\Delta\epsilon_c\} \quad 5.3$$

The change in stress during a time interval is given by

$$\{\Delta\sigma\} = [D]\{\Delta\epsilon_E\}$$
$$\{\Delta\sigma\} = [D](\{\Delta\epsilon_T\} - \{\Delta\epsilon_c\}) \quad 5.4$$

Defining the change in the strain energy during each time interval in terms of the stress and elastic strain increments as

$$\Delta S.E. = \frac{1}{2} \int_{Vol} \{\Delta \epsilon_E\}^T \{\Delta \sigma\} dVol \quad 5.5$$

and substituting for equations 5.3 and 5.4 gives

$$\Delta S.E. = \frac{1}{2} \int_{Vol} \{\Delta \epsilon_T - \Delta \epsilon_c\}^T [D] \{\Delta \epsilon_T - \Delta \epsilon_c\} dVol \quad 5.6$$

Defining the total strain increments in terms of the nodal displacement increments, equation 3.9, in equation 5.6 gives, as the elasticity matrix $[D]$ is symmetric,

$$\begin{aligned} U &= \frac{1}{2} \{\Delta \delta_i\}^T [A^{-1}]^T \int_{Vol} [B]^T [D] [B] dVol [A^{-1}] \{\Delta \delta_i\} \\ &\quad - \{\Delta \delta_i\}^T [A^{-1}]^T \int_{Vol} [B]^T [D] \{\Delta \epsilon_c\} dVol \\ &\quad + \frac{1}{2} \int_{Vol} \{\Delta \epsilon_c\}^T [D] \{\Delta \epsilon_c\} dVol \end{aligned} \quad 5.7$$

The potential energy expression is minimised with respect to the nodal displacement increments when the individual potential energy expressions for each element have been summed into the complete structure. This gives for each element

$$\begin{aligned} \frac{\partial (\Delta U)}{\partial (\Delta \delta_i)} = 0 &= [A^{-1}]^T \int_{Vol} [B]^T [D] [B] dVol [A^{-1}] \{\Delta \delta_i\} \\ &\quad - [A^{-1}]^T \int_{Vol} [B]^T [D] \{\Delta \epsilon_c\} dVol \end{aligned} \quad 5.8$$

for all $\{\Delta \delta_i\}$. The third term in equation 5.7 disappears and

the first expression in equation 5.8 is identical to the stiffness term of equation 3.7(a). This gives a solution of the form

$$[K]\{\Delta\delta_1\} = \{\Delta F_e\} \quad 5.8(a)$$

where $[K]$ is the structure stiffness matrix and $\{\Delta F_e\}$ are the nodal forces equivalent to the creep strains and are given by equation 5.9.

For each element

$$\{\Delta F_e\} = [A^{-1}]^T \int_{Vol} [B]^T [D] \{\Delta\epsilon_c\} dVol \quad 5.9$$

The load vector increment is calculated from the creep strain increments during each time interval. The total strain increments are found by equation 5.9 from the solution of equation 5.8 for the displacement increments. The elastic stress increments are found from equation 5.4 and these are compared with the stress levels during the time interval.

5.2.2 Multiaxial Stress-Strain Relationships

The usual stress-strain-time relationships for creep deformation are found and given as uniaxial test data for each material. To generate a set of equivalent nodal forces due to the creep during each time interval a knowledge of the creep strains in a multiaxial stress system is necessary. These multiaxial creep strains have to be determined from the uniaxial creep data.

The creep flow in a multiaxial stress system is found from the uniaxial creep test data using an equivalent uniaxial stress. This is identical to the concept used to determine the onset of yielding in plasticity problems. For any given material there is a function

of the three principal stresses which always has the same value regardless of the stress field, Lübnahn and Felgar (ref. 60). The Von Mises equivalent stress equations are based on this concept and have been used for the creep analysis. They are developed in Appendix 8.

The Von Mises equivalent uniaxial stress to a multiaxial stress field is given by

$$\sigma_e = \frac{1}{\sqrt{2}} \sqrt{(\sigma_x - \sigma_y)^2 + (\sigma_y - \sigma_z)^2 + (\sigma_z - \sigma_x)^2 + 6\tau_{xy}^2 + 6\tau_{yz}^2 + 6\tau_{zx}^2} \quad 5.10(a)$$

or in terms of the principal stresses is given as

$$\sigma_e = \frac{1}{\sqrt{2}} \sqrt{(\sigma_1 - \sigma_2)^2 + (\sigma_2 - \sigma_3)^2 + (\sigma_3 - \sigma_1)^2} \quad 5.10(b)$$

The equivalent incremental creep strain $\Delta\epsilon_{e_c}$ is a function of the equivalent uniaxial stress σ_e , the total equivalent strain ϵ_{e_c} , the temperature T if applicable and the time t

$$\Delta\epsilon_{e_c} = f(\sigma_e, \epsilon_{e_c}, T, t) \quad 5.11$$

The law is assumed to hold for both tensile and compressive stress fields.

The multiaxial strain increments are calculated from the equivalent uniaxial strain increments by assuming the Von Mises equations and Prandtl-Reuss flow rules, Hill (ref. 61). These show that the principal strain increments coincide with the axes of principal stress and are proportional to the principal stress deviations, Appendix 8. These equations include the constant volume condition for creep deformation and give the multiaxial creep strain increments as

$$\Delta\epsilon_{x_c} = \frac{\Delta\epsilon_{e_c}}{2\sigma_e} (2\sigma_x - \sigma_y - \sigma_z) \quad \text{etc.} \quad 5.12(a)$$

$$\Delta \epsilon_{xy_c} = \frac{3\Delta \epsilon_{e_c}}{2 \sigma_e} \quad xy \quad \text{etc.} \quad 5.12(b)$$

5.2.3 Uniaxial Stress-Strain-Time Relationships

To solve a problem in which there are stress redistributions it is necessary to determine the creep strain trajectory taking into account the stress variation with time. This is necessary when the solution technique used comprises small time increments during which the creep processes are assumed to take place under constant stress conditions.

The two most general methods of accumulating creep strain are the strain-hardening and time-hardening laws. The strain-hardening law assumes that the instantaneous creep rate is dependent on the stress, temperature and accumulated creep strain, and is independent of the loading time. The time-hardening law assumes that the creep rate is dependent on the stress, temperature and total loading time. Both these laws are shown in Fig. 5.1 together with the life-fracture law, Smith (ref. 57). The life-fracture law is obtained by scaling the rupture locus.

For ease of computation the time-hardening law is the simplest to use as the strain is given directly by the stress level and total elapse time in the empirical creep law. The strain-hardening law requires the calculation of an equivalent time corresponding to the stress level and total creep strain in the empirical creep law. This equivalent time has been found using Newton's method for the solution of general non-linear equations, see Appendix 9.

Although numerical results are given for both time-hardening and strain-hardening laws the latter has been used in general.

5.3 Programming Techniques

The flow diagram for the creep analysis of a beam, where the stresses are considered in one direction only, is given in Fig. 5.2. The initial elastic solution is found in the usual way by inverting the stiffness matrix and finding the nodal displacements from the applied loading. The stressing and creep algorithm takes the place of the usual stressing algorithm.

The initial pass through the algorithm (ICON = 0) is essentially identical to the stressing algorithm where the nodal displacements give the elastic strains directly. The stresses are found at every Gaussian integration point in every element of the structure. At each stressing point the creep strain increments for the first time increment are found and these are used to generate the equivalent nodal forces to the creep strain increments for each element. These forces are merged to form a loading vector for the complete structure. The changes in the nodal displacements due to these equivalent nodal forces are given by the inverse of the stiffness matrix of the structure and the new loading vector.

The changes in the elastic stresses over the time increment are found using the new displacement increments together with the creep strain increments. This checking pass (ICON = 1) uses a large number of parts of the algorithm previously used to find the elastic strains to find the total strain increments. The changes in the stresses are found at each Gaussian integration point and these are compared with the stress level at the beginning of the time increment. A check is made on the change of the equivalent uniaxial stress at all the mesh points in all the elements. When complete the changes in the stresses, the nodal displacements and the creep

strains for the previous time increment are assumed to be correct and all these items are updated. The creep strain increments over the next time increment are then calculated based on the stresses at the end of the last correct time increment. This pass through the algorithm (ICON = 2) generated an equivalent set of nodal forces for the creep strain increments found at each Gaussian integration point. When these have been summed for the whole structure a new set of nodal displacement increments is found. The checking pass (ICON = 1) is then made through the algorithm for each time increment.

Provided that the limits set on the variation of the stresses over each time increment are not exceeded the calculations proceed in this manner with one pass generating the creep strain increments followed by a pass checking these increments. The time increments increase as the calculations proceed. Should the limits set for the variation of the stresses be exceeded the calculations stop, the time increment is reduced and the algorithm is restarted (ICON = 2) using the last correct set of stresses, creep strains and nodal displacements. The calculations stop when the creep time exceeds a limit previously set.

The flow diagram for the creep analysis of thin shells of revolution, described in section 2.3.4.1 is given in Fig. 2.9. A more general flow diagram is given in Fig. 5.3 for the creep analysis of structures using the parametric family of finite elements in 3-dimensional space.

The algorithm used for the parametric element creep analysis is more efficient than that used for the beam and shell creep analyses as these have separate passes for the equivalent nodal

force generation and stress deviation check. The parametric element creep analysis algorithm, Fig. 5.3, incorporates both checking and force generation processes in a single pass.

The initial solution is found in the same way as described in section 3. This gives the entry to either the stressing or creep algorithms and it is usual to write this initial solution to backing store, usually magnetic tape, before the next stage is started. This enables a check on the idealisation to be made, by calculating the stress discontinuities at element boundaries, before the lengthy creep analysis begins.

The creep algorithm follows immediately the initial solution has been obtained. In this algorithm the stresses are found at the Gaussian integration points. This enables the equivalent nodal forces to be calculated by numerical integration from the creep strains equivalent to the multiaxial stresses over each time interval. These stresses are found from the latest nodal displacements, the thermal strains and the multiaxial creep strains. The multiaxial creep strains have to be retained in store for every Gaussian integration point and to reduce storage requirements only the minimum ^{number of} creep strain terms are retained in store. For each direct and shear stress component, and for the equivalent uniaxial stress, it is necessary to store

- 1) ϵ_c the total creep strain
- 2) $\Delta\epsilon_{c1}$ the last creep strain increment (now being checked)
- 3) $\Delta\epsilon_{c2}$ the new creep strain increment (now being found)

The last correct equivalent uniaxial stress and change in

equivalent stress during the last time interval also need to be retained as the algorithm proceeds.

The earlier programs for the creep analysis of beams and thin shells of revolution retained similar information on the total strains as the analysis proceeded. However it has been found to be more efficient to calculate the total strain from the last set of nodal displacements. These are continuously updated after each complete pass of the algorithm.

To reduce the storage requirements to a minimum the creep strains are calculated on the smallest lattice possible. Zienkiewicz (Ref. 63) has shown that good results can be obtained using a 2 x 2 x 2 Gaussian integration mesh.

The nodal displacements at the end of the last time increment are given by the total correct nodal displacements together with the last displacement increment. These are not necessarily correct as they are still being checked whilst the next set of creep strain increments are being calculated.

The elastic strains are then given as

$$\{\epsilon_E\} = \{\epsilon_T\} - \{\epsilon_c\} - \{\Delta\epsilon_c\} - \{\epsilon_{Therm}\} \quad 5.13$$

which incorporates equation 5.3 and where $\{\epsilon_T\}$, the total strain, is found from the nodal displacements, $\{\epsilon_c\}$, $\{\Delta\epsilon_c\}$, the creep strain and creep strain increment are retained in store and the thermal strain $\{\epsilon_{Therm}\}$ is found from the nodal temperatures. This gives a new set of stresses from which the new equivalent uniaxial stress can be found from equation 5.10(a). The new equivalent uniaxial stress is compared with its value at the last pass through the algorithm to ensure that the change in stress

is within the required limits. The change in the equivalent stress, provided that it is within the pre-set limits, is retained so that the equivalent uniaxial stress can be updated to its latest value when the checking part of the pass is complete.

The creep strain increments for the present time interval are calculated by either the strain-hardening or time-hardening laws. These increments are found by substituting the values of t and $t + \Delta t$ in the empirical creep law and noting the difference between each value of creep strain. The value of t is given directly by the elapse time for time-hardening solutions but is given as an equivalent time dependent on the strain-history for strain-hardening solutions. It is more accurate to calculate the creep strain increments directly than to take the creep rate at the beginning or mid-way through the time interval.

The creep strain increments are given for a multiaxial stress system by equations 5.12 and are used to find the equivalent nodal force terms as

$$\int_{Vol} [B]^T [D] \{\Delta \epsilon_c\} dVol = \sum_{j=1}^2 \sum_{k=1}^2 \sum_{l=1}^2 H_j H_k H_l \{f(\xi_j, \eta_k, \zeta_l)\} \quad 5.14(a)$$

where $\{f(\xi_j, \eta_k, \zeta_l)\} = [B]^T [D] \{\Delta \epsilon_c\} \det [J] \quad \xi = \xi_j, \eta = \eta_k, \zeta = \zeta_l$

At the end of each Gauss integration mesh the equivalent nodal forces for each element are found from equation 5.9 and are summed for the whole structure.

When the check on the variation of the stresses for all elements in the structure for the last time increment has been completed the creep strain increments and displacement increments are assumed correct. The total creep strain is then updated by $\Delta \epsilon_{c1}$ and the last creep strain increment $\Delta \epsilon_{c1}$ becomes the new creep strain

increment $\Delta\epsilon_{c2}$. The equivalent uniaxial stress is also updated together with the vector holding the last correct nodal displacements as these are now identical to the latest set of nodal displacements. Retaining these items allows a restart should the constant stress limits be exceeded.

The solution for the new set of displacement increments is found from the equivalent nodal forces and the inverted stiffness matrix stored from the initial elastic solution. For large problems where it is impossible to retain the inverted stiffness matrix in core, the re-solution facility of the frontal solution, section 4, has been used. It is imperative when using the frontal solution technique that the equivalent nodal forces due to the creep strain increments are formed in an identical order to that used when the stiffness matrices were generated in the initial part of the program.

The new set of displacements used for the next pass through the algorithm are given by the latest nodal displacements together with those displacement increments given by the equivalent nodal forces. The time increment is increased by an amount dependent on the empirical creep law. It is important that the time increment is as large as possible within the constraints imposed by the limits on the stress variation during the time interval, but does not exceed these limits as the time interval is increased.

When the limits imposed on the stress variation during a time increment are exceeded the algorithm has to be stopped and the calculations restarted from the last correct set of nodal displacements. The time interval is reduced and the last creep strain increment $\Delta\epsilon_{c1}$ is nulled in the creep data store. The

calculation then restarts using the same equations as used previously, but omitting the checking process during the first pass. The algorithm is most efficient when it is operating as a continuous cycle and not having to restart because the stress deviation limits have been exceeded.

A flow diagram for a general algorithm which enables different finite element types to be used in a structure subjected to creep deformation is given in Fig. 5.4. The algorithm is in effect identical to that described above except that it cycles through different element types in an identical order to that used when the stiffness terms of the structure were generated.

5.4 Numerical Examples

The creep analysis of a number of structures has been made using the algorithm given in Figs. 5.2, 5.3 and 5.4 as well as Fig. 2.9. These include a beam subjected to a constant bending moment, a thin pressurised cylinder and a thick ring and thick cylinder subjected to internal pressure. These analyses represent 1, 2 and 3-dimensional stress fields, and have shown that the algorithms accurately predict creep deformations. The solutions have been compared with approximate, finite difference, experimental and other finite element solutions.

The effect of neglecting some of the initial creep by varying the starting time of the creep calculations has been investigated.

5.4.1 Beam Subjected to a Constant Bending Moment

The creep deformation of a simply supported beam subjected to a constant bending moment has been analysed mathematically by

Popov (ref, 64). A finite element creep analysis using a beam finite element has been developed to observe and understand the processes involved during each time interval. The results have been compared with those of Popov.

The creep analysis is given in Appendix 10 for a beam finite element subjected to direct and bending forces. The results are given for a 10" simply supported beam, 2" wide and 6" deep, subjected to a constant bending moment of 162,000 in lbf. The elastic modulus of the material, oxygen free copper, is 1.41×10^6 lbf/in² and the empirical creep law from tension test creep curves at 165°C is given as

$$\epsilon_C = 2.68 \times 10^{-5} (e^{\sigma/7500} - 1) t^{0.372}$$

The variation in the stress across the tensile section of the beam is given in Fig. 5.5(a) for various times after the application of the load. These include both time-hardening and strain-hardening results. The compressive section is a mirror image of the stresses for the tensile half of the beam due to the loading being a constant bending moment with no tensile forces and the assumption that the creep laws are valid for both tensile and compressive stresses. The mid-span deflection with time is given in Fig. 5.5(b). The differences between the finite element solutions for the stresses and those given by Popov are very small and cannot be shown on these graphs. It can be seen that the redistribution of the stresses with time tends towards the steady state solution. The steady state solution occurs when the stress distribution across the beam is such that the variation of the creep rate is linear across the beam, i.e. no stress distribution occurs. The deflection rate for the beam tends towards the steady state solution as the time becomes

large as can be seen from the two lines in Fig. 5.5(b). This figure also shows that the creep deformation for extremely long times can be predicted approximately from the steady state solutions.

5.4.2 Effect of Initial Starting Time on Long Term Creep Analysis

It is desirable to reduce the number of incremental calculations required to obtain accurate creep solutions. The length of the time increment in the creep programs is adjusted as the solution proceeds. When the equivalent uniaxial stresses are being calculated the fractional changes in these stresses are evaluated. If the maximum change at any integration point is greater than a pre-set value the length of the time increment is reduced and conversely, if the change is smaller than the pre-set value, the length of the next time increment is increased.

In the initial stages of the solution of creep problems very short time increments are necessary as the stresses change very rapidly. It is doubtful if solutions for the early stages of creep of real structures are of much relevance as the effect of the initial condition of the material is uncertain. If accurate solutions are only required in the later stages then the number of incremental calculations may be reduced by neglecting some initial period of the material creep curves, i.e. the creep calculations are started from some finite time on the creep curves. The solutions so obtained converge towards the exact solutions as time increases.

An assessment of the above method of reducing the number of incremental calculations and its effect on the accuracy of the solutions may be made from some further results obtained for the

simply supported beam described in Section 5.4.1. The initial starting times for the creep solutions have been varied from 0.0 hr. to 1.0 hr. The errors in the stresses at various distances from the neutral axis after 10 hrs. are compared with the zero starting time solution. The number of incremental calculations for each solution are given in Table 5.1. It is seen that, for this problem, neglecting the initial period of the creep curves significantly reduces the number of incremental calculations with only a small loss in solution accuracy.

5.4.3 Thick Ring subjected to Internal Pressure

The creep deformation of a thick lead ring subjected to an internal pressure has been analysed experimentally by Fessler, Gill and Stanley (ref, 65). The elastic and creep deformation of this ring has been found using the 20 node isoparametric solid element. The idealisation comprises a coarse mesh of 3 of these elements in the radial direction, the ring axial thickness being modelled by a single element. A quadrant of the ring has been idealised by these 3 elements which each have an arc of 90°.

The effective creep strain is given by the empirical creep law

$$\epsilon_c = 3.02 \times 10^{-19} \sigma^{5.46} (t^{0.39} + 0.106t)$$

which includes both primary and secondary creep terms. The strain-hardening rule has been used for the accumulation of the creep strains in the finite element calculations.

The outside diameter hoop strains are calculated from the radial displacements and are compared with the experimental results and a computed finite difference solution in Fig. 5.6. Two sets of

experimental results are given in Fig. 5.6 and it is seen that there is good agreement between the finite element results and the experimental results at times greater than 10 hours. At smaller times the finite element results underestimate the creep strains, this discrepancy being caused by not starting the creep calculations at zero time. The difference between the present finite element solutions and the published finite difference solutions is very small for the creep deformation after small times have elapsed but increases as the creep strains become significant. The finite element solutions predict the creep deformations more accurately than the published computer results even with a very coarse idealisation.

Two finite element solutions are shown to compare the predicted creep deformations for different starting times of the creep calculations. The initial differences in the creep deformations become extremely small as the creep elapse time increases. This again shows that unless interest lies in the initial and short term creep effects the starting times for the creep calculations can be increased accordingly.

5.4.4 Thick Cylinder subjected to Internal Pressure

The creep deformation of a thick cylinder subjected to an internal pressure has to be analysed using in-plane constant strain triangular finite elements proposed by Greenbaum and Rubinstein (ref. 58). This problem has been analysed using a very coarse idealisation of 3 20-node isoparametric finite elements, Fig. 5.7(a) and the constraints impose zero axial straining but allow radial and hoop deformation.

The empirical creep law is given as

$$\epsilon_c = 6.4 \times 10^{-18} \sigma^{4.4} t$$

which contains only the secondary creep terms. The strain-hardening rule has been used for the accumulation of the creep strains.

The radial deformation of the inside and outside surfaces is given in Fig. 5.7(a) and agrees well with the solutions given by Greenbaum and Rubinstein. The stress distributions as a function of the radius are given in Fig. 5.7(b) for the elastic and steady state (10 hrs.) solutions. The agreement with the published results is extremely good considering the very coarse idealisation used. This also shows that a small Gaussian integration mesh, 2 x 2 x 2, is sufficient for the calculation of the creep strain components of the quadratic isoparametric finite elements.

The change in the value of Poisson's ratio from 0.499 for the published results to 0.450 for the finite element results, to overcome the ill-conditioning which occurs as Poisson's ratio approaches 0.5, has not affected the stress distributions.

Chapter 6 Stress Analysis of Turbine Casings

6.1 Introduction

The stress analysis of split turbine casings subjected to internal pressure and bolt loadings is carried out using the parametric family of finite elements described in Chapter 3 together with the frontal solution algorithm described in Chapter 4. It is desirable to obtain a satisfactory representation of the turbine casing using the least number of elements possible and the present solutions were planned for running on the S.R.C. Atlas computer. Solutions using many more elements are now possible using the 2M byte IBM 360/195 computer but it is still preferable to have as few elements as possible in any idealisation as the computing times are a power function of the number of degrees of freedom.

To determine satisfactory idealisations of turbine casings, plane strain solutions for turbine casing sections have been obtained using 8-noded in-plane isoparametric finite elements. These elements are the 2-dimensional equivalent of the 20-node isoparametric 3-dimensional elements and the test programs have required much less computing time and core store than would have been required with the 3-dimensional elements. 3-dimensional generalised plane strain solutions for some of these idealisations have been found for the cylindrical portion of the turbine casing for comparison with the 2-dimensional plane strain solutions. These gave an indication of the best mesh size for the shell portion of the turbine casing where the thick shell and transition parametric elements are used.

An exact geometric representation of the split turbine casing

would have required a prohibitive number of elements if the bolts and bolt holes were to be idealised exactly. An approximation to the bolt loading has been made by idealising the turbine casing without bolt holes and applying a set of forces equivalent to the bolt loads over the flange. The forces equivalent to the bolt loads give normal stresses on the flange face similar to those obtained from a generalised plane strain analysis of the casing for half a bolt pitch, where the bolt hole and loading are accurately modelled.

Results for stresses in a split turbine casing subjected to pressure loading and combined pressure and bolt loading are given. These stresses are compared with those given by Bellamy (ref. 7) for a photoelastic analysis of the same turbine casing. An approximate analysis using the thin shell of revolution finite element, described in Chapter 2, is given for the casing remote from the flange.

Results for the stresses in an inner turbine casing subjected to an axially varying pressure loading are given and are compared with those found in a photoelastic analysis by Kuzelka, (ref. 66).

6.2 2-Dimensional Analysis of the Cylindrical Portion of Split Turbine Casings

Finite element idealisations of the cylindrical section of the turbine casing of Kuzelka were used to determine optimum finite element meshes. This casing has a thicker flange than the final models tested by Bellamy, (ref. 7), but the distributions of hoop and radial stresses in the cylindrical sections are very similar. No direct photoelastic results are available for comparison

with the finite element results for a plane strain section subjected to constant pressure. The results given by Kuzelka are for an inner casing subjected to an axial variation of pressure and the stress distributions in each section can only be taken as a guide to the likely distributions when the section is subjected to constant pressure. An accurate finite element solution with which to compare solutions from coarser meshes was obtained from an idealisation using 72 8-node isoparametric elements with 4 elements through the shell section, Fig. 6.1(a). The 4 elements through the thickness were used to predict accurately the stress distribution in the region of the fillet radius. The hoop stresses at the outer and inner surfaces are shown in Fig. 6.1(b) and these agree in form with those of Kuzelka (ref. 66). The discontinuities at the element boundaries are very small. The largest discontinuities are around the fillet radius and to improve these a very fine mesh is required. As the discontinuities are very small the stress variation for the 72 element idealisation was taken to be very close to the exact solution.

In order to obtain solutions for a turbine casing using the Atlas computer it was necessary to use an idealisation with a relatively coarse mesh of elements. It was estimated that the maximum instantaneous front size possible was 200 when using the 20 node isoparametric elements. This corresponded to a mesh of 13 elements in the front with an idealisation of 12 sections.

To reduce the fine mesh of 72 elements to a coarse mesh the 4 elements used through the thickness are replaced by a single element. The analysis for single quadrilateral elements through the shell thickness in Chapter 3 shows that the stress variations through

the shell thickness can be accurately predicted with quite large arc lengths. It is satisfactory to represent the shell portion with few elements as the hoop stresses remain sensibly constant over this portion. A certain loss in accuracy occurs around the fillet radius when only a single element is used through the thickness. It might be preferable to sub-divide elements through the thickness at the fillet radius but this presents difficulties in the idealisation and also increases the number of elements in the front.

A 15 element idealisation of the section with a single element through the shell portion and 2 elements through the flange portion is given in Fig. 6.2(a). The hoop stress distribution for the inside and outside surfaces is given in Fig. 6.2(b). The stresses are very close to those given by the fine idealisation but the discontinuities are now more apparent, particularly around the fillet radius. This 15 element idealisation is acceptable but has too large an instantaneous size to be useful for the turbine casing analysis.

A coarse mesh of 9 8-node elements Fig. 6.3(a) was found to predict stress distributions similar to those predicted by the 15 element idealisation but with slightly larger discontinuities. The shell is idealised by 2 elements with 30° arc lengths and the number of elements around the fillet radius is reduced. The hoop stress distributions around the inside and outside faces of the turbine casing section are given in Fig. 6.3(b). The "looping" effect of the stresses in elements 1 and 2 is caused by the inability of the quadratic geometric functions to represent the co-ordinates of circular functions exactly.

The 9 element idealisation of the turbine casing section has been used in the 3-dimensional idealisation of the turbine casings. The instantaneous front size of the stiffness matrix using the 20 node isoparametric element is always less than 200.

6.3 3-Dimensional Plane Strain Analysis of the Cylindrical Portion of Split Turbine Casings

Generalised plane strain analyses of the turbine casing cylindrical section were carried out to ensure that the idealisations used for the 2-dimensional analysis gave comparable results for the full 3-dimensional analysis. These were for the same thicker flanged Kuzelka casing section and included an analysis using solely the 20-node isoparametric element and one using the "Ahmad" thick shell parametric element to model the shell portion of the casing. The analysis using the thick shell element was impossible with the equivalent 2-dimensional idealisation as no shell element exists in 2 dimensions.

The idealisation shown in Fig. 6.2(a) was used to compare the 2 and 3-dimensional analyses where 15 elements modelled the turbine casing section with a single element through the shell thickness. The 3-dimensional idealisation is shown in Fig. 6.4(a). The end faces are constrained to remain plane. The hoop stresses on the inside and outside surfaces for the idealisation using only the 20 node isoparametric elements are shown in Fig. 6.4(b). The stresses are independent of axial position and are plotted on a 2-dimensional plot. It can be seen that the distribution of the stresses for the 2-dimensional plane strain analysis of Fig. 6.2(b) is very similar to the 3-dimensional "generalised" plane strain

analysis of Fig. 6.4(b).

In the second 3-dimensional generalised plane strain analysis elements 1 and 2 of Fig. 6.4(a) were replaced by the thick shell parametric elements and element 3 by the transition parametric element. The remaining elements used to model the fillet radius and the flange are the original 20 node isoparametric elements. The hoop stresses for the inside and outside surfaces are shown in Fig. 6.4(c) and it may be seen that these are very similar to those obtained with the 20 node element idealisation Fig. 6.4(b). This shows that the thick shell elements with fewer degrees of freedom can accurately predict the stress distribution in the shell portion of the turbine casing.

6.4 Determination of Equivalent Bolt Loads

An accurate idealisation of the bolt holes in a turbine casing is impossible due to the very large numbers of elements required. A set of forces is required, equivalent to the bolt loading, which give stresses similar to the true stresses using the coarse 9 element mesh over the turbine casing section.

The stress distribution due to the actual bolt loads was found from a plane strain analysis of the cylindrical portion of the turbine casing over half a bolt pitch. The casing section is shown in Fig. 6.5 and the finite element idealisation is shown in Figs. 6.6(a) and 6.6(b). The shell portion of the casing was idealised with a coarse mesh as the stresses are sensibly constant over this region. The flange was idealised with 3 elements through the thickness and 11 elements over the flange area. The spot facing which included a large cut-out in the fillet radius was accurately

modelled. 57 20-node isoparametric elements were used with 1097 degrees of freedom and a maximum instantaneous size of 196. A number of analyses were carried out with different loading conditions to model the bolt loading.

The turbine casing section analysed is part of the lead turbine casing used by Bellamy (ref. 7) to predict the creep strains when the casing is subjected to a bolt and pressure loading. This has a very thin flange section and the contact stress distribution is different from the linear variation predicted by the normal simple eccentrically loaded column theories.

The bolt loading was initially applied in two ways, firstly as a uniform pressure over the spot facing and secondly as an infinitely stiff bolt with a constant vertical displacement over the spot facing.

The stresses normal to the flange face are given in Fig. 6.7(a) where the bolt load is applied as a uniform pressure over the spot facing. The bolt face is tending to rock about the outside edge and the majority of the compressive loading on the flange face is carried well away from the inside face. The sealing criterion of equal compressive stress to internal pressure is maintained with an internal pressure of 25 lbf/in² and a bolt load of 258 lbf. The stress contour for the flange face plot of Fig. 6.7(a) is an average plot of the stress distribution of Fig. 6.7(b) which shows the discontinuities in the normal stresses at element boundaries. These discontinuities are quite small and it is to be assumed that the idealisation is adequate. Concern was felt at the appearance of the stress peaks at diametrically opposite positions across the bolt hole. Comparison with the photoelastic

results of McKenzie (ref. 11) shows that these are to be expected, although with a thinner flange section they are more significant. These appear on subsequent plots and are not due to the constant pressure bolt loading. The displaced shape of the spot facing, Fig. 6.7(c) shows that the uniform pressure loading is not compatible with the deformed shape of the bolt head.

The second analysis of the bolt loading on the turbine casing constrained the displacements normal to the spot facing to be constant and the stresses normal to the flange face were determined. The stress contour plot for this loading is given in Fig. 6.8(a) and the discontinuities in the stresses over the flange face are given in Fig. 6.8(b). The stress distribution across the surface is smoother than in the previous case, Fig. 6.7(a), and the contact stresses at the inside of the casing are four times as high as those for the uniform pressure loading. Because the bolt is infinitely stiff in bending the normal stress distribution is symmetric about the bolt centre line. The stress peaks on either side of the bolt hole are still apparent but are reduced by the constant displacement condition of the bolt loading. The trough 90° round from the peaks which is apparent in all the plots should also be noted.

The true loading condition can only be found by modelling the bolt together with the turbine casing section. A bolt head has been positioned in a spot facing with no shank as the bolt bending stiffness is negligible compared with that of the surrounding flange. The bolting force has been applied as a point load on the top of the bolt head which allows the bolt head to rock, Fig. 6.9.

The bolt loads for the turbine casing model are applied through rubber pads to spigots which sit in the spot facing. There is no

bending resistance to be considered in the bolts and the bolt loads used for the finite element idealisation are identical to those used by Bellamy (ref. 7). The bolt loads are applied through steel spigots to the lead turbine casing. The distribution of the stresses normal to the flange face is given in a contour plot in Fig. 6.10(a). The internal pressure of 35 lbf/in^2 with the bolt load of 258 lbf. was calculated to be the opening pressure from a 2-dimensional analysis and this is verified on the contour plot. The discontinuities at the element boundaries are small and are shown in Fig. 6.10(b). The peaks on either side of the hole are quite large and are more prominent on the side nearest to the inside face. The contact pressure under the bolt head is shown in Fig. 6.10(c) and shows a fairly uniform radial distribution. The displacements under the bolt head are given in Fig. 6.10(d) and show a shearing effect of the bolt head due to the increased stiffness of the flange away from the bolt centre line. The displaced shape of the turbine casing section at the mid-bolt position is given in Fig. 6.10(e) and shows the greater stiffness of the flange compared with the shell portion of the casing.

The distribution of the stresses normal to the flange face for the lead turbine casing without bolt holes and individual bolt loads has been assumed to be that given in Fig. 6.10(a) between the bolt centres. To find the equivalent bolt loads which produce these stresses a 2-dimensional plane strain solution has been used. This comprises 9 8-node isoparametric elements idealising the thin flanged turbine casing section. The idealisation is given in Fig. 6.11(a) with the bolt hole and spot facing shown in Fig. 6.11(b). The loading which gave the best approximation to the stresses normal to the flange face comprised a load equivalent to $5/16$ of the bolt load

applied at node A and $11/16$ of the bolt load applied at node B. This loading also gives good continuity of the hoop stresses round the inside and outside faces of the casing section. This stress distribution is shown in Fig. 6.12 together with the normal stresses from the more accurate analysis.

This loading condition has been applied over a generalised plane strain section of the turbine casing to ensure that the normal stress distribution along the length of the element is constant. The loading distribution required to give constant stresses along the length of the element is identical to the ratios of the nodal forces equivalent to an equally distributed load over one face of the element.

6.5 Stress Analysis of an Inner Turbine Casing subjected to an Axial Variation of Pressure.

A model of an inner turbine casing has been analysed photoelastically by Kuzelka and Fessler (ref. 66). A finite element idealisation has been made of this inner turbine casing using 70 of the 20 node isoparametric finite elements. This provided an initial comparison of finite element and photoelastic results for split turbine casing models.

The inner turbine casing model is shown in Fig. 6.13 and comprises a relatively thick flange with a toroidal end closure and gland housing. The photoelastic model comprises two halves bonded together with no bolts or bolt holes through the flanges. The finite element idealisation, Fig. 6.14, comprises sections along the casing axis each with the 9 element mesh and has a total of 560 nodes with 1508 degrees of freedom and a maximum instantaneous front size of 173.

The photoelastic model was loaded by sealing the gland housing and standing the casing with the axis vertical on the gland housing end face. The axial pressure variation was applied by filling the open-ended turbine casing with mercury. The finite element model was loaded with a similar pressure variation along the axis of symmetry. A quadrant of the casing was analysed assuming the flanges remained closed by carrying tensile loads. Symmetry conditions were imposed by constraining the flange and mid-shell faces to deform in radial and axial directions. The deformation of the gland housing face has been predicted accurately by iterating from the previous solutions. When the end face is constrained to remain plane the initial elastic solution gives some axial tensile stresses over a small area of the gland housing face. Subsequent solutions were calculated allowing the area under tension in the previous solution to move axially. This process was repeated until the only area under compression was that which was constrained to remain plane.

The finite element results are for a steel casing with a Young's modulus of 3×10^7 lbf/in² and a Poisson's ratio of 0.3. The photoelastic model has a Young's modulus of approximately 1×10^3 lbf/in² and a Poisson's ratio of 0.5. Swannell (ref. 67) has shown that the variation of Poisson's ratio appears to have very little effect on the resulting stresses for 3-dimensional analyses although numerical ill-conditioning increases as the value approaches 0.5. Therefore the stresses from the finite element solution can be compared directly with those from the photoelastic analysis.

The displacements of the cylindrical portion of the casing at the mid-shell section, $\theta = 0^\circ$, and at the flange, $\theta = 90^\circ$, for the

finite element idealisation are given in Fig. 6.15 and are scaled to the displacements of the photoelastic model. The displaced shape of the cylindrical portion of the casing is very similar for both analyses although the mean displacement at the toroid/cylinder joint is somewhat larger in the finite element analysis.

The hoop stress distributions at the mid-shell section are given in Fig. 6.16(a) and are compared with the photoelastic results of Kuzelka, (ref. 66). The stress index is defined as the hoop stress in a cylindrical shell with the same internal and external diameters subjected to an internal pressure identical to that at the toroid/cylinder joint of the open-ended turbine casing. The stresses given by the finite element model are similar to the photoelastic results, although they diverge around the toroidal end closure. Greater bending stresses are predicted by the photoelastic analysis in the open end of the cylinder than by the finite element analysis. The finite element results for the hoop stresses on the inside surface at the flange face, $\phi=90^\circ$, are compared with those from the photoelastic analysis in Fig. 6.16(b). There is good agreement for the cylindrical portion of the casing but there are large differences at the gland housing end of the toroidal end closure and the increase in the hoop stresses near the boss is much greater in the finite element analysis. The majority of the axial load is carried by the outside edge of the flange end face and the compressive stresses in this region are extremely large. The finite element analysis is based on linear elastic theory and takes no account of the plasticity which probably occurs in the gland housing region of the flange face. This possibly accounts for the differences between the two analyses around the gland housing.

The meridional stress distributions on the mid-shell section, $\theta=0^\circ$, are given in Fig. 6.17 and are compared with the photoelastic results of Kuzelka (ref. 66). The meridional stresses are negligible in the cylindrical section but increase around the toroidal end closure. These agree in form with the photoelastic results where the largest meridional bending occurs in the toroid. The finite element results show that this bending changes in sign close to the gland housing. The photoelastic analysis does not show this reversal in bending because the stress distributions are not given beyond this point. It would appear from the stress distributions that the scales for the toroidal positions might be different as the plots over the first part of the toroid are very similar. The differences could be caused by the linear elastic analysis and the end constraints on the gland housing face.

A number of circumferential hoop distributions are given for the positions shown in Fig. 6.18. The stress distributions given in Fig. 6.19 are compared with some stress distributions from the photoelastic analysis. These agree in form with those of Kuzelka but have smaller hoop bending stresses. These differences are again probably due to the end constraints on the gland housing and the elastic analysis not taking account of non-linear effects as mentioned previously.

6.6 Finite Element Analysis of Split Turbine Casing

A finite element analysis of a scale model of a flanged steam turbine casing has been made using the parametric family of finite elements. The casing, also analysed photoelastically by Bellamy (ref. 7), is shown in Fig. 6.20 and incorporates scaled

down features of a number of turbine manufacturers designs. The casing comprises a central cylindrical section with toroidal and spherical end closures to the gland housings. The flange at the half joint stretches around the casing between the gland housings and has 22 bolt holes uniformly spaced along the flange centre line. The gland housings are bored out to accept a rotor and all outside surfaces intersecting the casing shell contain fillet radii.

The finite element idealisation of a quadrant of the turbine casing is given in Fig. 6.21(a) and shows the toroidal end closure in detail. This idealisation comprises 123 of the 20 node isoparametric finite elements with a total of 946 nodes, 2602 degrees of freedom and a maximum instantaneous front size of 181. The shell and flange sections have been idealised using the 9 element mesh through the turbine casing section described previously in section 6.2 and has been slightly modified for the spherical and toroidal end closures. A fine mesh has been used around the fillet radii where the shell intersects the gland housings to ensure that the elements do not become badly distorted in this region. The idealisation given in Fig. 6.21(b) shows the spherical end in more detail and also includes the node positions. The algorithms to produce computer plots of finite element idealisations for the PAFEC suite of programs are described in detail by Safavi (ref. 68).

The accurate idealisation of the bolt holes and loads requires a prohibitive number of elements and the equivalent bolt loading described in section 6.4 has been applied. The equivalent bolt loading comprises a band along the length of the flange, the

magnitude of which is directly proportional to the number of bolts for each element section. The loads are statically equivalent to the values found from the 2-dimensional analysis of section 6.4. Internal pressure has been applied on the inside surface of the casing together with a linearly decreasing pressure along the gland housing bores. The mid-shell plane, $\Theta=0^{\circ}$, and the flange face, $\Theta=90^{\circ}$, of the quadrant section of the turbine casing have been constrained to move axially and radially. It is assumed that a pressure tight seal is maintained over the flange face and that no opening occurs. The effect of the self-weight of the casing has been neglected.

The turbine casing has been analysed for two loading conditions. Initially an internal pressure was applied to compare the finite element results with the photoelastic results obtained by Bellamy (ref. 7) for the same casing. The two halves of the photoelastic model were glued together over the flange faces to maintain a pressure tight seal and the pressure loads were applied by creating a vacuum in the casing. The second loading condition was a combined internal pressure and flange bolt loading and is the initial solution for the creep analysis of the turbine casing. The creep results for this loading condition are given in Chapter 7.

6.6.1 Turbine Casing subjected to Internal Pressure Loading

The meridional variation in the hoop stresses in the shell section of the turbine casing, $\Theta=0^{\circ}$, the mid-shell position between the flanges, is given in Fig. 6.23. The meridional positions are shown in Fig. 6.22. These results show that the largest hoop bending occurs in the fillet radius and end closure at the toroidal end of

the casing. The hoop bending is very small in the cylindrical part of the casing and is very similar to that found in the 2-dimensional plane strain analysis of the turbine casing section given in section 6.1. The hoop bending in the spherical end of the casing is small compared with that at the toroidal end. The stresses are found at the element boundaries and at the mid-side positions. The stresses at element boundaries are the average of the values given by every element with a common boundary to give a continuous stress distribution. The largest discontinuities occur where the stresses are changing most rapidly. The double peak in the hoop stress distribution around the fillet radius between the gland housing and toroidal end closure can be partly accounted for by the discontinuities between adjacent elements at this point. However a similar double peak occurs in the fillet radius at the spherical end closure and this cannot be attributed to discontinuities in the stresses at the element junctions. In a previous photoelastic analysis of a 3-diameter pressure vessel, section 2.3.2.4, the results showed a double trough in the meridional stress variation round a knuckle on the opposite side to the fillet radius due to an increase in material thickness in this area. Similarly the double peak in the stress distributions can probably be attributed to the large material increase below the end closure fillet radii where the gland housing bore joins the inside surface of the end closures.

The variation of the meridional stresses for 3 radial positions round the shell and at the flange face, ($\theta = 0^\circ, 30^\circ, 60^\circ, 90^\circ$) are compared with the photoelastic results of Bellamy (ref. 7) and are shown in Figs. 6.24. The meridional bending is larger around

the fillet radius between the gland housing and toroidal end closure and the double peak in the meridional stress distributions around the fillet radii at both end closures is again apparent. Bellamy (ref. 7) has investigated the stress distributions around the toroidal end of the turbine casing. The finite element results agree well with the photoelastic results for the meridional stress distribution in the casing although greater bending is apparent in the cylindrical section of the photoelastic model. At the mid-shell section, $\Theta=0^\circ$ Fig. 6.24(a), the mean meridional stress in the cylindrical part of the casing agrees well for both sets of results. However the mean meridional stress in the cylinder for the other shell sections, $\Theta=30^\circ$ and $\Theta=60^\circ$, is less in the photoelastic analysis than that given by the finite element analysis. The stress distributions around the toroidal end closure and fillet radius are in good agreement for all the shell sections, $\Theta=0^\circ, 30^\circ, 60^\circ$, although the photoelastic results do not show the double peak around the fillet radius. The meridional stress distributions over the flange face, $\Theta=90^\circ$ Fig. 6.24(d), show reasonable agreement for both analyses. The finite element results indicate that the meridional bending in the flange at the cylindrical section of the casing is larger than any meridional bending in the shell section at the same position but smaller than that given by the photoelastic analysis. The flange in the photoelastic model is less stiff than that in the finite element idealisation due to the bolt holes not being idealised. The differences between the photoelastic and finite element results for the meridional stresses in the casing may be due to the photoelastic analysis being based on small deformation theory. The radial deformation along the

cylindrical portion of the shell is large due to the higher flexibility of the model at the beginning of the stress freezing cycle but it is doubtful whether this accounts for all the discrepancies.

The circumferential hoop stress distributions at the toroidal end of the turbine casing are given for the meridional positions shown in Fig. 6.26 and are compared with some photoelastic results given by Bellamy (ref. 7). The hoop stress distributions, Figs. 6.26, show very little hoop bending in the cylindrical portion of the turbine casing. The hoop bending increases round the toroidal end closure to a maximum at the toroid/fillet radius junction, $\phi=90^{\circ}$. The hoop stress distributions in the cylindrical portion of the turbine casing are very similar to the 2-dimensional finite element plane strain results described in section 6.2 and shown in Fig. 6.3(b). Therefore the cylindrical part of the turbine casing away from the end closures can be accurately analysed as a plane strain 2-dimensional model.

The hoop stress distributions from the photoelastic analysis, Figs. 6.26, agree in form with the finite element results, particularly around the toroidal end closure, but show increased bending in the shell section at all meridional positions. The bending is most acute in the cylindrical part of the turbine casing and shows a large reversal in hoop bending at the mid-cylinder position. It would appear that the hoop strain distribution in the photoelastic model around the cylindrical part of the casing is very large and is causing the differences in the meridional and hoop stress results from both analyses. This would imply, noting the large change in hoop bending stress, that the casing has slightly

buckled due to the vacuum applied to load the casing.

6.6.2 Turbine Casing subjected to Internal Pressure and Bolt Loading

The meridional variation of the hoop stresses at the mid-shell section of the split turbine casing subjected to an internal pressure and a bolt loading just sufficient to maintain a pressure tight seal is given in Fig. 6.27. The hoop stress distribution is very similar to that given for internal pressure loading only, Fig. 6.23, although the hoop bending has increased in the cylindrical section of the casing. The double peak in the stress distribution around the fillet radii at each end closure is still apparent and a double trough has now appeared on the inside surface below the fillet radius at the toroidal end.

The variation of the meridional stresses in the turbine casing is given for 3 meridional shell sections, $\Theta = 0^\circ$, 30° , 60° , and for the flange face, $\Theta = 90^\circ$, in Figs. 6.28. The meridional stress distributions are very similar to those for the internal pressure loading only, Figs. 6.24, but the meridional bending in the cylindrical shell sections is slightly greater. The mean meridional stresses in the flange face Fig. 6.28(d) are much lower than for the internal pressure loading case, Fig. 6.24(d) and the bending stresses are similarly reduced. The reduction in the meridional stresses in the flange is due to the Poisson effect of the compressive bolting stresses normal to the flange face.

The hoop stress distributions for the meridional positions shown in Fig. 6.25 are given in Figs. 6.29. The hoop stress distributions for the cylindrical part of the casing show the increased bending caused by the bolt loading and its effect on the inside surface

stresses close to the flange face. The hoop stresses around the fillet radius give an indication of the approximate stresses between the bolt holes as the spot facings in the lead model cut into the fillet radius. The largest hoop bending stresses occur in the toroidal end closure, the greatest being at the toroid/fillet radius junction, $\phi=90^\circ$. The hoop stress distributions in the cylindrical part of the casing can be compared with the 2-dimensional plane strain results shown in Fig. 6.12. These results agree in form at the mid-cylinder section.

6.7 Approximate Analysis of the Shell Portion of the Split Turbine Casing using the Thin Shell of Revolution Ring Finite Element

In the shell section of a split turbine casing the stress distribution can be approximated by assuming the casing to be an axisymmetric structure. A meridional section of the split turbine casing at the mid-shell position, $\Theta=0^\circ$, has been idealised using the axisymmetric thin shell of revolution ring finite element described in Chapter 2. This idealisation is shown in Fig. 6.30 and comprises 15 of the higher order displacement function elements with 16 nodes and 107 degrees of freedom. The gland housings and knuckles have been approximated by shell elements of the same thickness as the turbine casing shell and are therefore much thinner than the actual bosses. The axisymmetric casing was loaded with an internal pressure applied at the inside surface of the shell.

The meridional variation of the hoop stresses in the axisymmetric shell is given in Fig. 6.31, and agrees very closely with the results obtained for the mid-shell hoop stresses, Fig. 6.23, using

a 3-dimensional idealisation of the casing. These results show very little hoop bending in the cylindrical part of the casing and corroborate the 2-dimensional and full 3-dimensional idealisations which showed very little hoop bending in the cylindrical shell. The stress distributions for the axisymmetric thin shell idealisation show the stress discontinuities at the element boundaries and give an indication of the accuracy of the solution.

The meridional stress distribution in the axisymmetric shell is given in Fig. 6.32 and is compared with the photoelastic results obtained by Bellamy (ref. 7). These stress distributions agree well around the toroid but the axisymmetric model indicates that there is very little bending in the cylindrical part of the casing. The agreement with the 3-dimensional model, Fig. 6.24(a) is extremely good particularly away from the gland housings. The differences are caused by the shell approximation to the bosses and knuckles at the end closures and are directly comparable with those for the complete 3-dimensional analysis. The meridional stresses in the fillet radius, toroidal end closure and cylindrical shell for the axisymmetric approximation to the turbine casing compare extremely well with the results from the more accurate idealisation at the mid-shell section, $\theta = 0^\circ$, ^{and} _^ the photoelastic analysis. This shows that the stress distributions for the split turbine casing away from the flanges can be adequately predicted by an approximate axisymmetric finite element idealisation.

Chapter 7 Creep Deformation of a Turbine Casing Model

7.1 Introduction

The creep deformation of a flanged model turbine casing, Fig. 6.20, has been investigated experimentally by Bellamy (ref. 7.). The creep deformation of this model turbine casing has been calculated using the finite element programs described previously. These creep analyses include those of both a 3-dimensional model of the turbine casing, Fig. 6.21, and a simplified axisymmetric approximation of the model turbine casing, Fig. 6.30.

7.2 Empirical Creep Law

Bellamy (ref. 7) has produced an empirical uniaxial creep law from tests on lead dumb-bell specimens cut from a number of lead model turbine casings. The creep law was formulated from constant stress tests in the range 1000-1600 lbf/in² and found to be $\epsilon_c = 1.291 \times 10^{-21} \sigma^{5.417} t^{0.513}$ which contains only primary creep terms. Initial finite element solutions were found using this creep law for both the 3-dimensional and axisymmetric idealisations. The creep strains predicted from both finite element models were found to be of the order of 100 times less than those measured from strain gauges on the actual lead model. Comparison of the initial strains showed these to be in good agreement with those in the model and it was felt that the stress levels predicted from the initial stress analysis were reasonably accurate.

The calculated maximum equivalent stresses in the shell, remote from the flanges, were less than 400 lbf/in². The creep strain predicted by the above creep law for such stress is about 1 μ strain

(microstrain) in 500 hours and this agrees with the creep strains in the finite element solutions. However Bellamy measured increases in total strain after 500 hours in excess of 100 μ strain. Subsequent creep tests were made on the uniaxial dumb-bell specimens at lower stress levels, i.e. 400 lbf/in², and no major divergence from the empirical creep law was apparent.

No explanation could be found for the discrepancy between the finite element and experimental results, and it was decided to obtain creep solutions for the casing using a creep law selected to give significant creep in a reasonable time.

The original empirical law given by Bellamy (ref. 7) could have been used if the creep calculations had been continued to 10⁷ hours instead of the usual 10³ hours but this would have been extremely expensive in computing time. The uniaxial creep law used to predict the creep deformation of the turbine casings in the following section is a modified version of the empirical creep law found by Bellamy. This modified law, $\epsilon_c = 1.291 \times 10^{-19} \sigma^{5.417} t^{0.513}$, gives creep strains 100 times greater than those predicted by the empirical creep law given by Bellamy and is close to that used by Fessler, Gill and Stanley (ref. 65) to predict the creep deformation of thick lead rings.

7.3 Creep Deformation of 3-Dimensional Finite Element Idealisation of Lead Turbine Casing.

The finite element idealisation used to predict the creep deformation is the same as that used for the stress analysis in Chapter 6. The casing is shown in Fig. 6.20 and the idealisation, which comprises 123 20-node isoparametric elements is shown in

Figs. 6.21(a) and (b). The initial stress analysis is the first set of calculations in the creep process and is checked for discontinuities to ensure that the idealisation is satisfactory before the creep calculations proceed.

The values of strain and stress are plotted at the inner and outer Gauss integration points. The Gauss integration mesh used for the 3-dimensional creep analysis was a 2 x 2 x 2 mesh for each element and the creep history was stored only at the Gauss points. For the shell parts of the casing only one element is used through the thickness and it is not justifiable to extrapolate from the Gauss points to obtain the surface stresses and strains as these do not vary linearly through the thickness.

7.3.1 Deformation of Lead Turbine Casing Model

The axial and radial deformation of the flange and shell of the turbine casing model at 4 axial positions is given in Figs. 7.1. The deformations are plotted for a number of times between the creep calculation starting time of 10^{-3} hours and the final creep time of 10^3 hours. Comparison of the axial displacements in the mid-shell and flange at the toroid-cylinder and cylinder-sphere joints shows a circumferential variation in the axial displacements. The axial deformations over the boss end faces and the mid-cylinder section are identical for each section and therefore these sections remain plane. The circumferential variation of the axial displacements in the model turbine casing remain reasonably constant but increase steadily with time as creep deformation takes place, Fig. 7.1(a).

The radial displacements are given at the mid-shell and flange faces for the 3 axial positions in the cylindrical portion of the

turbine casing. Figs. 7.1(c) and 7.1(d) show the creep deformation of radial and axial sections of the turbine casing. The radial displacements at the flange face initially increase due to creep deformation but as the stresses redistribute the radial displacements decrease quite rapidly. A strange inflection occurs in the radial displacement in the shell at the mid-cylinder position which tends to arch the shell. At the same time the radius at the mid-cylinder flange face decreases rapidly whilst the shell radius at $\Theta = 45^\circ$ increases rapidly. This gives an extremely distorted casing section Fig. 7.1(c). The axial deformation of the casing increases gradually with time, the flange length increasing more rapidly than the shell.

7.3.2 Variation of Strain and Stress in the Model Turbine Casing due to Creep Deformation

The variation of strains and stresses at 0, 10, 1000 hours due to creep deformation of the model turbine casing, Fig. 6.21, is given in Figs. 7.3 and Figs. 7.5-7.7. The meridional distribution of the strains and stresses is given at the mid-shell position remote from the flanges. The key to the meridional positions of Fig. 7.3 is given in Fig. 7.2 together with the convention used to describe the distributions at the inside and outside Gaussian integration points at different times. This convention is used for all the figures showing variations of strain and stress with time. The distributions are given at the starting time, 0 hours, part way into the creep deformation, 10 hours, and at the end of the creep calculations, 1000 hours. The circumferential distributions of the strains and stresses are given in Fig. 7.4. The key to the

circumferential positions is shown in Fig. 7.4 and the convention for the distributions at various times is identical to that given in Fig. 7.2. The circumferential distributions of meridional and circumferential strain, meridional, circumferential, and equivalent uniaxial (effective) stress and the variation of the effective stress distributions over the flange section at 3 axial positions are given. These give a clear indication of the exact way in which the stresses in the flange redistribute.

The increase in the circumferential strains in the shell of the turbine casing is most significant in the cylindrical section, Fig. 7.3(a). The circumferential strains at the inside have more than doubled and the circumferential bending has increased by a factor of 4 over the cylinder and by an even greater amount at the toroid/cylinder joint. Similarly the circumferential strains and bending in the toroid close to the boss fillet radius have increased. There is very little increase in circumferential strain in the spherical end closure. The meridional bending in the shell section of the turbine casing remains relatively unchanged in the cylinder, Fig. 7.3(b). However the meridional bending increases in both end closures and in the region of the boss fillet radius at the toroidal end closure. The greatest increases in the meridional strains occur where the meridional stresses are most significant, Fig. 7.3(d), although this is not true for the spherical end closure where the meridional stresses are similar to those in the cylinder. The increase in the meridional strains in the spherical end closure boss is negligible. The finite element creep analysis predicts the largest meridional creep strains to be in the same position as those found by Bellamy (ref. 7), i.e. on the inside surface of the toroidal end

closure, and the strain distributions round the toroid follow similar patterns.

The meridional distributions of circumferential and meridional stress, Figs. 7.3(c) and (d), show little change in the mean values but increases in the bending stresses. These increases in bending stress are greatest close to the toroidal end closure fillet radius. In general the circumferential bending stresses reduce, particularly in the cylinder, but the meridional bending stresses increase in both end closures close to the cylinder/end closure joints. The meridional variation of the effective stress distribution shows that the greatest changes occur in the fillet radius between the boss and the toroidal end closure, in the toroid close to the toroid/cylinder joint and in the cylinder. In general the effective stresses tend to even out and variations of effective stress through the thickness are reduced. However the highest stresses do not relax as would be expected if the casing was an axisymmetric body. The reason for the increase in the values of the largest effective stresses can be seen from the circumferential distribution of the strains and stresses.

The circumferential distribution of the meridional and circumferential strains and stresses, and the effective stresses are given at 3 axial positions. These are the mid-toroid position where the meridional stresses were found to be greatest in the elastic analysis, the toroid/cylinder joint and the mid-cylinder position. The strain and stress distributions in the spherical end closure are smaller than those in the toroidal end closure and are therefore less significant. The creep deformation of the casing can be envisaged most easily by considering the strain and stress distributions at

the mid-cylinder position, Figs. 7.5. The changes in circumferential strain are large particularly close to the flange/shell fillet radius. The circumferential strains in the fillet radius become extremely large due to the high initial stresses in the fillet radius caused by the bolt loading. In the fillet radius and flange the circumferential stresses at the outside surface are parallel to the surface. The circumferential bending of the shell close to the flange, caused initially by the flange having a stiffening effect in the radial direction, increases as creep deformation proceeds. The membrane stresses remain reasonably constant but the bending stresses increase by a factor of 4 in 1000 hours. The increase in bending caused by the stiffening effect of the flange causes circumferential bending to spread further into the shell. A circumferential bending moment, gradually increasing with time, spreads into the shell and attempts to force the flange to move radially outwards.

At the same time the large compressive stresses in the flange caused by the bolt loading are redistributed over the complete flange section and into the base of the shell. In practice as the flange deforms under the bolt loads the bolt loading relaxes and the stresses in the flange due to bolting up forces reduce. The finite element model uses a constant bolt force for all the creep calculations so that it is identical with the lead turbine casing model where the bolt loads were applied through a spring system.

In general the effective stresses in the casing increase as creep deformation proceeds but decrease in the flange beneath the bolts. This is clearly seen in Fig. 7.5(d), where the initial effective stresses due to the bolt loads are in excess of 1000 lbf/in^2 and these redistribute rapidly as creep takes place. The stresses in

the flange are dominated by large compressive stresses normal to the flange face in a narrow band beneath the equivalent bolt loadings. These result in large negative creep strains which help to spread the bolt load gradually across all the flange. To compensate for negative creep strains normal to the flange face, positive axial and radial creep strains are formed by the constant volume criterion. Consequently the axial deformation of the flange increases and there is a slight increase in the meridional membrane and bending stresses in the shell.

At the other 2 axial positions, mid-toroid and toroid/cylinder joint, similar effects are noticed although the meridional stiffening effect of the end closure is more significant and the circumferential bending is greatly reduced. The circumferential bending in the shell close to the flange at the toroid/cylinder joint remains reasonably constant although the creep strains increase rapidly. However the circumferential moment increases rapidly in this region due to the stress redistribution in the flange. Large increases in the meridional strain in the shell close to the flange at the toroid/cylinder joint and the mid-toroid position are caused by the increase in meridional creep strain in the flange due to the bolt loads. This meridional deformation of the flange causes increased bending in the shells forming the end closures.

The effect of the flanges on the creep deformation and stress redistribution is a dominating one. The creep deformations are constrained by the flanges in 2 ways,

- a) the effect of the flanges around the end closure
- b) the closing effect of the flanges due to bolt loading.

The boss and flanges form a large part of the end closures. To

carry the circumferential strain caused by the pressure load the flange at the cylinder/end closure joints deforms radially inwards relative to the mid-shell. The cylinder, not constrained by the heavy bosses on the end closure and with no radial restraint similar to that carried by a toroid or sphere deforms more freely but is still restricted by the flange. The radial deformation of the flange, Fig. 7.1 (c), is less than that of the shell. The deformed shape of the casing would normally attempt to open the inside of the flange by rocking on the outside of the flange face but this is impossible due to the bolt loads maintaining a pressure tight seal. Consequently bending stresses caused by keeping the flange closed appear at the shell/flange junction. Combining the end closures and the cylinder causes meridional bending at the junctions due to the mismatching of radial deformations. The end closures attempt to restrict the radial deformation of the flange face thus causing even greater circumferential bending in the cylindrical shell.

As creep deformation takes place the bending stresses in the shell increase due to the stress redistribution of compressive stresses in the flange and the stiffening effects of the flange. The radial deformation of the flanges initially increases due to the circumferential bending but decreases as axial deformation becomes significant and causes the casing to deform into an elliptic cross section.

7.4 Axisymmetric Approximation of the Creep Deformation of a Turbine Casing

The creep deformation of the lead turbine casing has been found using the axisymmetric thin shell of revolution finite element described in Chapter 2. The idealisation and key to the meridional positions are shown in Fig. 7.8. The variation of the circumferential

strains with time is given in Fig. 7.9(a) and shows the increase in the circumferential strains in the cylindrical portion of the casing and around the fillet radii at the bosses. The circumferential strain distribution due to creep given by the axisymmetric approximation of the turbine casing underestimates that given by the full 3-dimensional analysis. The meridional strain distribution with time is again underestimated by the axisymmetric approximation. Although the initial stresses in the casing are in agreement the stresses in the axisymmetric analysis redistribute and the creep strains are consequently not as large as those predicted by the 3-dimensional analysis where the shell stresses increase due to the stress redistribution in the flange. The axisymmetric analysis gives an indication of the creep strains in the turbine casing although these are underestimated.

7.5 Computation of Creep Deformation of a Turbine Casing

The 3-dimensional finite element idealisation, shown in Fig. 6.21, has 123 20-node isoparametric finite elements, with 946 nodes and 2602 degrees of freedom with a maximum instantaneous size of 181. The initial solution has used the frontal solution described in Chapter 4, while the creep analysis has used the resolution technique described in Chapter 4 and the creep algorithm described in Chapter 5. The 3-dimensional analysis has been found using the IBM 360/195 computer at the SRC Rutherford High Energy Laboratory. The program uses 396,000 8 bit Bytes and the initial solution took 223 seconds, whereas the creep analysis has taken 2 hours with 116 time increments for the creep analysis starting at 10^{-3} hours and finishing at 10^3 hours. The axisymmetric approximation to the turbine

casing comprised 15 thin shell of revolution finite elements, with 16 nodes and 107 degrees of freedom. The inverted stiffness matrix can be held in store and the analysis was carried out on the Nottingham University KDF-9 computer. This analysis required 19,000 48 bit words of store and the creep analysis from 10^{-3} hours to 10^3 hours was achieved in 16 minutes. The variations in the stresses were limited to 10% through each time increment for both analyses although the Gauss meshes were $2 \times 2 \times 2$ for the 3-dimensional analysis and 4×3 for the axisymmetric analysis. The IBM 360/195 computer is estimated to be 100 times faster than the KDF-9 computer.

Chapter 8 Discussion

8.1 Introduction

The finite element method has been used to determine the stresses in turbine casings subjected to internal pressure and bolt loadings. The analyses use both solid 3-dimensional isoparametric finite elements and axisymmetric thin shell of revolution finite elements. The computed stress distributions have been compared with results from photoelastic model tests. The creep deformation of a model turbine casing has been found using both axisymmetric thin shell and 3-dimensional isoparametric finite elements.

8.2.1 Elastic Analysis

The elastic stress distributions in two model flanged turbine casings, subjected to internal pressure, have been calculated using the finite element method and the results have been compared with photoelastic analyses obtained by Bellamy(ref. 7) and Kuzelka (ref. 66). The closed turbine casing has been idealised using two types of finite element.

The simpler analysis comprised 15 thin shell of revolution finite elements which were used to determine the stresses in the shell portion of the turbine casing. The casing was idealised as an axisymmetric body and the results obtained describe the meridional variation in the stress distribution away from the flange. A more complete 3-dimensional idealisation modelled a quadrant of the turbine casing using 123 20-node isoparametric elements. The results from the axisymmetric analysis agreed well with those obtained from the more exact idealisation indicating

that for this casing the flanges had little effect on the stresses in the casing remote from the flanges.

The finite element solutions for the stresses in the toroidal end closure of the closed turbine casing show good agreement with the photoelastic results obtained by Bellamy (ref. 7). The finite element solutions did not predict the large bending stresses found in the cylinder of the photoelastic model. The photoelastic model was loaded during the stress freezing cycle by applying an internal vacuum which gave significant deformations but did not cause the casing to buckle. The finite element analyses are based on small deformations and as no account has been taken of the large radial deformations in the cylinder a small error in predicting the stresses is to be expected. The finite element analyses also take no account of stresses caused by the effects of critical loads, i.e. buckling, and it is known that the photoelastic model was close to this condition at the start of the stress freezing cycle. Further, comparison of the initial elastic meridional strains in the lead turbine casing model with those found from the finite element solutions gave good agreement. The 3-dimensional finite element solution gave reasonable continuity of strains and stresses across element boundaries, despite the coarse idealisation, and showed good agreement with the axisymmetric finite element analysis for the shell portion of the turbine casing.

The stress distribution in the flange of the 3-dimensional finite element model can only be a good approximation of the stresses between bolt holes as the true stress distribution beneath the bolt heads is extremely complex. To determine the true stress distribution in a turbine casing requires a very fine idealisation to model the

bolts and bolt holes individually. A finite element idealisation of this type is too large for the majority of modern computers and consequently a coarser idealisation with approximate bolt loadings must be used. The coarse mesh of the turbine casing model gives a good indication of the strength of the casing, in particular the restraining effect of a bulky flange on a relatively thin shell. The data generation required for a complicated mesh used to idealise a complex engineering structure such as a turbine casing can take months to prepare, even though a relatively coarse idealisation has been chosen. The idealisation used to model the closed turbine casing was chosen so that the solution of the elastic stresses could be found on the S.R.C. Atlas Computer in under 2 hours. The availability of much larger and faster computers has since made it possible to refine the idealisation and obtain elastic solutions in a fraction of the time.

An inner turbine casing has been analysed both photoelastically and using the finite element method. The 3-dimensional finite element solution using a coarse idealisation comprising 70 20-node isoparametric finite elements gave results comparable with those found from the photoelastic analysis by Kuzelka (ref. 66). The difference between the two solutions is principally in toroidal end closure, particularly in the region of the boss. Altering the end constraints of the boss in the finite element analysis had a significant effect on the stresses in the toroidal end closure. The stresses normal to the boss face were extremely large and parts of the boss may possibly have become plastic during the early stages of the stress freezing cycle used in the photoelastic analysis. The effects of plasticity on the stresses in the gland

housing boss of the inner turbine casing have not been investigated but are expected to be significant.

The shell of revolution finite element idealisation gives results for the stress distributions in the shell of the closed turbine casing model which are comparable with the full 3-dimensional finite element analysis. For this idealisation the turbine casing model is treated as an axisymmetric body. This approximation can only be used to predict the stresses away from the flange in turbine casings where the flange thickness is small compared with the shell radius. The axisymmetric approximation of the inner turbine casing gave poor results for the stresses in the shell, as the flange thickness was a significant proportion of the shell radius.

8.2.2 Creep Analysis

The creep deformations of a closed lead turbine casing model have been found using both of the finite element idealisations used for the elastic analysis. The 3-dimensional idealisation comprised 123 20-node isoparametric finite elements and the axisymmetric approximation comprised only 15 thin shell of revolution finite elements. The two creep analyses, finite element and lead model, were expected to show reasonable agreement but the initial finite element results were found to predict creep deformations of approximately 1% of those found in the lead turbine casing model by Bellamy (ref. 7). The differences are due to the empirical uniaxial creep law predicting smaller creep strains than were found in the lead turbine casing model at equivalent stresses. The mathematical creep calculations depend solely on the empirical uniaxial creep law and as this law contains very high power functions

of stress, small errors can be easily magnified. To determine the stress redistribution in a model turbine casing an empirical creep law was used which was known to give noticeable creep strains in a relatively short time, i.e. 10^3 hours.

The creep algorithms have to be extremely efficient as creep solutions demand large amounts of computing time usually with large core store requirements. Many techniques are used to improve the method of solution of creep problems to reduce computing time. The simplest method is to reduce the number of elements in an idealisation and the order of the Gaussian integration mesh used to store and determine creep information. These changes not only reduce the core store requirements but drastically reduce the computing time. The computing time can also be reduced by starting the creep calculations at a small positive time, say 10^{-3} or 10^{-2} hours, when calculating the creep deformations after 10^3 hours and using the largest time increments possible. It has been shown in Chapter 5 that neglecting the initial creep deformation has very little effect on the creep strains at some distant time. It is questionable whether physical creep strains for times less than 10^3 hours can be accurately measured and whether the resulting empirical creep laws can be used to predict the creep deformations at very small times.

By optimising all the parameters involved in the creep analysis an efficient solution may be obtained. However careful checks must be made within the algorithm to ensure that the solution does not become divergent or oscillatory. This can occur when there is too large a variation in stress during each time increment, caused by the time increments being a large proportion of the creep elapse

time. When the empirical creep law contains only primary and secondary terms the solution has become unstable when the time increments begin to decrease as the solution proceeds.

To find the creep strains and stresses on the outside surfaces of a structure it is necessary to extrapolate their values from those at the Gaussian integration points. A fine Gauss integration mesh is required through the element thickness to predict the creep strains and stresses at the outside surfaces as their variation through the thickness is a complicated power function.

The thin shell of revolution finite element has been shown to be extremely powerful and economical for predicting the stresses and creep in the shell sections of the flanged turbine casing. The idealisation usually requires very few elements and very little data.

8.2.3 Economics of Solutions

The computing times used to analyse the flanged model turbine casing for the full 3-dimensional and axisymmetric approximations are compared in Appendix 11. An idea of the relative times required to generate the data can be obtained by considering the total number of degrees of freedom, number of nodes and elements.

Clearly the axisymmetric thin shell of revolution is extremely efficient and is to be recommended if interest lies in the elastic stresses in the shell of the casing. For all other areas of the casing, and to a certain extent in the shell in the creep analysis, the flange has a dominating effect which cannot be neglected. As the flange thickness to shell radius ratio increases, the ratio for the present model is 17%, the flange dominates the deformation

and an axisymmetric approximation cannot be used.

8.3 Future Work

The present turbine casing model was based on a number of turbine manufacturers designs and is a very much simplified version of any practical turbine casing. The flange design is unrealistic for a high pressure turbine casing and consequently the pressure applied to the shell is very much lower than that which this shell would be expected to carry. The stress levels in the shell are quite small compared with the flange stresses and consequently any creep deformation occurs in the flange of the turbine casing. The use of the finite element method in predicting the stresses and creep deformations of a model turbine casing has been shown. A more realistic model turbine casing with very much thicker flanges and perhaps steam inlet and outlet pipes should be analysed. For a thicker flanged model a very much higher internal pressure can be applied with the same bolt loads before leakage occurs. The stresses in the shell will be much higher whilst those in the flange will be reduced, and greater creep deformation of the shell will occur. Also with stress levels within the range used to determine the empirical creep law for the lead, a better agreement between the finite element and lead model results can be expected.

The present finite element analysis has not taken into account the variation of temperature over the turbine casing. A realistic loading of a turbine casing includes hot and cold starts, rapid load changes and "two-shifting" where the turbine is shut down overnight. The temperature transients during these load changes are known to cause thermal fatigue damage, whereas the majority of

creep occurs at base load when the turbine is at its hottest. Future work should include the effect of temperature on the creep deformation of the turbine casing and the analyses should include both steady-state and transient temperature calculations.

The creep algorithms can be improved by using time marching techniques to reduce the computing time. Such a method, e.g. Runge-Kutta, predicts the creep deformations at some distant time by determining the creep deformations at a few initial times. This greatly reduces the total number of solutions required by the creep algorithm.

The structure can be broken down into a number of "substructures" each of which could be treated as a "super"-element. Substructuring not only reduces the amount of computer core store required to run a creep program but also the amount of data required to describe the structure.

The work reported here has shown the power of the finite element method for predicting the stresses and creep deformation of a complex structure such as a flanged turbine casing. The solutions demand the use of large fast computers and the cost of such calculations can be exorbitant. The creep deformation and stress redistribution of prototype or production turbine casings can be calculated in this way before any initial damage due to bad design or operation can take place. The finite element analysis provides more information about a prototype structure than experimental modelling techniques can provide in a much shorter time.

Acknowledgements

I would like to thank Professor A.G. Smith for making the facilities of the Department of Mechanical Engineering at Nottingham University available to me during this work.

My grateful thanks go to my supervisor, Dr J.J. Webster, for his guidance and support during this project. Jeff Webster's willingness to discuss problems, however trivial, and his friendly advice have been invaluable to me during this work. I would also like to thank Dr. H. Fessler together with Dr. J. Webster for their patience in listening to regular progress reports on the research project. My thanks also go to Bob Bellamy, who did the experimental work, for his co-operation during this project.

I wish to thank the Science Research Council for supporting this project and for making computer facilities available at the Atlas Computer Laboratory. I would like to thank the staff of the Atlas Computer Laboratory for their help and co-operation and in particular Dave Parker for his help in running my programs on the IBM 360/195 computer, without which the creep results would not have been obtained.

The work has been carried out using the PAFEC suite of finite element programs. I would like to thank all members of the PAFEC group for their co-operation and help, and in particular Dr. R.D. Henshell whose advice and enthusiasm has been extremely useful. I would also like to thank Barbara Martin for uncomplainingly punching the many computer programs and data packs.

Finally my thanks go to my wife, Judith, who not only typed this thesis and produced a few of the diagrams, but also encouraged me

to pursue this research and has borne the load very well.

Appendix 2. Stiffness Terms for Thin Shell of Revolution Finite Element.

$$\text{Strain Energy } V = \frac{1}{2} \{\delta\}^T [A^{-1}]^T \int_0^1 [B]^T [D'] [B] ds [A^{-1}] \{\delta\}$$

$$\begin{aligned} \text{where } V = & \frac{Et^3}{24(1-\nu^2)} \int_0^1 \left(u^2 \left(\frac{12}{t^2} \left(\frac{n^2}{r} + \frac{(1-\nu)}{2} \frac{\cos^2 \phi}{r} \right) + \frac{n^2 \sin \phi}{r^2 r_s} \right. \right. \\ & \left. \left. + \frac{\cos^2 \phi (1-\nu)}{r^2} \left(\frac{r}{r_s^2} - \frac{3 \sin \phi}{r_s} + \frac{3 \sin^2 \phi}{r} \right) \right) \right. \\ & + 2uv.n \frac{\cos \phi}{r} \left(\frac{12}{t^2} \left(1 + \frac{(1-\nu)}{2} \right) + \frac{1}{r_s^2} + \frac{(1-\nu)}{2} \frac{\sin \phi}{rr_s} \right) \\ & + 2uwn \left(\frac{12}{t^2} \left(\frac{\sin \phi}{r} + \frac{\nu}{r_s} \right) + \frac{1}{r^2} \left(\frac{n^2}{r_s} + \cos^2 \frac{(1-\nu)}{2} \left(\frac{3 \sin \phi}{r} - \frac{1}{r_s} \right) \right) \right) \\ & - u \frac{\partial u}{\partial s} \cos \phi (1-\nu) \left(\frac{12}{t^2} + \frac{1}{r} \left(\frac{r}{r_s^2} - \frac{3 \sin \phi}{r_s} + \frac{3 \sin^2 \phi}{r} \right) \right) \\ & + 2u \frac{\partial v}{\partial s} n \nu \left(\frac{12}{t^2} + \frac{\sin \phi}{rr_s} \right) \\ & - 2u \frac{\partial w}{\partial s} n \frac{\cos \phi}{r} \left(\frac{1}{r_s} + \frac{(1-\nu)}{2} \left(\frac{3 \sin \phi}{r} - \frac{1}{r_s} \right) \right) \\ & - 2u \frac{\partial^2 w}{\partial s^2} n \nu \frac{\sin \phi}{r} \\ & + \frac{v^2}{r} \left(\cos^2 \phi + n^2 \frac{(1-\nu)}{2} \right) \left(\frac{12}{t^2} + \frac{\sin^2 \phi}{r^2} - \frac{3 \sin \phi}{rr_s} + \frac{3}{r_s^2} \right) \\ & + 2vw \cos \phi \left(\frac{12}{t^2} \left(\frac{\sin \phi}{r} + \frac{\nu}{r_s} \right) + \frac{\sin \phi}{r} \left(\frac{\sin^2}{r^2} - \frac{2 \sin}{rr_s} + \frac{1}{r_s^2} \right) \right. \\ & \left. + \frac{n^2}{r^2} \left(\frac{2}{r_s} - \frac{\sin \phi}{r} + \frac{(1-\nu)}{2} \left(\frac{3}{r_s} - \frac{\sin \phi}{r} \right) \right) \right) \end{aligned}$$

$$\begin{aligned}
 & - v \frac{\partial u}{\partial s} n(1-\nu) \left(\frac{12}{t^2} + \frac{\sin \phi}{rr_s} \right) \\
 & + 2v \frac{\partial v}{\partial s} \nu \cos \phi \left(\frac{12}{t^2} + \frac{1}{r_s^2} \right) \\
 & - 2v \frac{\partial w}{\partial s} \left(\frac{\cos^2 \phi}{r} \left(\frac{2}{r_s} - \frac{\sin \phi}{r} \right) + n^2 \frac{(1-\nu)}{2} \left(\frac{3}{rr_s} - \frac{\sin \phi}{r^2} \right) \right) \\
 & - 2v \frac{\partial^2 w}{\partial s^2} \nu \frac{\cos \phi}{r_s} \\
 & + w^2 \left(\frac{12}{t^2} \left(\frac{r}{r_s^2} + \sin \phi \left(\frac{1}{r} + \frac{2\nu}{r_s} \right) \right) + \left(\frac{1}{r_s} - \frac{\sin \phi}{r} \right) \left(\frac{r}{r_s^3} - \frac{\sin^3 \phi}{r^2} + 2n^2 \frac{\sin \phi}{r^2} \right) \right. \\
 & \qquad \qquad \qquad \left. + \frac{n^2}{r^3} \left(n^2 + 2(1-\nu) \cos^2 \phi \right) \right) \\
 & - w \frac{\partial u}{\partial s} \frac{n}{r} (1-\nu) \left(\frac{3 \sin \phi}{r} - \frac{1}{r_s} \right) \\
 & + 2w \frac{\partial v}{\partial s} \left(\frac{12}{t^2} \left(\nu \sin \phi + \frac{r}{r_s} \right) + \frac{\nu n^2}{rr_s} \right) \\
 & - 2w \frac{\partial w}{\partial s} \frac{\cos \phi}{r} \left(\sin \phi \left(\frac{1}{r_s} - \frac{\sin \phi}{r} \right) + \frac{n^2}{r} (3-2\nu) \right) \\
 & - 2w \frac{\partial^2 w}{\partial s^2} \left(\frac{1}{r_s} \left(\sin \phi - \frac{r}{r_s} \right) + \frac{n^2 \nu}{r} \right) \\
 & + \left(\frac{\partial u}{\partial s} \right)^2 \frac{(1-\nu)}{2} \left(\frac{12r}{t^2} + \frac{r}{r_s^2} - \frac{3 \sin \phi}{r_s} + \frac{3 \sin^2 \phi}{r} \right) \\
 & + \frac{\partial u}{\partial s} \cdot \frac{\partial w}{\partial s} \frac{n}{r} (1-\nu) \left(\frac{3 \sin \phi}{r} - \frac{1}{r_s} \right)
 \end{aligned}$$

$$\begin{aligned}
 & + \left(\frac{\partial v}{\partial s} \right)^2 \left(\frac{12r}{t^2} + \frac{\sin \phi}{r_s} \right) \\
 & - 2 \frac{\partial v}{\partial s} \frac{\partial w}{\partial s} \frac{\partial \cos \phi}{r_s} \\
 & - 2 \frac{\partial v}{\partial s} \frac{\partial^2 w}{\partial s^2} \sin \phi \\
 & + \left(\frac{\partial w}{\partial s} \right)^2 \left(\frac{\cos^2 \phi}{r} + \frac{2n^2}{r} (1-\lambda) \right) \\
 & + 2 \frac{\partial w}{\partial s} \frac{\partial^2 w}{\partial s^2} \lambda \cos \phi \\
 & + \left(\frac{\partial^2 w}{\partial s^2} \right)^2 r \quad \left. \right) ds
 \end{aligned}$$

For axisymmetric case $n = 0$ and $V = 2 \times V$

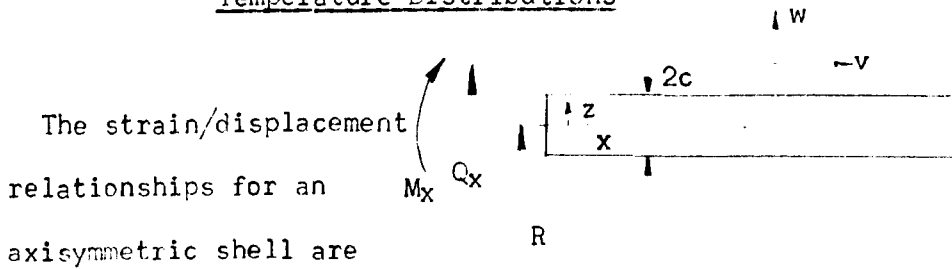
Appendix 3. Equivalent Nodal Force Terms for Axisymmetric Thin Shell
of Revolution subjected to Thermal Strains.

$$\text{Strain Energy } V = \frac{-2\pi E\alpha}{(1-\nu^2)} \{\delta\}^T [A^{-1}]^T \int_0^1 [B]^T \{DD'\} ds$$

where $\{DD'\}$ is given by

$$\left\{ \begin{array}{l} 0 \\ \cos\phi \left(T((1+\nu)t + \frac{t^3}{12} \left(\frac{1}{r_s^2} - \frac{2\sin\phi}{rr_s} + \frac{\sin^2\phi}{r^2} \right)) + \frac{\Delta T t^2}{12} \left(\frac{1}{r_s} \frac{(2+3\nu)}{2} - \frac{\sin\phi}{2r} \right) \right) \\ Tt \left((1+\nu) \left(\frac{r}{r_s} + \sin\phi \right) + \frac{t^2}{12} \left(\frac{r}{r_s^3} - \frac{\sin\phi}{r^2} + \frac{\sin^3\phi}{r^2} - \frac{\sin^2\phi}{rr_s} \right) \right) + \frac{\Delta T t^2}{12} \left(\frac{2\sin\phi}{r_s} \right. \\ \left. + \nu \frac{\sin\phi}{r_s} - \frac{r}{2r_s^2} - \frac{\sin^2\phi}{2r} \right) \\ 0 \\ Ttr(1+\nu) + \frac{\Delta T t^2}{12} \left(\frac{r}{r_s} \left(\frac{1+\nu}{2} \right) + \sin\phi \left(1 + \frac{\nu}{2} \right) \right) \\ -\frac{Tt^3}{12} \cos\phi \left(\left(\frac{1+\nu}{r_s} - \frac{\nu}{r_s} + \frac{\sin\phi}{r} \right) - \frac{\Delta T t^2}{12} \cos\phi (1+\nu) \right) \\ -\frac{Tt^3}{12} \left(\sin\phi - \frac{r}{r_s} \right) - \frac{\Delta T t^2 r}{12} (1+\nu) \end{array} \right\}$$

Appendix 4. Thermal Stresses in Cylinders subjected to Axisymmetric Temperature Distributions



The strain/displacement relationships for an axisymmetric shell are

given by

$$\epsilon_x = \frac{\partial v}{\partial x} - z \frac{\partial^2 w}{\partial x^2} - \alpha T \quad A4.1 (a)$$

$$\epsilon_\theta = \frac{w}{R} - \alpha T \quad A4.1 (b)$$

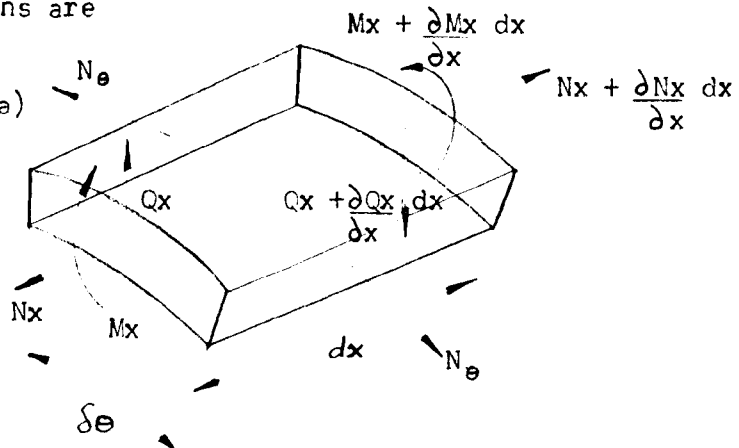
The Equilibrium Equations are

$$\frac{\partial Q_x}{\partial x} = -\frac{1}{R} N_\theta \quad A4.2 (a)$$

and $Q_x = \frac{\partial M_x}{\partial x} \quad A4.2 (b)$

which gives

$$\frac{1}{R} N_\theta + \frac{\partial^2 M_x}{\partial x^2} = 0 \quad A4.3$$



Defining the stress resultants N_x and N in terms of the stresses given by equations A4.1 give

$$N_x = \frac{E}{(1-\nu^2)} 2c \left(\frac{\partial v}{\partial x} + \nu \frac{w}{R} - (1+\nu) \alpha N_T \right) \quad A4.4 (a)$$

$$\text{where } N_T = \frac{1}{2c} \int_{-c}^c T dz \quad A4.4 (b)$$

Defining the cylinder as having no axial constraint, i.e. $N_x = 0$

$$\text{then } N_\theta = 2cE \left(\frac{w}{R} - \alpha N_T \right) \quad A4.4 (c)$$

The bending moment M_x is given by

$$M_x = \frac{E}{(1-\nu^2)} \frac{2c^3}{3} \left(\frac{\partial^2 w}{\partial x^2} + (1+\nu) \alpha M_T \right) \quad \text{A4.5 (a)}$$

$$\text{where } M_T = \frac{3}{2c^3} \int_{-c}^c T_z dz \quad \text{A4.5 (b)}$$

Substituting for N_θ and M_x in equation A4.3 gives the usual shell equation

$$\frac{\partial^4 w}{\partial x^4} + 4\beta^4 w = 4\beta^4 R \alpha N_T - (1+\nu) \alpha \frac{\partial^2 M_T}{\partial x^2} \quad \text{A4.6 (a)}$$

$$\text{where } 4\beta^4 = 3 \frac{(1-\nu^2)}{R^2 c^2} \quad \text{A4.6 (b)}$$

Substitution of the temperature profile equation

$$T(x, z) = \frac{1}{2} T^* \frac{(1-z)}{c} e^{-x/R} \quad \text{A4.7}$$

gives the displacement function as

$$w = e^{-\beta x} \left(C_1 \cos \beta x + C_2 \sin \beta x \right) + A e^{-x/R} \quad \text{A4.8 (a)}$$

$$\text{where } A = \frac{T^* R \alpha}{2} \left(\frac{1 + \frac{c}{3R(1-\nu)}}{1 + \frac{1}{4\beta^4 R^4}} \right) \quad \text{A4.8 (b)}$$

For case (1) No end constraints where $Q_x = 0$ and $M_x = 0$ at $x = 0$

$$C_1 = \left(\frac{T^* \alpha (1+\nu)}{4c\beta^2} - \frac{A}{2\beta^2 R^2} \right) \left(1 - \frac{1}{\beta R} \right) \quad \text{A4.9 (a)}$$

$$\text{and } C_2 = \frac{A}{2\beta^2 R^2} - \frac{\alpha(1+\nu) T^*}{4\beta^2 c} \quad \text{A4.9 (b)}$$

For case (2) with zero slope at $x = 0$ i.e. $Qx = 0$ and $\frac{\partial w}{\partial x} = 0$ at $x = 0$

$$C_1 = \frac{A}{2\beta R} \left(\frac{1}{2\beta^2 R^2} - 1 \right) - \frac{T^* \alpha (1 + \nu)}{8 \beta^3 c R} \quad \text{A4.10 (a)}$$

$$\text{and } C_2 = \frac{A}{2\beta R} \left(1 + \frac{1}{2\beta^3 R^2} \right) - \frac{T^* \alpha (1 + \nu)}{8 \beta^3 c R} \quad \text{A4.10 (b)}$$

Appendix 5. Equivalent Nodal Forces Terms for Axisymmetric Thin Shell
subjected to Creep Deformation.

$$\text{Strain Energy } V = - \frac{2\pi E\alpha}{(1-\nu^2)} \{\delta\}^T [A^{-1}]^T \int_0^1 [B]^T \{D_{\text{CREEP}}\} ds$$

where $\{D_{\text{CREEP}}\}$ is given by

$$\left\{ \begin{array}{l} - \frac{(1-\nu)}{2} \cos\phi \left(\frac{r+z \cdot \sin\phi}{r^2} \right)^2 \gamma_{\phi\theta c} \\ \\ \cos\phi \left(1 + \frac{z}{r_s} \right)^2 (\nu\epsilon_{\phi c} + \epsilon_{\theta c}) \\ \\ \frac{(r+z \cdot \sin\phi)}{r_s} (\epsilon_{\phi c} + \nu\epsilon_{\theta c}) + \sin\phi \left(1 + \frac{z}{r_s} \right) (\nu\epsilon_{\phi c} + \epsilon_{\theta c}) \\ \\ \left(\frac{r+z \cdot \sin\phi}{r} \right)^2 \frac{(1-\nu)}{2} \gamma_{\phi\theta c} \\ \\ (r+z \cdot \sin\phi) \left(1 + \frac{z}{r_s} \right) (\epsilon_{\phi c} + \nu\epsilon_{\theta c}) \\ \\ -z \cos\phi \left(1 + \frac{z}{r_s} \right) (\nu\epsilon_{\phi c} + \epsilon_{\theta c}) \\ \\ -z (r+z \cdot \sin\phi) (\epsilon_{\phi c} + \nu\epsilon_{\theta c}) \end{array} \right.$$

Appendix 6 Transition Parametric Finite Element Constraints

Constraints are made to the displacements on the mid-surface nodes of one face of a quadratic isoparametric finite element to force the normals to remain straight after deformation, see Fig. 3.5. Deformation is allowed by constraining the mid-surface node to lie on a line connecting the corner nodes without inhibiting the strain energy terms due to through thickness straining.

The constraints imposed are given by equations 3.38. The processes involved in modifying the stiffness and loading matrices can be described by considering merely one displacement.

$$\delta_{13} = \frac{1}{2}(\delta_1 + \delta_5) \tag{A6.1}$$

Substituting for these displacements in the strain energy equations gives

$$S.E. = \frac{1}{2} \left\{ \delta_1, \dots, \delta_5, \dots, \delta_{13}, \dots \right\}^T [K] \begin{Bmatrix} \delta_1 \\ \vdots \\ \delta_5 \\ \delta_{13} \end{Bmatrix} - \left\{ \delta_1, \dots, \delta_5, \dots, \delta_{13}, \dots \right\}^T \{F_e\} \tag{A6.2}$$

Substituting for δ_{13} in terms of δ_1 and δ_5 gives the modified stiffness terms as

$K_{11} + \frac{1}{2}K_{13,1} + \frac{1}{4}K_{13,13}$	$, K_{12} + \frac{1}{2}K_{13,2}$	$, K_{14} + \frac{1}{2}K_{13,4}$	$, K_{15} + \frac{1}{2}K_{1,13} + \frac{1}{2}K_{15,5}$	$, K_{16} + \frac{1}{2}K_{13,6}$
$K_{21} + \frac{1}{2}K_{2,13}$	$, K_{22}$	$, K_{24}$	$, K_{25} + \frac{1}{2}K_{2,13}$	$, K_{26}$
	$, K_{33}$			
$K_{41} + \frac{1}{2}K_{4,13}$	$, K_{42}$	$, K_{44}$	$, K_{45} + \frac{1}{2}K_{4,13}$	$, K_{46}$
$K_{51} + \frac{1}{2}K_{13,1} + \frac{1}{2}K_{5,13}$	$, K_{52} + \frac{1}{2}K_{13,2}$	$, K_{54} + \frac{1}{2}K_{13,4}$	$, K_{55} + K_{13,5} + \frac{1}{4}K_{13,13}$	$, K_{56} + \frac{1}{2}K_{13,5}$
$K_{61} + \frac{1}{2}K_{6,13}$	$, K_{62}$	$, K_{64}$	$, K_{65} + \frac{1}{2}K_{6,13}$	$, K_{66}$

and

$$\{F_{e'}\} = \left\{ \begin{array}{l} F_{e1} + \frac{1}{2}F_{e13} \\ F_{e2} \\ F_{e4} \\ F_{e5} + \frac{1}{2}F_{e13} \end{array} \right\}$$

Appendix 7 Decomposition of [D] matrices into [U]^T[U] form

The stress/strain relationship for 3-dimensional analysis is given by

$$\{\sigma\} = [D] \{\epsilon\}$$

where

$$[D] = \frac{E}{(1+\nu)(1-2\nu)} \begin{bmatrix} 1-\nu & \nu & \nu & 0 & 0 & 0 \\ & 1-\nu & \nu & 0 & 0 & 0 \\ & & 1-\nu & 0 & 0 & 0 \\ & & & \frac{1-2\nu}{2} & 0 & 0 \\ & & & & \frac{1-2\nu}{2} & 0 \\ & & & & & \frac{1-2\nu}{2} \end{bmatrix}$$

symmetric

The [D] matrix can be decomposed in lower and upper triangular form

$$[D] = [L][U]$$

where $[L] = [U]^T$

The upper triangular matrix [U] is given by

$$[U] = \sqrt{\frac{E}{(1+\nu)(1-2\nu)}} \begin{bmatrix} \sqrt{(1-\nu)} & \sqrt{\frac{\nu}{1-\nu}} & \sqrt{\frac{\nu}{1-\nu}} & 0 & 0 & 0 \\ 0 & \sqrt{\frac{1-2\nu}{1-\nu}} & \sqrt{\frac{\nu(1-2\nu)}{1-\nu}} & 0 & 0 & 0 \\ 0 & 0 & \sqrt{1-2\nu}\sqrt{1-\nu} & 0 & 0 & 0 \\ 0 & 0 & 0 & \sqrt{\frac{1-2\nu}{2}} & 0 & 0 \\ 0 & 0 & 0 & 0 & \sqrt{\frac{1-2\nu}{2}} & 0 \\ 0 & 0 & 0 & 0 & 0 & \sqrt{\frac{1-2\nu}{2}} \end{bmatrix}$$

Similarly for the thick shell analysis the stress/strain relationship is given by

$$\{\sigma'\} = [D'] \{\epsilon'\}$$

where

$$[D] = \left(\frac{E}{1-\nu^2} \right) \begin{bmatrix} 1 & \nu & 0 & 0 & 0 \\ & 1 & 0 & 0 & 0 \\ & & \frac{1-\nu}{2} & 0 & 0 \\ & & & \frac{1-\nu}{2K} & 0 \\ \text{symmetric} & & & & \frac{1-\nu}{2K} \end{bmatrix}$$

This is decomposed to

$$[D'] = [U']^T [U']$$

where $[U']$ is given by

$$[U'] = \sqrt{\frac{E}{1-\nu^2}} \begin{bmatrix} 1 & \nu & 0 & 0 & 0 \\ 0 & \sqrt{1-\nu^2} & 0 & 0 & 0 \\ 0 & 0 & \sqrt{\frac{1-\nu}{2}} & 0 & 0 \\ 0 & 0 & 0 & \sqrt{\frac{1-\nu}{2K}} & 0 \\ 0 & 0 & 0 & 0 & \sqrt{\frac{1-\nu}{2K}} \end{bmatrix}$$

Appendix 8 Von Mises and Prandtl-Reuss Flow Rules

Creep deformation and plastic flow are very similar processes and the flow rules used to describe plastic flow are identical to those used to determine the creep deformations. For any given material there is a function of the three principal stresses which always has the same value regardless of the stress state. This function is used to equate the stress states in uniaxial, biaxial and multiaxial stress fields. This enables the creep strains in a multiaxial stress field to be determined from the empirical creep laws.

Stress Invariants

The principal stresses for a 3-dimensional stress field are given by Timoshenko and Goodier (ref. 69) as the solution to equations A8.1.

$$l(\sigma_x - \sigma) + m\tau_{xy} + n\tau_{xz} = 0 \quad \text{A8.1(a)}$$

$$l\tau_{xy} + m(\sigma_y - \sigma) + n\tau_{yz} = 0 \quad \text{A8.1(b)}$$

$$l\tau_{xz} + m\tau_{yz} + n(\sigma_z - \sigma) = 0 \quad \text{A8.1(c)}$$

where l, m and n are direction cosines of the stress field.

These equations are a set of 3 homogeneous linear equations which have a non-zero solution if

$$\begin{vmatrix} (\sigma_x - \sigma) & \tau_{xy} & \tau_{xz} \\ \tau_{xy} & (\sigma_y - \sigma) & \tau_{yz} \\ \tau_{xz} & \tau_{yz} & (\sigma_z - \sigma) \end{vmatrix} = 0 \quad \text{A8.2}$$

If A8.2 is expanded then the equation may be written as

$$\sigma^3 - I_1\sigma^2 - I_2\sigma - I_3 = 0 \quad \text{A8.3(a)}$$

where $I_1 = \sigma_x + \sigma_y + \sigma_z$ A8.3(b)

$$I_2 = -(\sigma_x\sigma_y + \sigma_y\sigma_z + \sigma_z\sigma_x) + \tau_{xy}^2 + \tau_{xz}^2 + \tau_{yz}^2 \quad A8.3(c)$$

$$I_3 = \sigma_x\sigma_y\sigma_z + 2\tau_{xy}\tau_{xz}\tau_{yz} - \sigma_x\tau_{yz}^2 - \sigma_y\tau_{xz}^2 - \sigma_z\tau_{xy}^2 \quad A8.3(d)$$

The stresses, $\sigma_x, \sigma_y, \sigma_z, \tau_{xy}, \tau_{xz}, \tau_{yz}$ depend on the choice of the initial x, y, z axes, but the roots of equation A8.3(a), the principal stresses, are independent of this choice. I_1, I_2 and I_3 must therefore remain unchanged and are termed "invariant".

Hence because I_1 is invariant by a change of axes

$$\sigma_x + \sigma_y + \sigma_z = \sigma_1 + \sigma_2 + \sigma_3 \quad A8.4$$

Creep Flow Rules

It is assumed that hydrostatic pressure does not cause any appreciable plastic deformation. Johnson (ref. 54) has shown that a change in hydrostatic pressure has no effect on creep rates. In developing a flow rule for creep deformation it is usual to subtract the hydrostatic stress from the direct stress to give the "stress deviation". It is assumed that the creep flow is dependent on the stress deviations.

The "mean normal stress" is defined as

$$s = \frac{(\sigma_x + \sigma_y + \sigma_z)}{3} = \frac{(\sigma_1 + \sigma_2 + \sigma_3)}{3} \quad A8.5$$

The most important condition for creep flow is that the creep process is invariant to the axes. As the mean normal stress does not affect the creep flow process the flow rule must depend on the invariants of the stress deviations.

The invariants of the stress I_1, I_2, I_3 have been found and the invariants of the stress deviation J_1, J_2, J_3 are found in a similar manner

$$J_1 = s_x + s_y + s_z \quad A8.6(a)$$

$$J_2 = -(s_x s_y + s_y s_z + s_z s_x) + s_{xy}^2 + s_{yz}^2 + s_{zx}^2 \quad A8.6(b)$$

where $s_x = \sigma_x - s$ etc. and $s_{xy} = \tau_{xy}$ A8.7

J_1 vanishes as $(s_x + s_y + s_z) = 0$ and using this in J_2 gives

$$J_2 = \frac{1}{2}(s_x^2 + s_y^2 + s_z^2) + s_{xy}^2 + s_{yz}^2 + s_{zx}^2 \quad \text{A8.8(a)}$$

$$= \frac{1}{6} \left((\sigma_x - \sigma_y)^2 + (\sigma_y - \sigma_z)^2 + (\sigma_z - \sigma_x)^2 \right) + \tau_{xy}^2 + \tau_{yz}^2 + \tau_{zx}^2 \quad \text{A8.8(b)}$$

which when referred to principal axes gives the second invariant

as

$$J_2 = \frac{1}{2}(s_1^2 + s_2^2 + s_3^2) \quad \text{A8.9(a)}$$

$$= \frac{1}{6} \left((\sigma_1 - \sigma_2)^2 + (\sigma_2 - \sigma_3)^2 + (\sigma_3 - \sigma_1)^2 \right) \quad \text{A8.9(b)}$$

The simplest relationship of $f(J_1, J_2, J_3) = 0$, is that J_2 should be constant as J_1 is always zero and J_3 leads to a very complex set of equations.

In the case of a uniaxial stress field this relationship gives J_2 as

$$J_2 = \sigma_x^2 / 3$$

This value of σ_x can be considered to be an equivalent stress σ_e to the multiaxial stress field

$$\sigma_e = \frac{1}{\sqrt{2}} \sqrt{(\sigma_x - \sigma_y)^2 + (\sigma_y - \sigma_z)^2 + (\sigma_z - \sigma_x)^2 + 6\tau_{xy}^2 + 6\tau_{yz}^2 + 6\tau_{zx}^2} \quad \text{A8.10}$$

i.e. $\sigma_e = \sigma_x$ for uniaxial stress fields.

For plastic flow this relationship between the multiaxial stress field and an equivalent uniaxial stress has been shown by Hencky (Hill ref, 61 and Jaeger ref.62) to imply that yielding occurs when the elastic strain energy of distortion reaches a critical value. Nadai (ref. 70) states that plastic flow occurs when the shear stress acting over an octahedral plane reaches a certain value which is proportional to the second invariant of stress deviation. The creep flow rules are based on an equivalent uniaxial

stress to a multiaxial stress field to determine the equivalent uniaxial creep strains.

The multiaxial creep strains are calculated from the equivalent uniaxial creep strains using the Levy-Von Mises and Prandtl-Reuss flow rules, Hill (ref. 61). The Levy-Von Mises flow rules are based on Saint-Venants principle that the principal axes of strain increment coincide with the axes of principal stress. This was extended by Prandtl-Reuss for elasto-plastic and creep equations. As the creep strain increments are proportional to the stress deviations the multiaxial creep strain increments can be found from the equivalent uniaxial creep strain increments.

For a uniaxial stress field the stress deviation is given by

$$s_e = \frac{2\sigma_e}{3} \quad \text{A8.11(a)}$$

In multiaxial analysis the stress deviations are given by

$$s_x = \frac{1}{3} (2\sigma_x - \sigma_y - \sigma_z) \quad \text{etc.} \quad \text{A8.11(b)}$$

$$s_{xy} = \tau_{xy} \quad \text{A8.11(c)}$$

This gives the multiaxial creep strain increments as

$$\Delta\epsilon_{xc} = \frac{\Delta\epsilon_{ec}}{2\sigma_e} (2\sigma_x - \sigma_y - \sigma_z) \quad \text{etc.} \quad \text{A8.12(a)}$$

$$\Delta\epsilon_{xyc} = \frac{\Delta\epsilon_{ec}}{\sigma_e} \frac{3}{2} \tau_{xy} \quad \text{etc.} \quad \text{A8.12(b)}$$

The constant volume condition for creep flow is included in equations A8.12(a), i.e. $\epsilon_x + \epsilon_y + \epsilon_z = 0$.

Appendix 9 Newton's Method for Solving Non-Linear Equations

A non-linear equation of the form

$$x = f(t)$$

can be solved by a method of successive approximations. The curve of the function is shown in Fig. A.9 and it is required to find the value of t when $x=x_0$.

An arbitrary time t is chosen and the equivalent value of x is evaluated

$$x = f(t)$$

This value is in error by $x-x_0$ and a second approximation can be made using the slope of the curve at x, t .

This slope is given as $f'(t)$.

The next approximation of t is given as

$$t' = t - \frac{(x - x_0)}{f'(t)}$$

Successive approximations are made until the differences between x and x_0 are small enough that no significant variation of t is made by the next approximations.

Care must be taken if $f'(t)$ ever approaches zero as the equations become ill-conditioned.

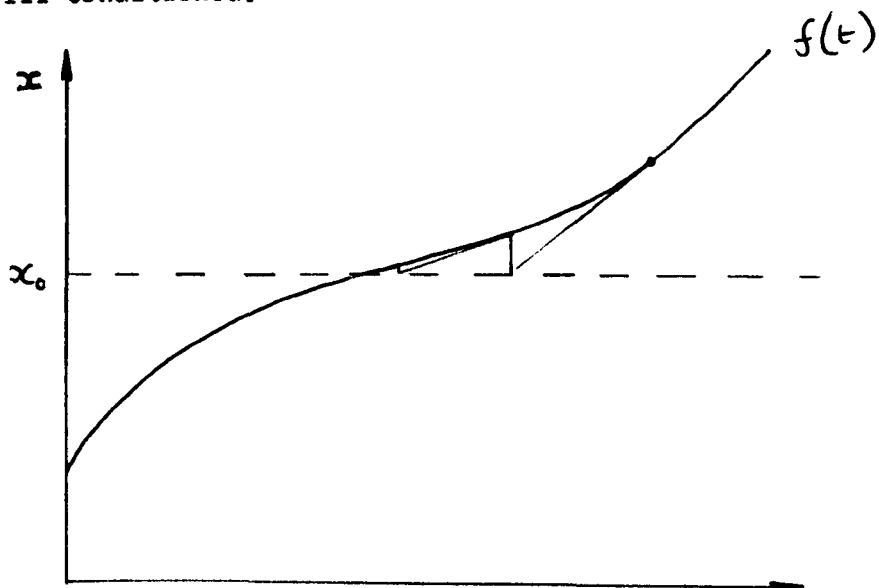


Fig A.9

Appendix 10 Creep Analysis applied to a Beam Finite Element

A beam finite element with 12 degrees of freedom, 3 translations and 3 rotations at each node, has been adapted for creep analysis. The displacement functions, translations normal to the principal axes and torsional rotations, are defined as polynomial functions of the beam length.

$$\begin{aligned} u_y &= a_1 + a_2x + a_3x^2 + a_4x^3 \\ u_z &= b_1 + b_2x + b_3x^2 + b_4x^3 \\ \theta_x &= c_1 + c_2x \\ u_x &= d_1 + d_2x \end{aligned} \tag{A10.1}$$

The z axis is the major axis, the y axis the minor axis and the x axis the polar axis of the beam.

The equivalent nodal force expression, given by equation 5.9 for the creep strain increments, can be further simplified by using the constant volume condition.

$$\epsilon_{x_c} + \epsilon_{y_c} + \epsilon_{z_c} = 0$$

$$\{\Delta \delta_i\}^T \{\Delta F_e\} = 2G \int_{Vol} \{\epsilon_T\}^T \{\Delta \epsilon_C\} dVol \tag{A10.2}$$

Considering the loading on a beam element, this usually comprises a bending moment about the major axis or a tensile or compressive force along the beam length or any combination of these. $\epsilon_y \Delta \epsilon_{y_c}$ and $\epsilon_z \Delta \epsilon_{z_c}$ are negligible compared with $\epsilon_x \Delta \epsilon_{x_c}$ and are neglected. This gives the equivalent nodal force expression

$$\{\Delta \delta_i\}^T \{\Delta F_e\} = 2G \int_{Vol} \epsilon_x \Delta \epsilon_{x_c} dVol \tag{A10.3}$$

The total strain in the x direction about the major axis considering tension and bending is given by

$$\epsilon_x = \frac{\partial u_x}{\partial x} - y \cdot \frac{\partial^2 u_y}{\partial x^2} \quad \text{A10.4(a)}$$

where $\frac{\partial^2 u_y}{\partial x^2} = \frac{1}{R}$ the radius of curvature by the Engineer's Theory of Bending.

$$\text{Hence } \epsilon_x = d_2 - 2a_3y - 6a_4xy \quad \text{A10.4(b)}$$

from equations A10.1 the displacement functions,

The vector of displacement function coefficients is given by defining the displacements at the nodes by the $[A]$ matrix

$$\begin{Bmatrix} a_1 \\ a_2 \\ \vdots \\ \vdots \\ d_2 \end{Bmatrix} = [A^{-1}] \{\Delta \delta_i\} \quad \text{A10.5}$$

The strains are then given by

$$\epsilon_x = \{\Delta \delta_i\}^T [A^{-1}] \{P(x,y)\} \quad \text{A10.6}$$

where $\{P(x,y)\}^T = \{0 \ 0 \ -2y \ -6xy \ 0 \ 0 \ 0 \ 0 \ 0 \ 0 \ 0 \ 1\}^T$

Differentiating with respect to the change in nodal displacements gives the equivalent nodal forces as

$$\{\Delta F_e\} = [A^{-1}]^T \int_{Vol} \{P(x,y)\} \Delta \epsilon_{xc} \, dVol \quad \text{A10.7(a)}$$

$$\{\Delta F_e\} = [A^{-1}]^T \int_0^1 \int_{-d/2}^{d/2} \{P(x,y)\} \{\Delta \epsilon_{xc}\} \, dydx \quad \text{A10.7(b)}$$

This is found by Gaussian quadrature numerical integration for each time interval.

Appendix 11 Computation of Turbine Casing Finite Element Idealisations

2-Dimensional Plane Strain Analysis of Turbine Casing Section

Idealisation :- Fig. 6.1(a)

72 x 8 node Isoparametric Finite Elements

No. of Nodes :- 261

No. of Degrees of Freedom :- 504

Maximum Instantaneous Size :- 40

Computer :- S.R.C. Atlas

Store :- 24,000 48 bit words

CPU Time :- 376 secs.

3-Dimensional Plane Strain Analysis of Turbine Casing Section

Idealisation :- Fig. 6.4(a)

15 x 20 node Isoparametric Finite Elements

No. of Nodes :- 175

No. of Degrees of Freedom :- 134

Maximum Instantaneous Size :- 23

Computer :- Nottingham University KDF-9

Store :- 23,000 48 bit words

CPU Time :- 1661 secs.

3-Dimensional Plane Strain Analysis of Turbine Casing with Bolts

Idealisation :- Fig. 6.6

57 x 20 node Isoparametric Finite Elements

No. of Nodes :- 457

No. of Degrees of Freedom :- 1097

Maximum Instantaneous Size :- 196

Computer :- S.R.C. IBM 360/195

Store :- 262,000 8 bit Bytes (i.e. 85,000 32 bit words)

CPU Time :- 86 secs.

Stress Analysis of Inner Turbine Casing

Idealisation :- Fig. 6.14

70 x 20 node Isoparametric Finite Elements

No. of Nodes :- 560

No. of Degrees of Freedom :- 1508

Maximum Instantaneous Size :- 173

Computer :- S.R.C. IBM 360/195

Store :- 252,000 8 bit Bytes (i.e. 63,000 32 bit words)

CPU Time :- 117 secs.

Also

Computer S.R.C. Atlas

Store :- 54,000 48 bit words

CPU Time 3615 secs.

Stress Analysis of Split Turbine Casing

a) 3-Dimensional Analysis

Idealisation :- Fig. 6.21

123 x 20 node Isoparametric Finite Elements

No. of Nodes :- 946

No. of Degrees of Freedom :- 2602

Maximum Instantaneous Size :- 181

Computer :- S.R.C. IBM 360/195

Store :- 374,000 8 bit Bytes (i.e. 93,000 32 bit words)

CPU Time :- 223 secs.

b) Axisymmetric Approximation

Idealisation :- Fig. 6.30

15 x 2 node Shell of Revolution Finite Elements

No. of Nodes :- 16

No. of Degrees of Freedom :- 107

Computer :- Nottingham University KDF-9

Store :- 9,000 48 bit words

CPU Time :- 337 secs.

Creep Analysis of Split Turbine Casing

a) 3-Dimensional Analysis

Idealisation :- Fig. 6.21

123 x 20 node Isoparametric Finite Elements

No. of Nodes :- 946

No. of Degrees of Freedom :- 2602

Maximum Instantaneous Size :- 181

Computer :- S.R.C. IBM 360/195

Store :- 374,000 8 bit Bytes (i.e. 93,000 32 bit words)

CPU Time :- 7030 secs.

No. of Time Increments :- 116

Gaussian Integration Mesh :- 2x2x2

b) Axisymmetric Approximation

Idealisation :- Fig. 6.30

15 x 2 node Isoparametric Finite Elements

No. of Nodes :- 16

No. of Degrees of Freedom :- 107

Computer :- Nottingham University KDF-9

Store :- 24,000 48 bit words

CPU Time :- 959 secs.

No. of Time Increments :- 32

Gaussian Integration Mesh :- 4 x 3

Table 2.1 Axisymmetric Thin Shells of Revolution Subjected to Thermal

Strains

Radius/Thickness ratio 10:1

$$\alpha = 1.1 \times 10^{-5} \text{ in/in}^\circ\text{C}$$

$$E = 3.0 \times 10^7 \text{ lbf/in}^2$$

$$\lambda = 0.3$$

T_0 = mid-surface temperature = 50°C

ΔT_0 = temperature difference across the shell thickness = -100°C

	Meridional Stress		Circumferential Stress	
	Inside	Outside	Inside	Outside
Cylinder				
Standard (Roark)	-23,600	23,600	-23,600	23,600
Finite Element	-24,050	23,090	-23,880	23,270
Sphere				
Standard (Roark)	-23,600	23,600	-23,600	23,600
Finite Element	-24,520	22,610	-24,090	22,790

TABLE 2.2 Comparison of Thin Shell Theory to Finite Element Analysis for a Long Cylinder Subjected to Creep

Radial displacement w mm

Radius a = 100 mm

Thickness h = 5 mm

Internal Pressure p = 0.75 kg/mm²

Poisson's ratio ν = 0.3

Young's Modulus E = 1.8 x 10⁴ kg/mm²

Creep Constant A = 4.36 x 10⁻⁹ (kg/mm²)^{-4.66} hr^{-0.218}

with Stress constant n = 4.66

and Time constant m = 0.218

Empirical Creep Law = $A \sigma^n t^m$

Thin Shell Creep Equation

$$\frac{Ehw}{2pa} = \left(1 - \frac{\nu}{2}\right) + \left(\frac{3}{4}\right)^{(n+1)/2} (EA) \left(\frac{pa}{h}\right)^{n-1} t^m$$

Time Hrs	Total Disp Theory	Total Disp F.E.	Creep Disp Theory	Creep Disp less 10 ⁻⁵ hrs Theory	Creep Disp F.E.	Error %
0	0.85	0.832	-	-	-	-
0.1	1.27	1.208	0.4205	0.4198	0.376	10.43
1.0	1.54	1.453	0.6945	0.6938	0.621	10.49
10.0	2.0	1.866	1.148	1.1473	1.034	9.88
100.0	2.75	2.548	1.897	1.8963	1.716	9.51

All displacements are given in the dimensionless form $\frac{Ehw}{pa^2}$

Value of Equivalent Stress for Thin Shell Theory = 12.99 kg/mm²

Average value of Equivalent Stress for Finite Element Analysis = 12.67 kg/mm²

Error in Equivalent Stress = 2.464%.

Table 3.1 Gaussian Quadrature Integration Constants

The integral $\int_{-1}^1 f(x) dx$ is given by the summation

$$\int_{-1}^1 f(x) dx = \sum_{i=1}^n H_i f(a_i)$$

where H_i and a_i are the weighting factor and variable respectively.

These values are given (ref. 21) below for n values up to $n=6$

n	a_i	H_i
2	± 0.577350269	1.000
3	± 0.7745966692	0.5555555556
	0.000	0.8888888889
4	± 0.8611363116	0.3478548451
	± 0.3399810436	0.6521451549
5	± 0.9061798459	0.2369268851
	± 0.5384693101	0.4786286705
	0.000	0.5688888889
6	± 0.9324695142	0.1713244924
	± 0.6612093865	0.3607615730
	± 0.2386191861	0.4679139346

Table 5.1 Effect of Neglecting Initial Periods of Material Creep Laws

Rectangular cross section beam subjected to constant bending moment.

Bending moment = 1.62×10^5 lbf/in

Cross section depth = 6 in

Cross section width = 2 in

Young's modulus = 1.41×10^6 lbf/in²

Poisson's ratio = 0.3

Creep Law

$$\epsilon_c = 2.68 \times 10^{-5} (e^{\sigma/7500} - 1)t^{0.372}$$

Change of equivalent stress during time increment < 0.1%

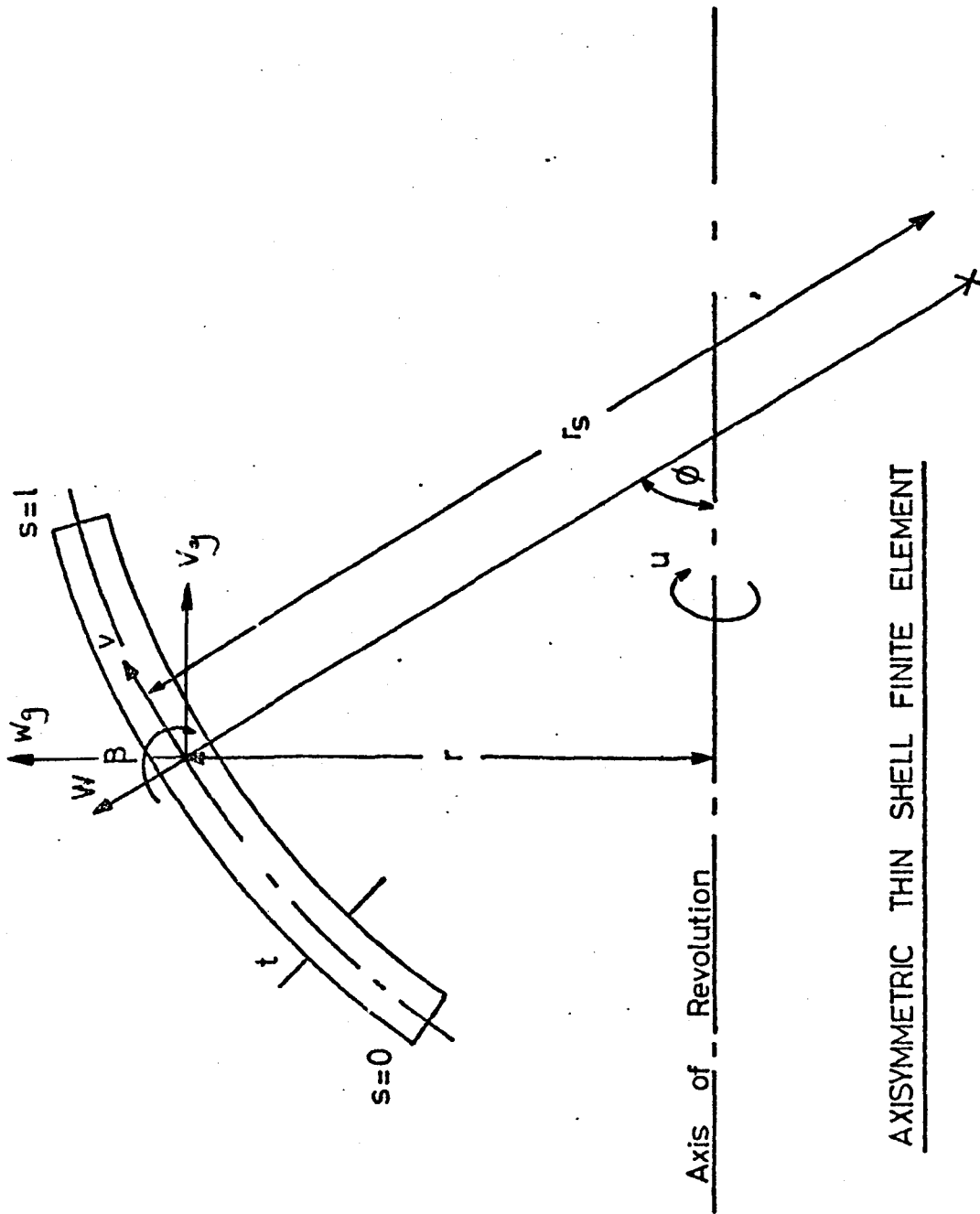
Distance from	Starting Times hrs.				
	0.0	0.001	0.01	0.1	1.0
N.A.	Stress lbf/in ²	Percentage error after 10 hrs. in stress compared with the zero starting time solution			
0.550	2.729×10^3	-0.146	-0.51	-1.355	-3.55
1.576	7.432×10^3	-0.054	-0.23	-0.61	-1.63
2.389	1.067×10^4	0	0	+0.094	+0.28
2.880	1.236×10^4	+0.081	+0.16	+0.64	+1.69
3.0	1.250×10^4	+0.1	+0.2	+0.85	+2.2
No. of Time Increments	176	175	168	152	113

Change in Time Increment

If previous increment within limit $t' = 3 \times t$

If previous increment outside limit $t' = t/3$ and

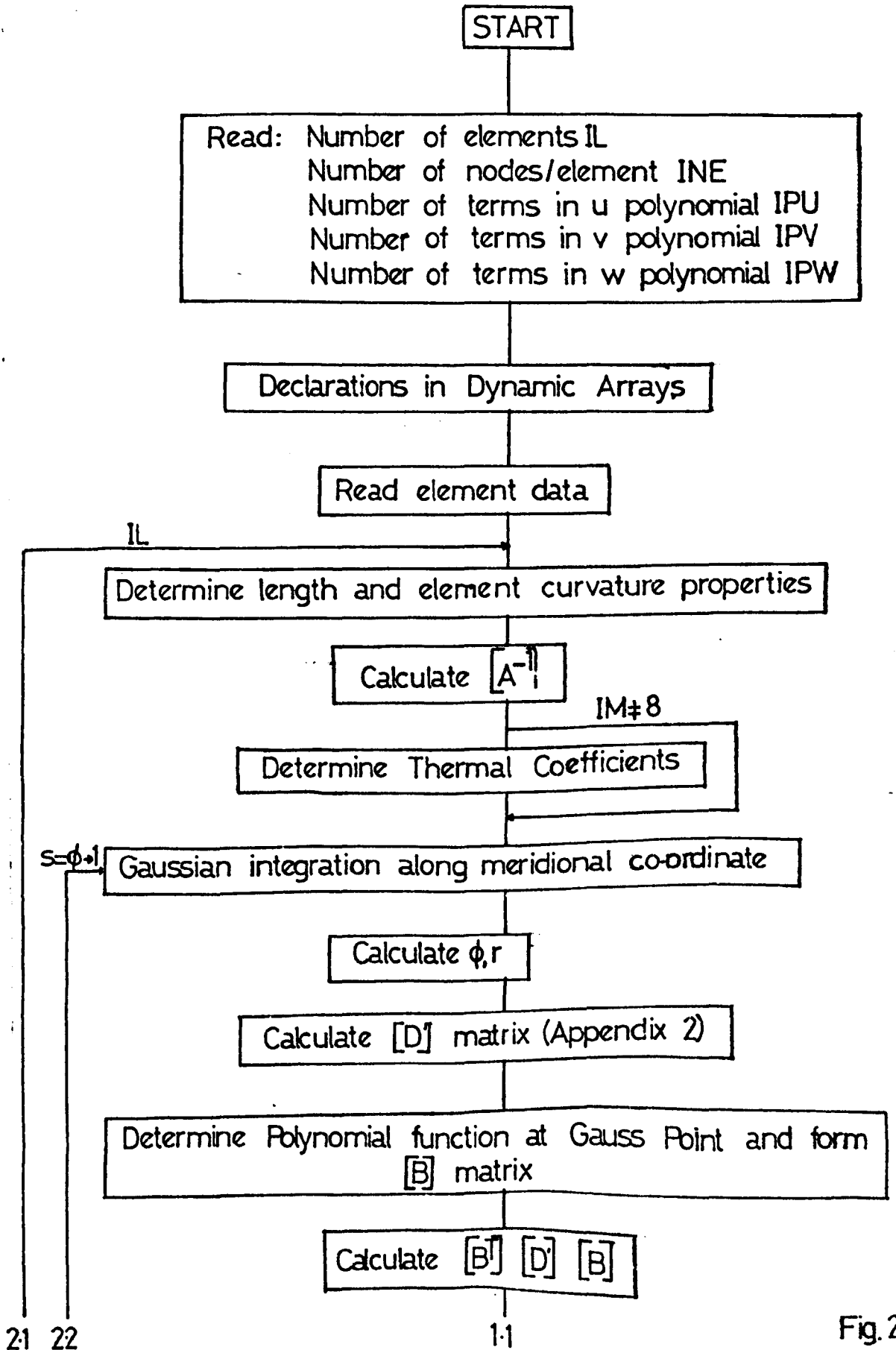
unsatisfactory step repeated.



AXISYMMETRIC THIN SHELL FINITE ELEMENT

Fig.2.1

FLOW DIAGRAM FOR THIN SHELL OF REVOLUTION RING FINITE ELEMENT ALGORITHM

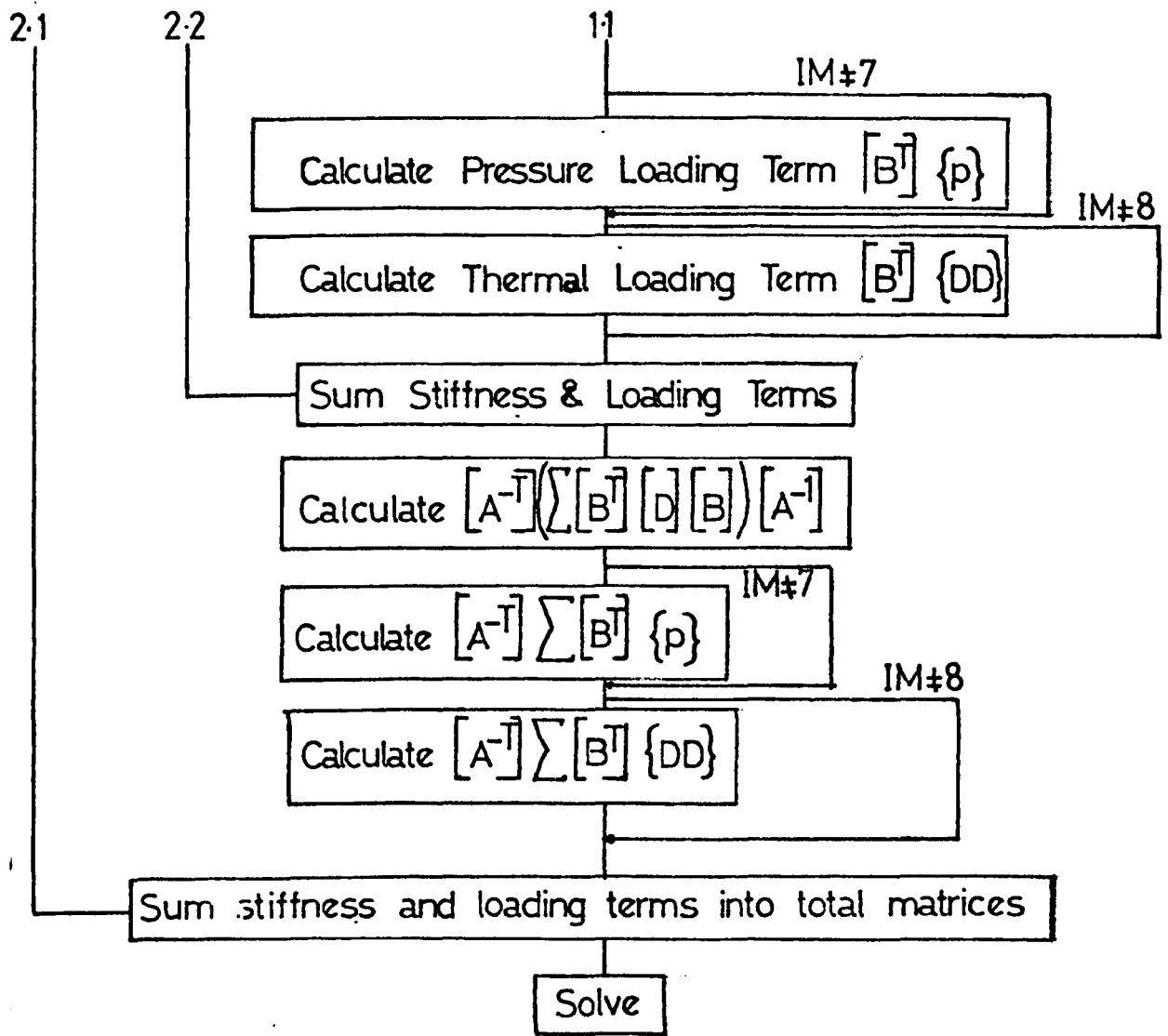


2:1 2:2

1:1

Fig. 2:2

FLOW DIAGRAM FOR THIN SHELL OF REVOLUTION RING
FINITE ELEMENT ALGORITHM (Continued).



Stiffness Matrices for Thin Shell Ring Finite Element.

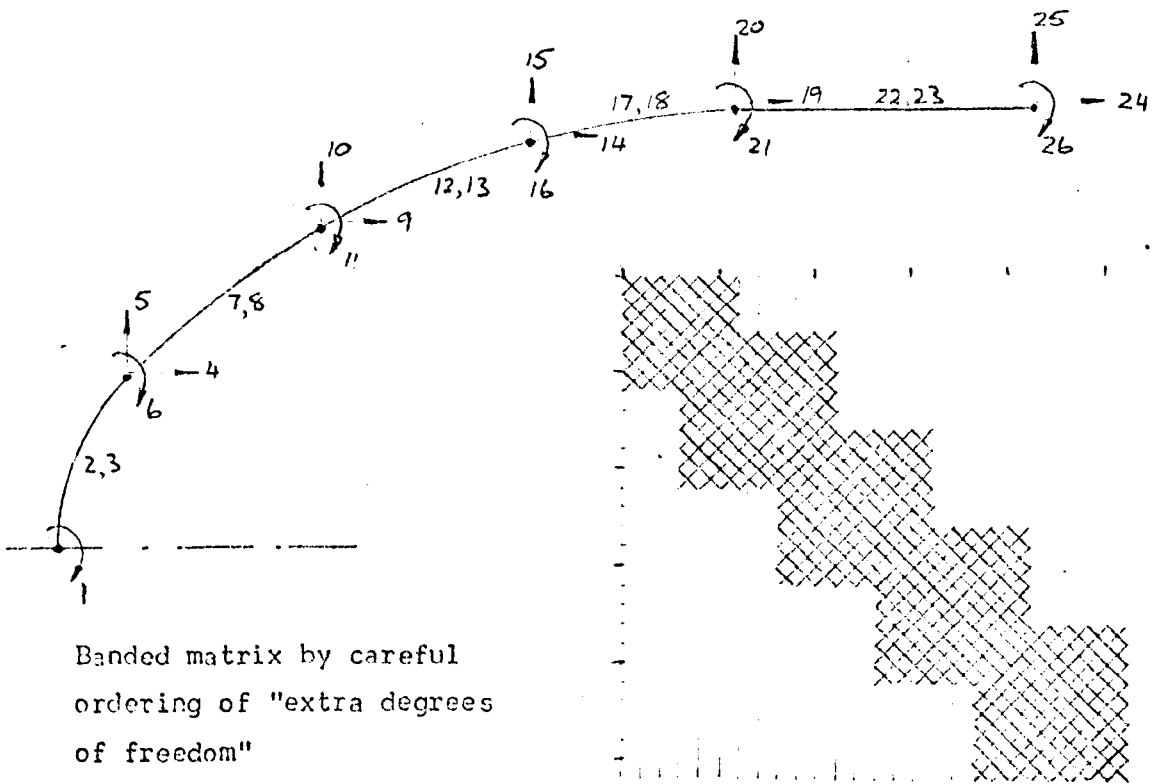
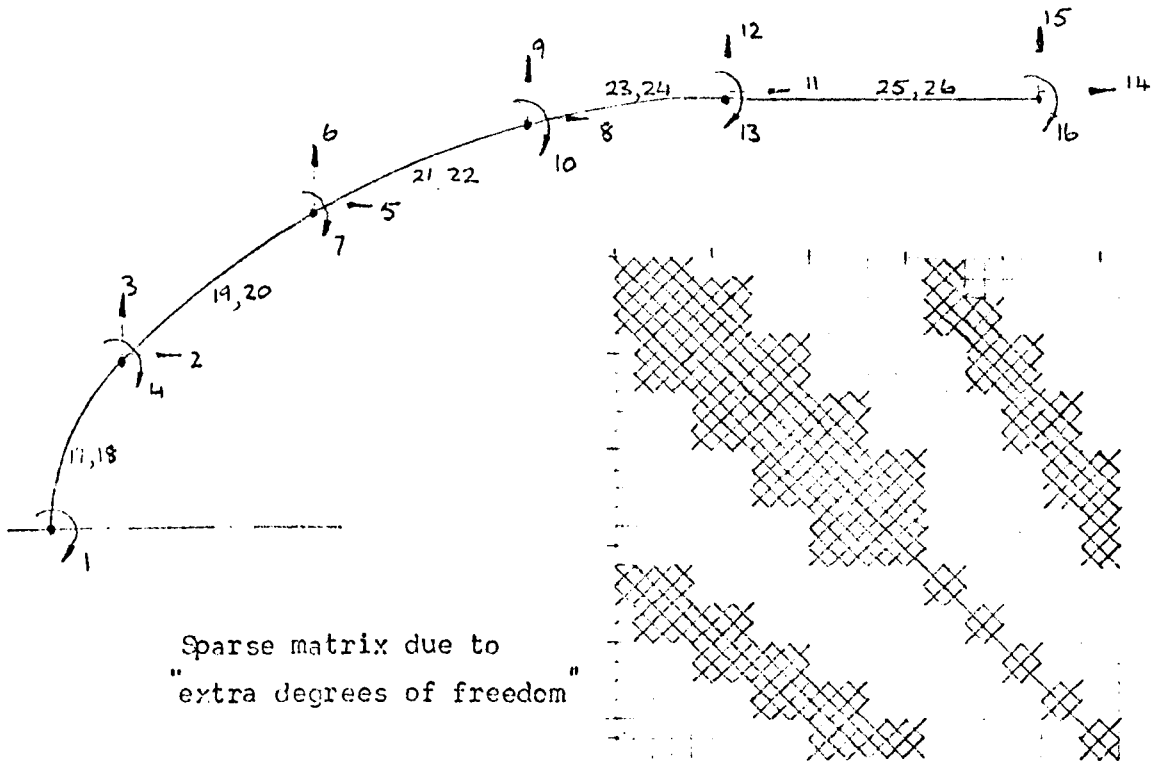
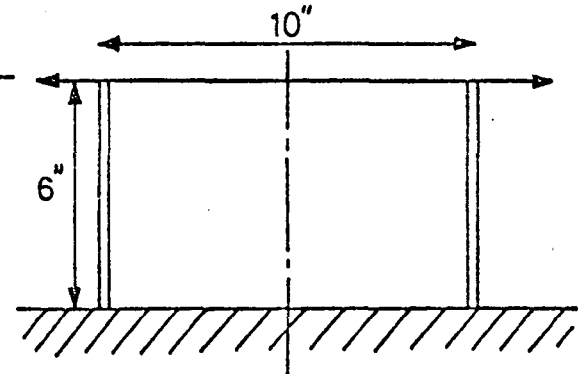
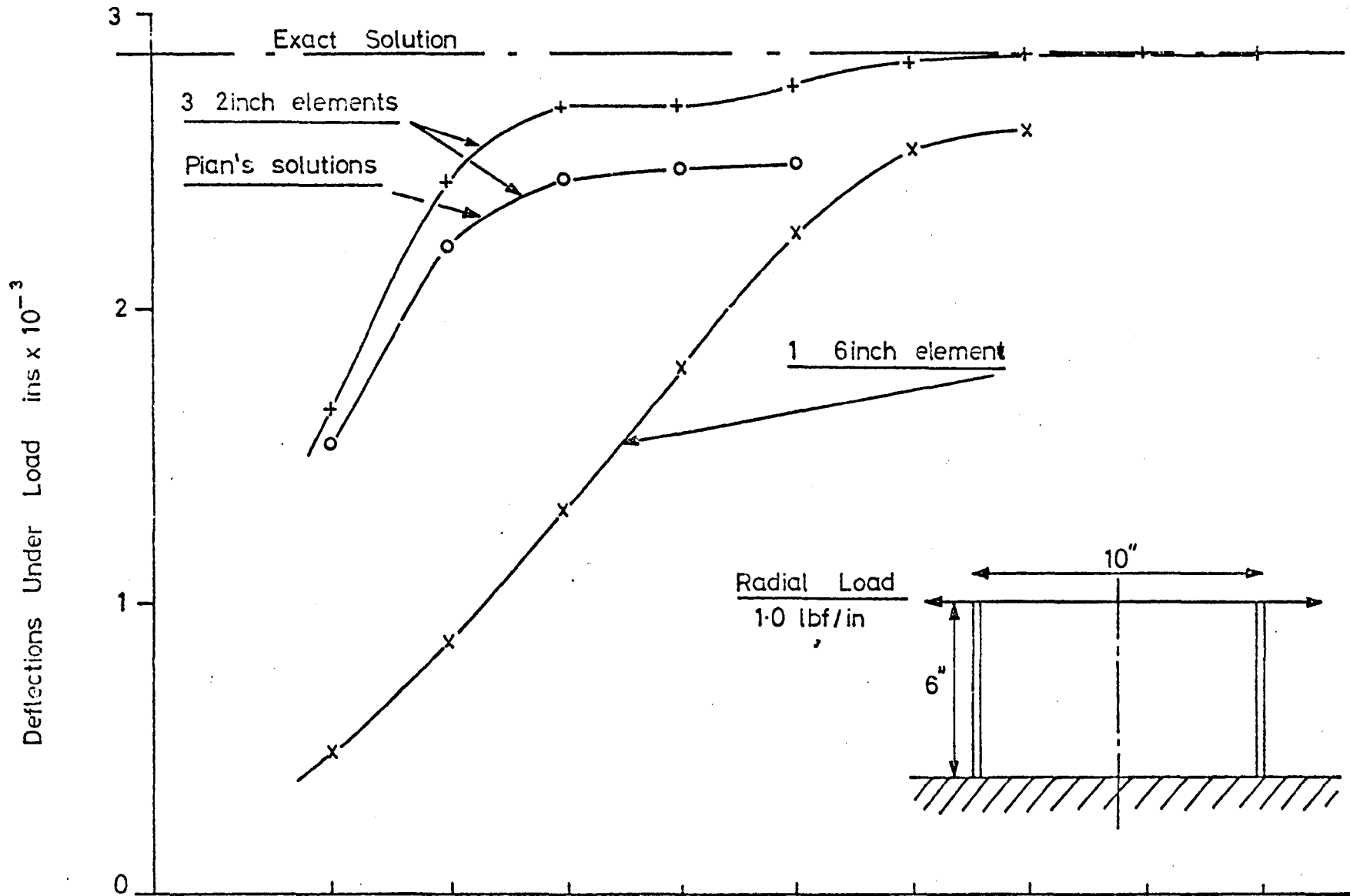


Fig. 2.3

PIAN'S CYLINDER TEST

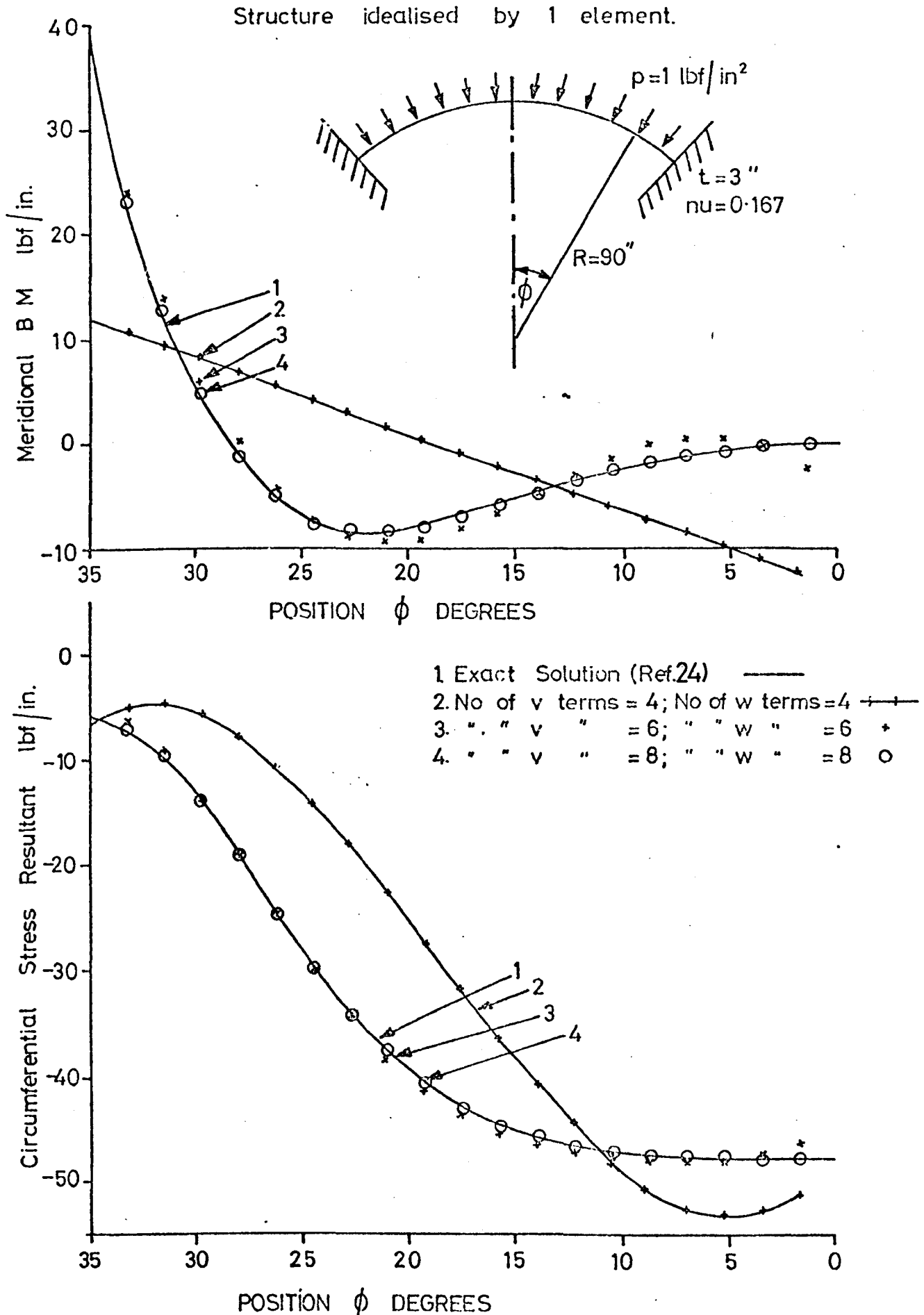


No of v terms (Pian)	4 (2)	5 (2)	6 (2)	7 (3)	8	9	10	11	12
" " w " "	4	5	6	7	8	9	10	11	12
Total No of degrees of freedom	3 elements (Pian) 15 (9)	21 (12)	27 (15)	33 (21)	39	45	51		
1 element	5	7	9	11	13	15	17		

Fig. 2.4

PRESSURISED SPHERICAL CAP

Fig.2.5(a)



PRESSURISED SPHERICAL CAP

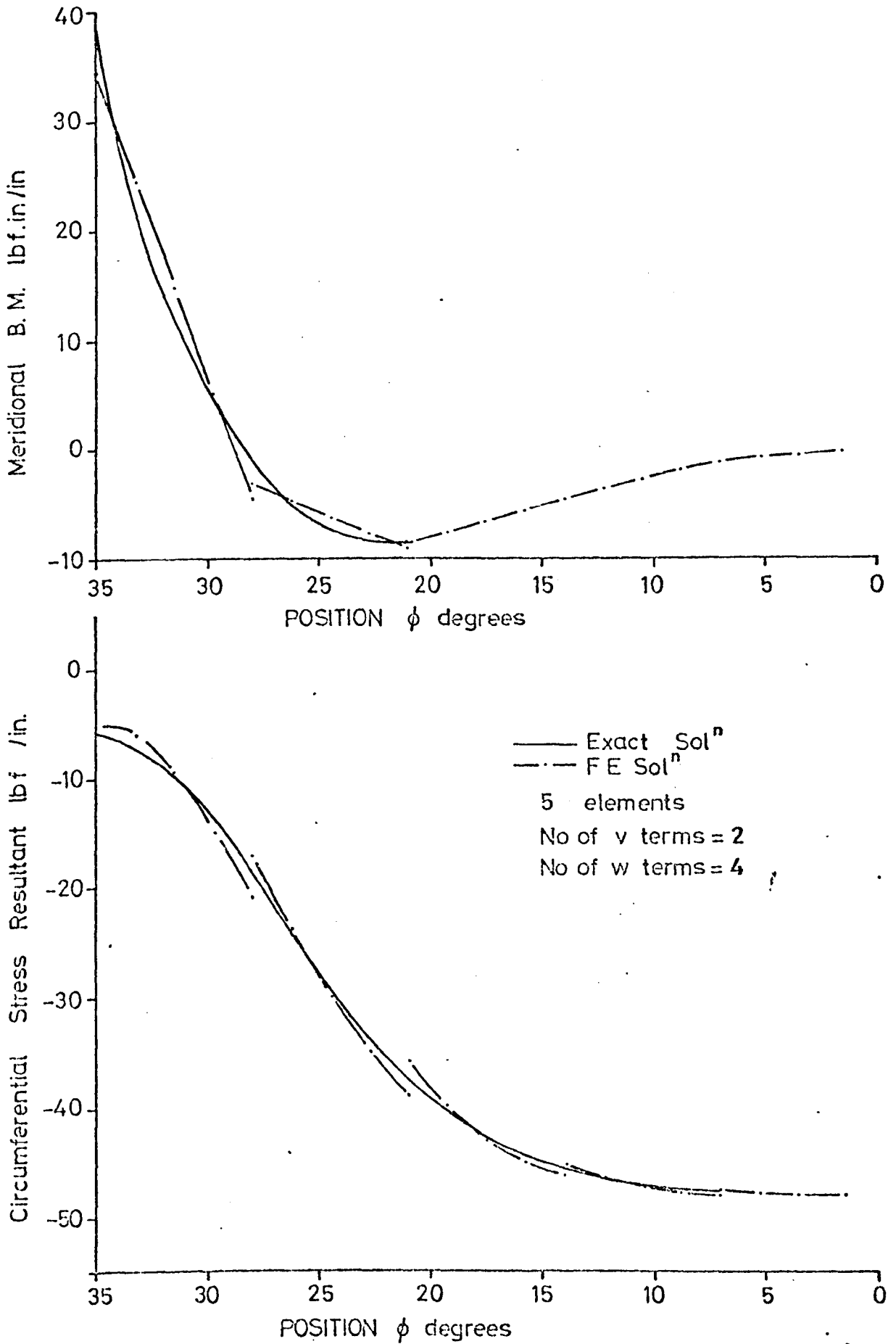
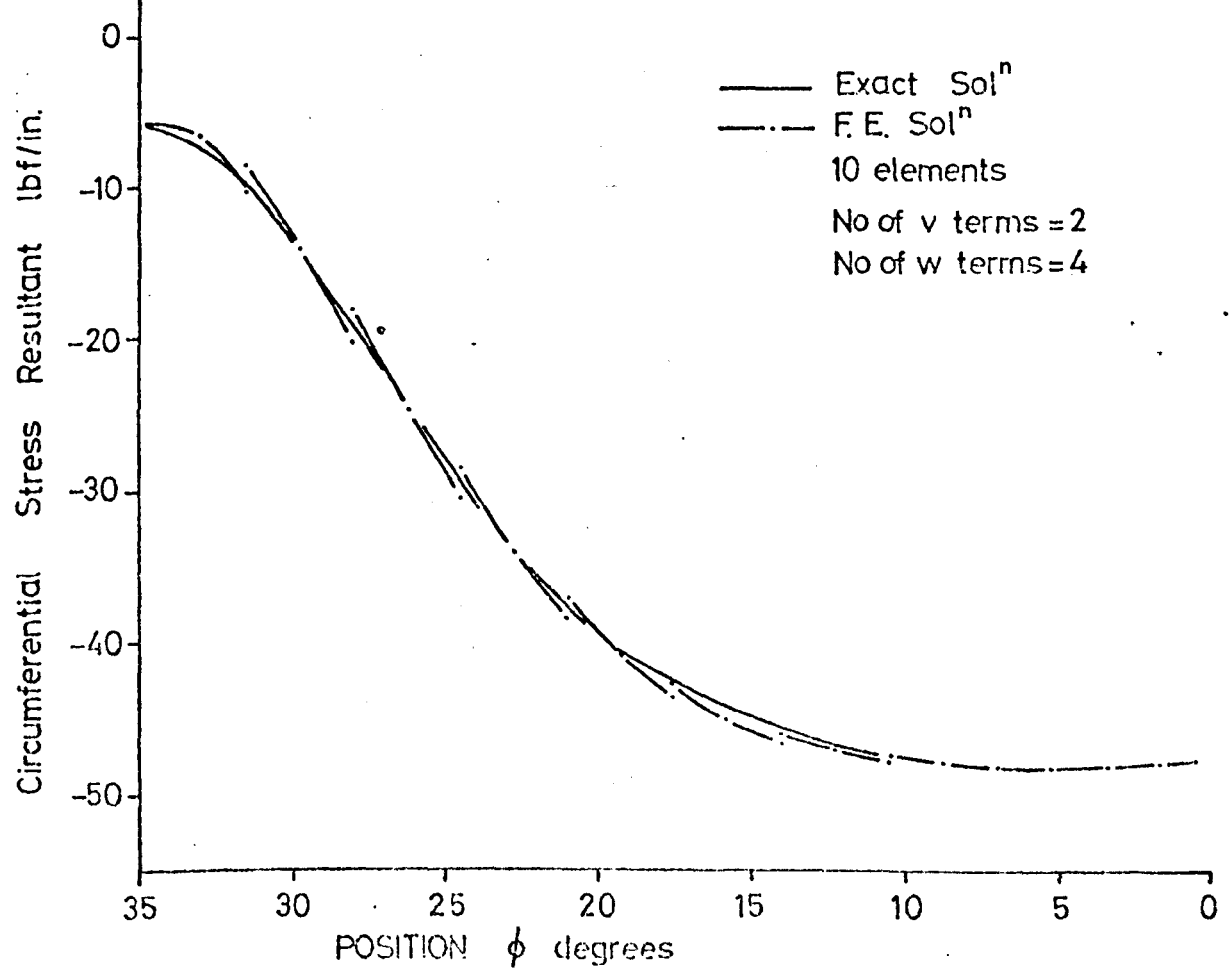
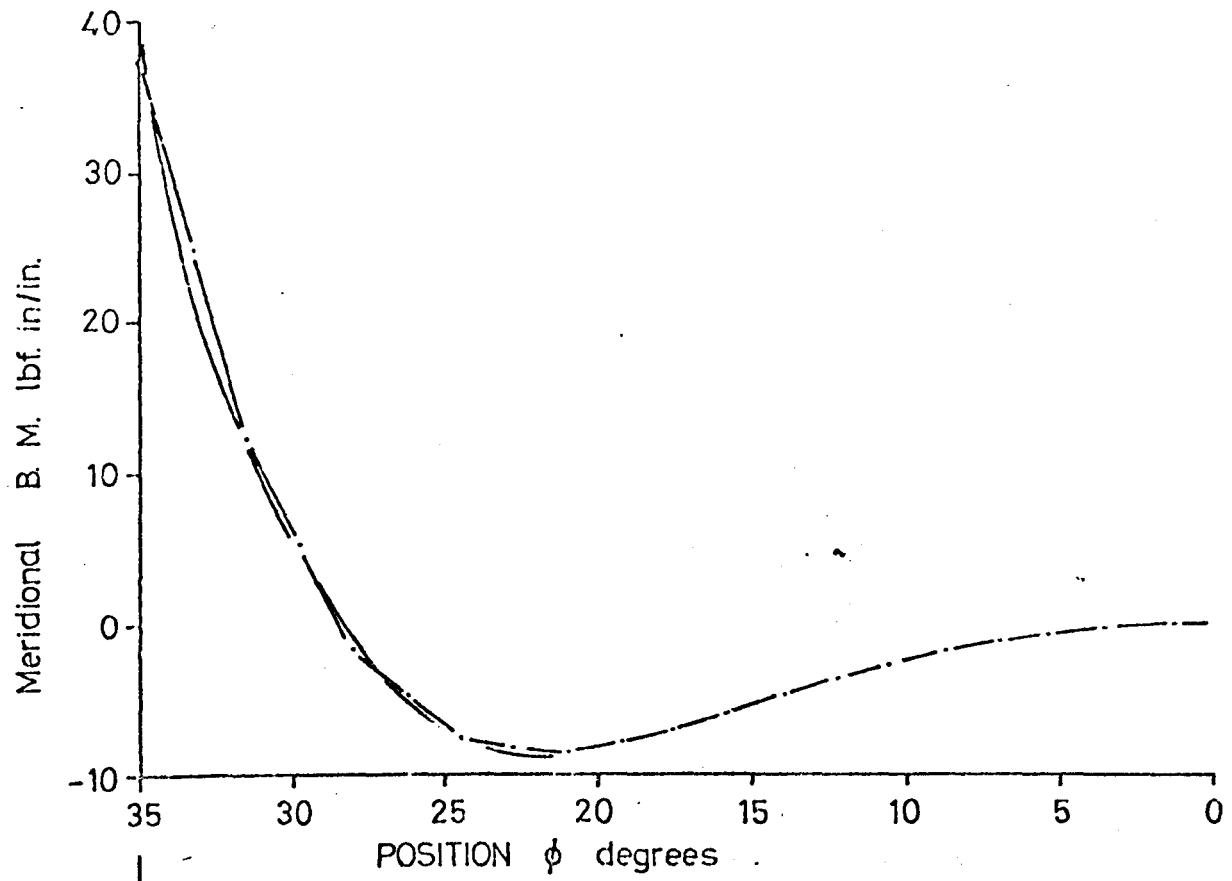
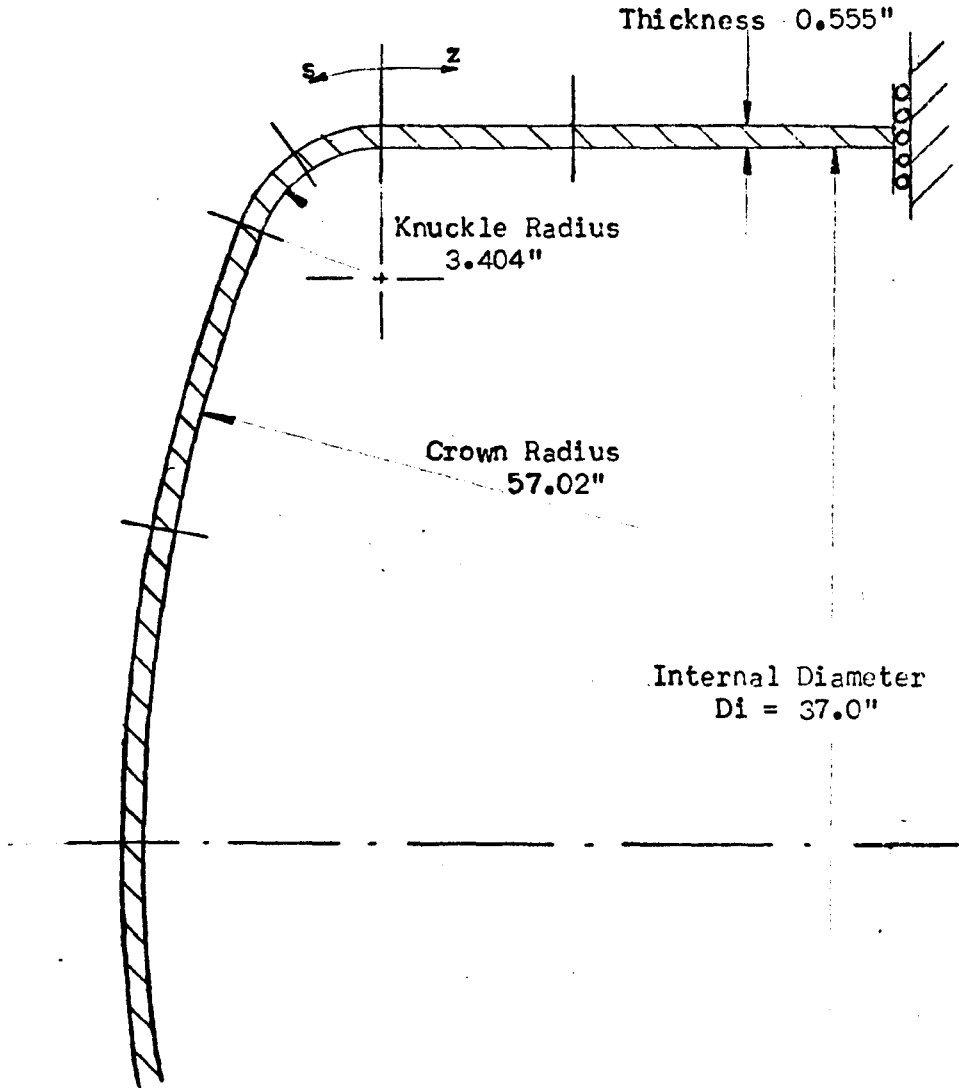


Fig. 25(c)

PRESSURISED SPHERICAL CAP



Torispherical Drumhead Idealisation



No. of elements 6

No. of v terms 6

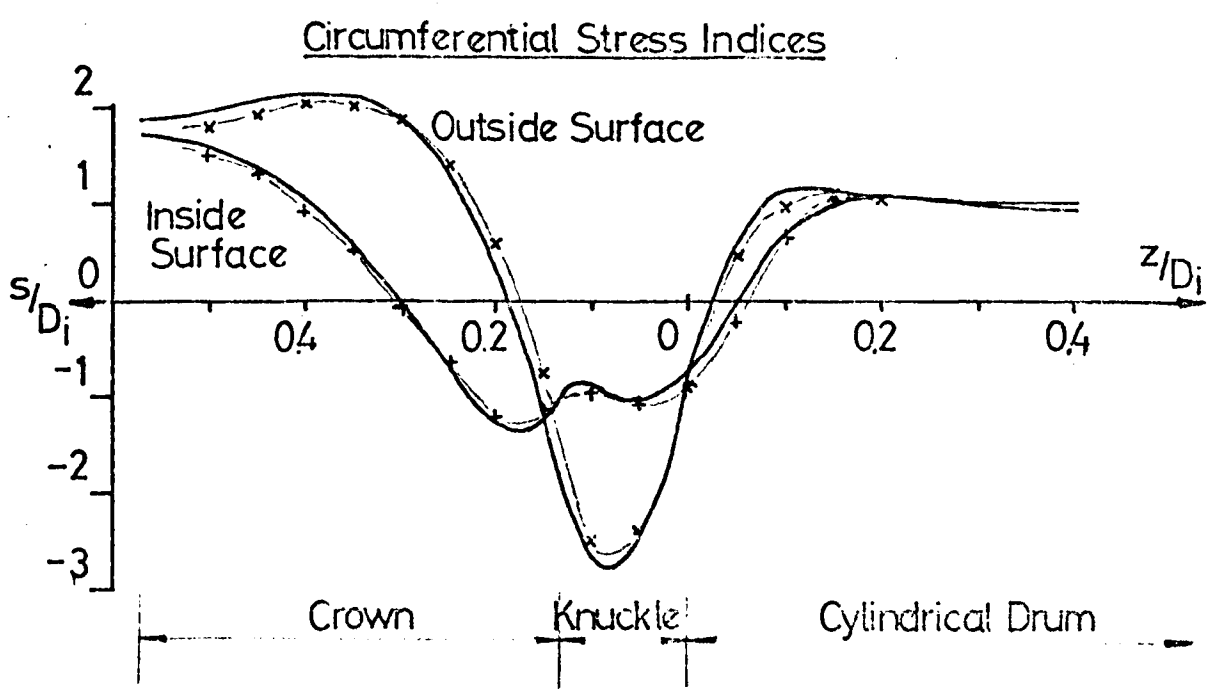
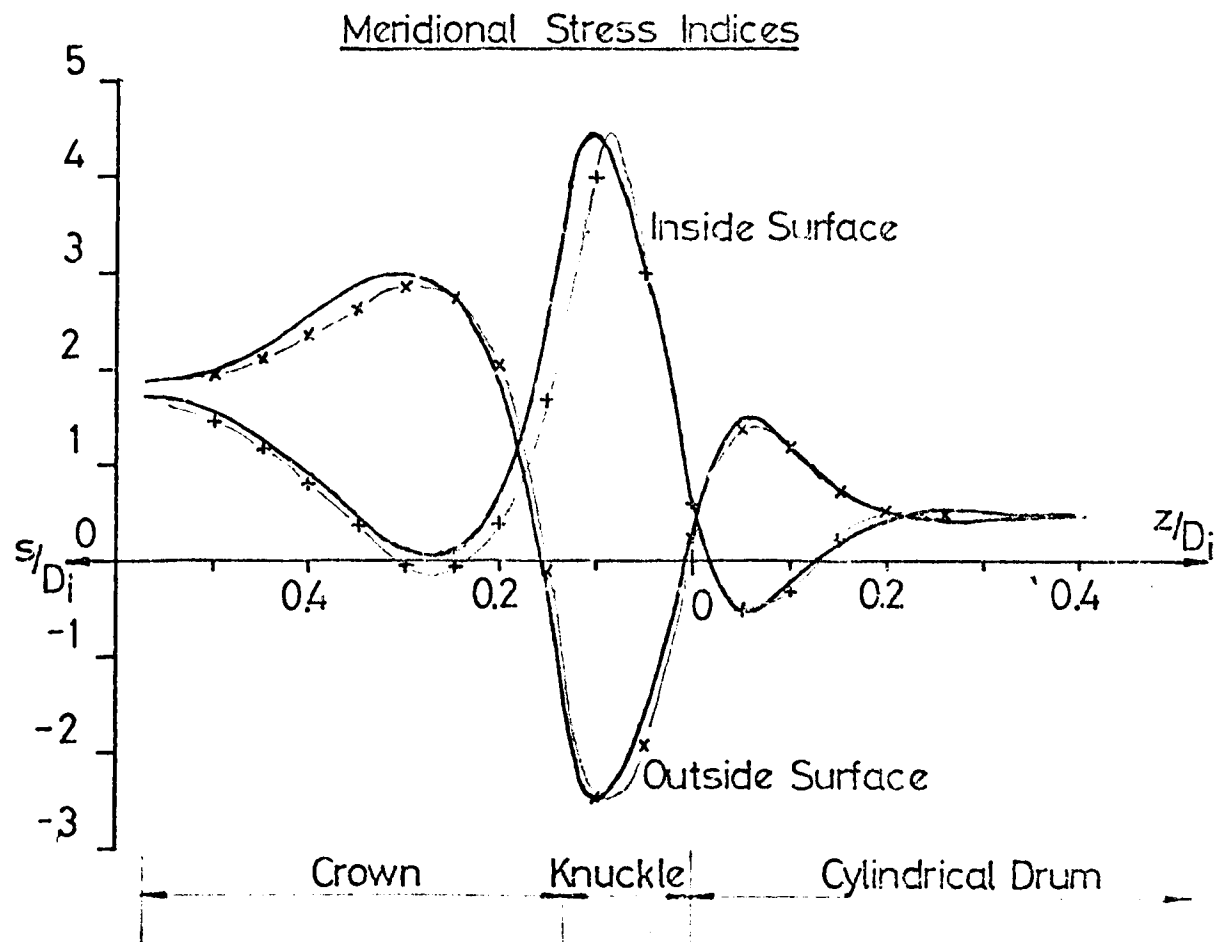
No. of w terms 6

Total No. of Degrees of Freedom 53

Stress index = $\frac{pD_i}{2t} = 33.333 \text{ lbf/in}^2$

Fig. 2.6(a)

ELASTIC STRESSES IN TORISPHERICAL DRUMHEADS



— Finite Element Analysis
-x-x- } Experimental Analysis (ref. 25)
-+-+ }

Fig 2.6(b)

DEGENERATED 3 DIAMETER PRESSURE VESSEL

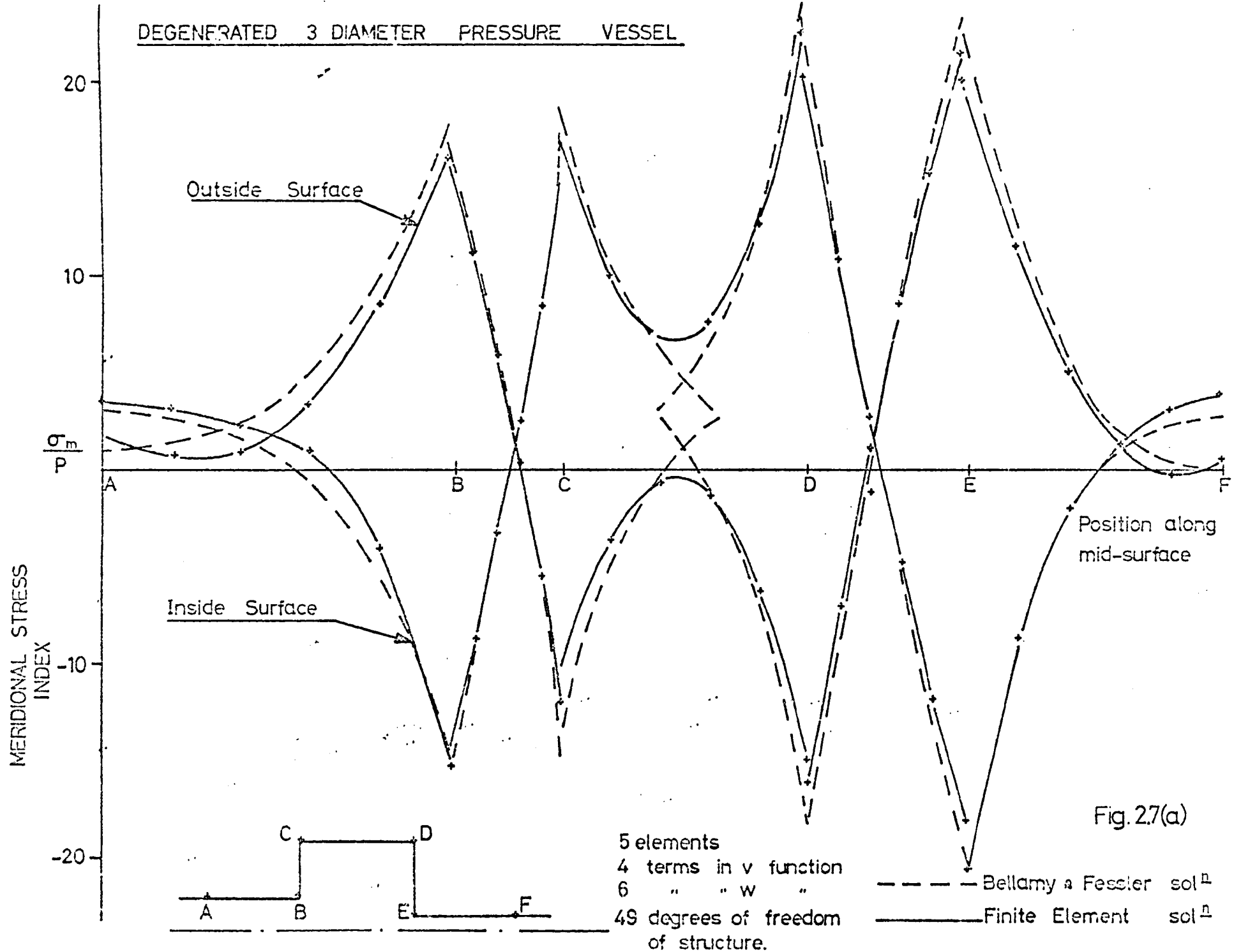
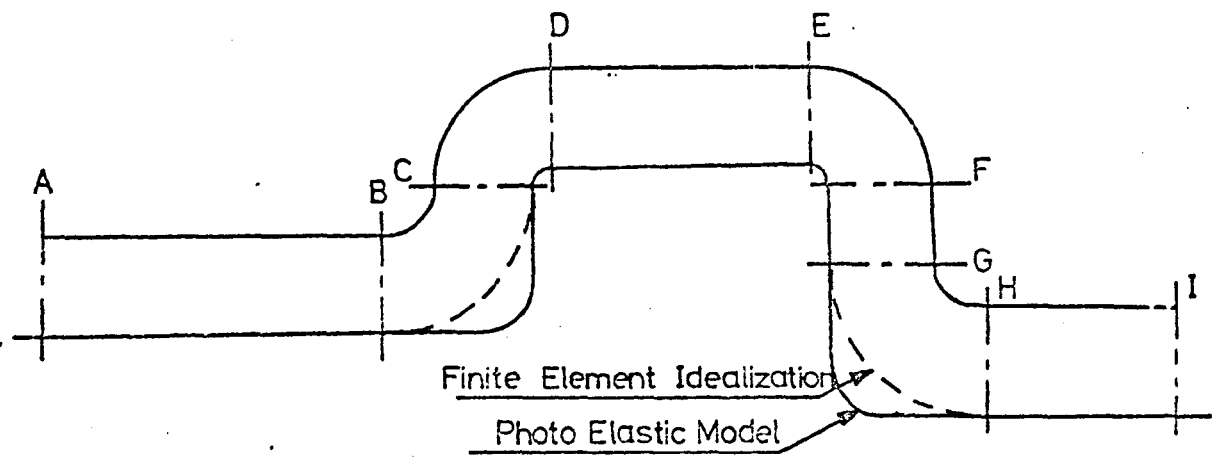


Fig. 27(a)



FINITE ELEMENT IDEALIZATION OF 3-DIA VESSEL.

Fig.27(b)

THREE DIAMETER CYLINDER RESULTS

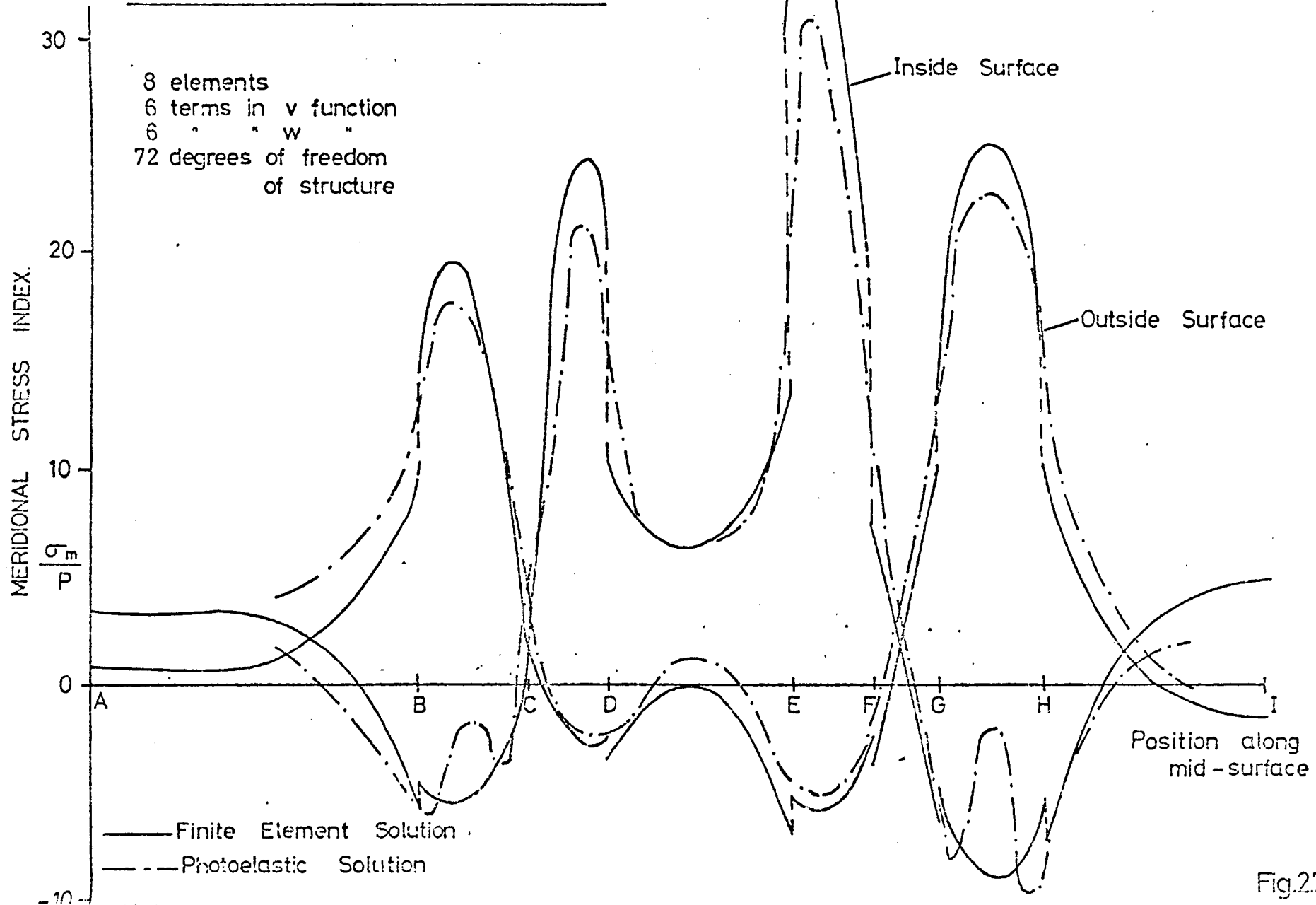


Fig.27(c)

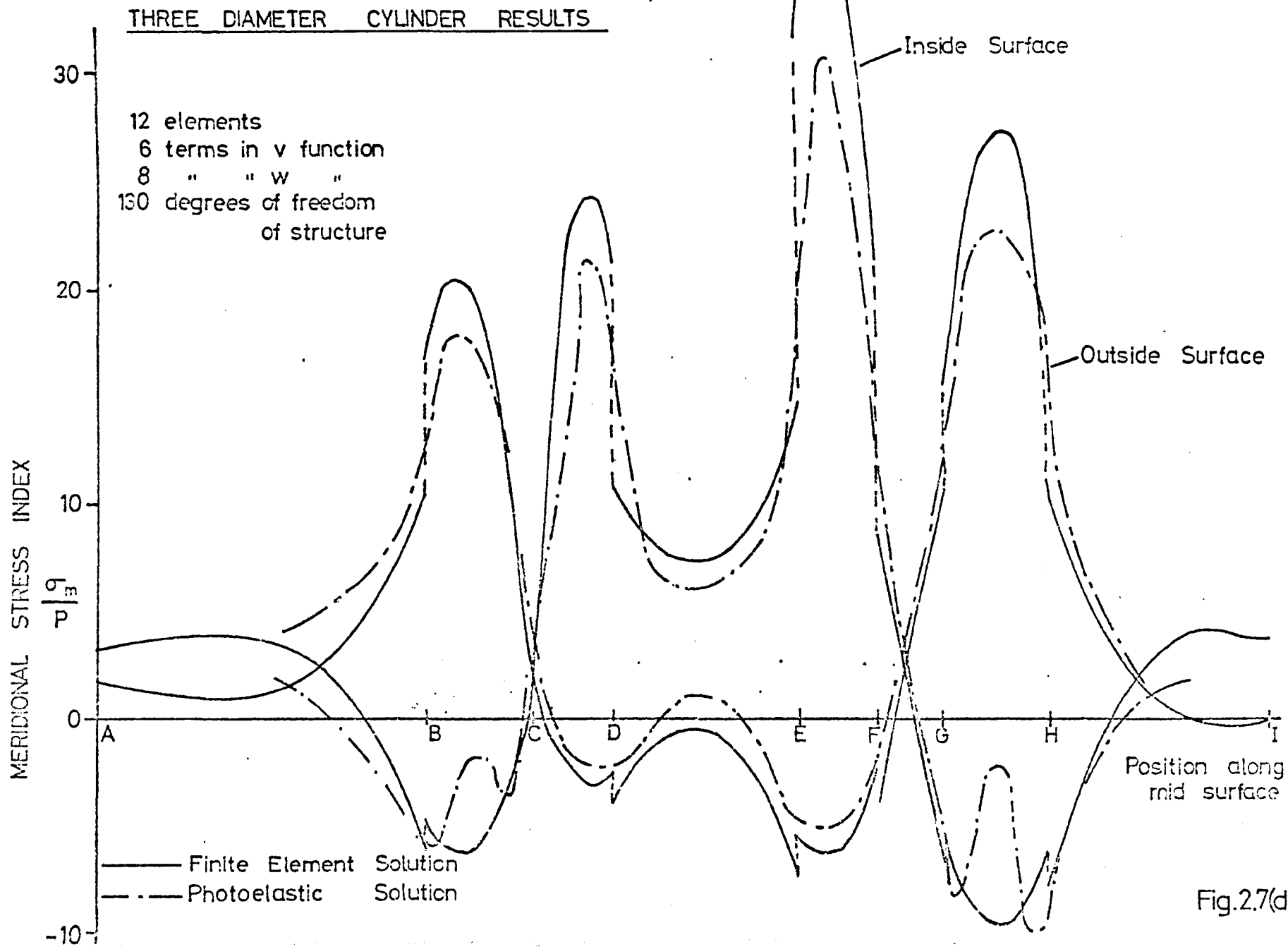
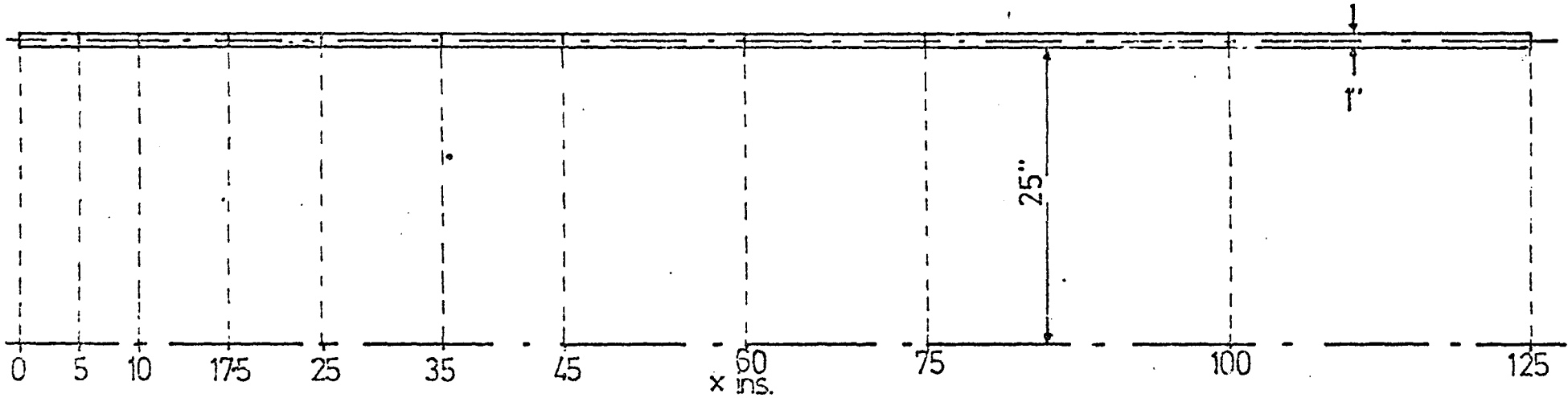


Fig.2.7(d)

SEMI-INFINITE CYLINDER

FINITE ELEMENT IDEALISATION



INTERNAL WALL TEMPERATURE PROFILE

$$T(x,z) = 50 \left(1 - \frac{2z}{h}\right) e^{-x/r}$$

$$E = 3 \times 10^7 \text{ lbf/ins.}$$

$$\alpha = 1.1 \times 10^{-5} / ^\circ\text{C}$$

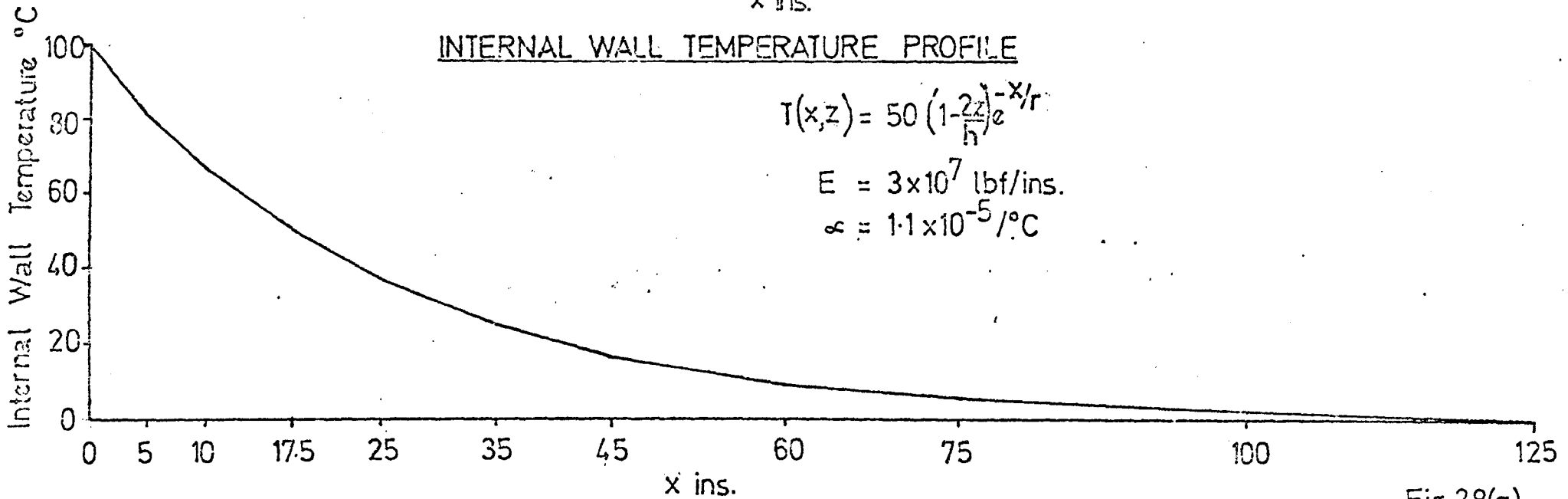


Fig.28(a)

SEMI-INFINITE CYLINDER SUBJECTED TO
A VARYING INTERNAL WALL TEMPERATURE

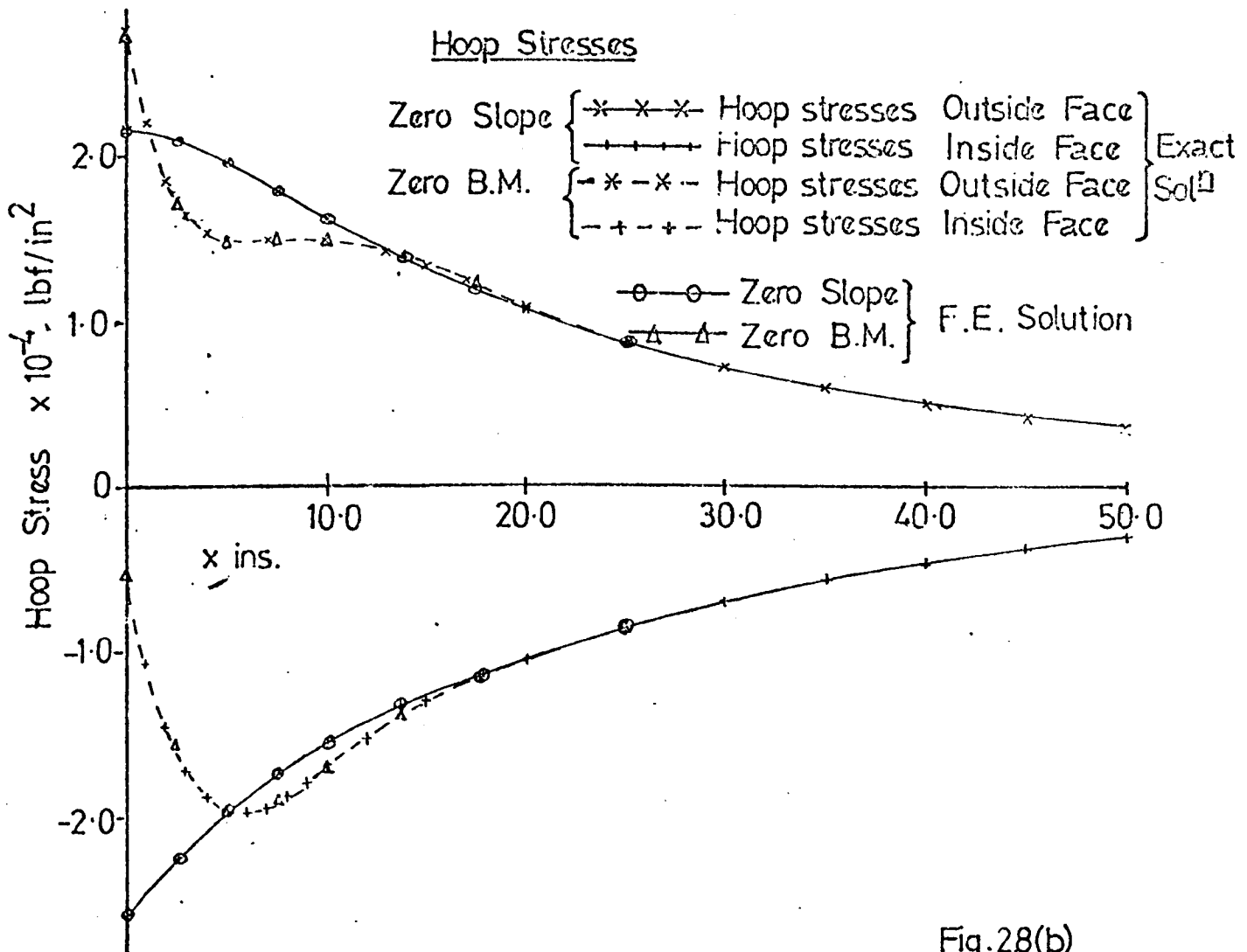
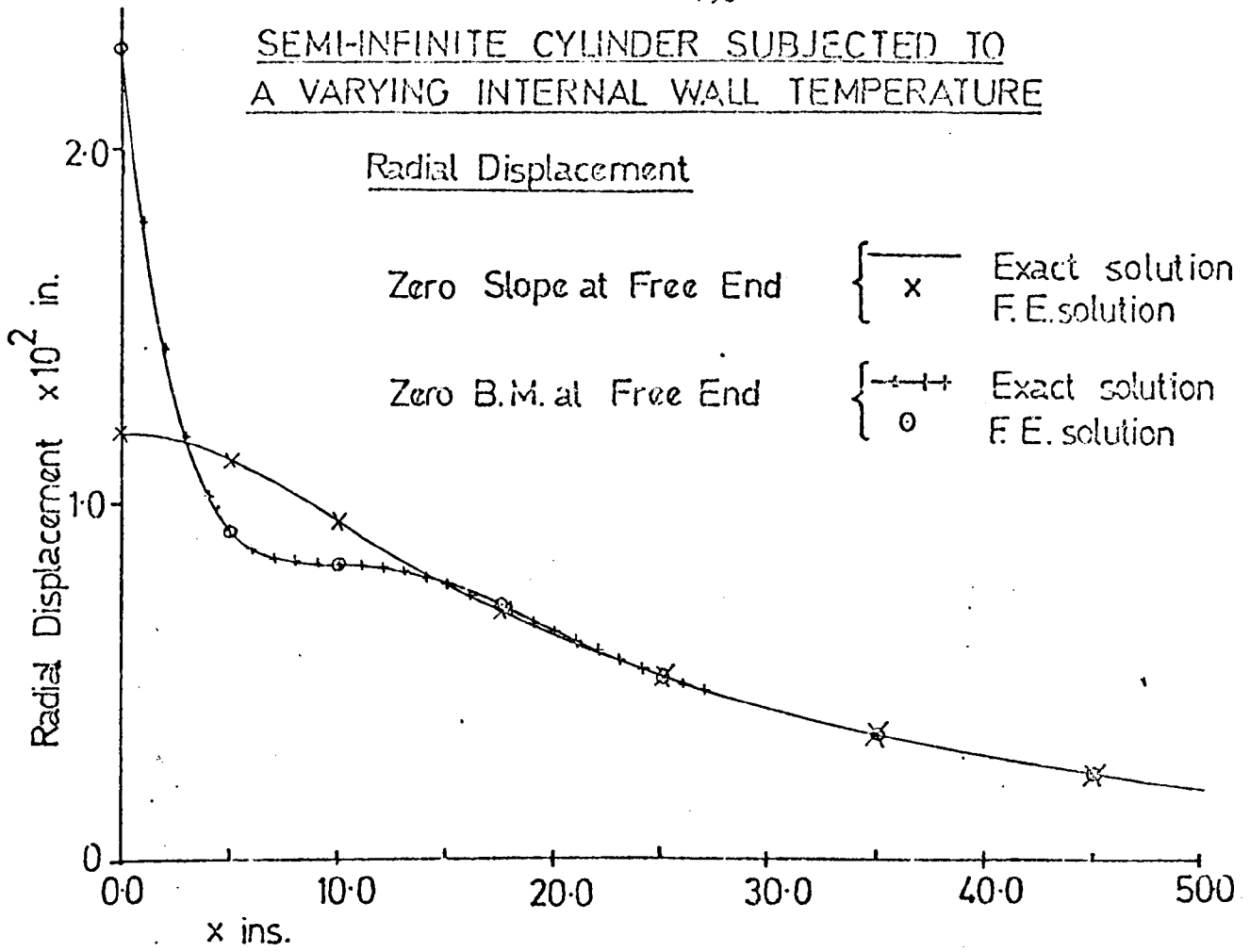
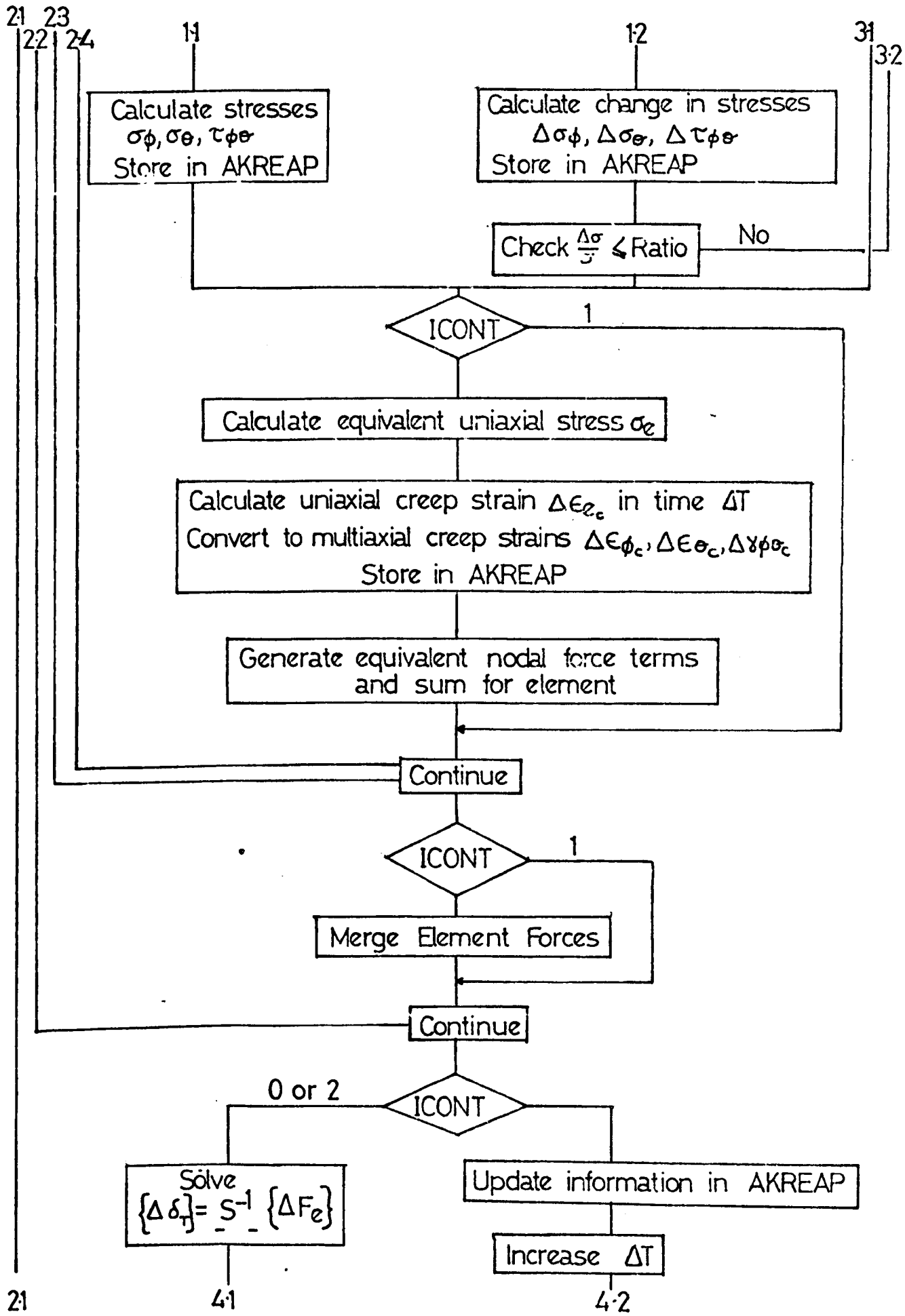
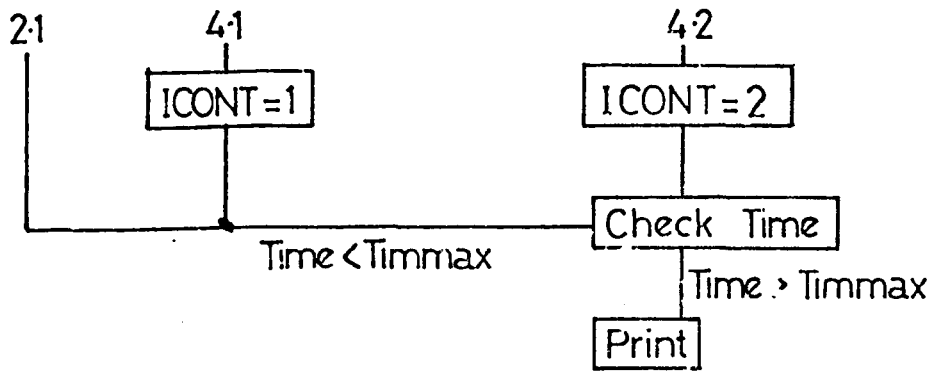


Fig.28(b)

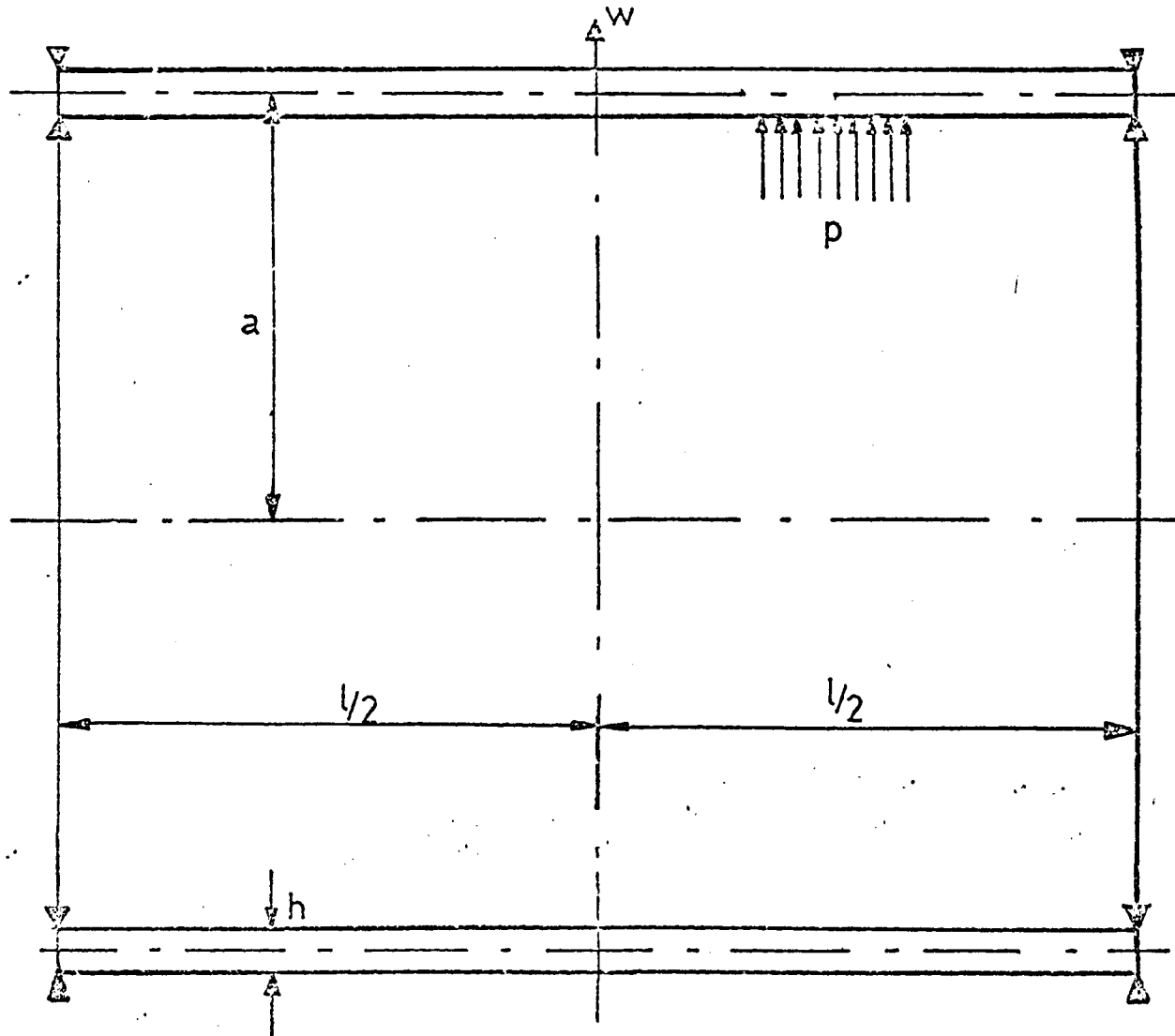
FLOW DIAGRAM FOR CREEP ANALYSIS OF THIN SHELL OF REVOLUTION FINITE ELEMENT(Continued)



FLOW DIAGRAM FOR CREEP ANALYSIS OF THIN SHELL OF REVOLUTION FINITE ELEMENT (Continued)



SIMPLY SUPPORTED SHELL



$a = 100 \text{ mm.}$
 $h = 5 \text{ mm.}$
 $l = 109.3 \text{ mm.}$
 $p = 0.75 \text{ kg/mm}^2$

Creep Law
 $\epsilon = A \sigma^n t^m$

where

$$A = 4.36 \times 10^{-9} \left(\frac{\text{Kg}}{\text{mm}^2} \right)^{-4.66} \text{ sec}^{-0.218}$$

$n = 4.66$

$m = 0.218$

$E = 1.8 \times 10^4 \text{ Kg/mm}^2$

$\nu = 0.3$

$\frac{pa}{h} = 15 \text{ Kg/mm}^2$

$$\alpha^2 = \frac{\sqrt{\beta(1-\nu^2)}}{4} \frac{l^2}{ah} = \pi^2$$

Fig. 2.10(a)

CREEP DEFORMATION OF SIMPLY SUPPORTED CYLINDER

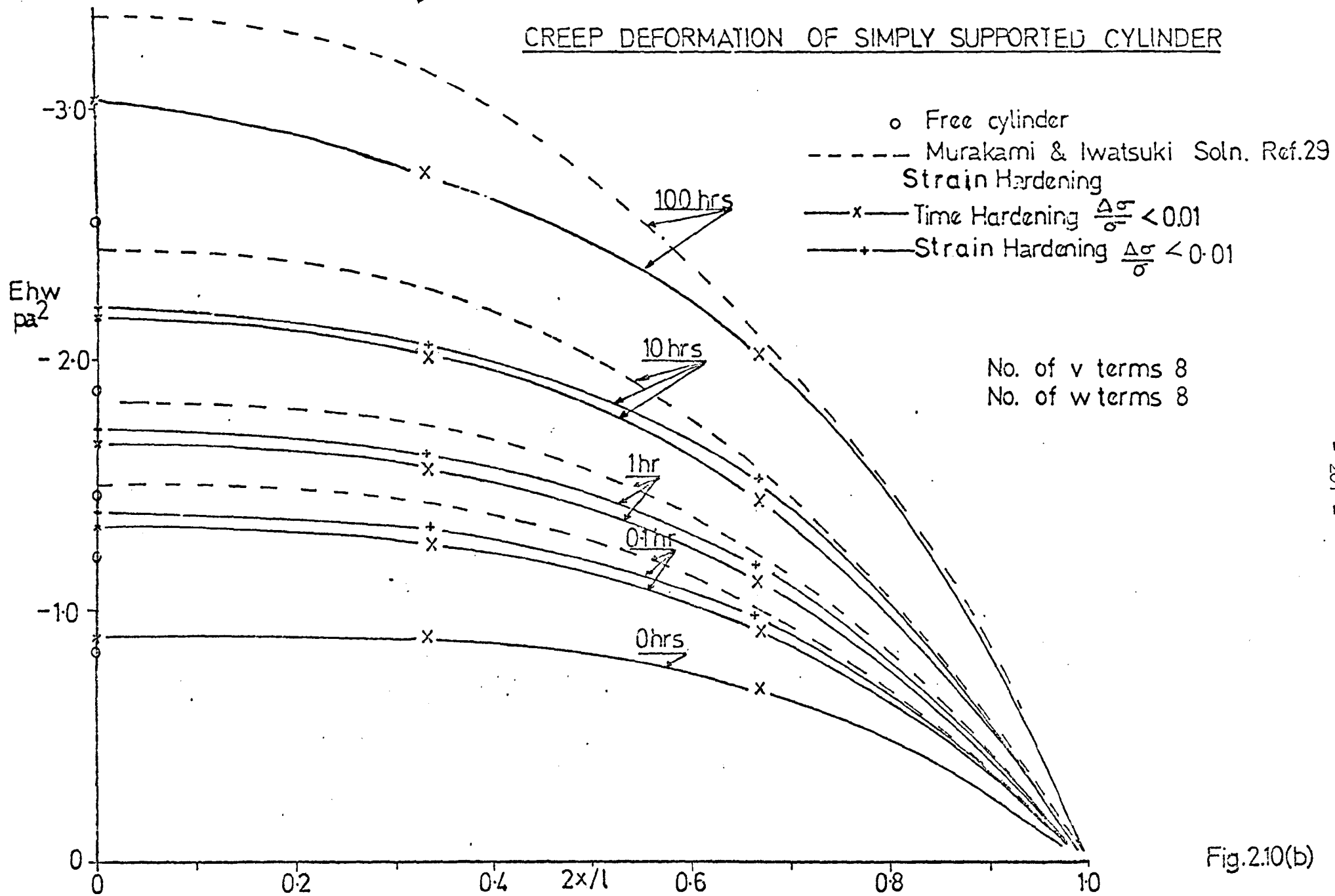
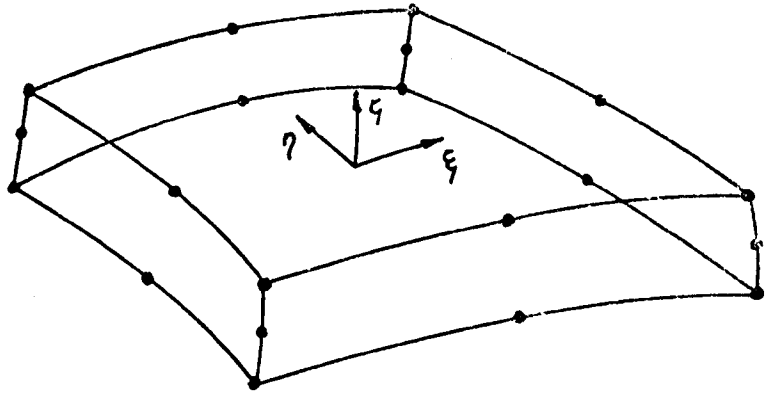
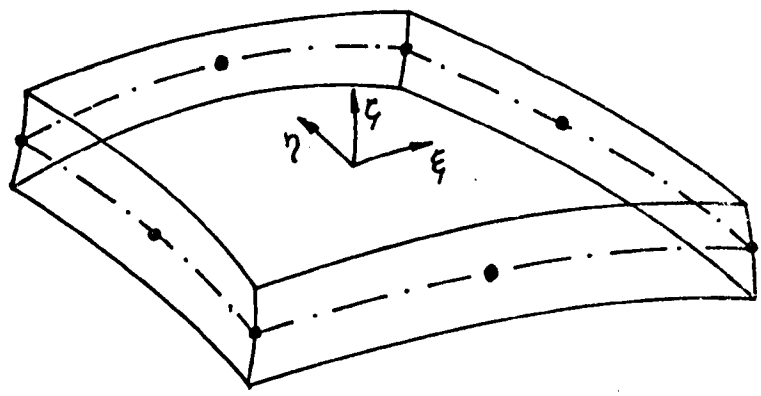


Fig.2.10(b)

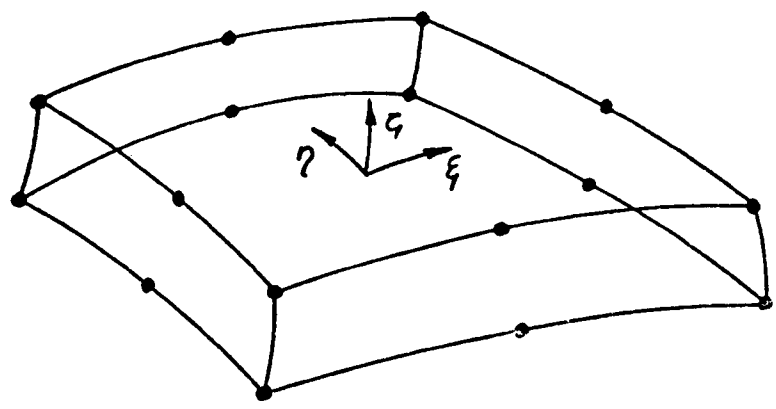
Parametric Finite Elements



20 node quadrilateral Isoparametric Finite Element

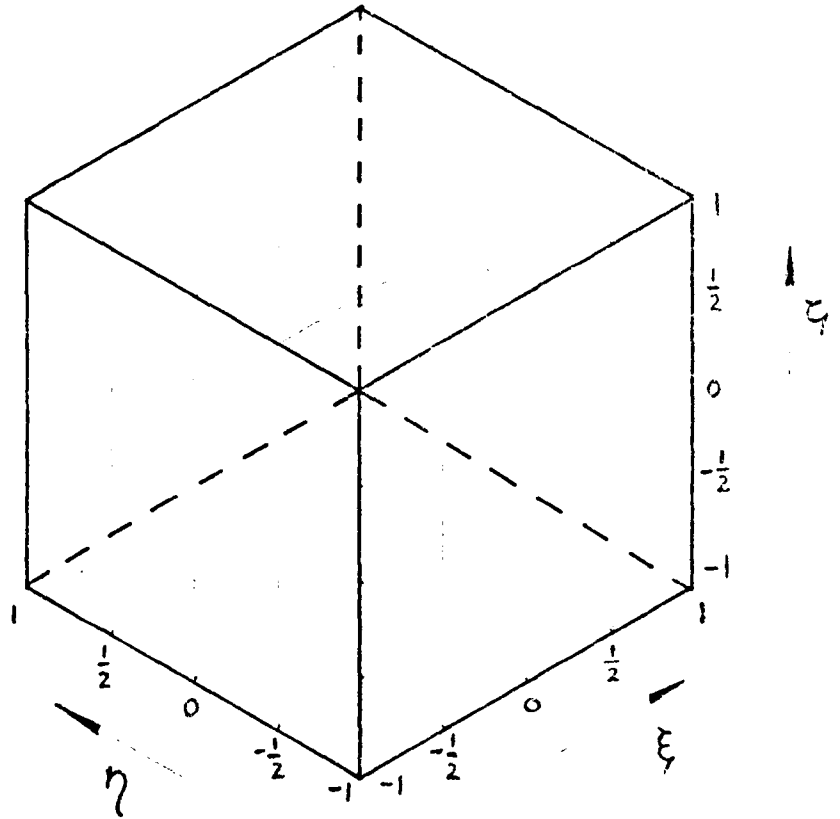


8 node "Ahmad" shell Finite Element



16 node Thick shell parametric Finite Element

Mapping of Parametric Finite Elements



Cube defined in Curvilinear Coordinates ξ, η, ζ "mapped" into Cartesian Coordinates x, y, z

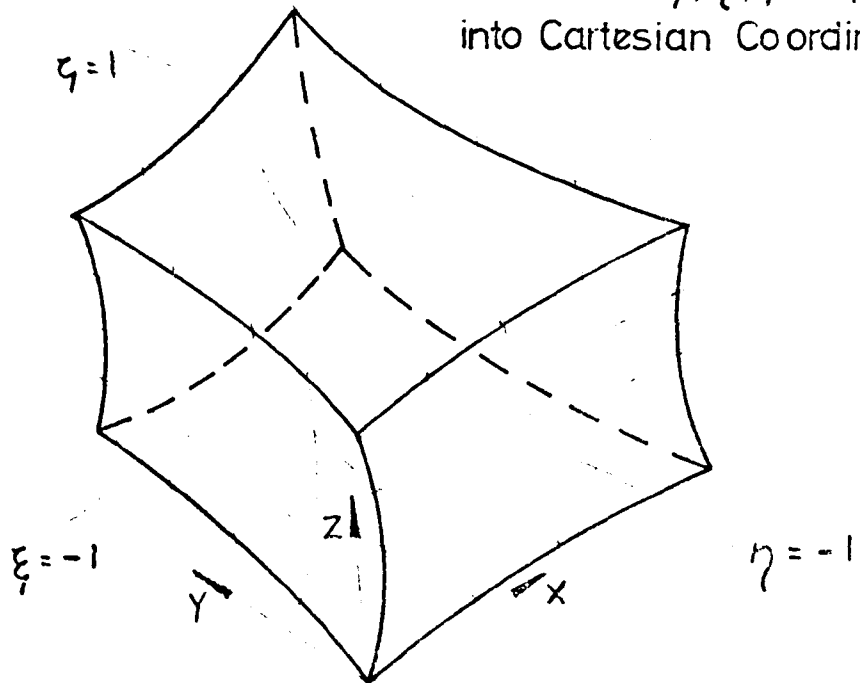
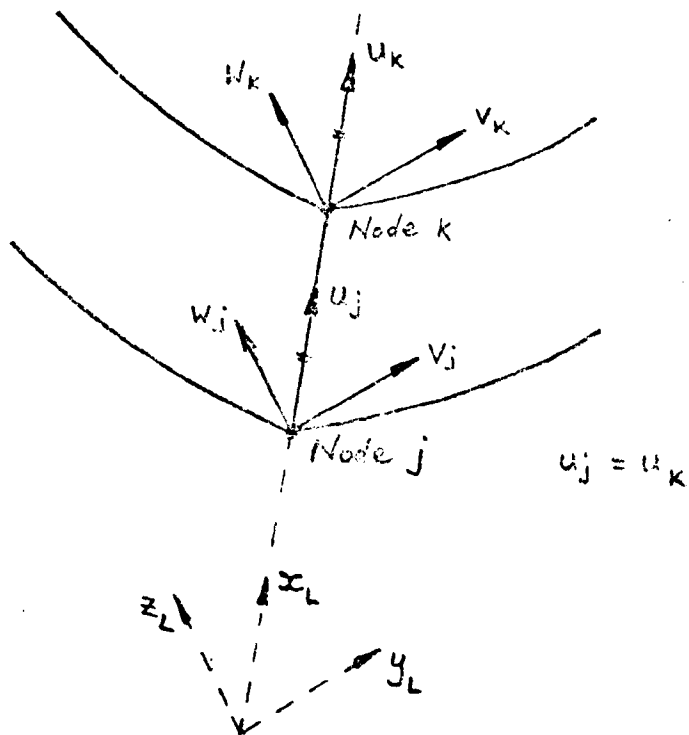


Fig 32

Thick Shell and "Ahmad" Parametric Finite Element

Nodal Displacements

Thick Shell Finite Element



"Ahmad" Shell Finite Element

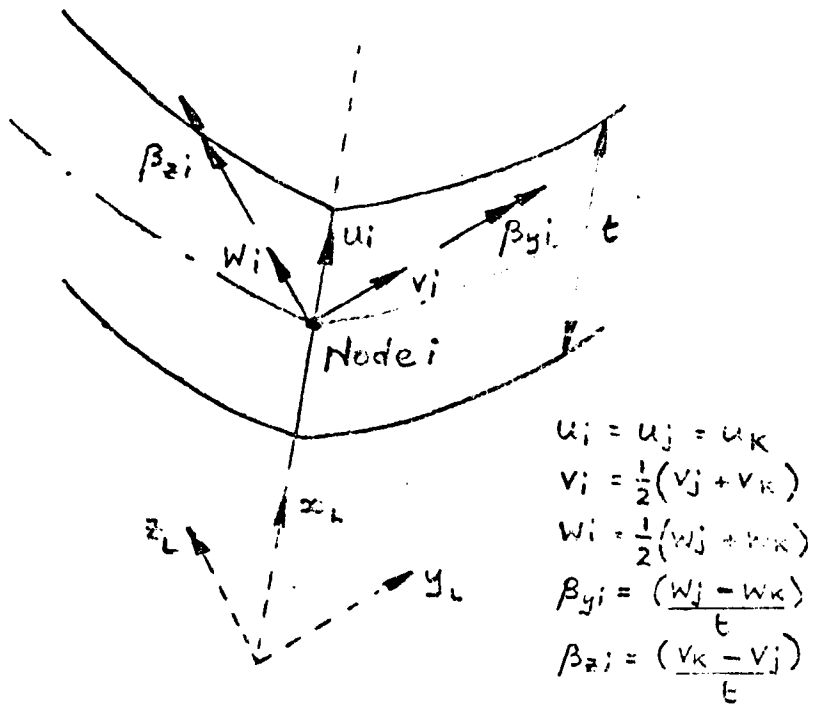


Fig.33

Thick Shell and Iso-parametric Finite Element
Junction Constraints

Coupling Outside Nodes

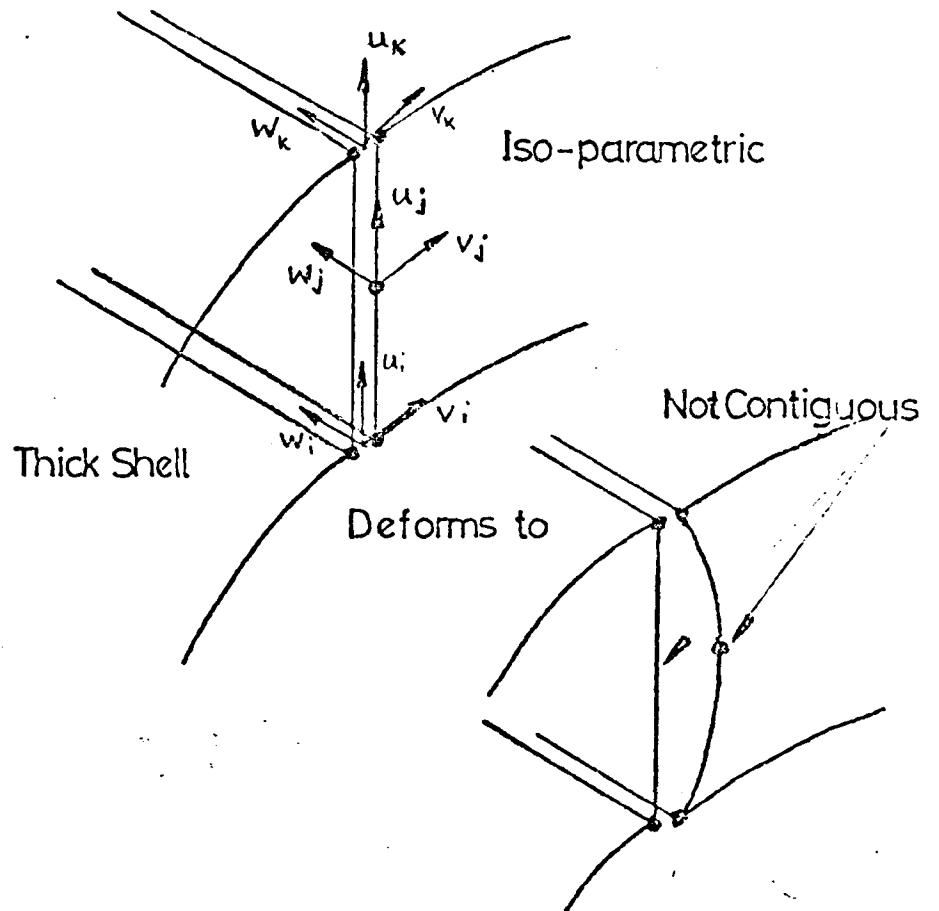


Fig.34

Transition Parametric Finite Element Topology and Displacement Constraints

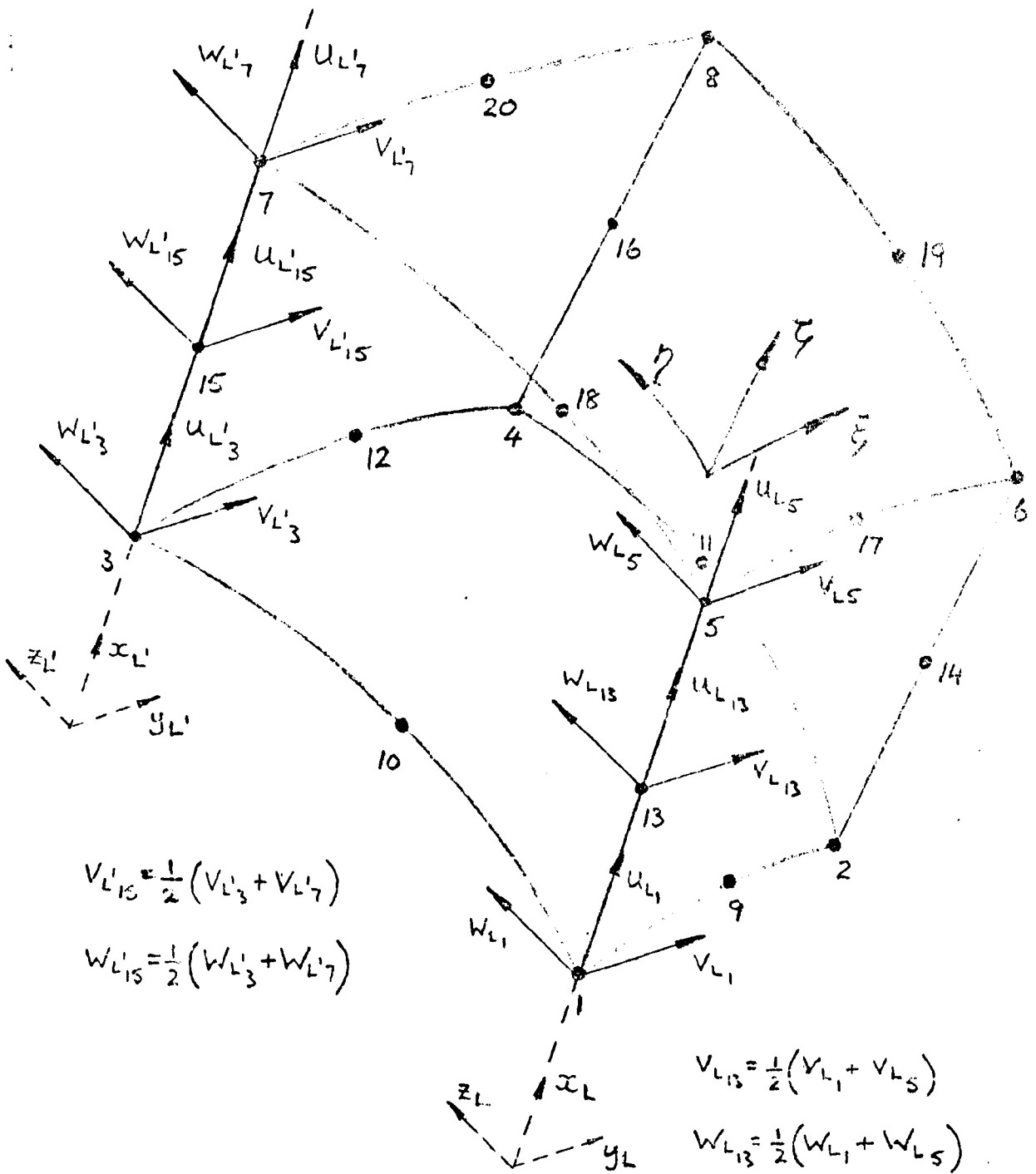
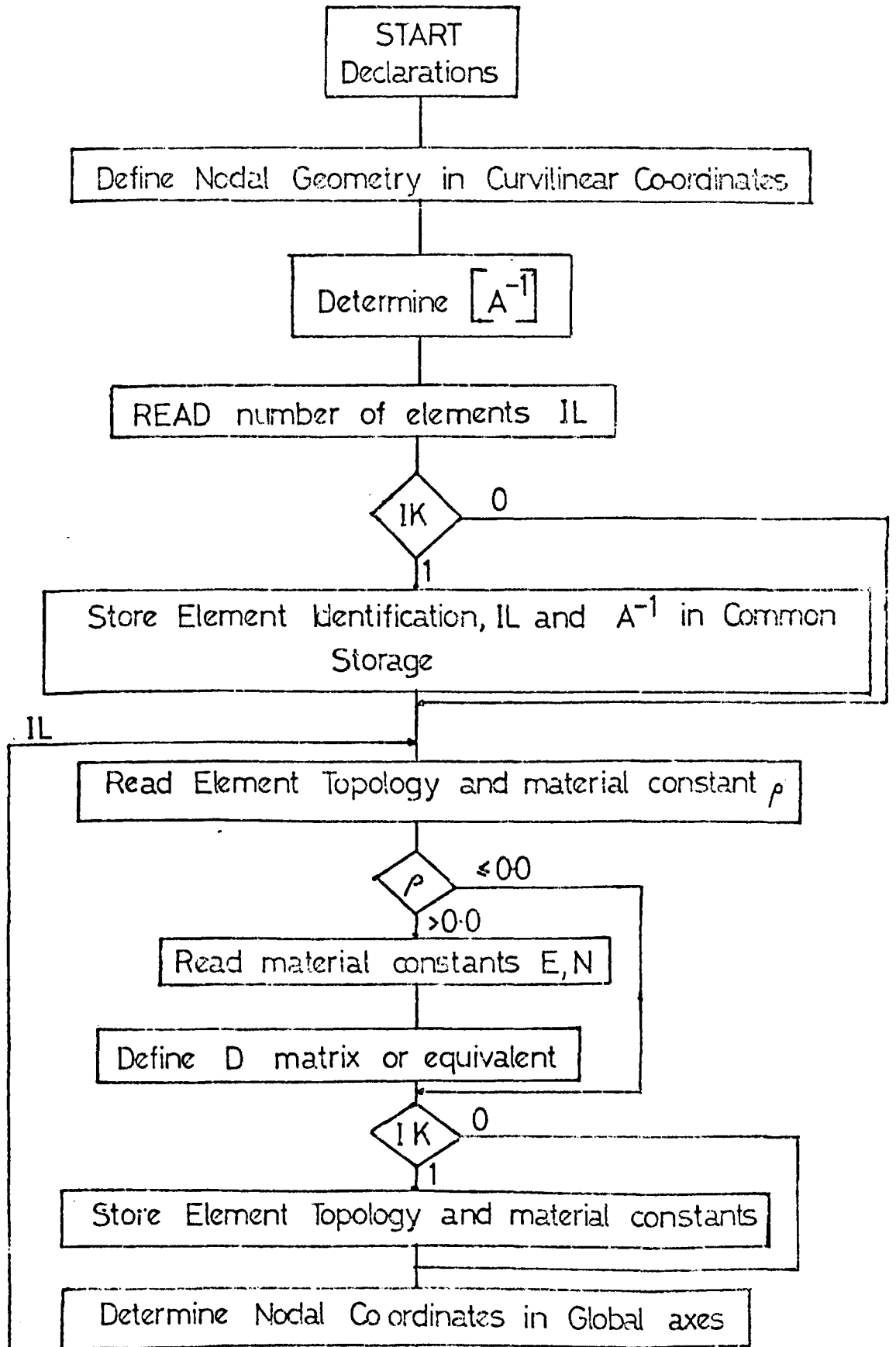


Fig.35

20 NODE ISO-PARAMETRIC STIFFNESS AND LOADING
MATRICES FLOW DIAGRAM



20 NODE ISO PARAMETRIC STIFFNESS AND LOADING
MATRICES FLOW DIAGRAM (Continued)

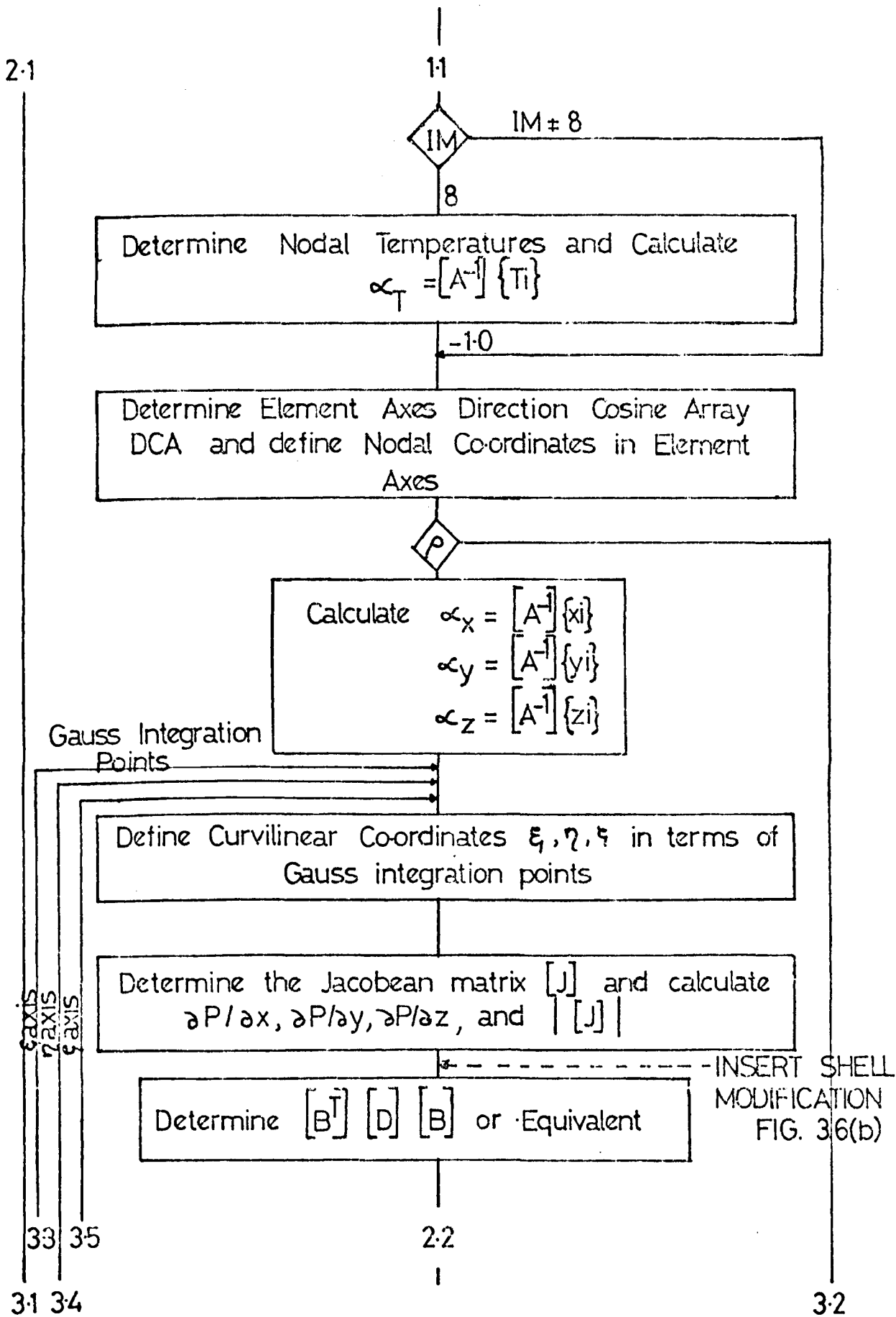


Fig.36(a) cont.

20 NODE ISO PARAMETRIC STIFFNESS AND LOADING
 MATRICES FLOW DIAGRAM (Continued)

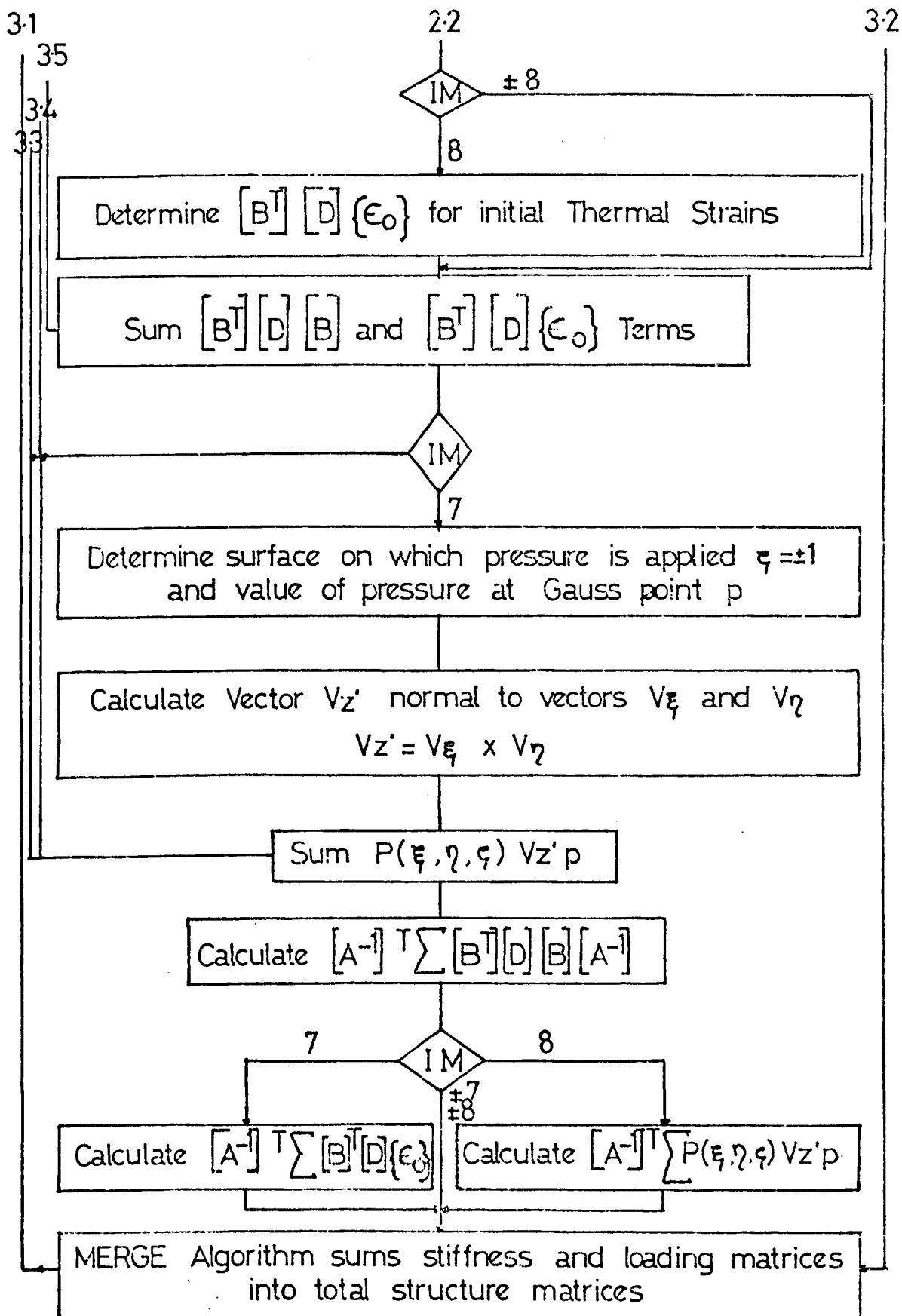


Fig.36(a) cont.

THICK SHELL PARAMETRIC FINITE ELEMENT

Extra Portion of Flow Diagram to be added to Fig. 36(a)

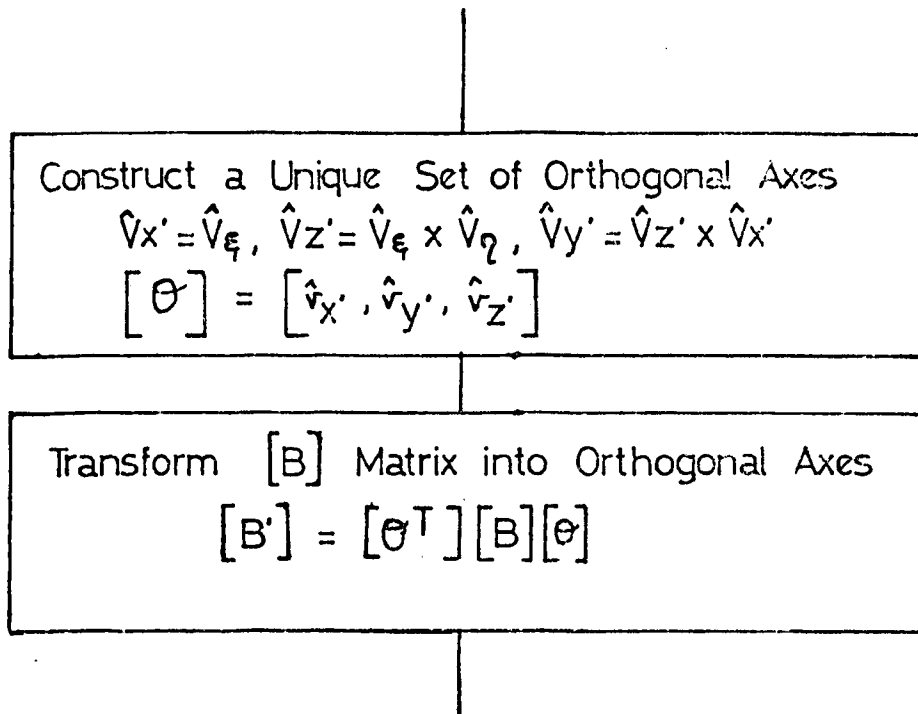


Fig. 36(b)

TRANSITION PARAMETRIC FINITE ELEMENT

Extra Portion of Flow Diagram to be added to Fig. 36(a)

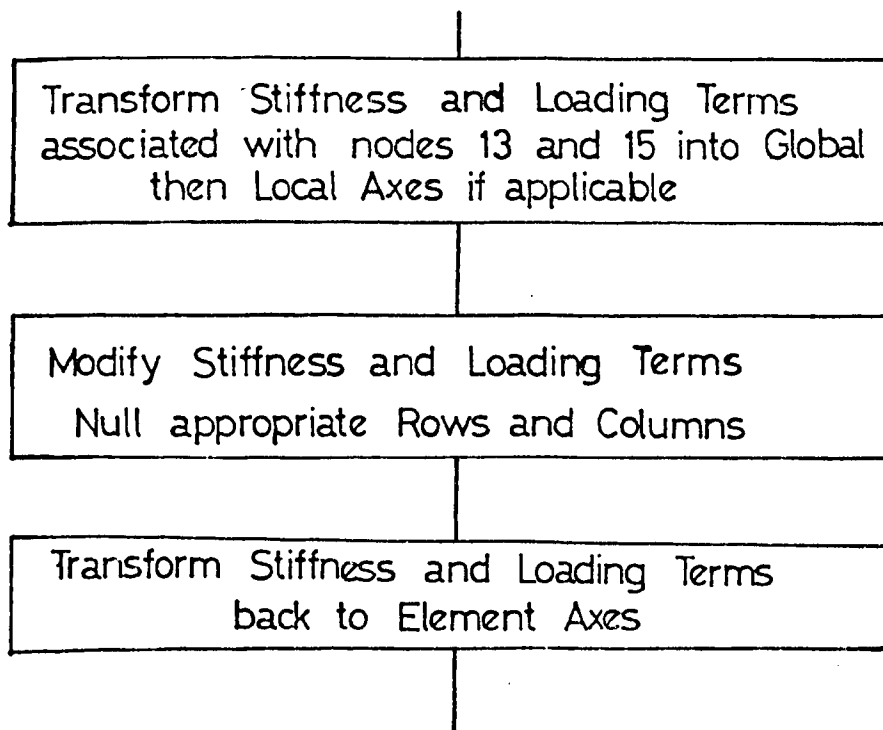
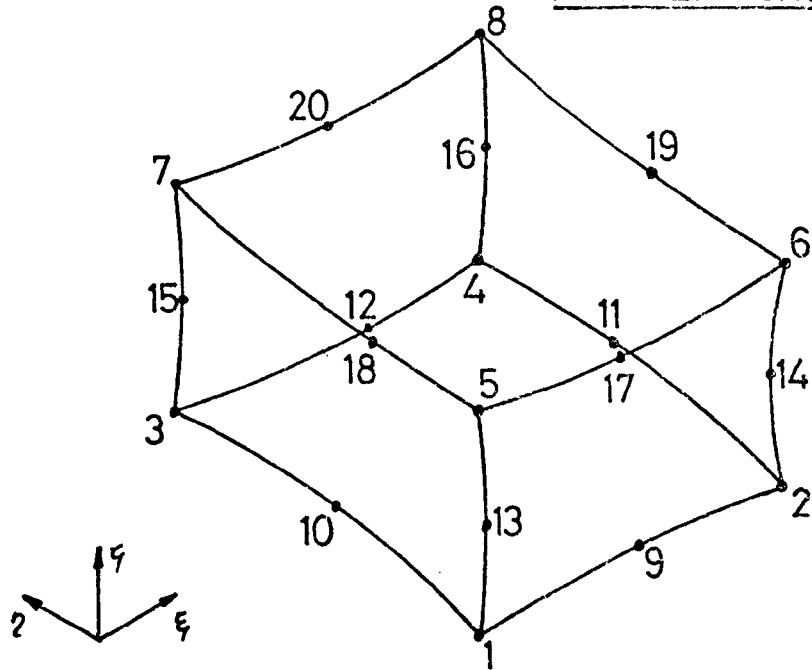


Fig. 36(c)

Element Topology for Quadratic Parametric
Finite Elements

Isoparametric and Transition Parametric
Finite Elements



Thick Shell Parametric Finite Element

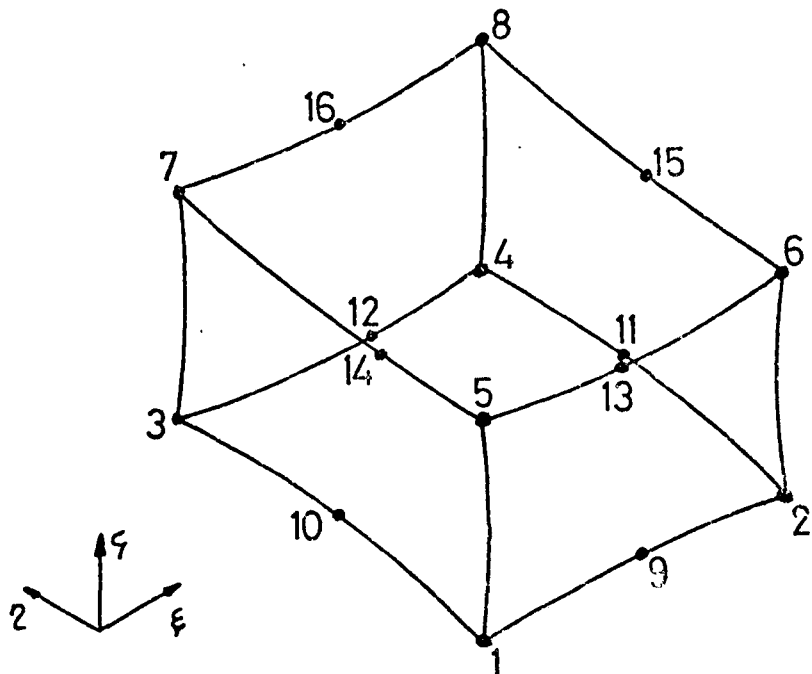
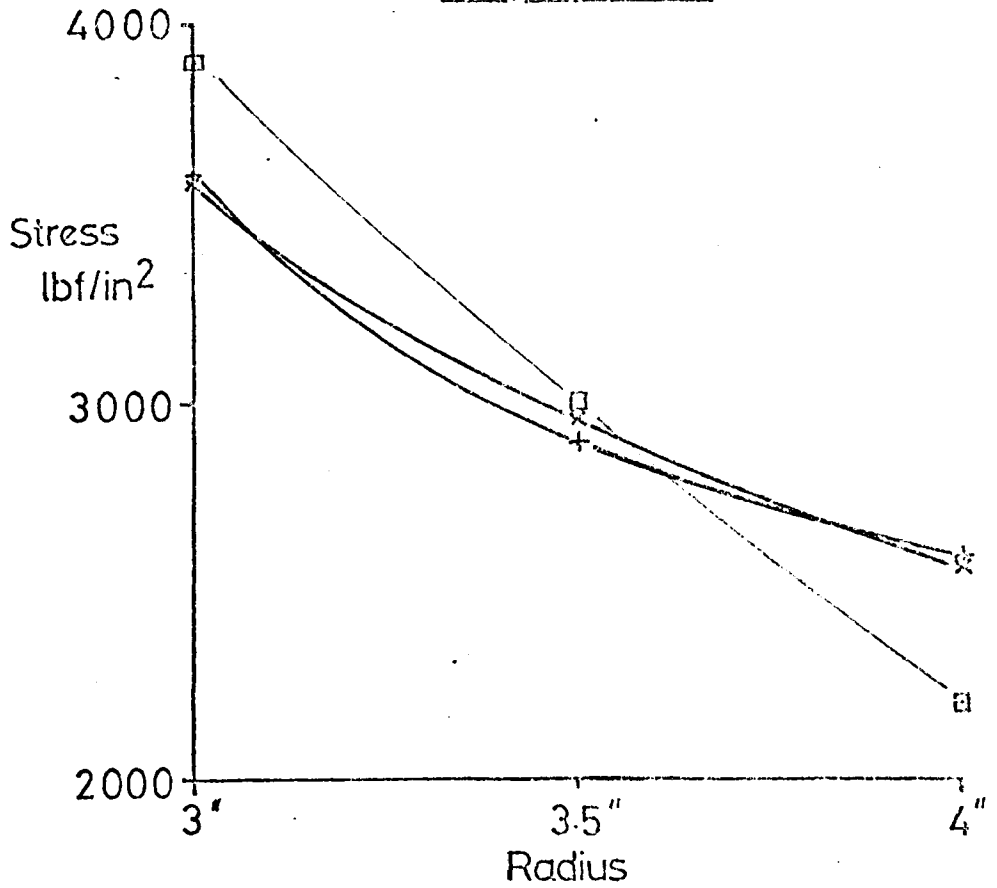


Fig 37

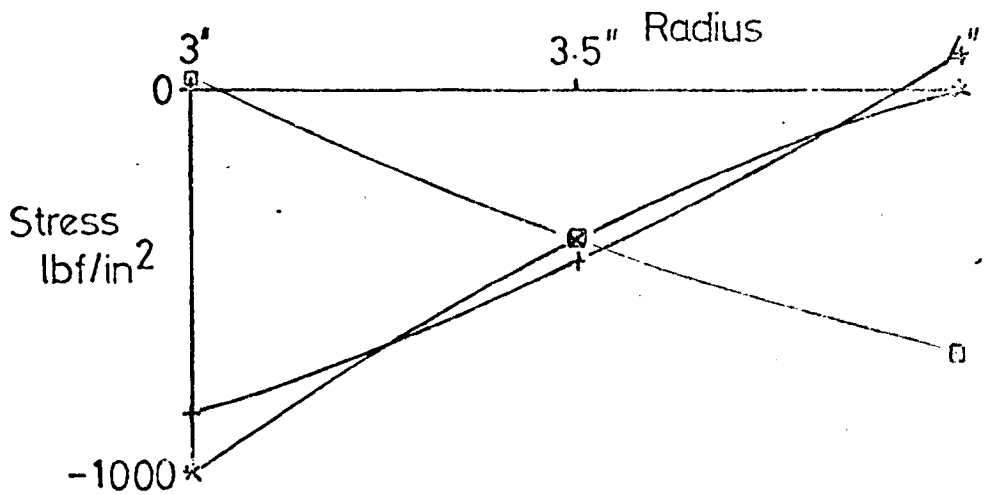
Pressurised Thick Cylinder

ID=6", OD=8", Pressure=1000 lbf/in², Sector=22 1/2°

Hoop Stresses



Radial Stresses



Key

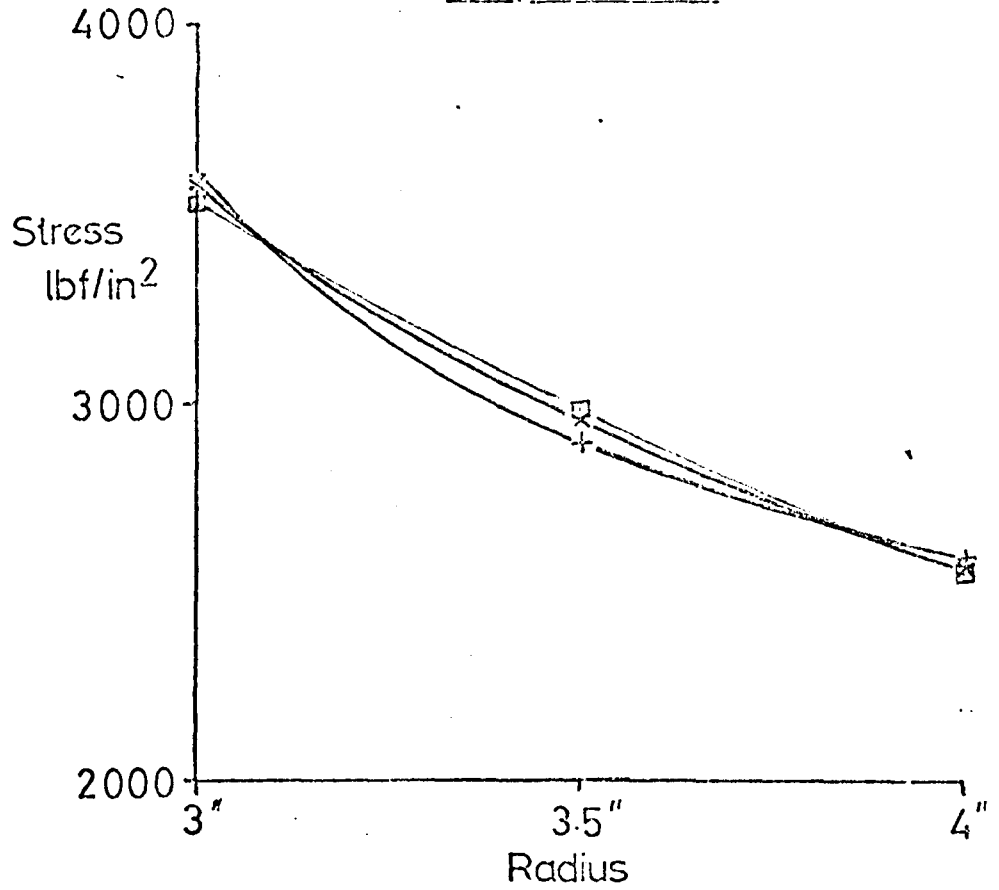
- x—x Lamé solution
- Linear isoparametric F.E. solution
- +—+ Quadratic " " "

Fig 3.8(a)

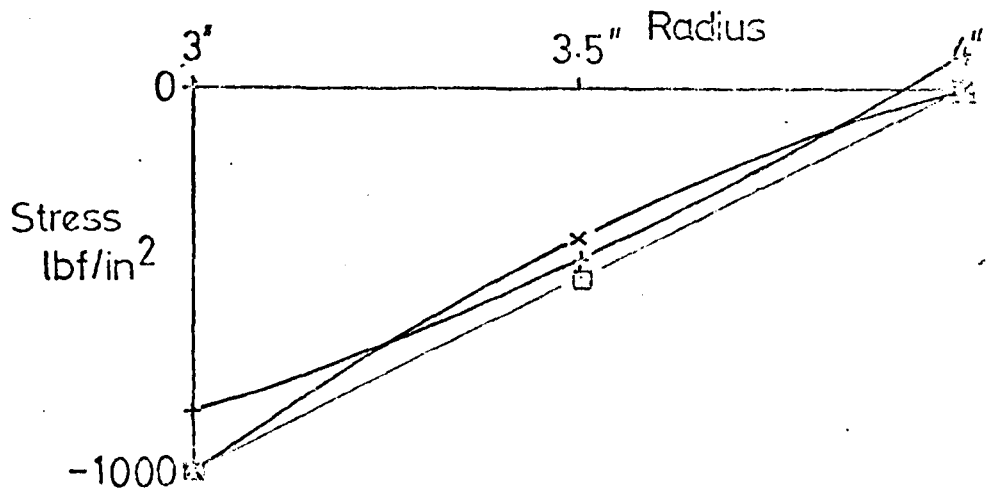
Pressurised Thick Cylinder

ID=6", OD=8", Pressure=1000 lbf/in², Sector=22½°

Hoop Stresses



Radial Stresses



Key

- x—x Lamé solution
- Quadratic Thick Shell Parametric F.E. solution
- +—+ " Isoparametric F.E. solution

Fig 3.8(b)

Pressurised Thick Cylinder Idealised
by 3 Isoparametric Finite Elements

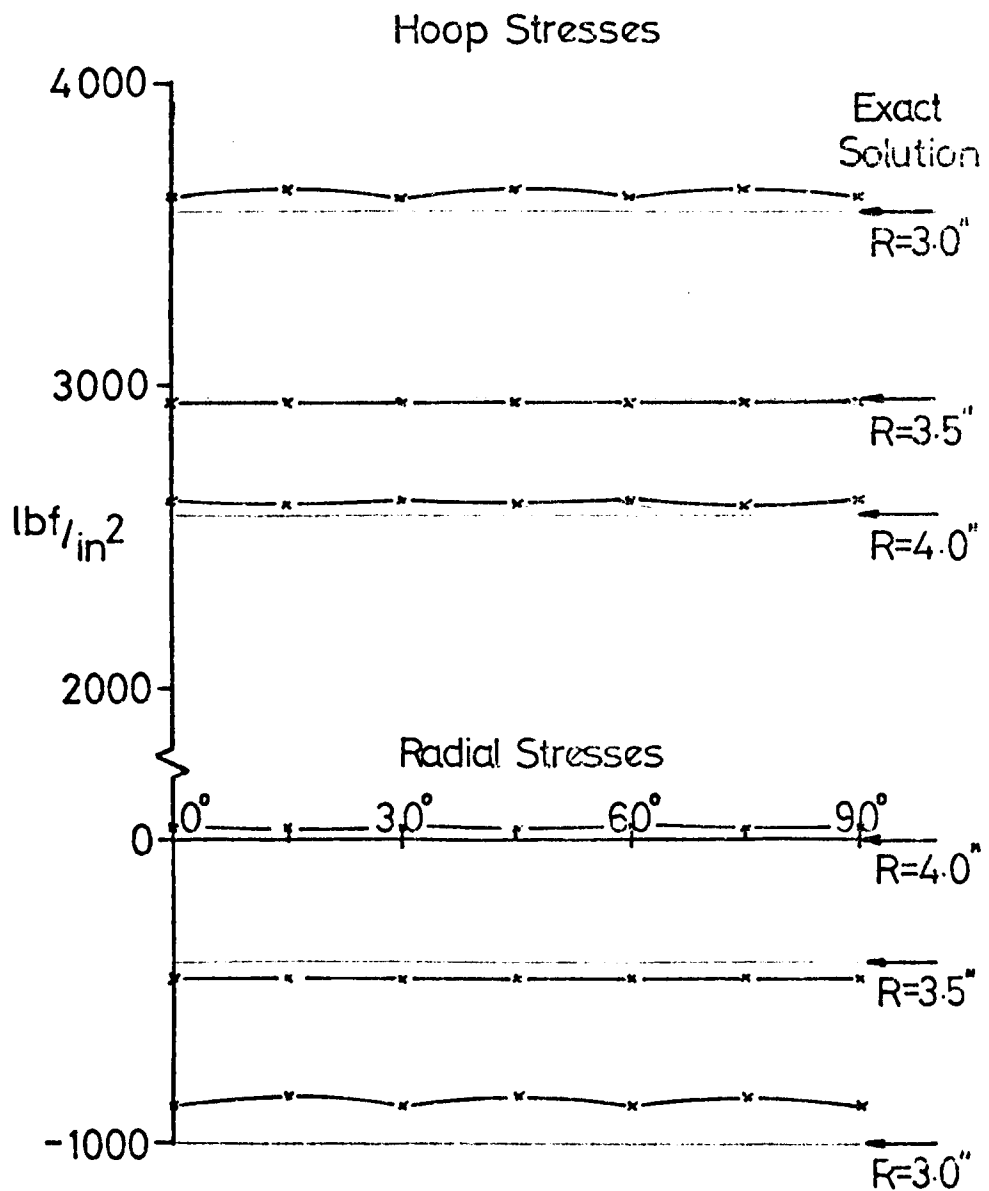
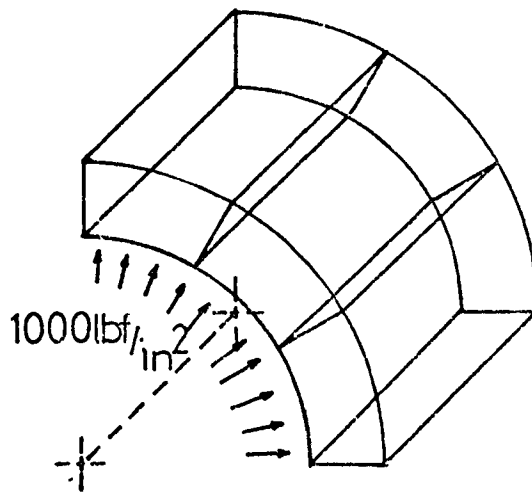


Fig.3.9(a)

Pressurised Thick Cylinder Idealised
by 3" Thick Shell Parametric
Finite Elements

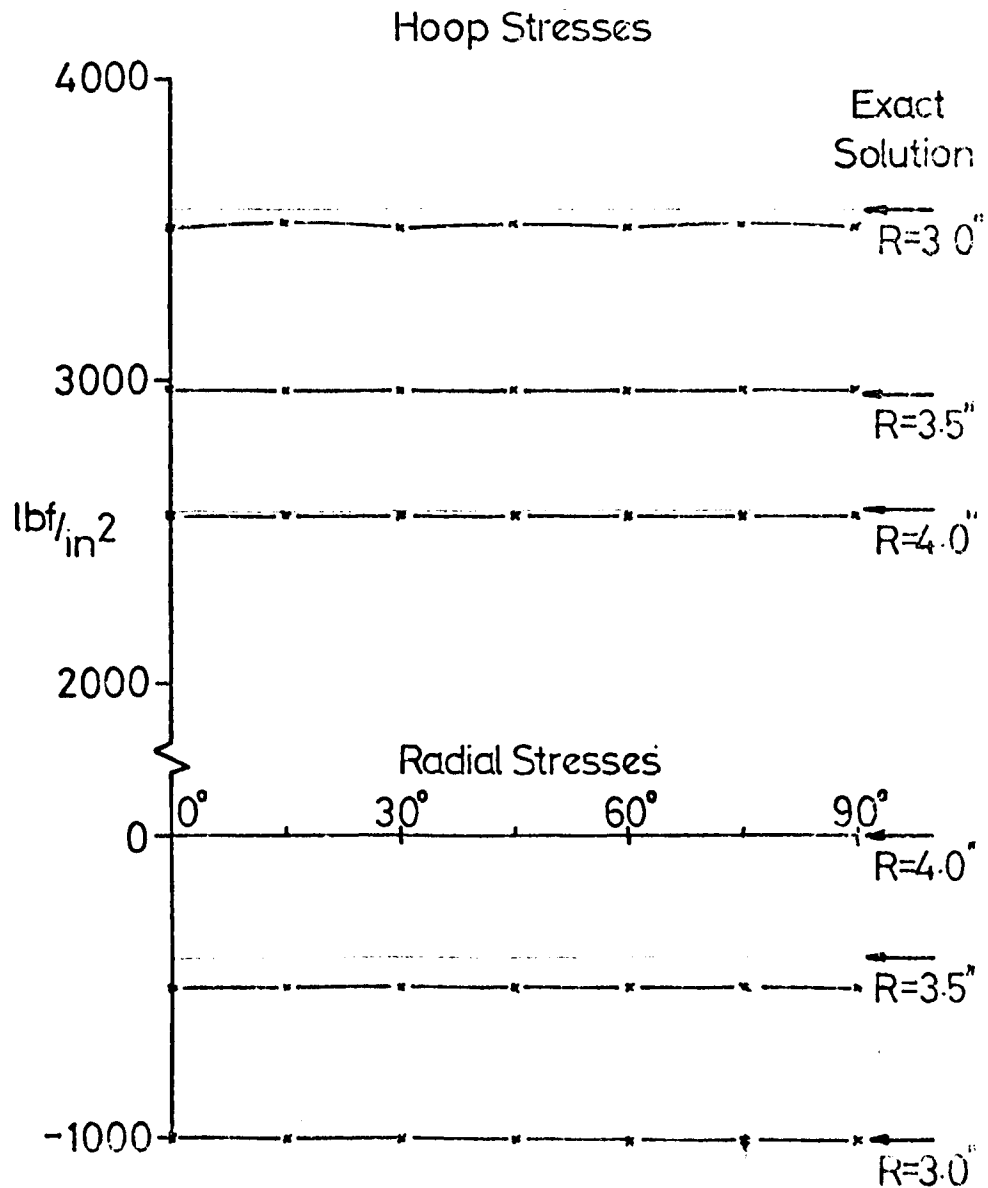
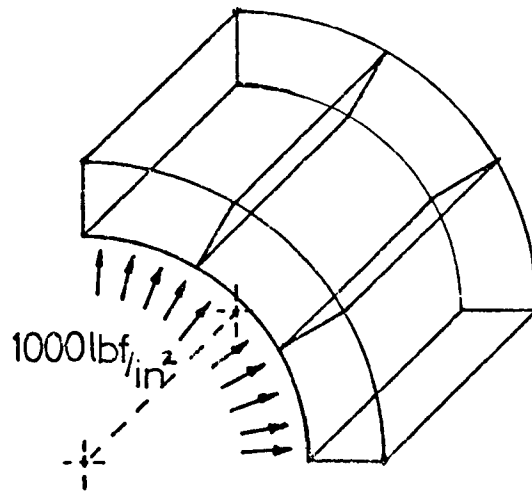
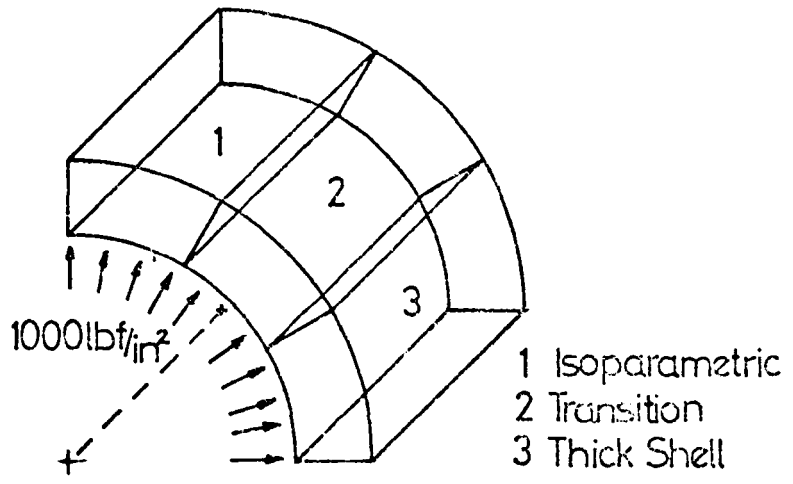


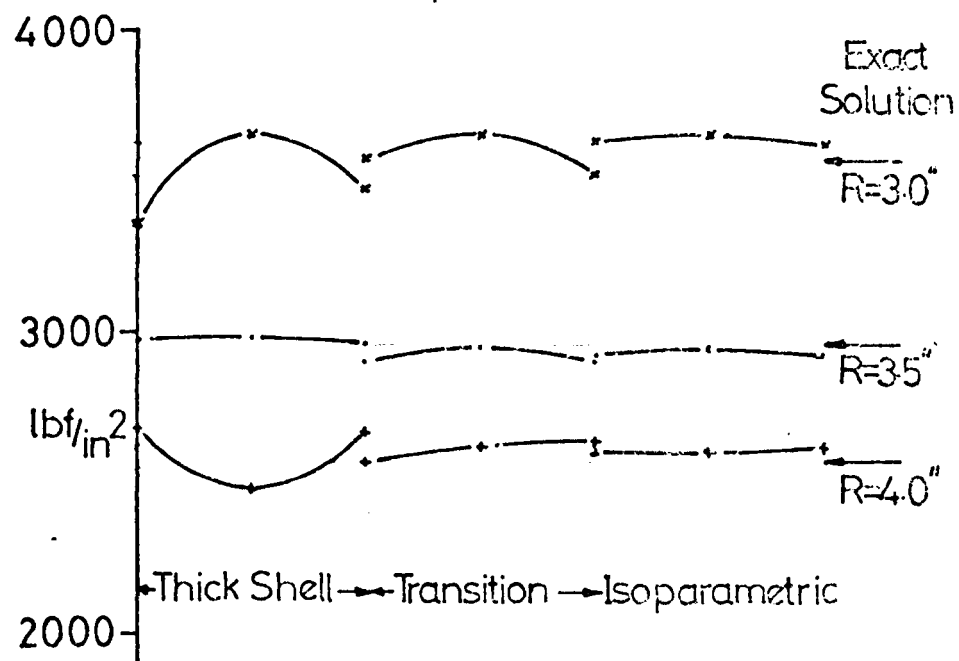
Fig39(b)

Thick Cylinder Idealised by Isoparametric, Transition and Thick Shell Parametric

Finite Elements



Hoop Stresses



Radial Stresses

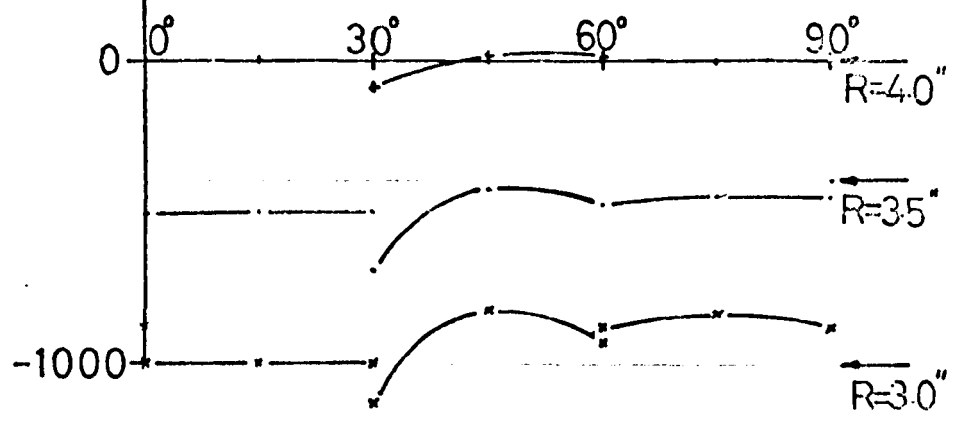


Fig.3.10

FLOW DIAGRAM FOR MERGE ALGORITHM

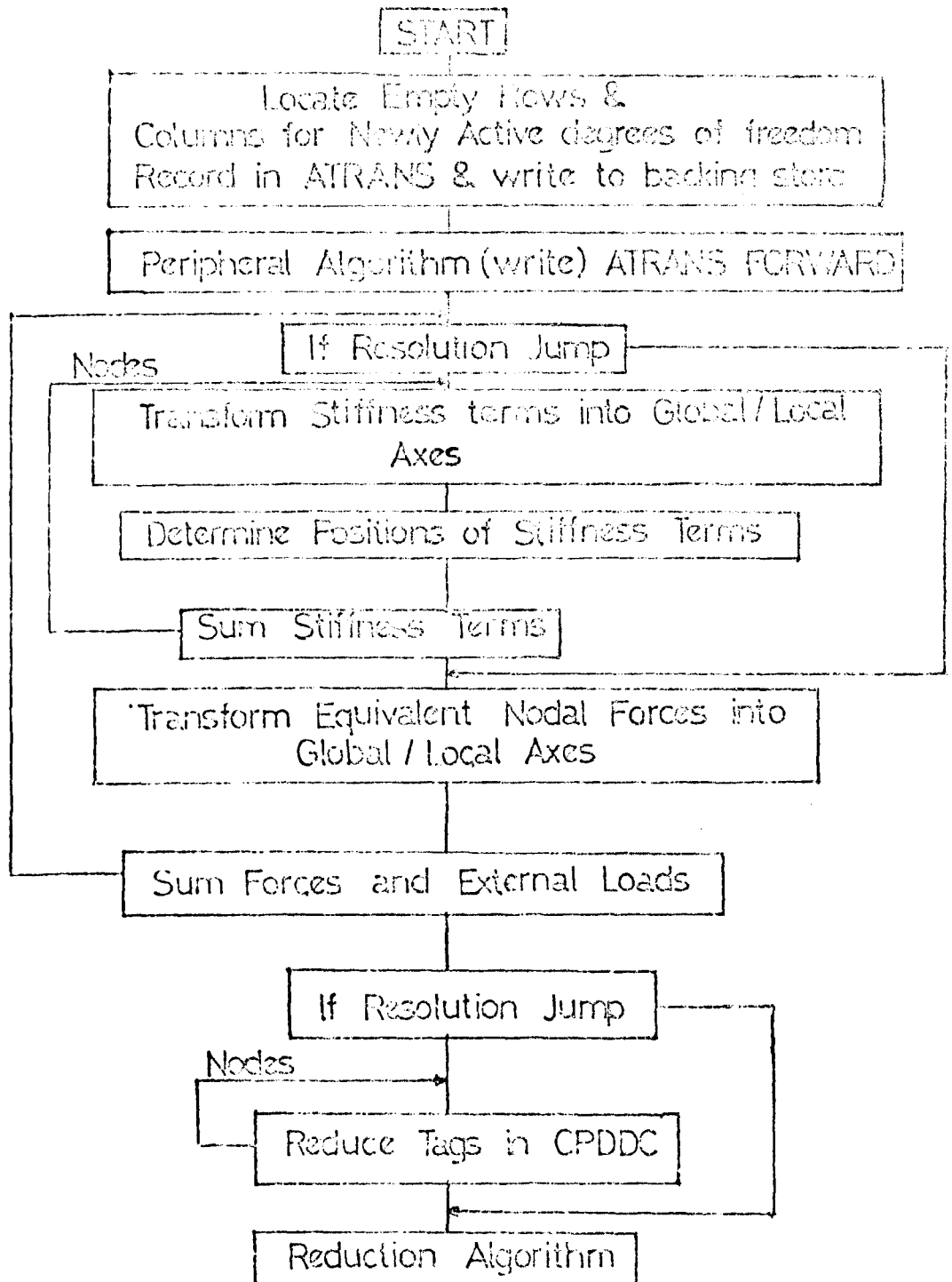


Fig. 4-1

FLOW DIAGRAM FOR REDUCTION ALGORITHM

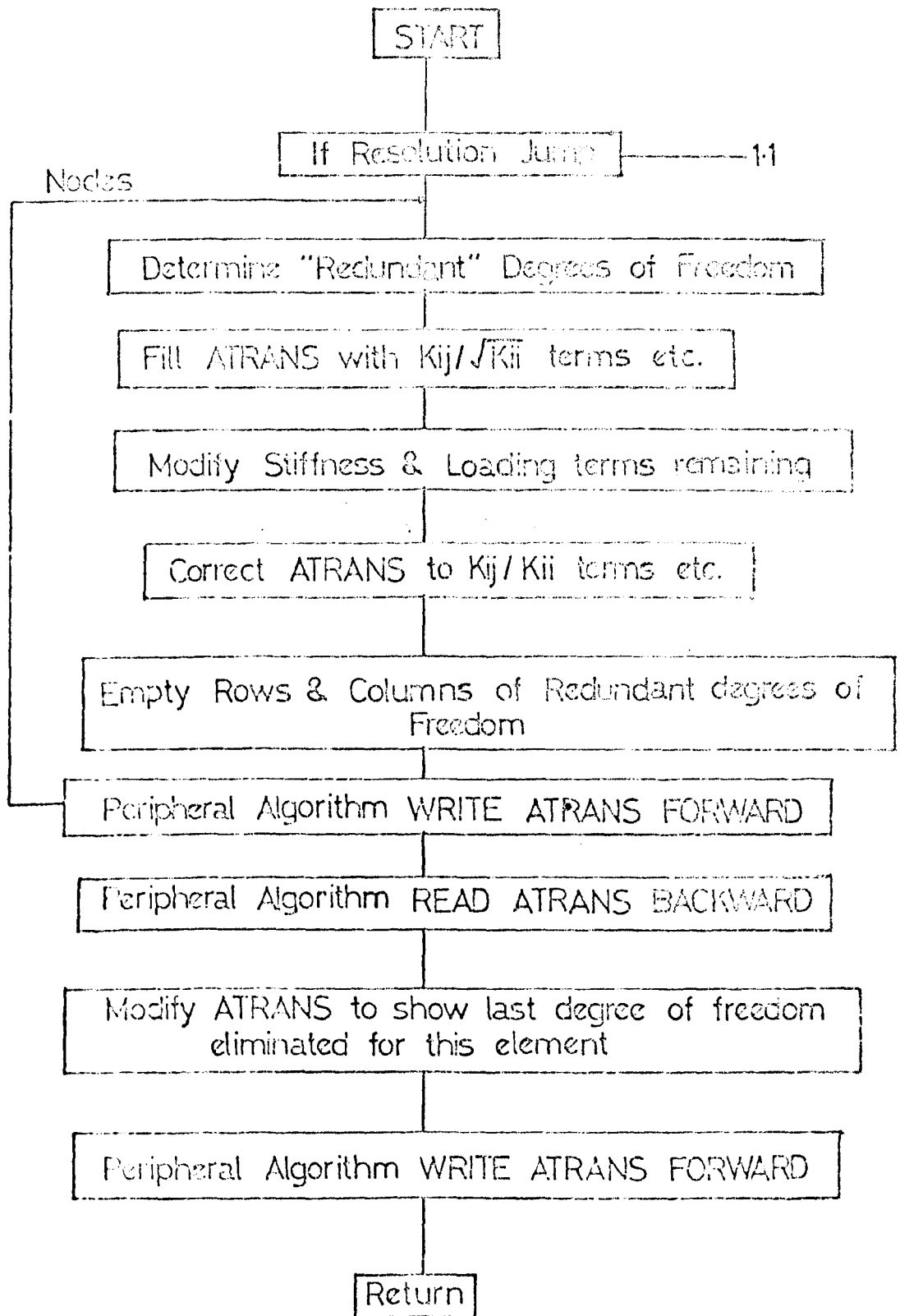


Fig. 42(a)

FLOW DIAGRAM FOR REDUCTION ALGORITHM (Continued)
RESOLUTION STAGE

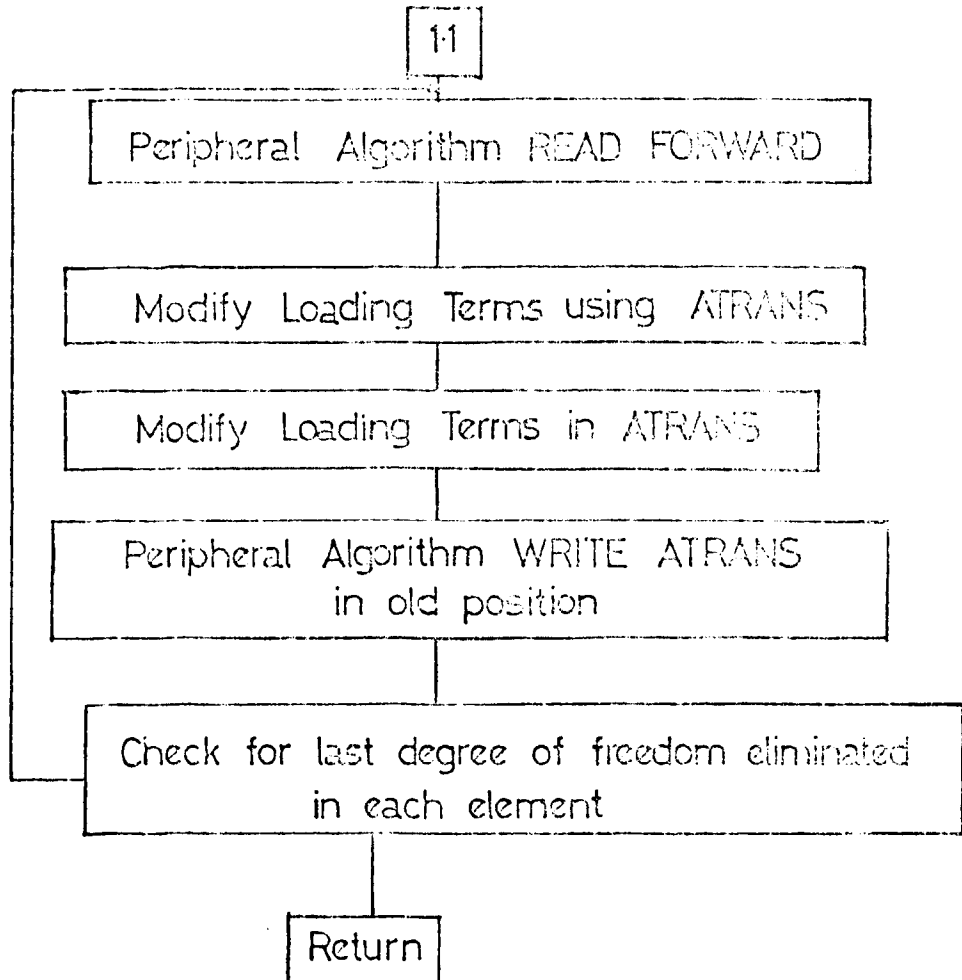


Fig. 4-2(b)

FLOW DIAGRAM FOR BACK-SUBSTITUTION ALGORITHM

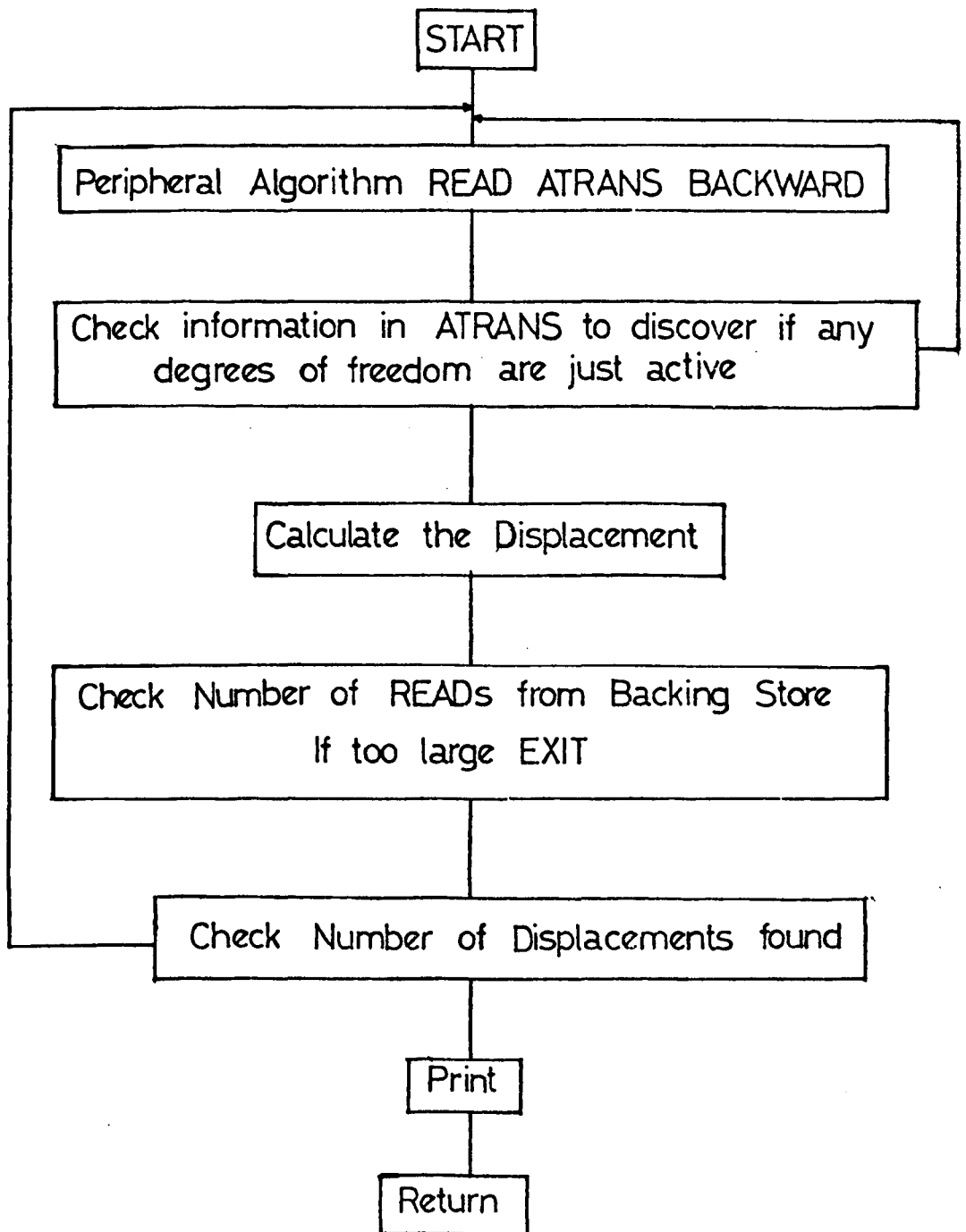


Fig. 4.3

FLOW DIAGRAM FOR PERIPHERAL HANDLING ALGORITHM

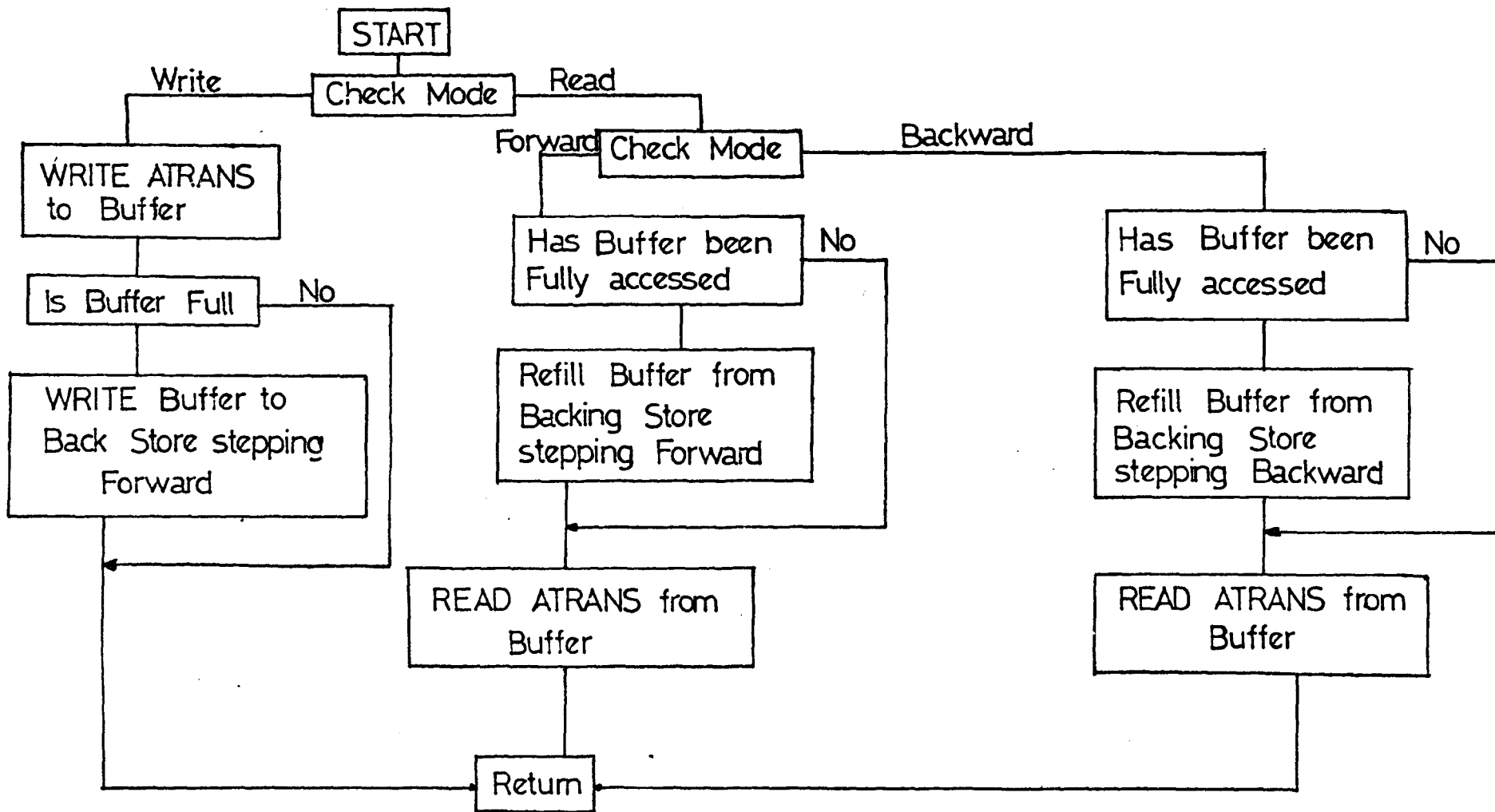
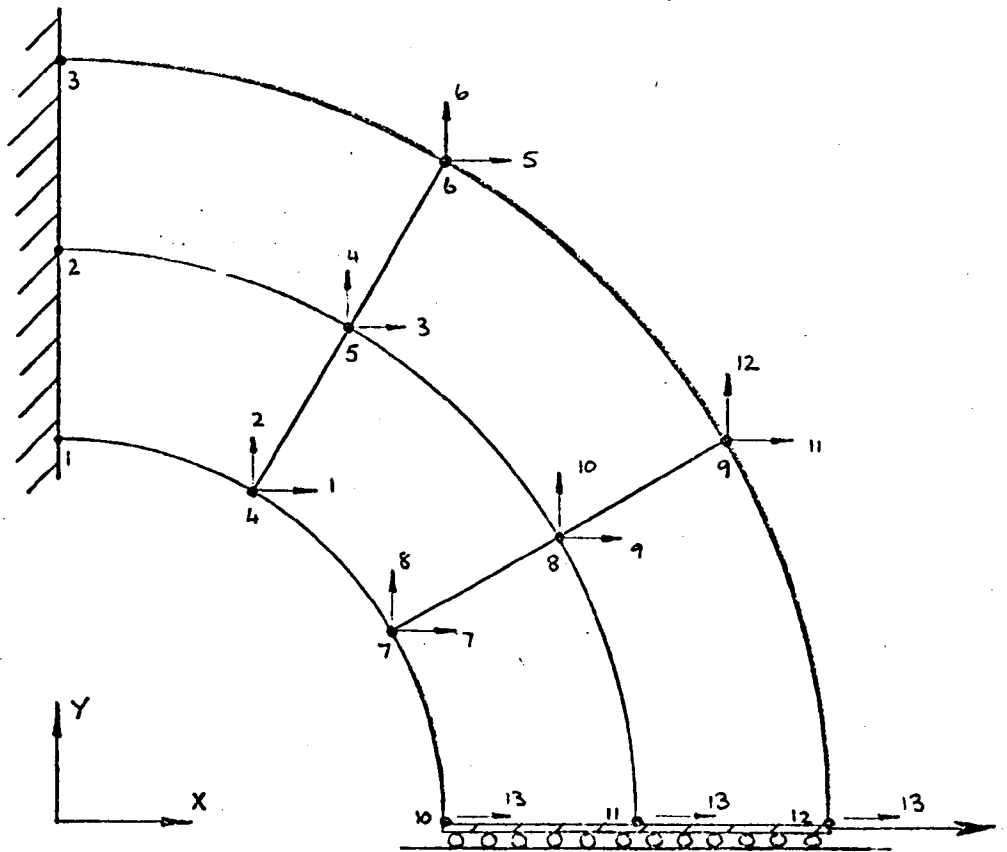


Fig. 4.4

Simple Example without Reduction Data



CPDDC ARRAY

Node	Global Co-ordinates			Degrees of Freedom	
	X	Y	Z	u	v
1	0.000	2.000	0.000	0	0
2	0.000	3.000	0.000	0	0
3	0.000	4.000	0.000	0	0
4	1.000	1.732	0.000	1	2
5	1.500	2.598	0.000	3	4
6	2.000	3.464	0.000	5	6
7	1.732	1.000	0.000	7	8
8	2.598	1.500	0.000	9	10
9	3.464	2.000	0.000	11	12
10	2.000	0.000	0.000	13	0
11	3.000	0.000	0.000	13	0
12	4.000	0.000	0.000	13	0

Stiffness matrix before solution by matrix inversion

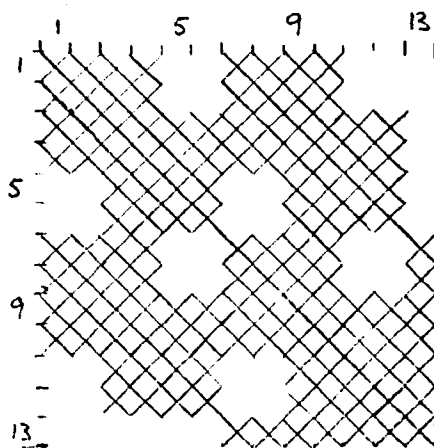
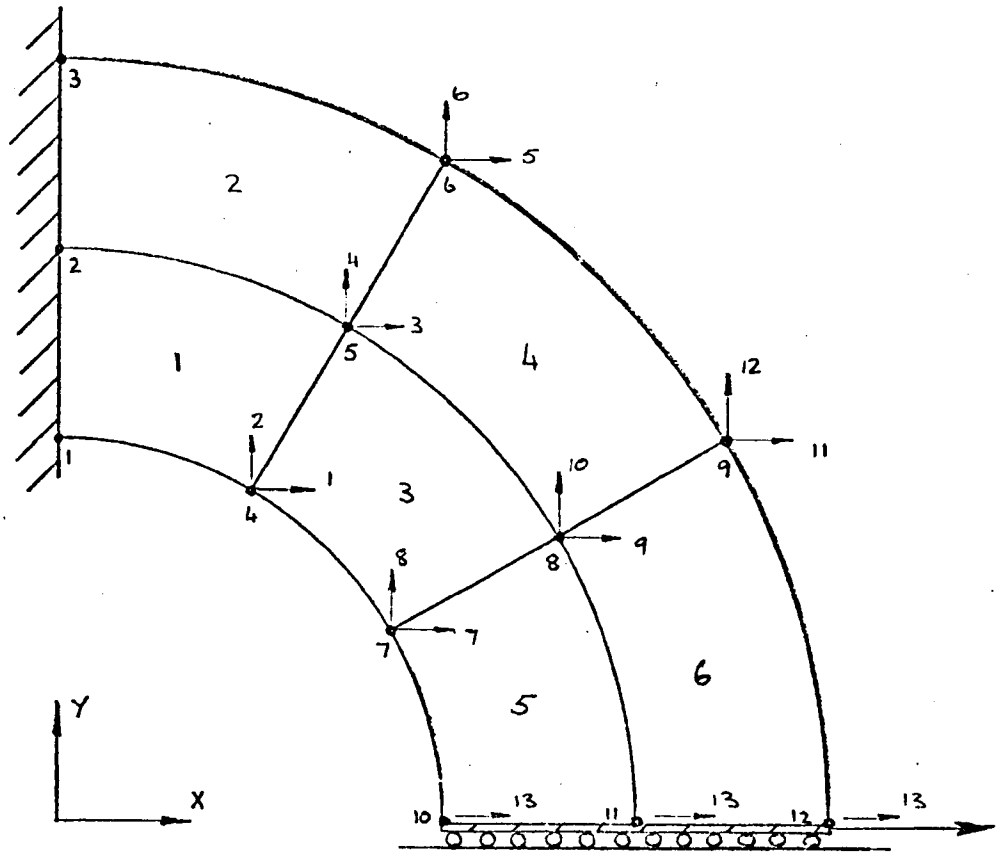


Fig.4.5(a)

Simple Example with Data for Frontal Solution



CPDDC ARRAY

Node	Global Co-ordinates			Degrees of Freedom	
	X	Y	Z	u	v
1	0.000	2.000	0.000	0.000	0.000
2	0.000	3.000	0.000	0.000	0.000
3	0.000	4.000	0.000	0.000	0.000
4	1.000	1.732	0.000	1.020	2.020
5	1.500	2.598	0.000	3.040	4.040
6	2.000	3.464	0.000	5.020	6.020
7	1.732	1.000	0.000	7.020	8.020
8	2.598	1.500	0.000	9.040	10.040
9	3.464	2.000	0.000	11.020	12.020
10	2.000	0.000	0.000	13.020	0.000
11	3.000	0.000	0.000	13.030	0.000
12	4.000	0.000	0.000	13.010	0.000

ELEMENT TOPOLOGY

1	4	2	5
2	5	3	6
4	7	5	8
5	8	6	9
7	10	8	11
8	11	9	12

Fig.4.5(b)

Activity and Reduction of equations for Frontal Solution
applied to the Simple Example of Fig. 4.5 (b).

Positions of Degrees of Freedom in Stiffness Matrices

A →											
1	2	3	4								Activity Vector for Element 1
											No degrees of freedom reduced out
1	2	3	4	5	6						Activity Vector for Element 2
											No degrees of freedom reduced out
1	2	3	4	5	6	7	8	9	10		Activity Vector for Element 3
1	2										Redundant degrees of freedom reduced out
11	12	3	4	5	6	7	8	9	10		Activity Vector for Element 4
		3	4	5	6						Redundant degrees of freedom reduced out
11	12	13				7	8	9	10		Activity Vector for Element 5
						7	8				Redundant degrees of freedom reduced out
11	12	13						9	10		Activity Vector for Element 6
11	12	13						9	10		Redundant degrees of freedom reduced out

← Maximum instantaneous size = 10

Transfer vector ATRANS

At point 'A' ATRANS contains

0	1	2	3	4	0	0	0	0	0	0	0	0
---	---	---	---	---	---	---	---	---	---	---	---	---

indicating newly active degrees of freedom.

When a degree of freedom is being reduced out ATRANS contains

i	$\frac{K_{i1}}{K_{ii}}$	$\frac{K_{i2}}{K_{ii}}$...	$\frac{K_{i(i-1)}}{K_{ii}}$	$\frac{K_{i(i+1)}}{K_{ii}}$...	$\frac{K_{iid}}{K_{ii}}$	$\frac{F_i}{K_{ii}}$...	$\frac{F_{iilo}}{K_{ii}}$	K_{ii}

where i gives the position of the degree of freedom being reduced out,

idf the degree of freedom, id the maximum instantaneous size,

ilo the number of loading conditions,

K_{ij} gives the stiffness term in row i, column j,

and F_{ij} gives the loading term in row i, column j.

Fig. 4.5 (c)

Activity and Reduction of equations for Frontal Solution
applied to the Simple Example of Fig. 4.5 (b).

Modified Element Ordering.

The Elements are called in the new order

1 - 3 - 5 - 2 - 4 - 6

by modifying the element topology.

ELEMENT TOPOLOGY

```

1.  4  2  5
4.  7  5  8
7 10  8 11
2  5  3  6
5  8  6  9
8 11  9 12
    
```

Positions of Degrees of Freedom in Stiffness Matrices

1 2 3 4	Activity Vector for Element 1
	No degrees of freedom reduced out
1 2 3 4 7 8 9 10	Activity Vector for Element 3
1 2	Redundant degrees of freedom reduced out
13 3 4 7 8 9 10	Activity Vector for Element 5
7 8	Redundant degrees of freedom reduced out
13 5 3 4 6 9 10	Activity Vector for Element 2
	No degrees of freedom reduced out
13 5 3 4 6 11 9 10 12	Activity Vector for Element 4
5 3 4 6	Redundant degrees of freedom reduced out
13 11 9 10 12	Activity Vector for Element 6
13 11 9 10 12	Redundant degrees of freedom reduced out

← Maximum instantaneous size = 9

Fig. 4.5 (d)

Accumulation of Creep Strain

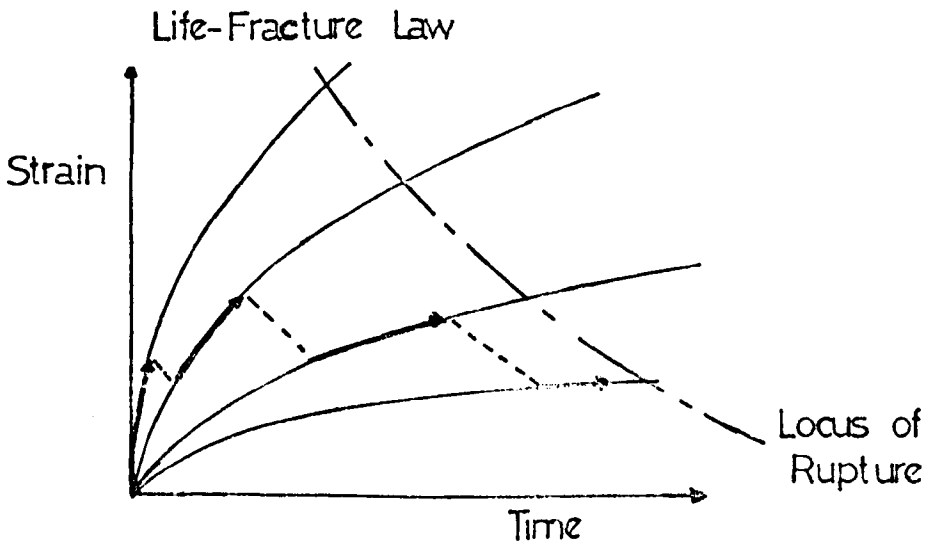
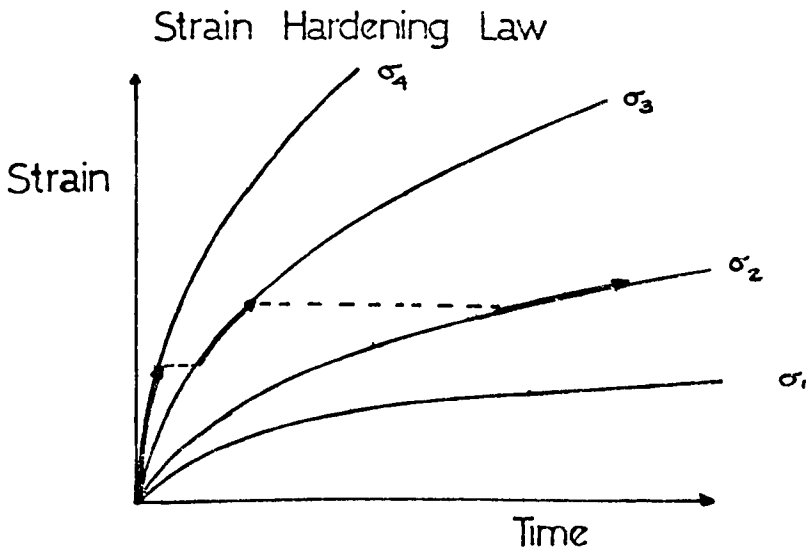
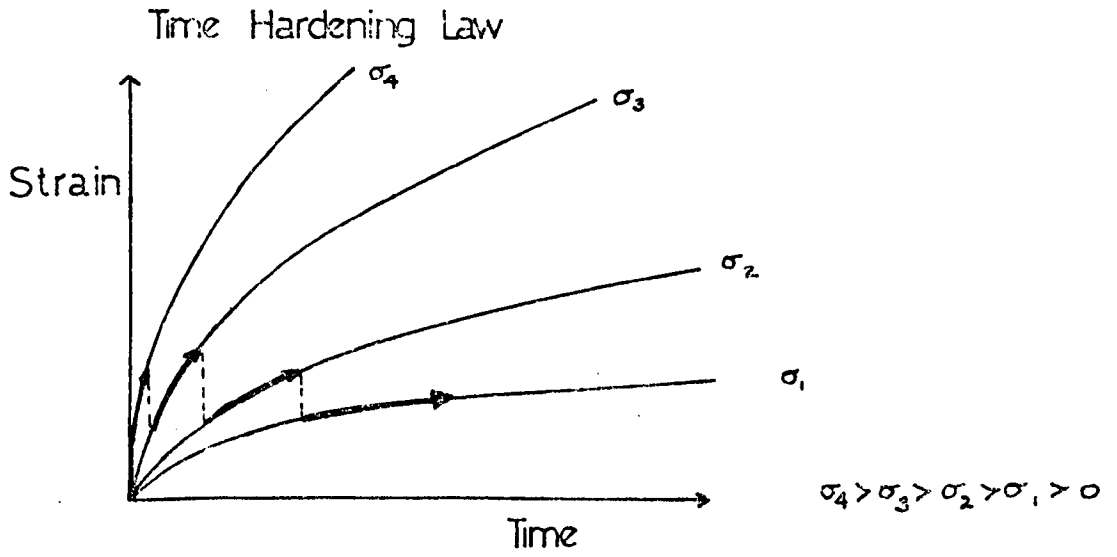
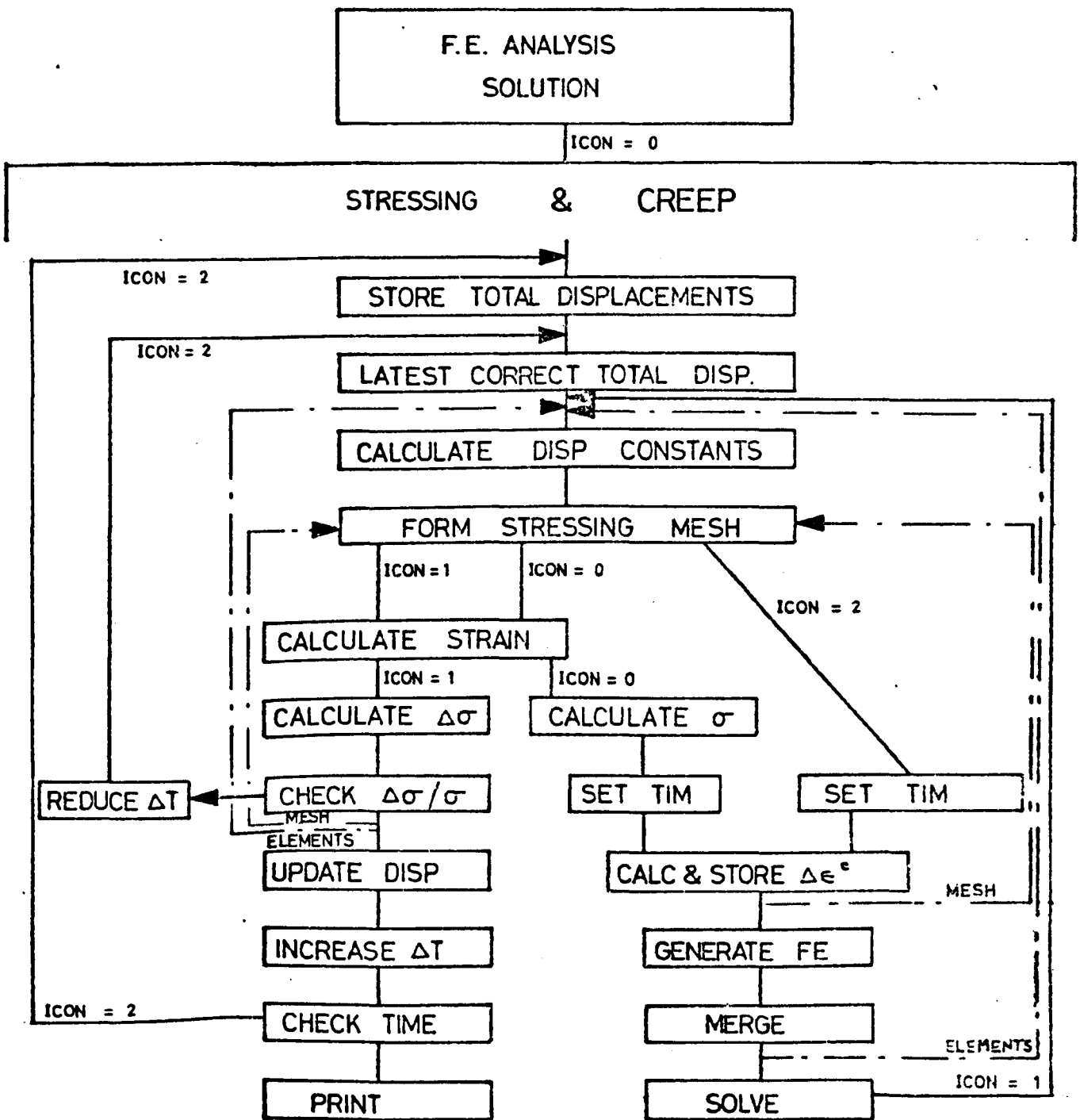


Fig. 51

CREEP LOGIC FLOW DIAGRAM.



ICON = 0 : Initial Solⁿ
 ICON = 1 : Incremental Check
 ICON = 2 : Incremental Solⁿ

Fig.5.2

CREEP LOGIC FLOW DIAGRAM

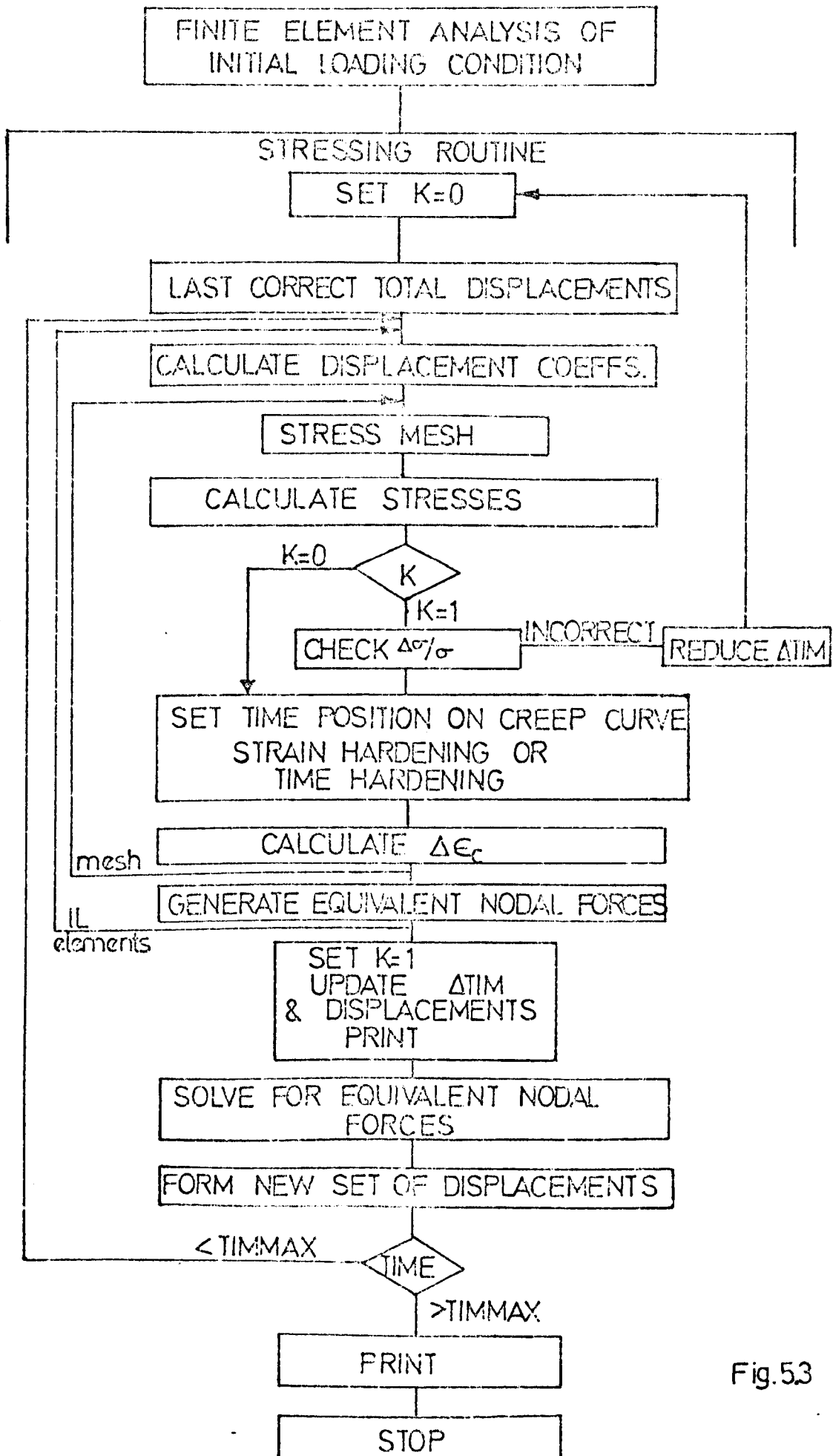


Fig.53

CREEP LOGIC FLOW DIAGRAM

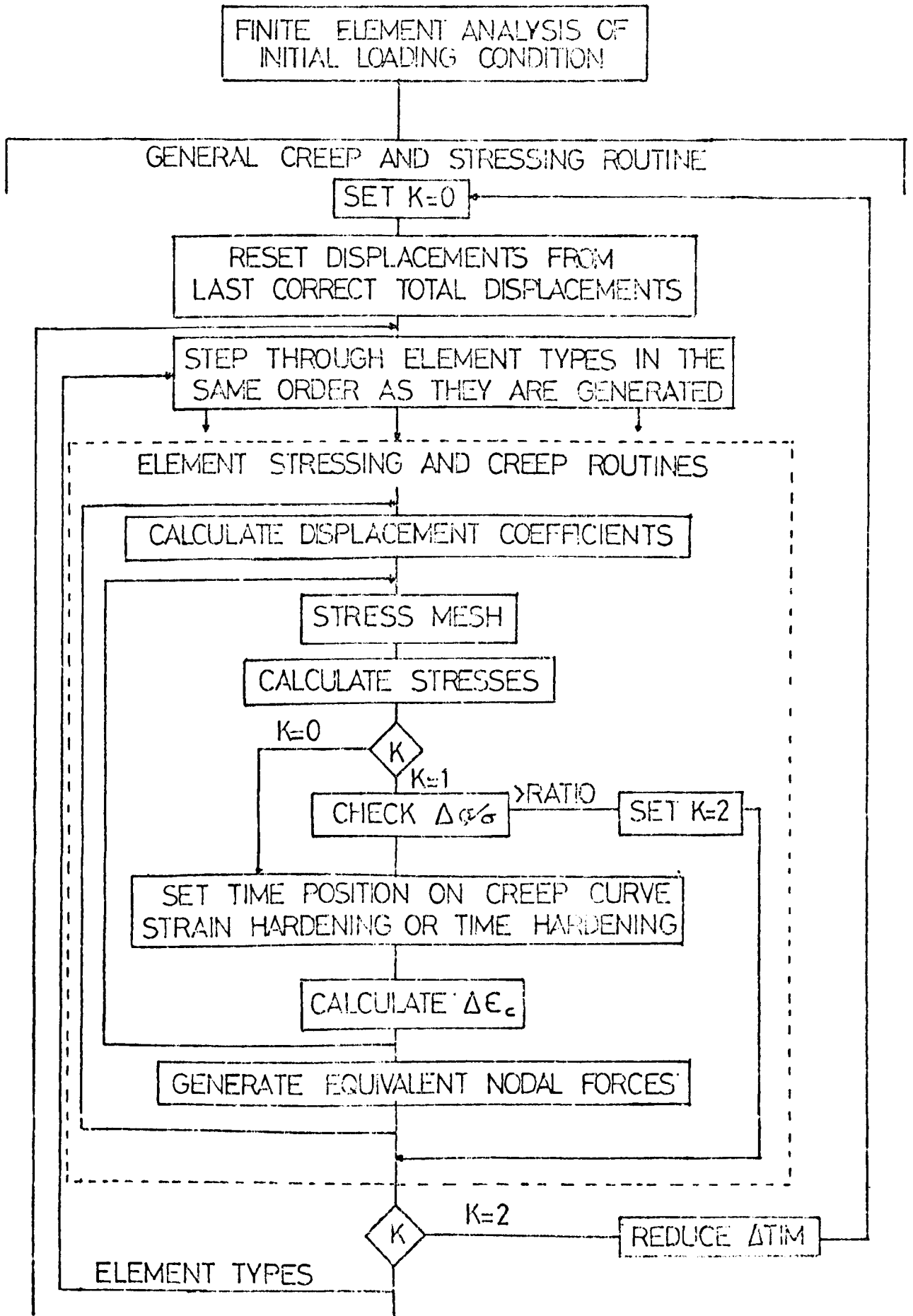


Fig.54

CREEP LOGIC FLOW DIAGRAM(CONTINUED)

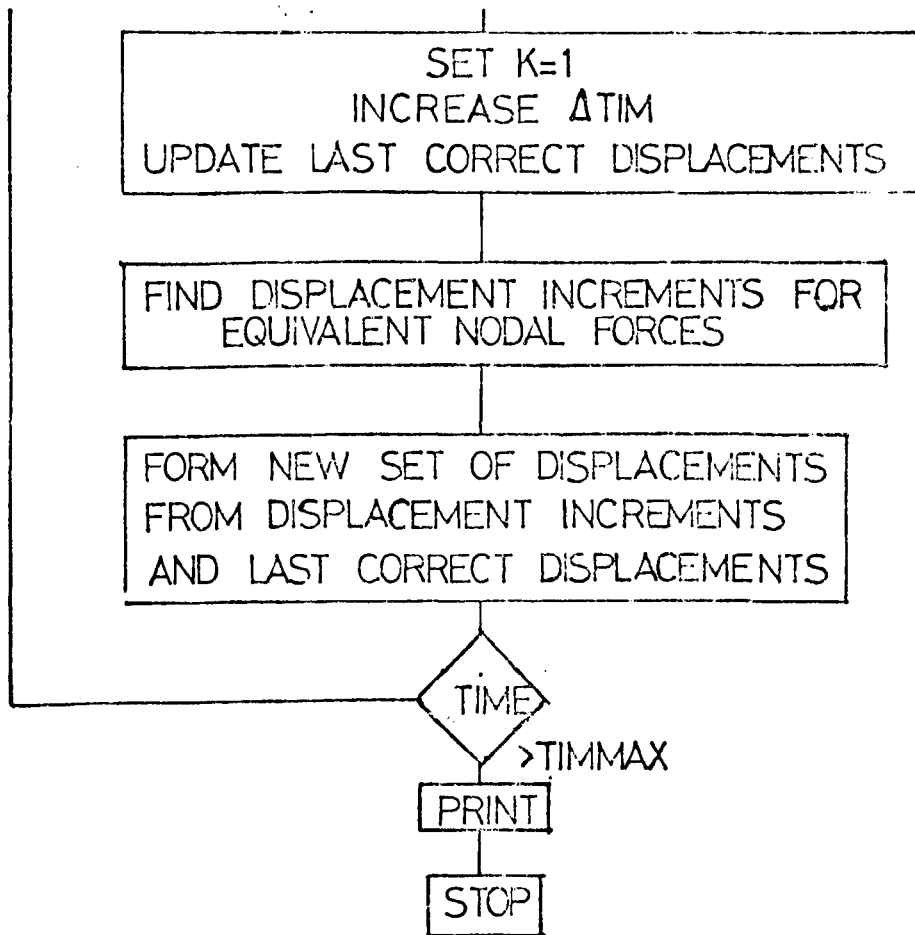
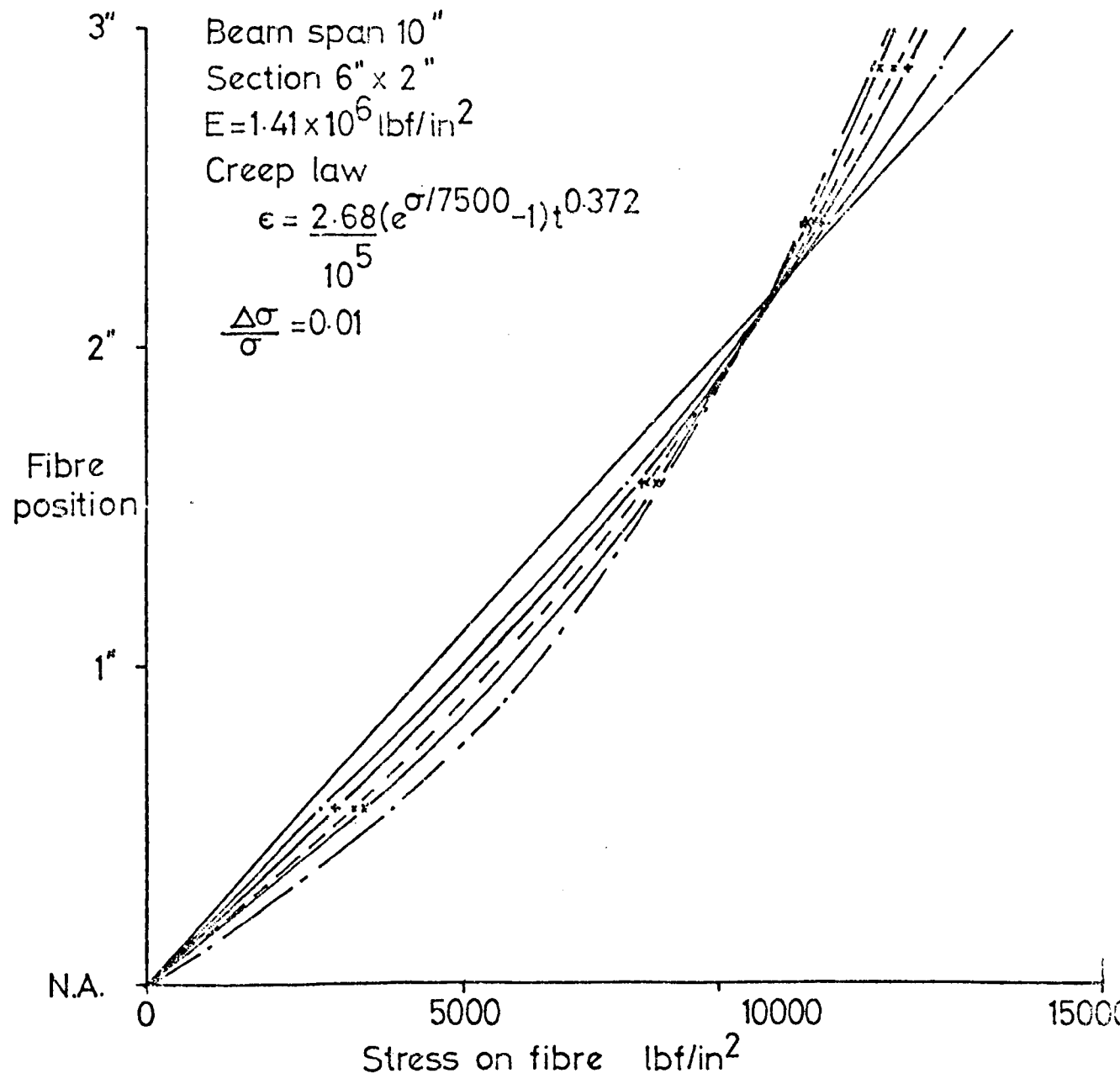


Fig. 54(cont)

Stress Distribution in a Beam Subjected to a Constant Bending Moment

Stresses above Neutral Axis



- 0 hrs. solution
- · - · - 10 hrs. Time Hardening solution
- +—— 100 hrs. " " "
- *—— 1000 hrs. " " "
- x--- 1000 hrs Strain " "
- · - · - Steady State solution

Fig 5.5(a)

Creep Deflection of a Simply Supported Beam
Subjected to a Constant Bending Moment

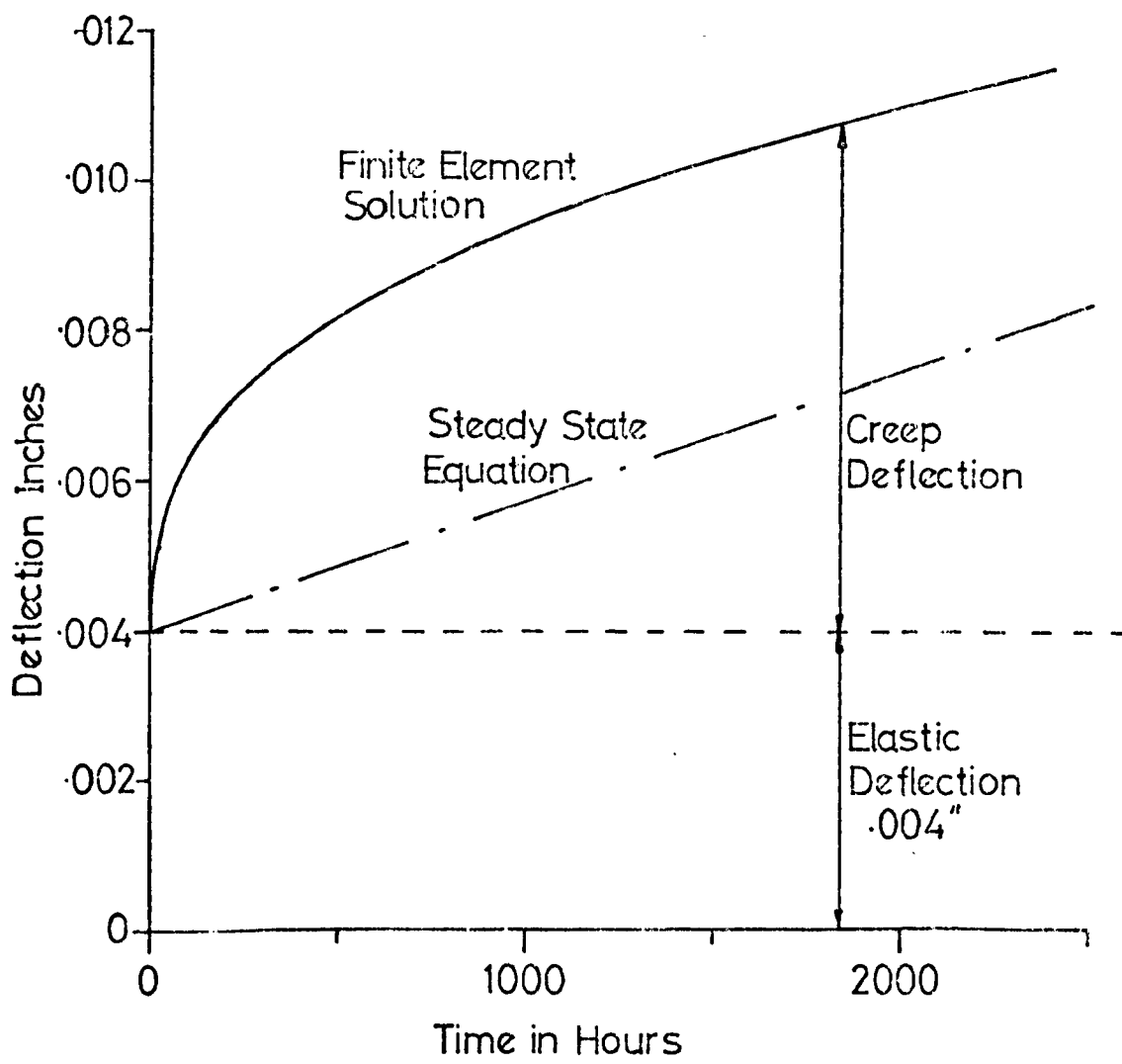


Fig. 5.5(b)

Outside Diameter Hoop Strains
in Thick Rings

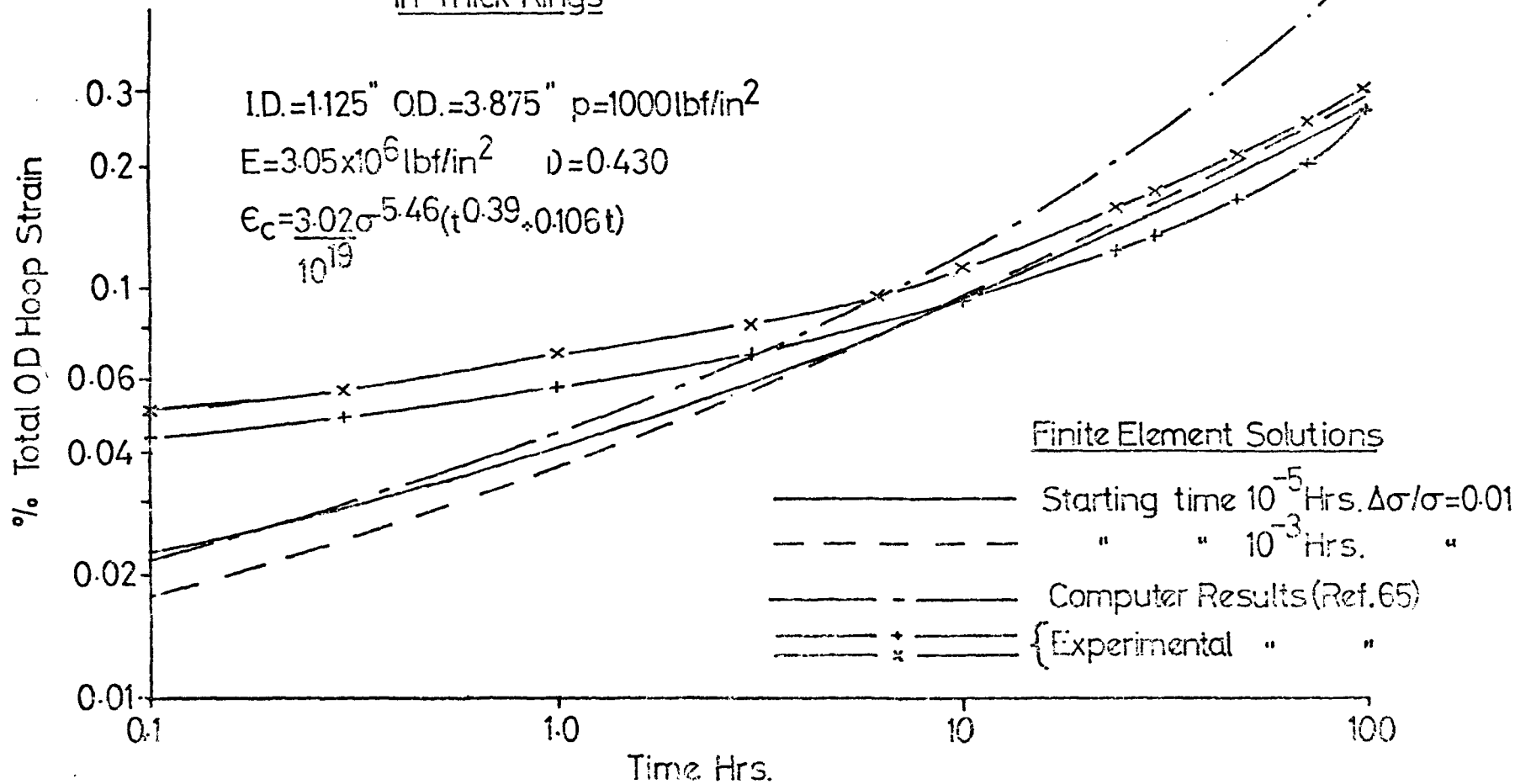
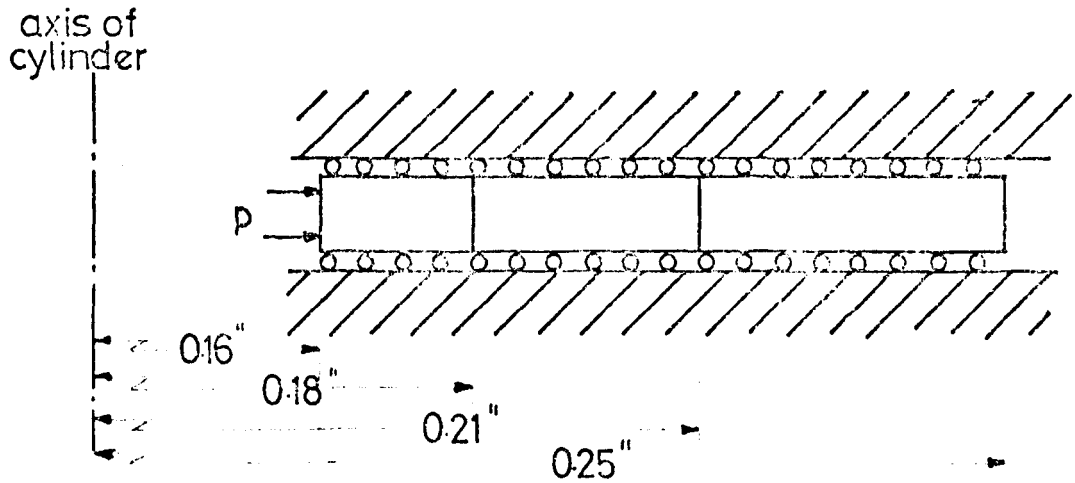


Fig.5.6

Thick Pressurised Cylinder

Idealisation



3 x 20 noded solid Isoparametric elements over 90° arc

Internal Pressure $p = 365 \text{ lbf/in}^2$

Young's Modulus $2 \times 10^7 \text{ lbf/in}^2$

Poisson's Ratio 0.450

$\epsilon_c = 6.4 \times 10^{-18} \sigma^{4.4} t$

Radial Deformation

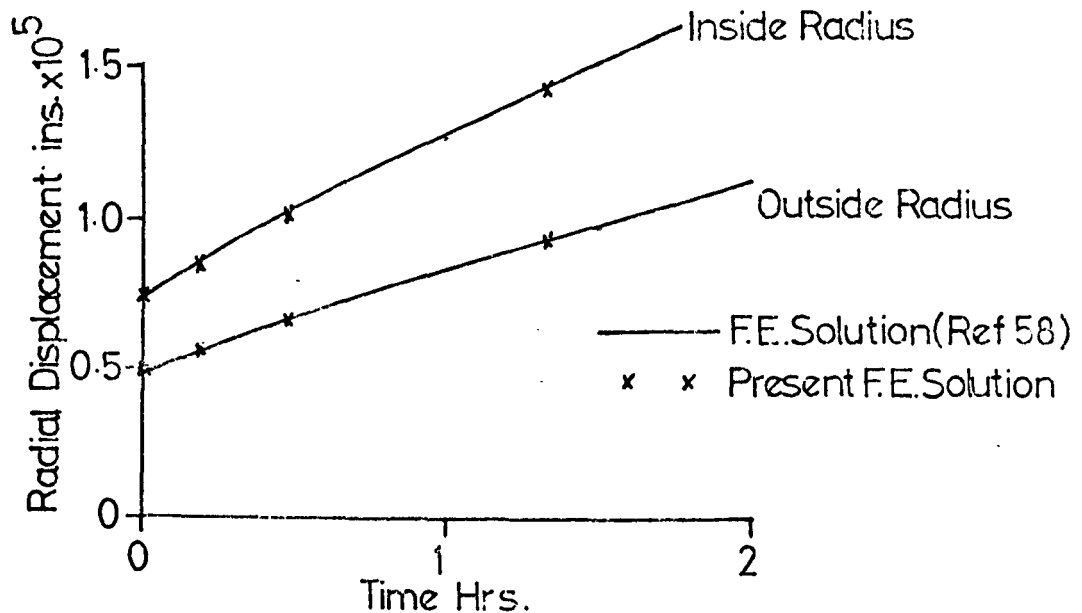
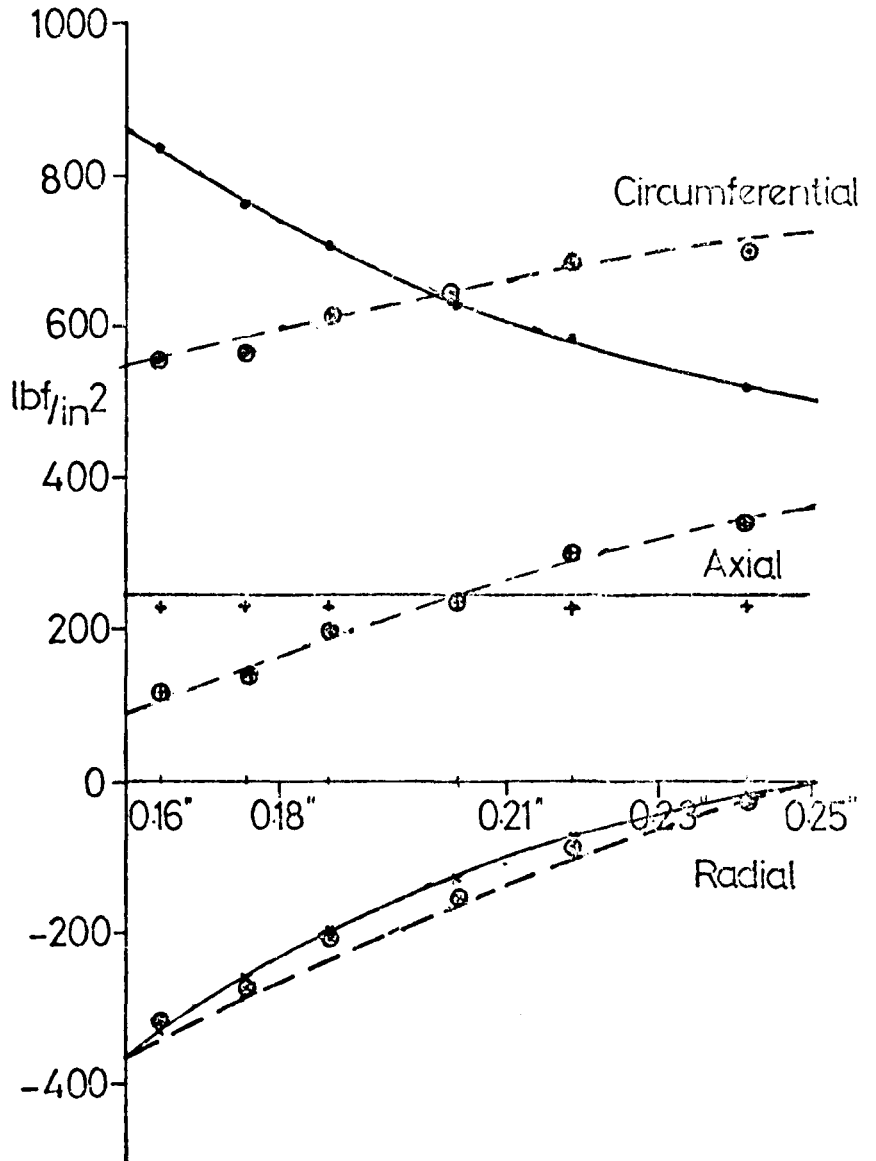


Fig 5.7(a)

Stress Distribution for a Thick Cylinder

Elastic and Steady State

Solutions



— Exact Elastic Lamé Solution

- - - Steady State Solution (ref.58)

Finite Element Solution

• • • • Circumferential Stress (Elastic)

⊙ ⊙ ⊙ ⊙ " " (Time=10Hrs)

* * * * Radial Stress (Elastic)

⊕ ⊕ ⊕ ⊕ " " (Time=10Hrs)

+ + + + Axial Stress (Elastic)

⊕ ⊕ ⊕ ⊕ " " (Time=10Hrs)

Fig 57(b)

TWO-DIMENSIONAL IDEALISATION OF TURBINE CASING
72 x 8 NODE ISOPARAMETRIC QUADRILATERAL ELEMENTS

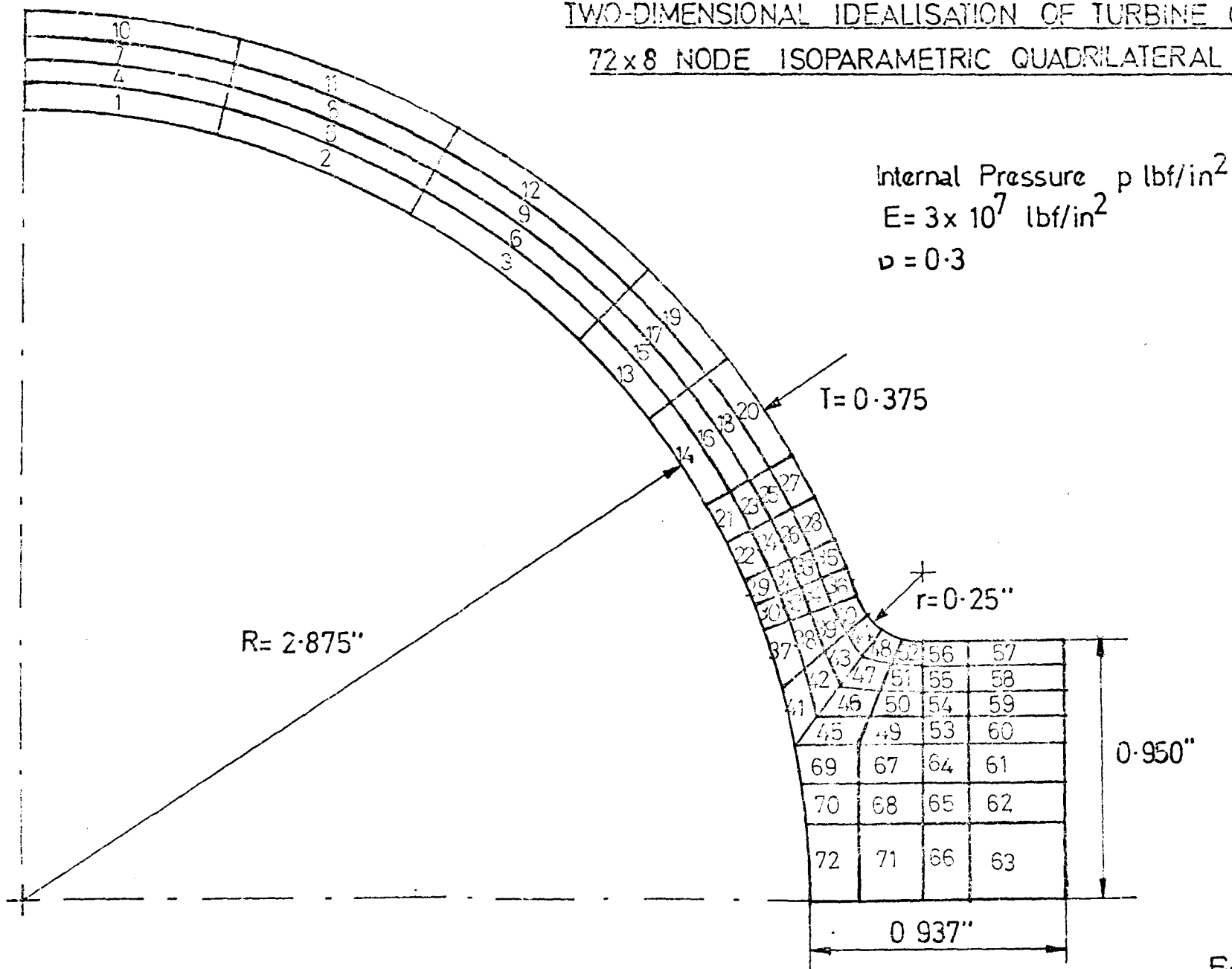


Fig.6.1(a)

HOOP STRESSES FOR 72 ELEMENT IDEALISATION

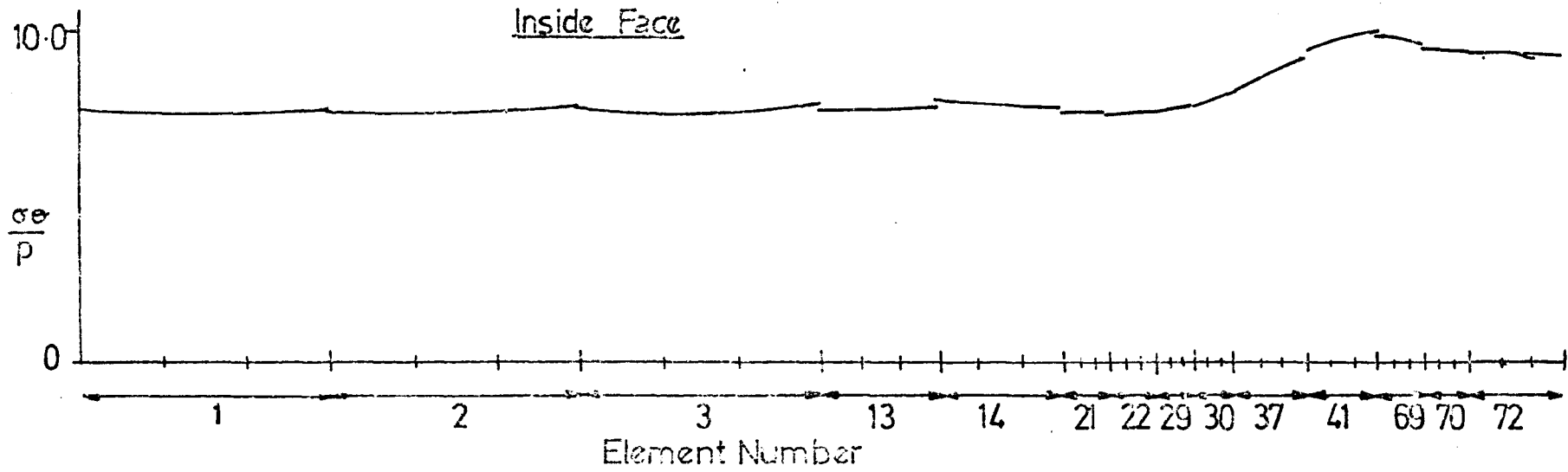
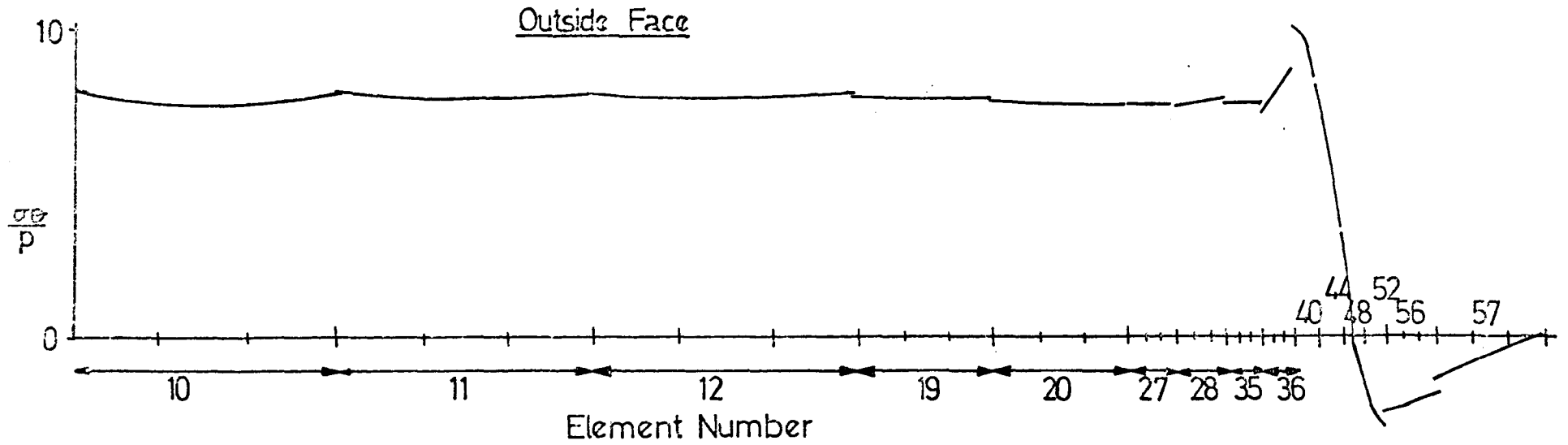


Fig.6.1(b)

TWO DIMENSIONAL IDEALISATION OF TURBINE CASING
15 x 8 NODE ISOPARAMETRIC QUADRILATERAL ELEMENTS

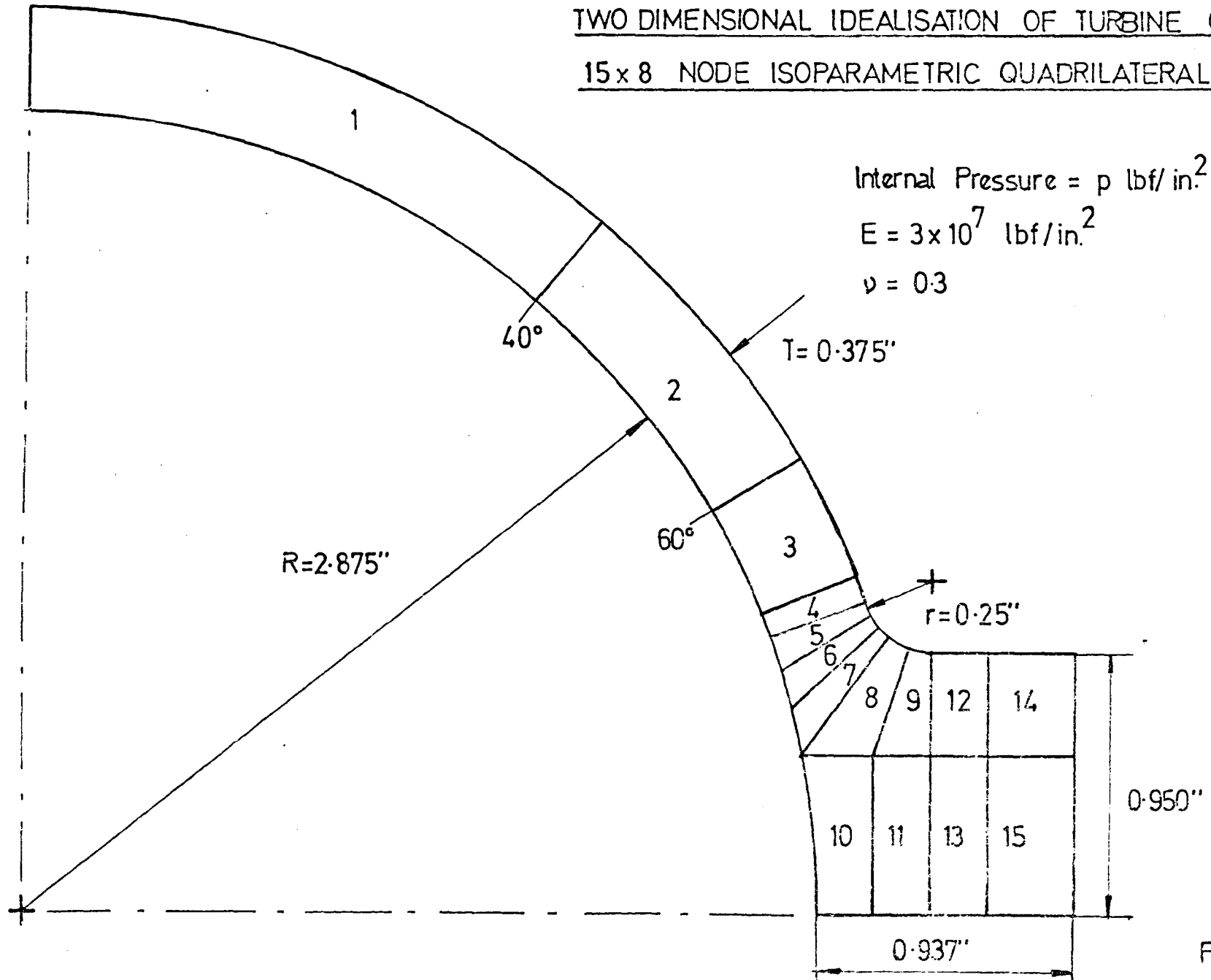


Fig. 6.2(a)

HOOP STRESS FOR 15 ELEMENT IDEALISATION

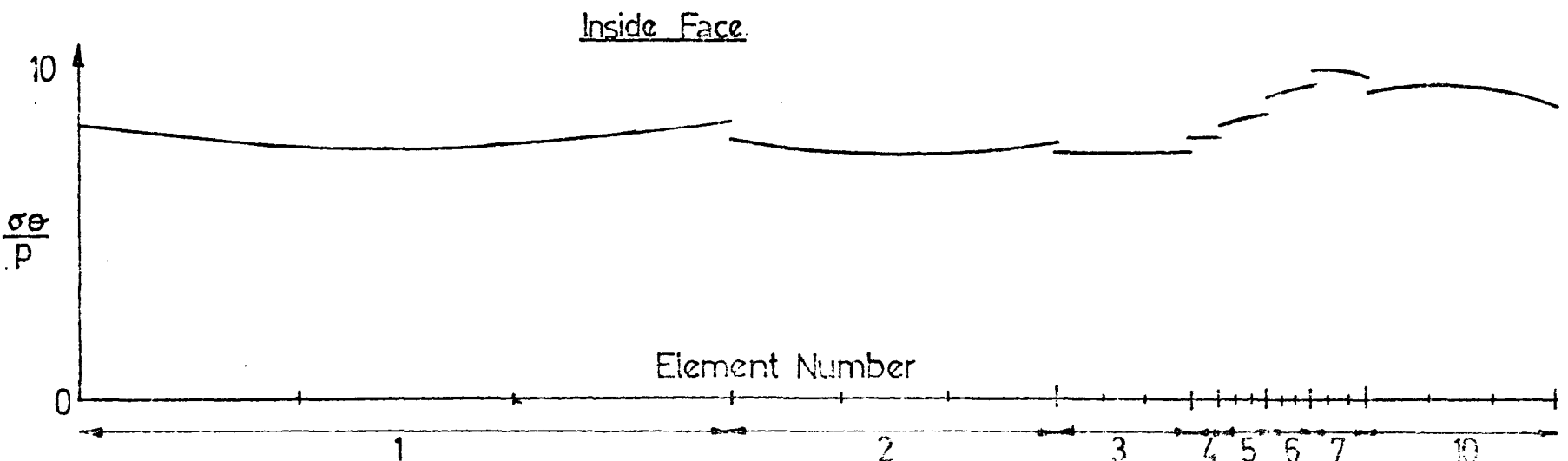
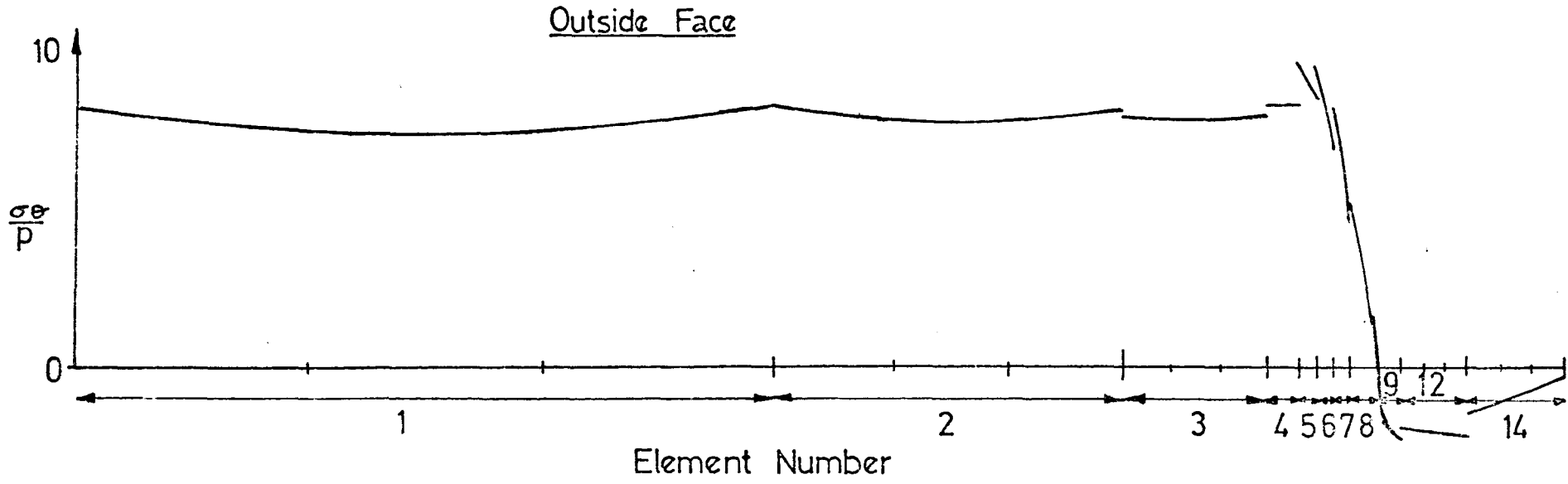


Fig 6.2(b)

TWO DIMENSIONAL IDEALISATION OF TURBINE CASING

9x8 NODE ISOPARAMETRIC QUADRILATERAL ELEMENTS

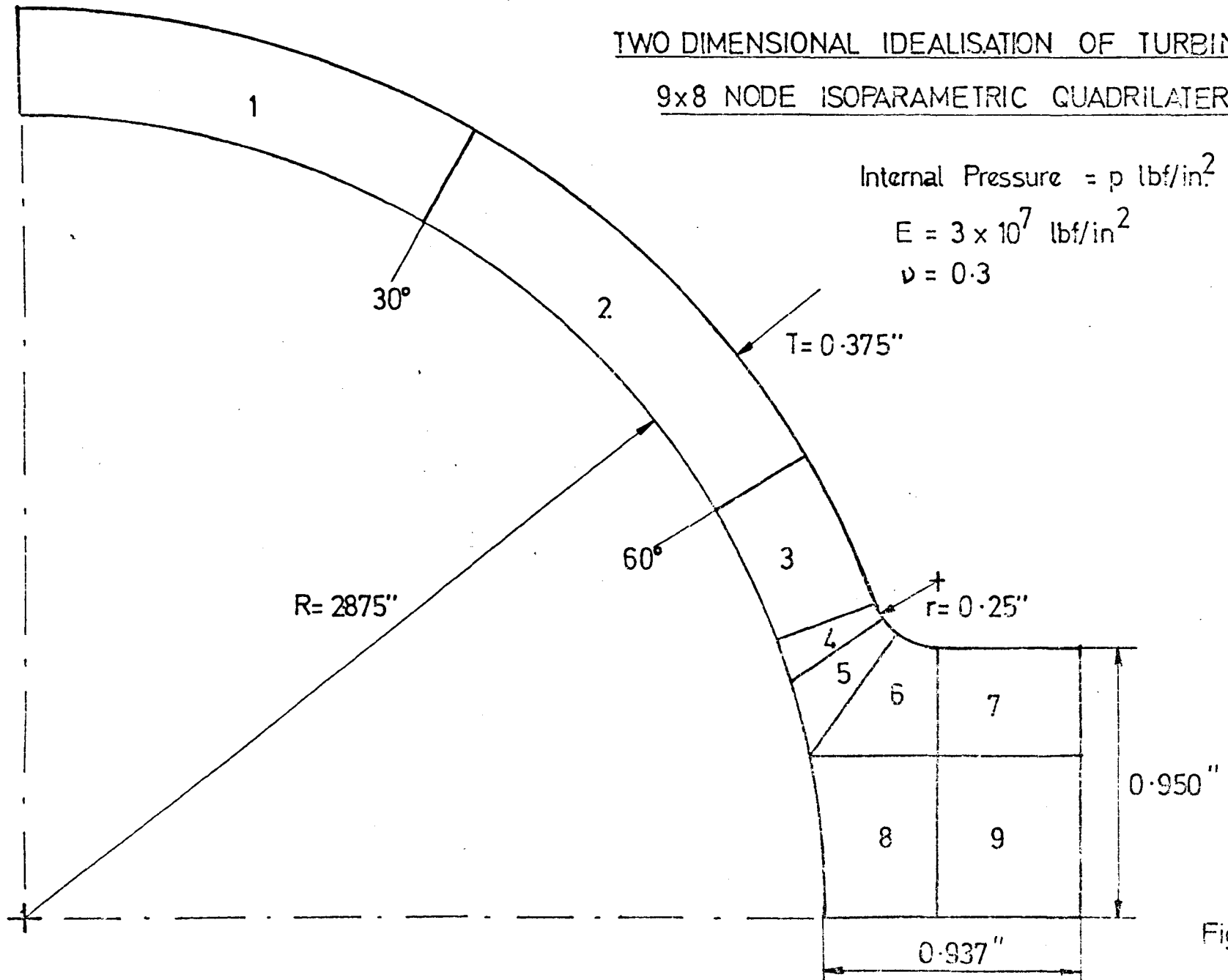


Fig.6.3(a)

HOOP STRESSES FOR 9 ELEMENT IDEALISATION

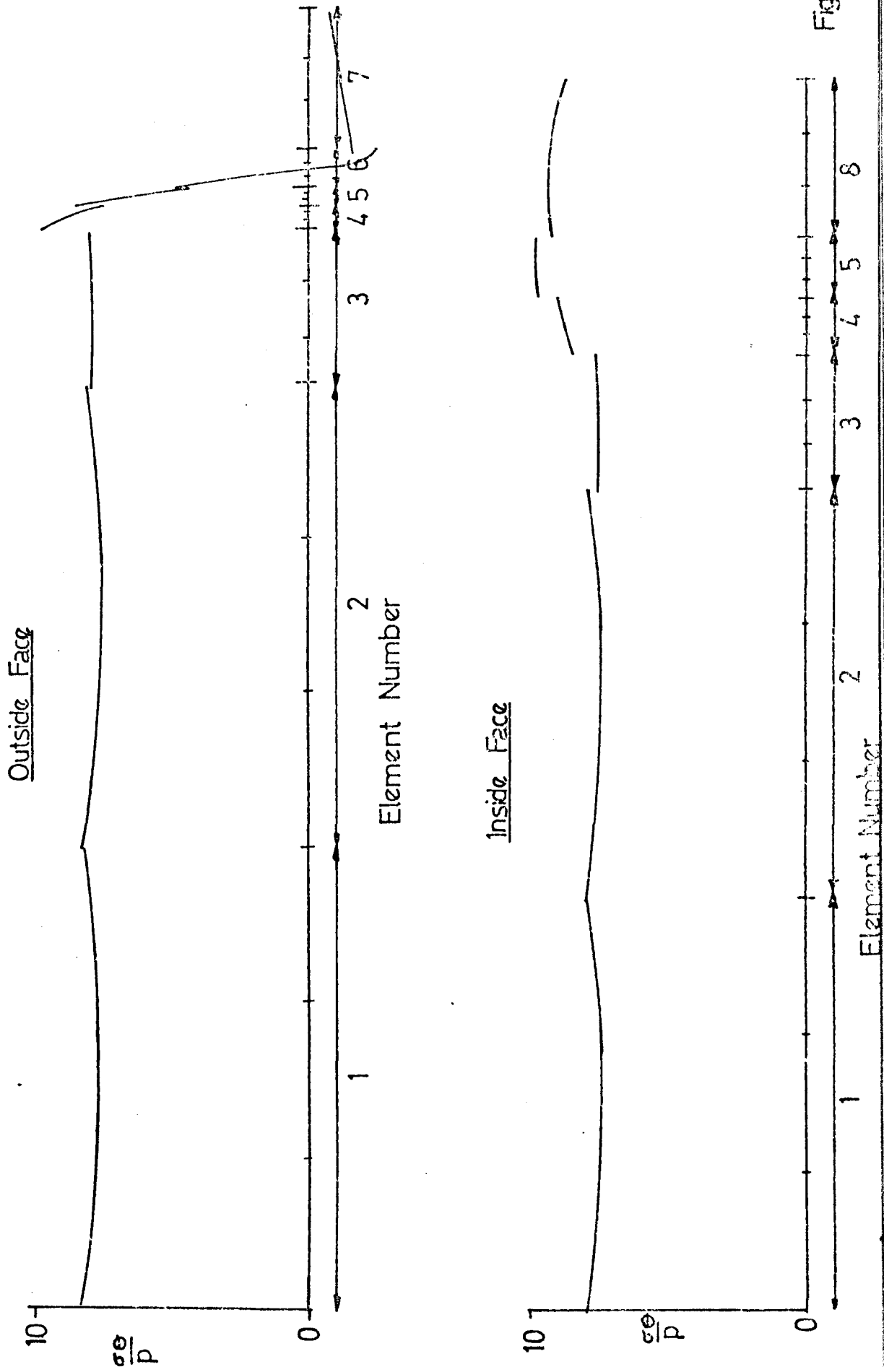
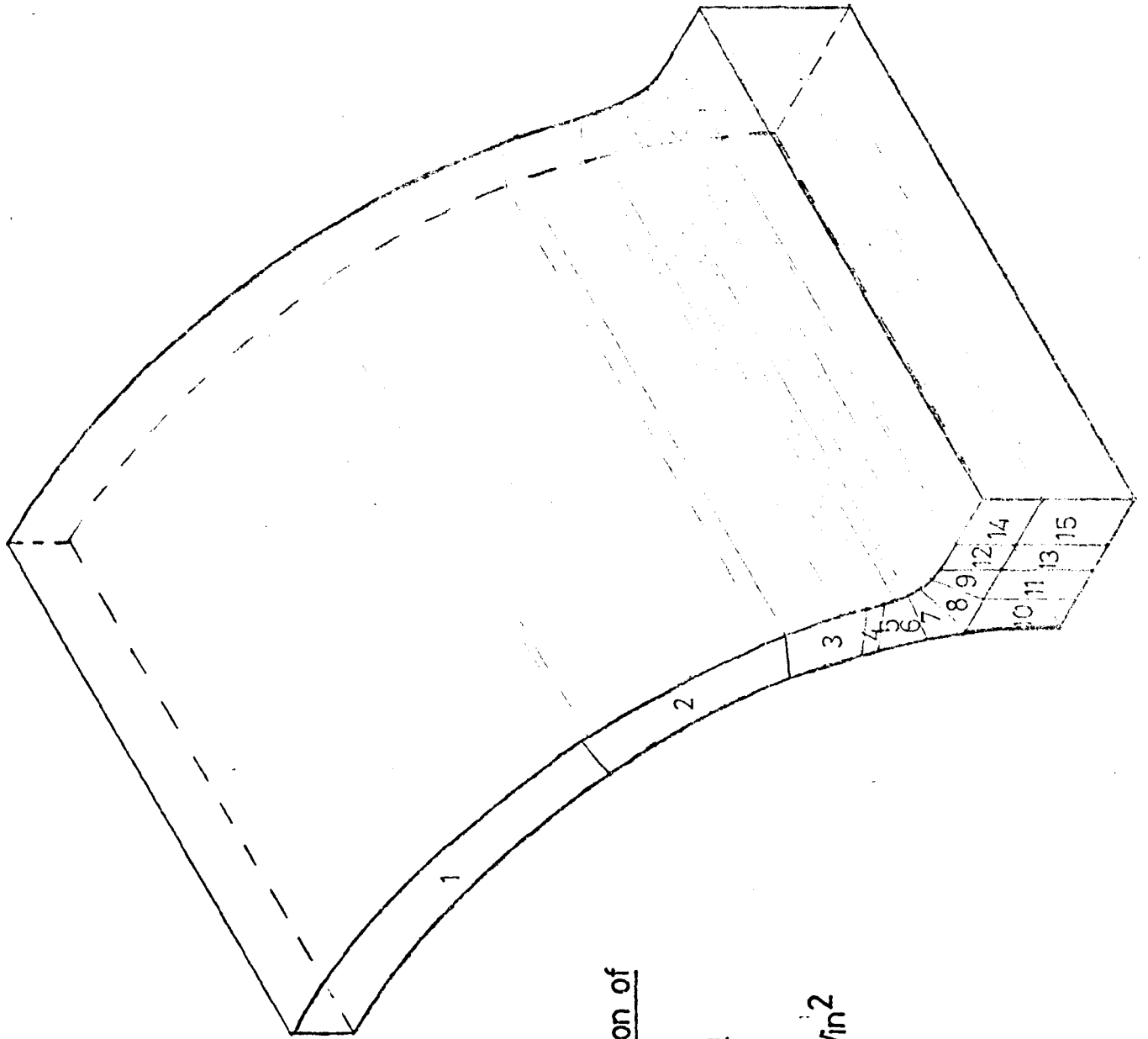


Fig. 6.3(b)



Three Dimensional Idealisation of

Turbine Casing Section

Internal Pressure p lbf/in²

$E=3 \times 10^7$ lbf/in²

$\nu=0.3$

Fig.6.4(a)

HOOP STRESSES FOR 3 DIMENSIONAL IDEALISATION

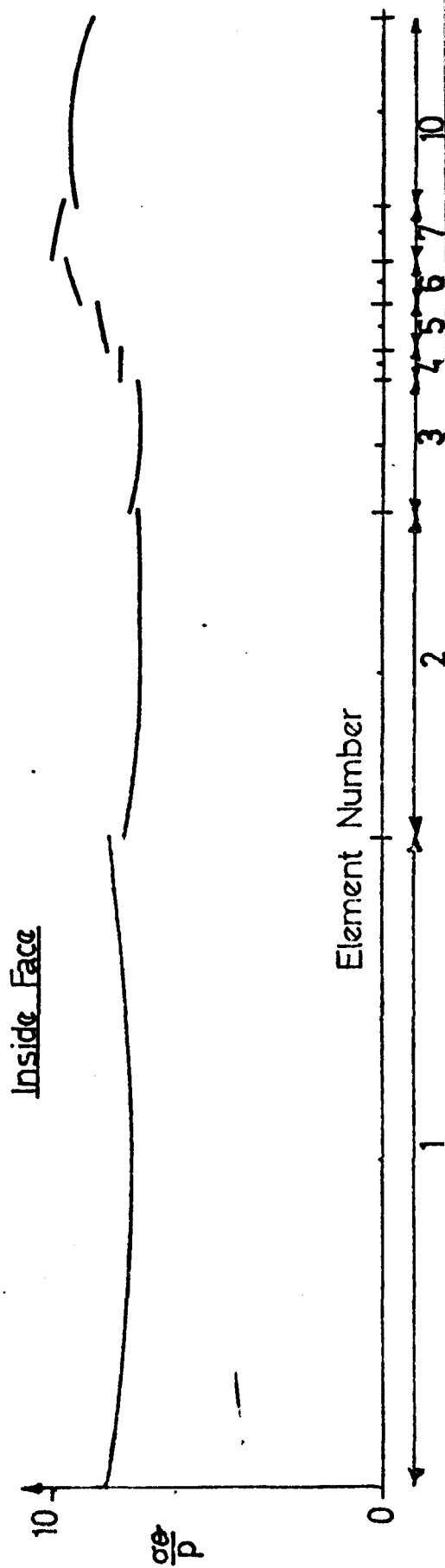
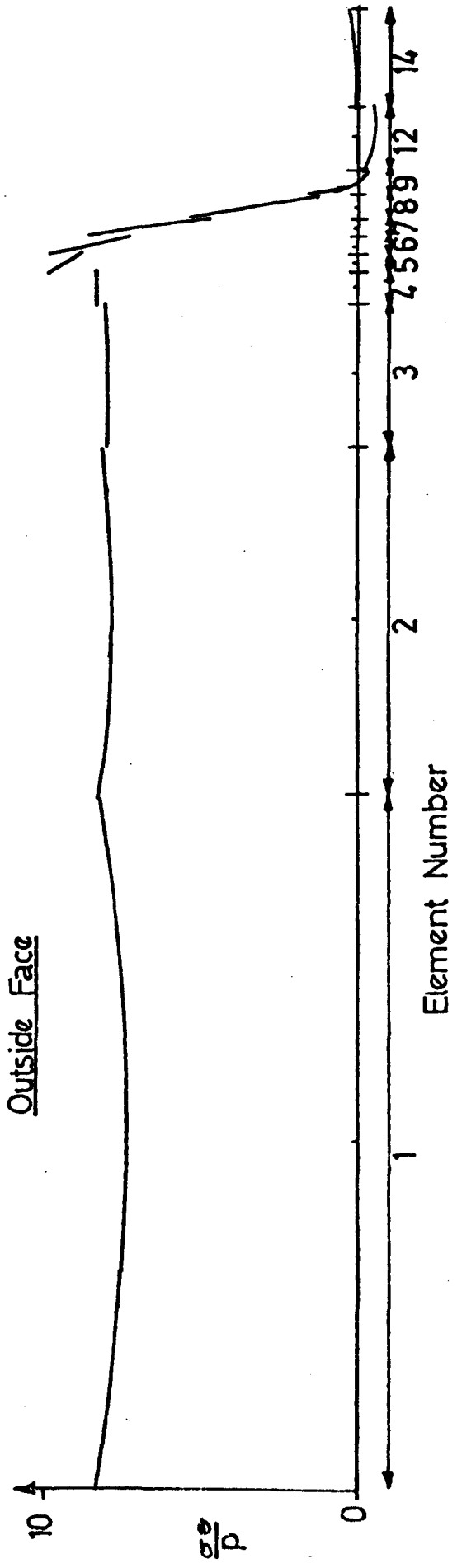


Fig.6.4(b)

Hoop Stresses for 3 Dimensional Idealisation Using Thick Shell,
Transition and Isoparametric Elements

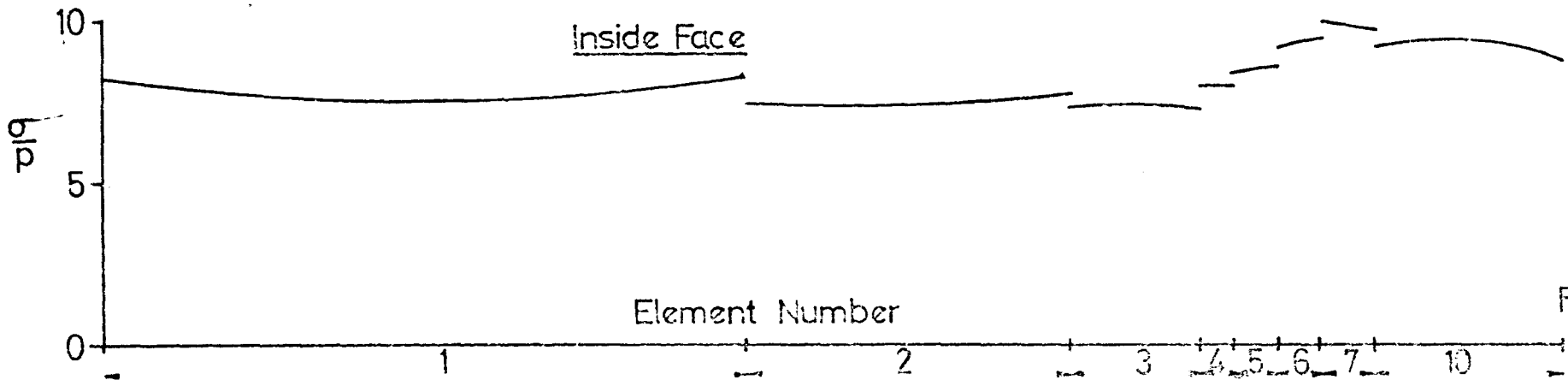
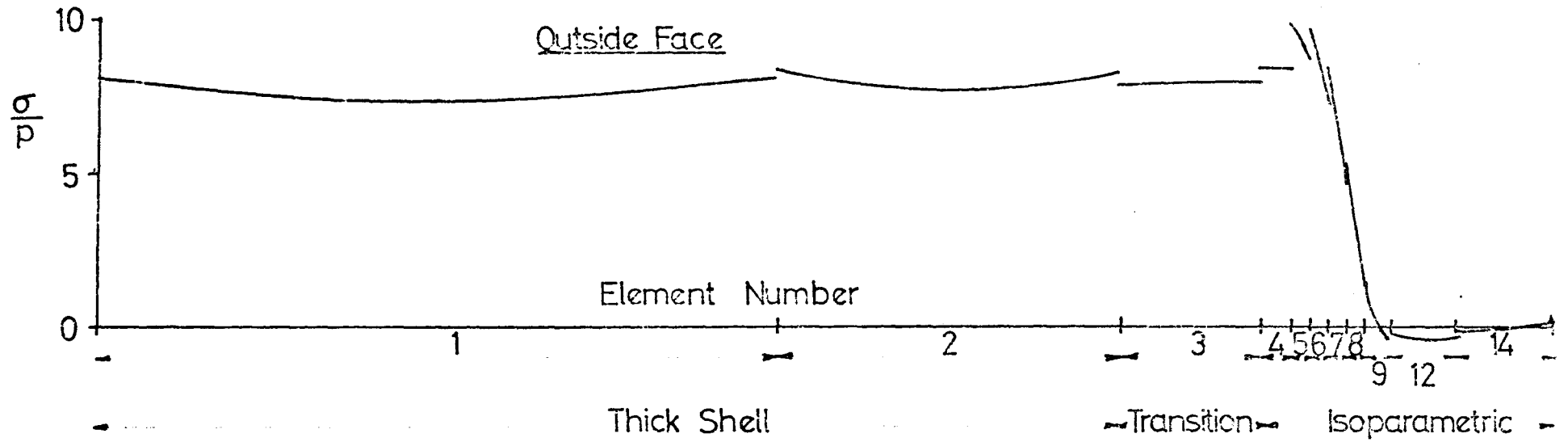


Fig.6.4(c)

Detail of Half a Bolt Pitch of the Turbine Casing
Flange showing the Bolt Hole and the
Spot Facing

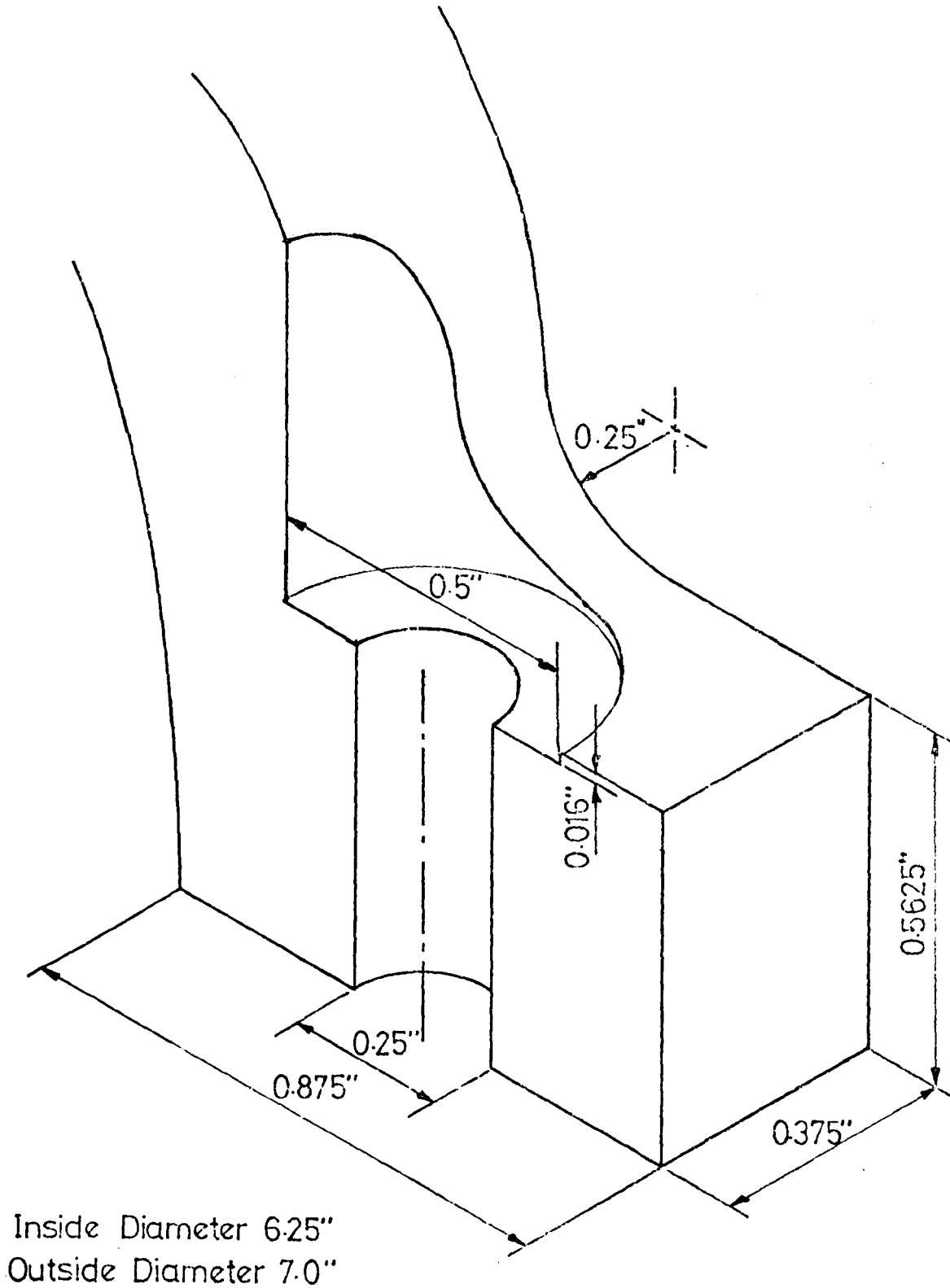
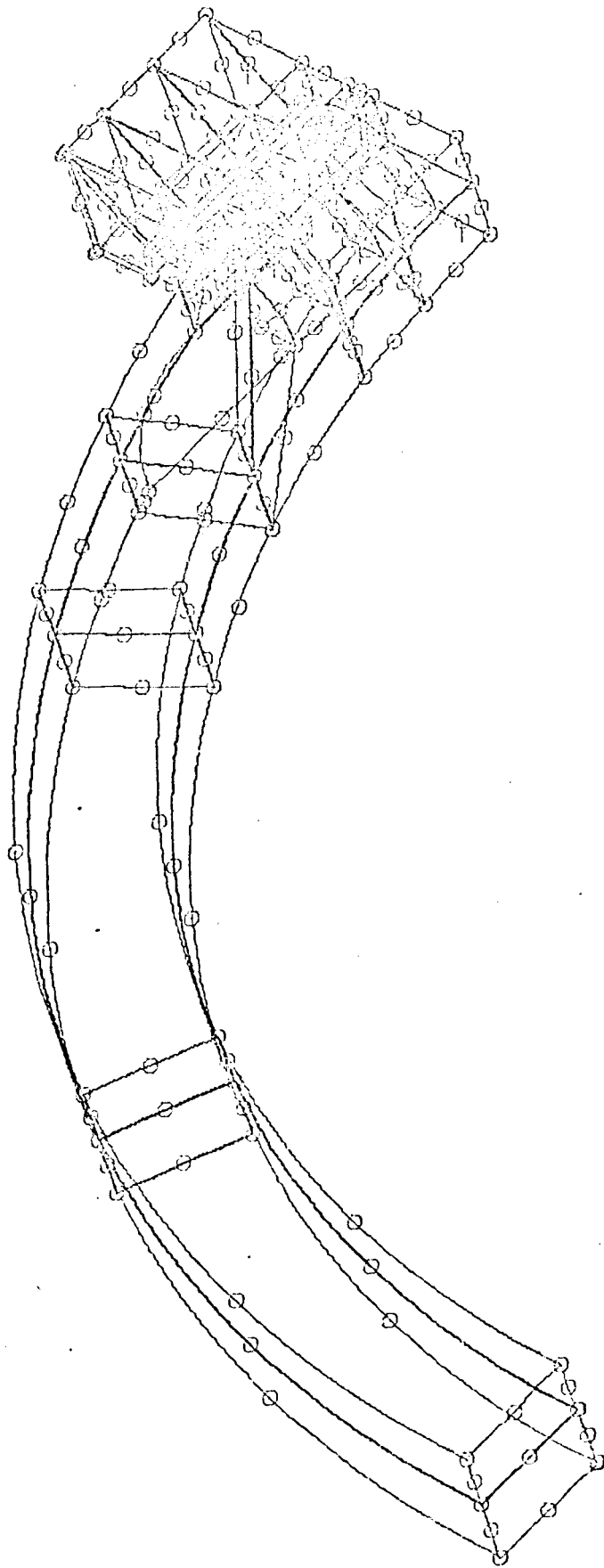


Fig 6.5



Finite Element Idealisation of a Turbine Casing Section
Half a Bolt Pitch

Finite Element Idealisation of a Turbine Casing Section
Half a Bolt Pitch

Enlarged View of the Flange
Portion of Fig. 6.6(a)

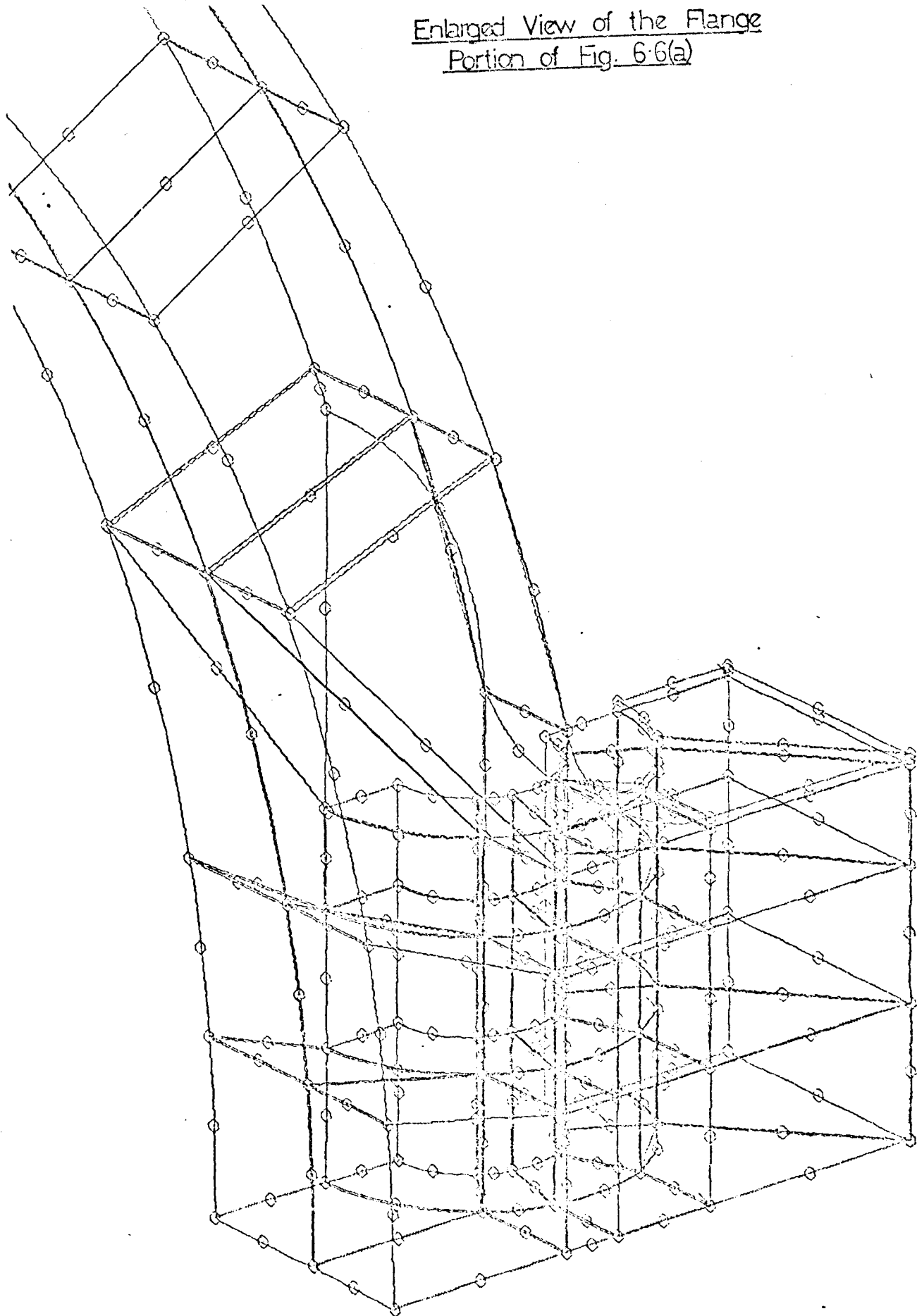


Fig. 66(b)

Flange Contact Stresses for a Constant Pressure Loading over the Spot Facing.

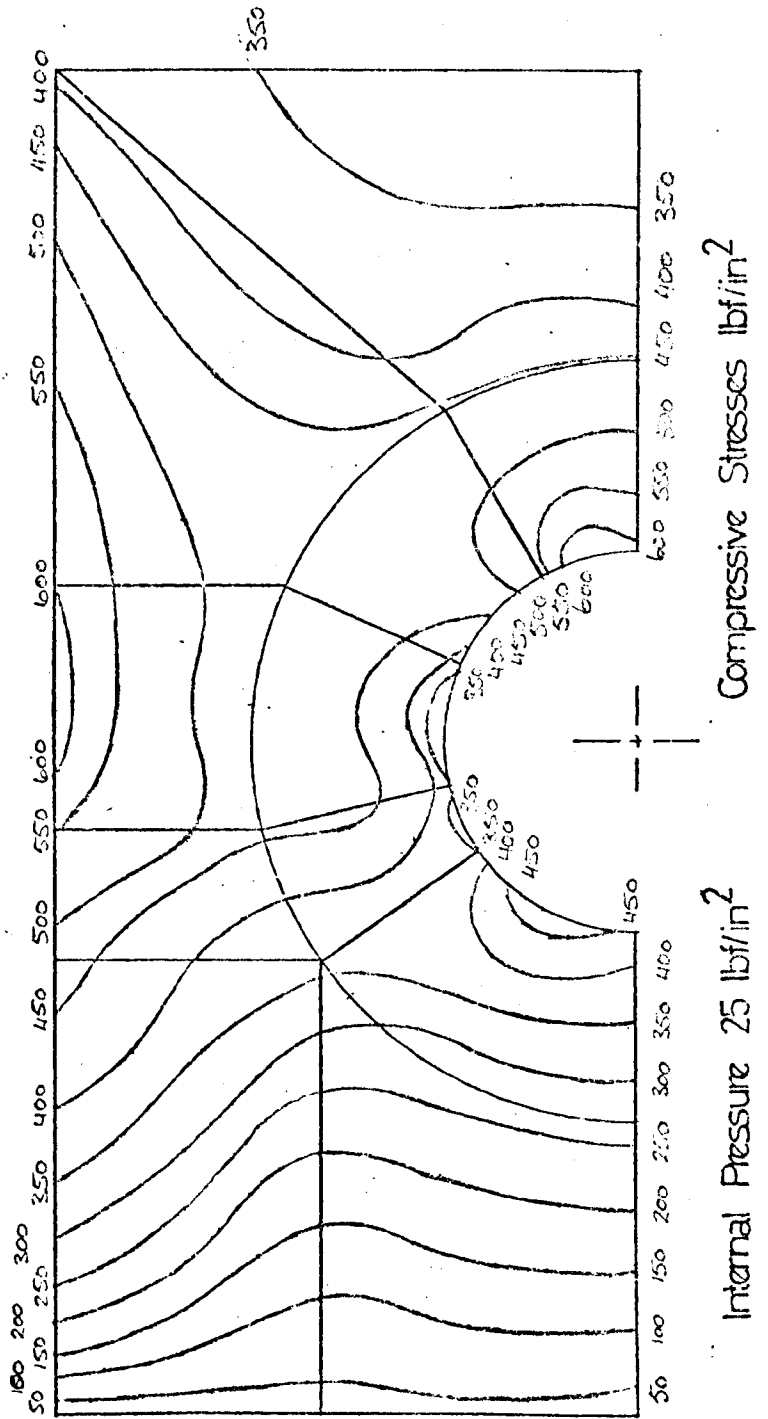


Fig. 67(a)

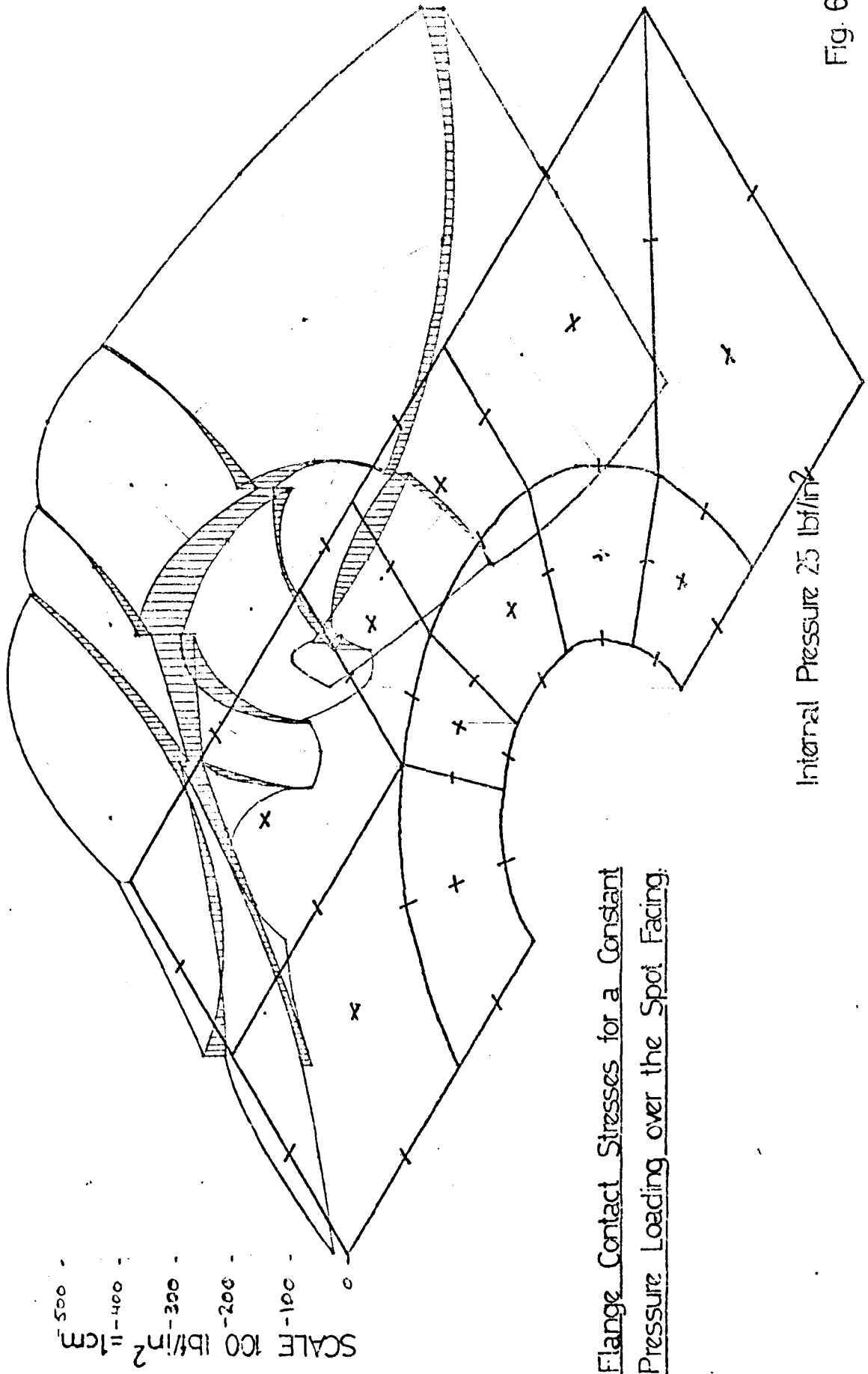


Fig. 67(b)

Displaced Shape of Spot Facing Due to Bolt Load Applied as a Constant Pressure over the Spot Facing

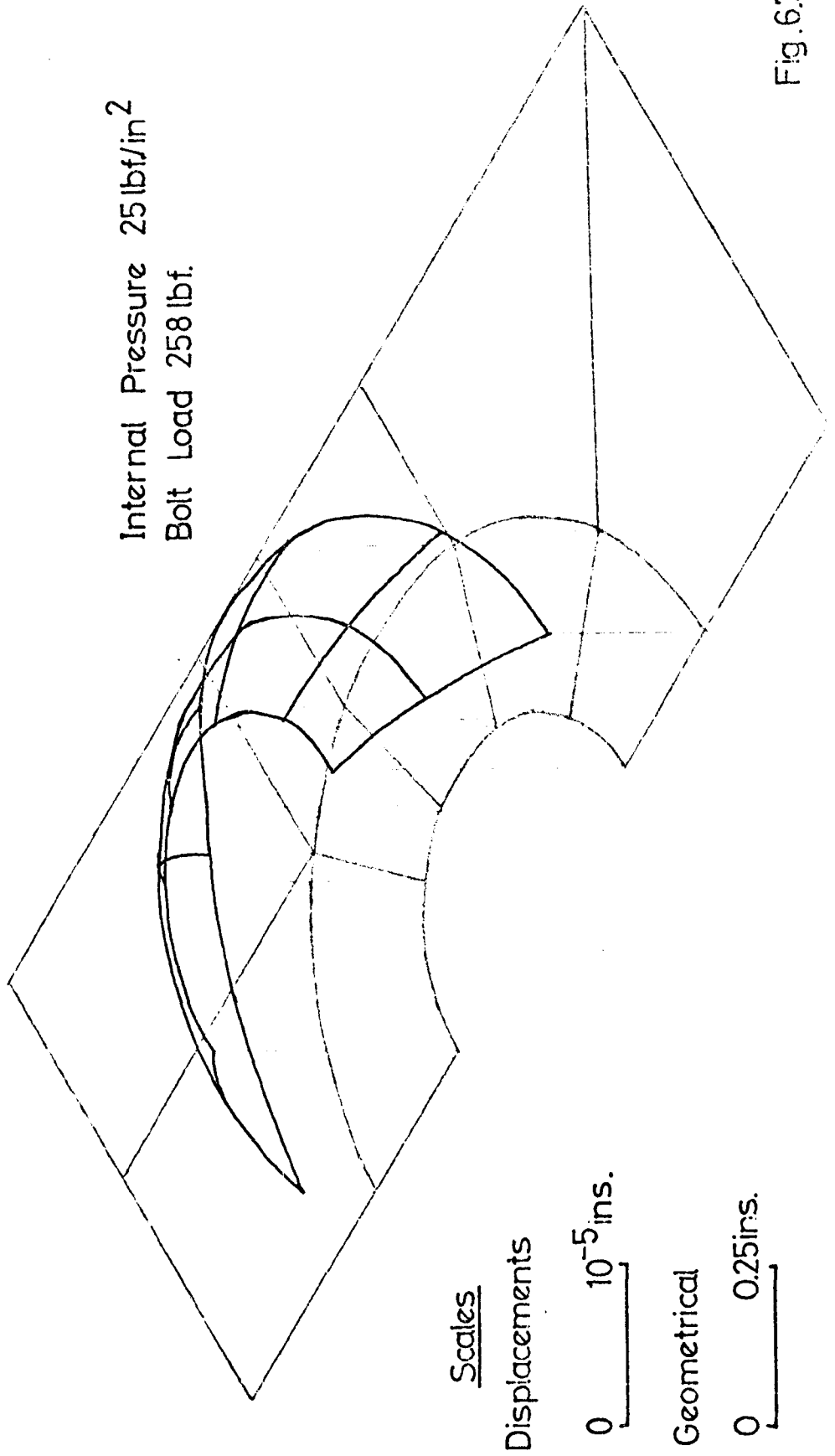


Fig. 67(c)

Flange Contact Stresses for a Constant Displacement over the Spot Facing.

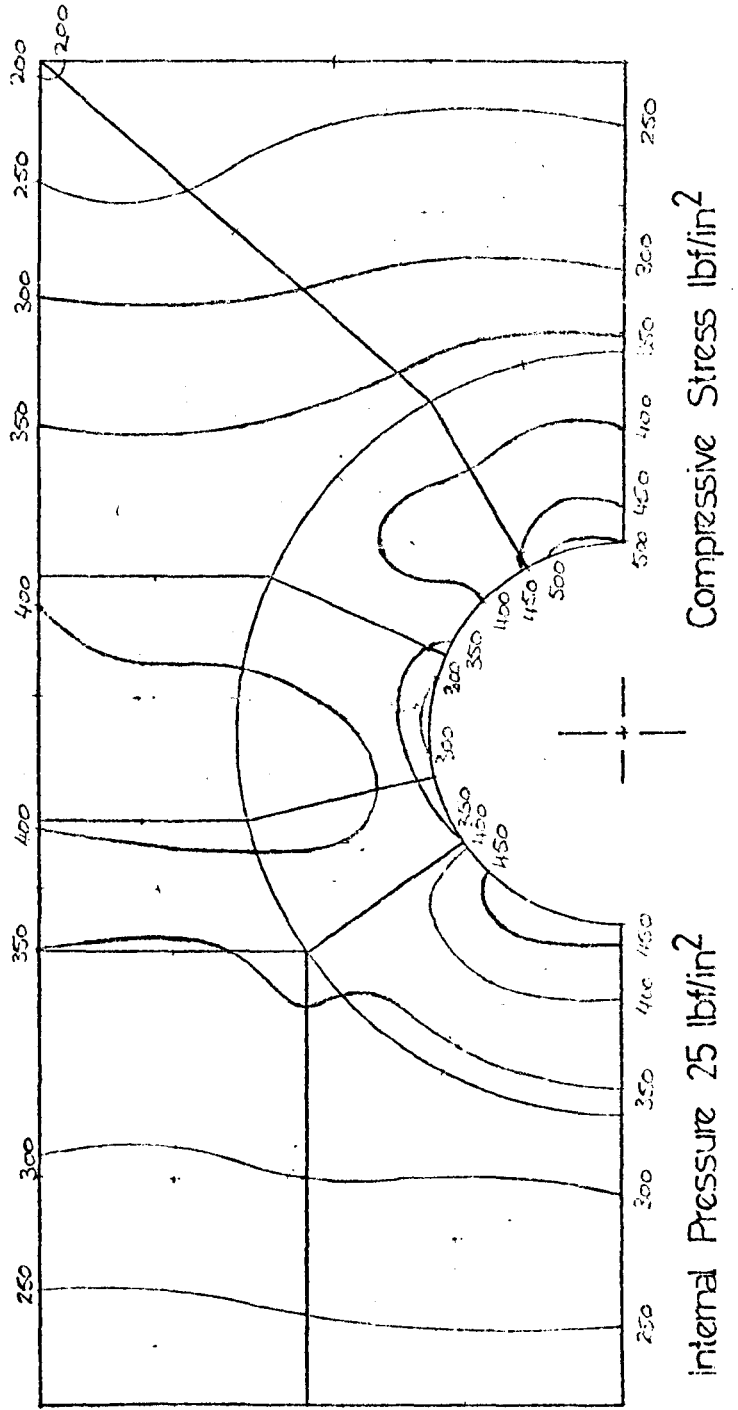
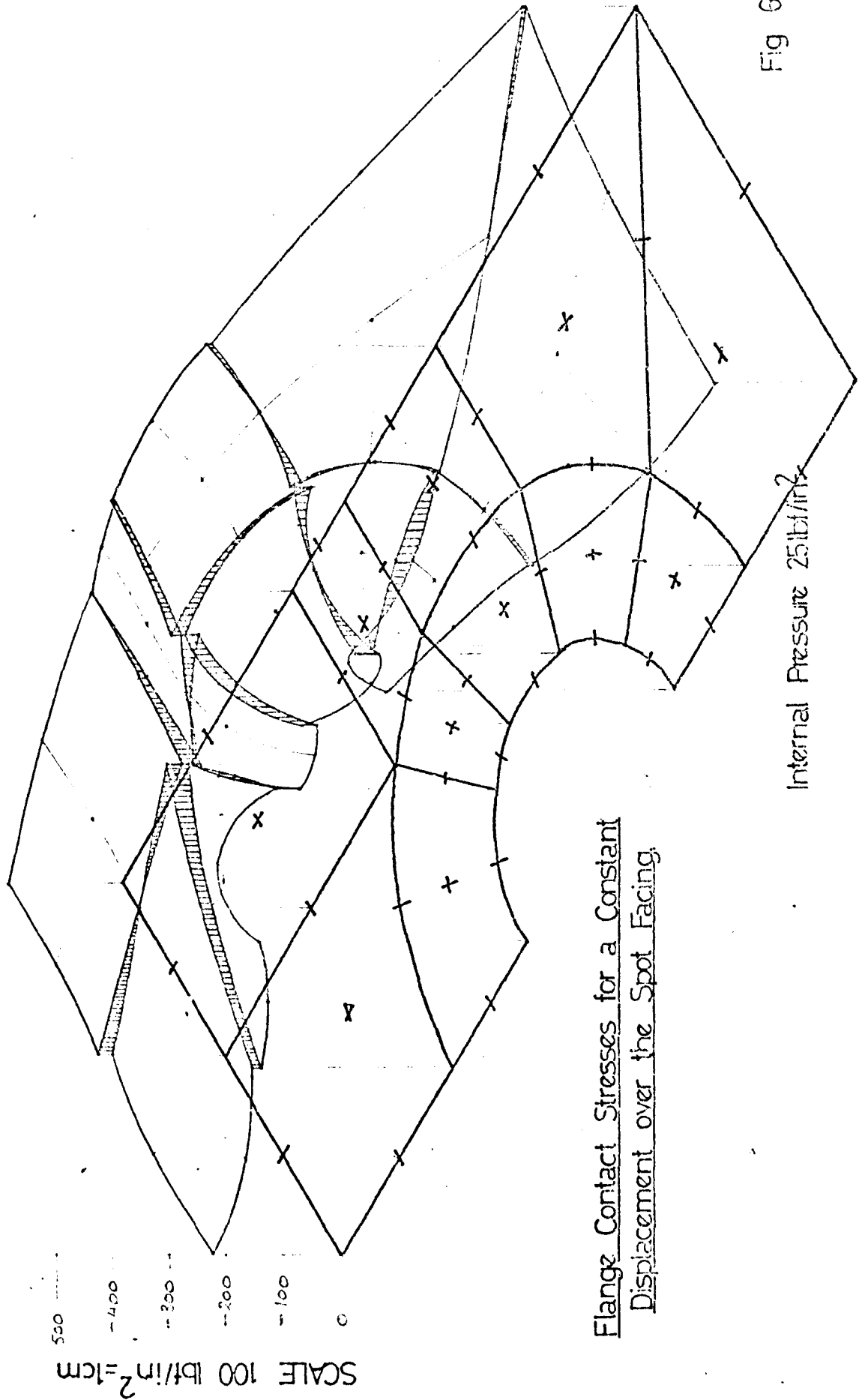


Fig. 68(a)



Flange Contact Stresses for a Constant Displacement over the Spot Facing.

Fig 68(b)

Internal Pressure 25 lb/in²

Application of Bolt Load to Turbine
Casing Flange

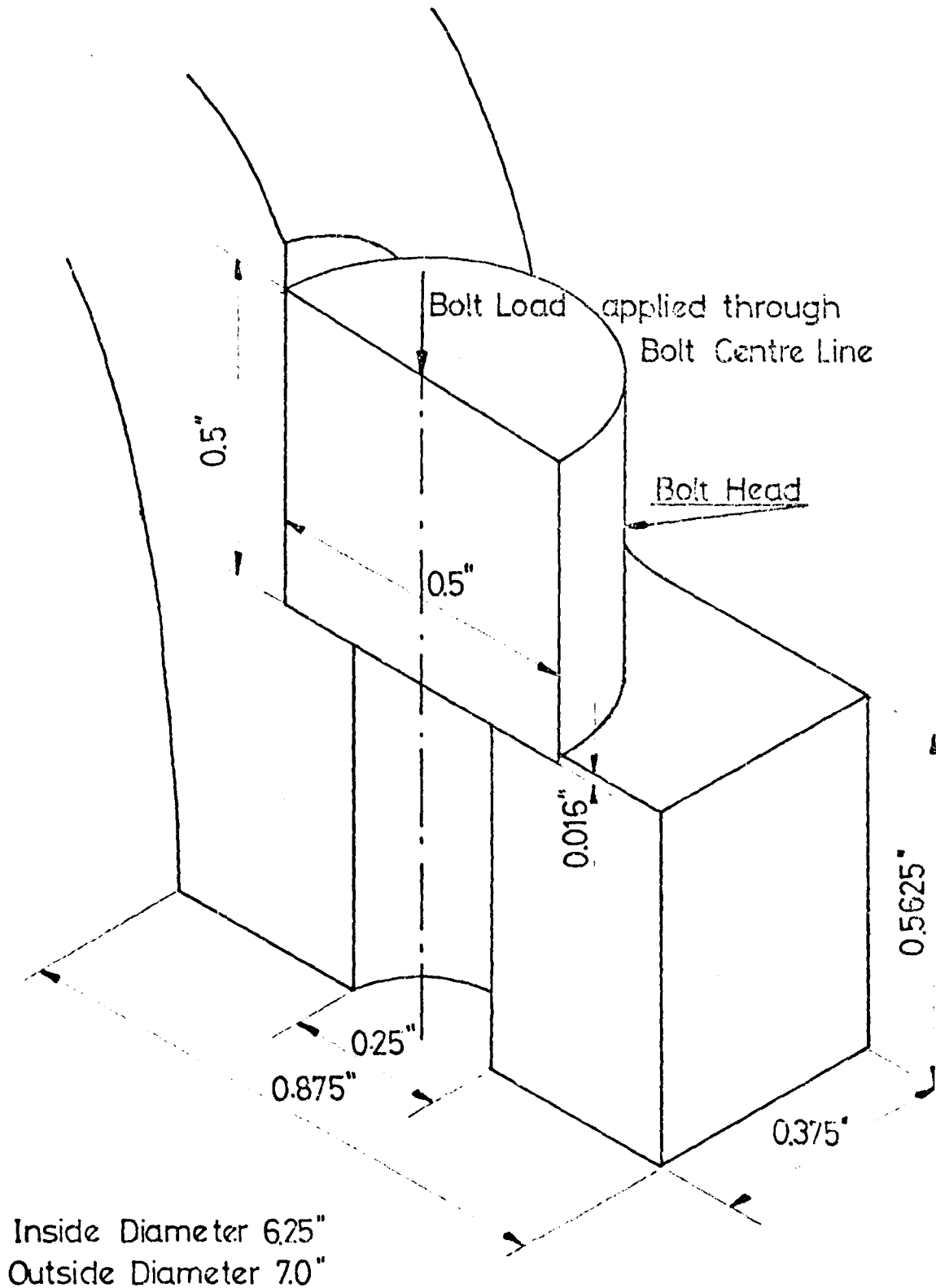
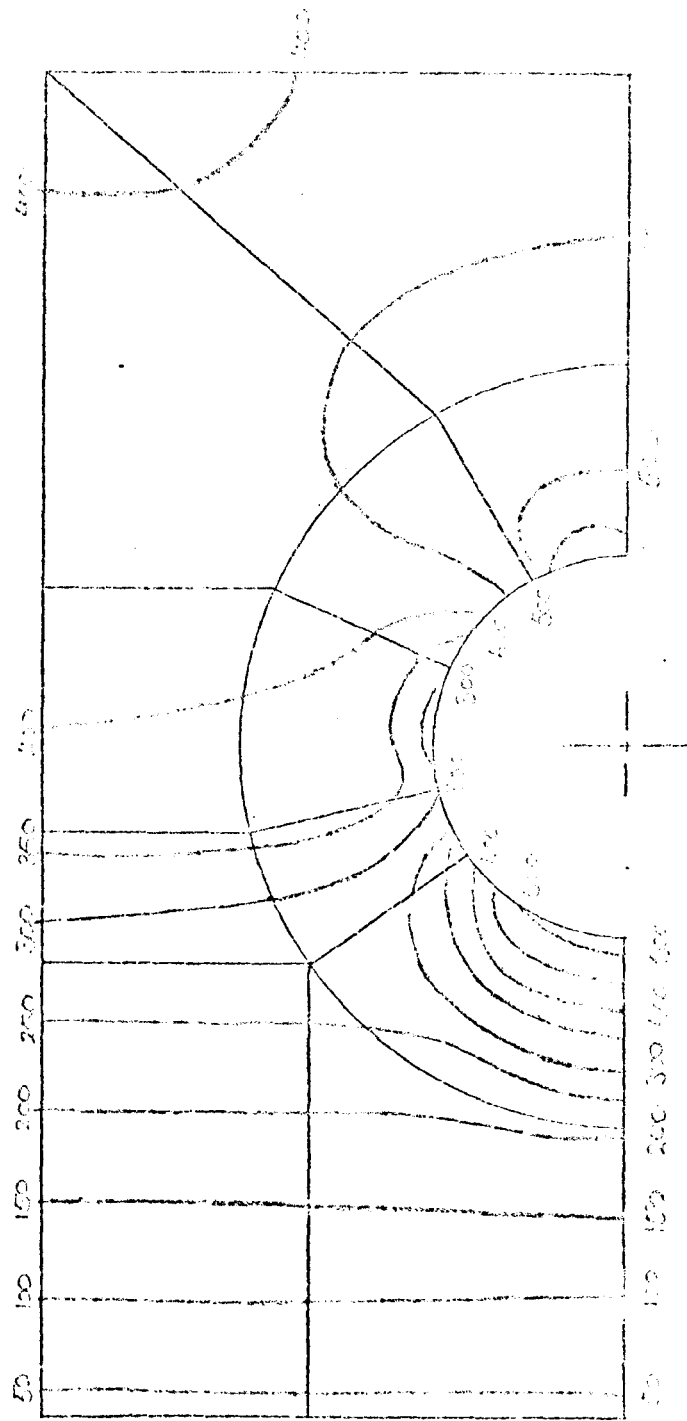


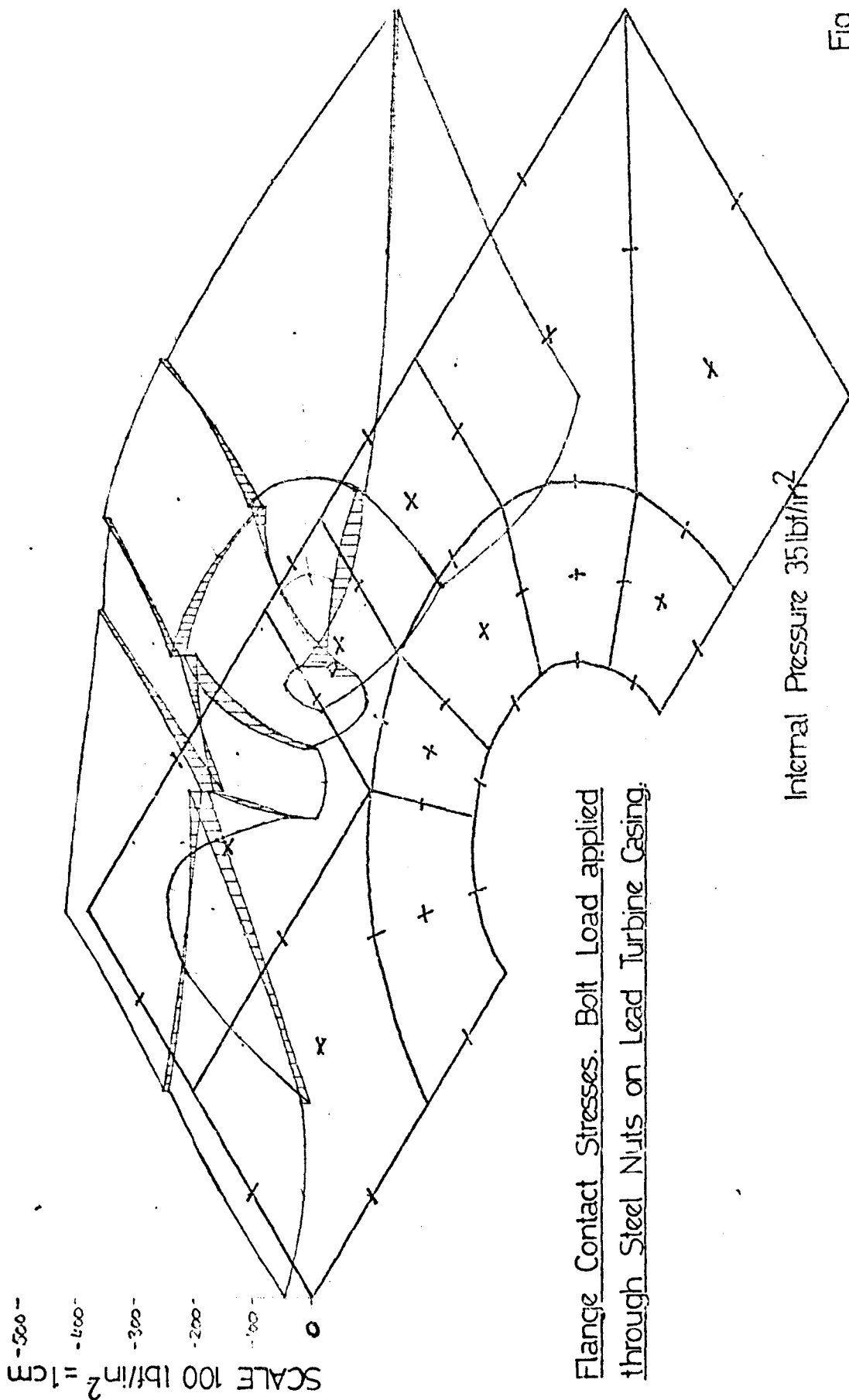
Fig 6.9

Flange Contact Stresses. Bolt Load applied through Steel Nuts on Lead Turbine Casing.



Internal Pressure 35 lb/in²

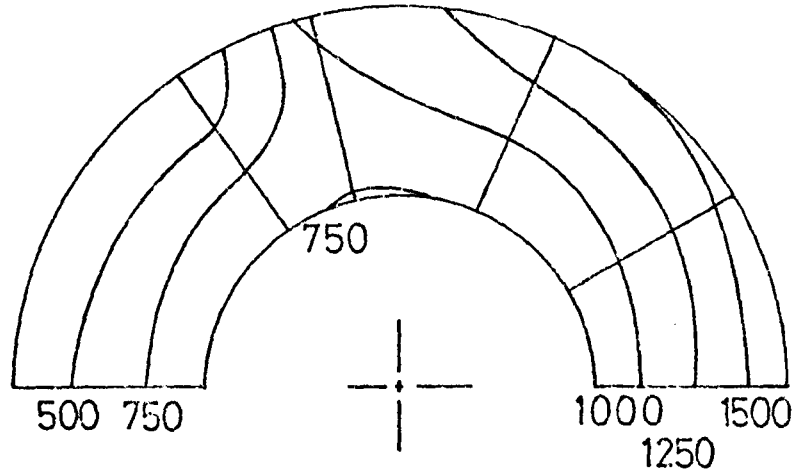
Compressive Stresses lb/in²



Flange Contact Stresses. Bolt Load applied through Steel Nuts on Lead Turbine Casing.

Fig. 6-10(b)

Contact Pressure between Bolt Head
and Flange Spot Facing



Compressive Stresses lbf/in²

Fig 6.10(c)

Displaced Shape of the Bolt Head/Spot
Facing Contact Area

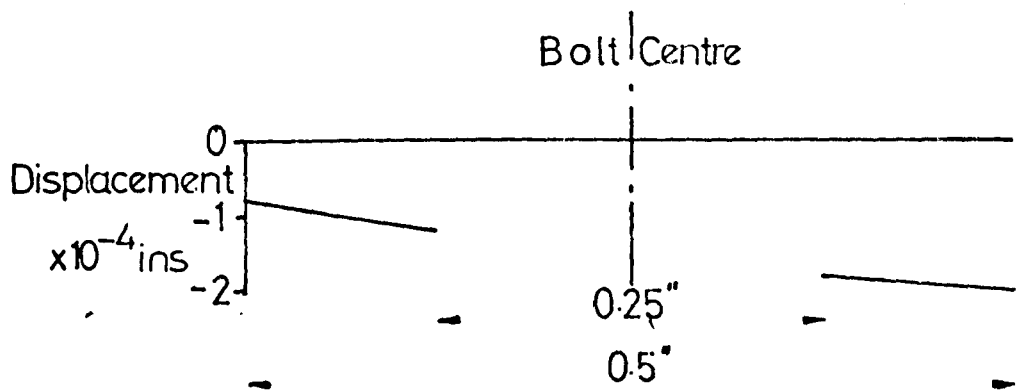


Fig 6.10(d)

Displaced Shape of the Lead Turbine
Casing at the Mid-Bolt Position

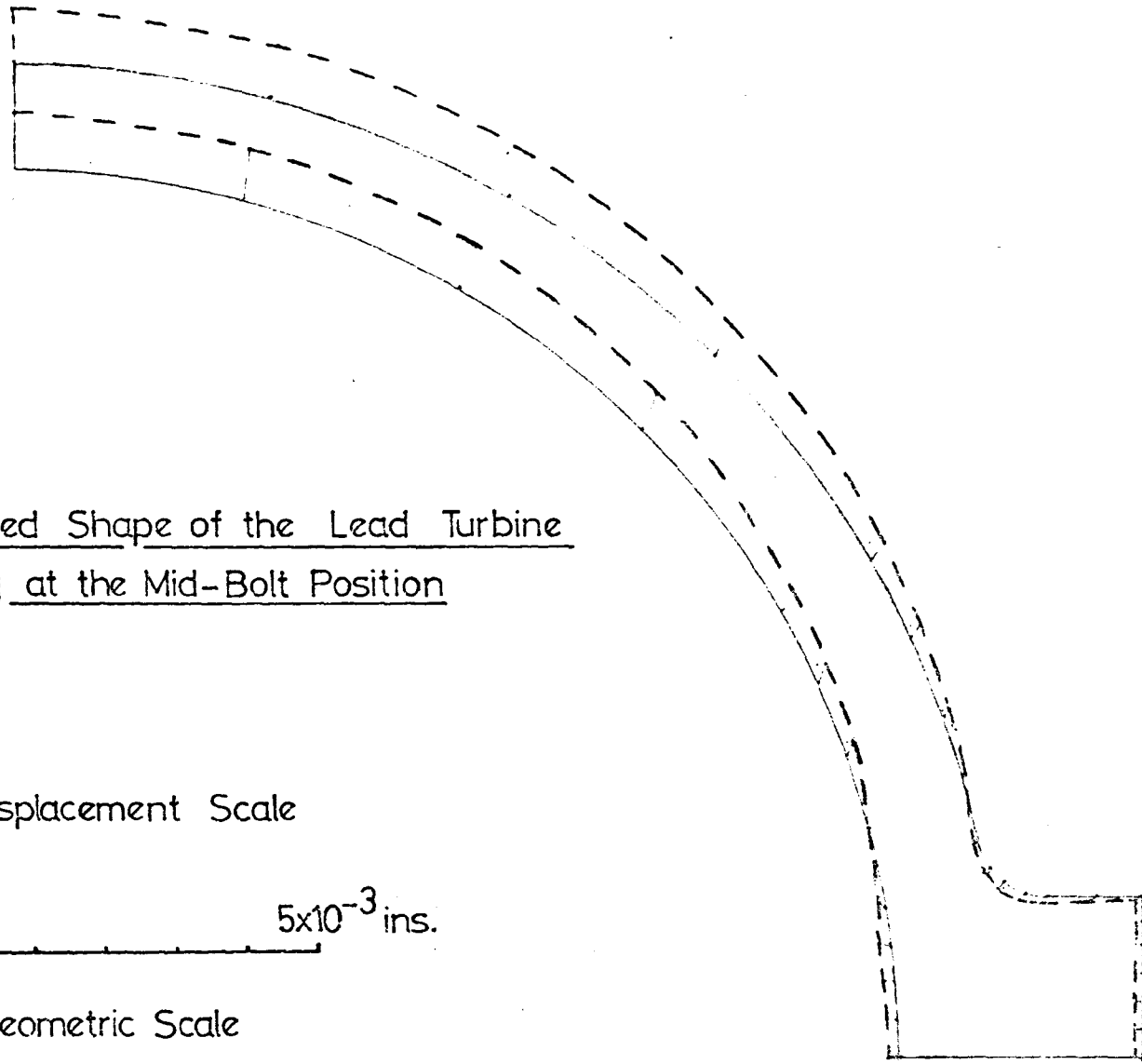
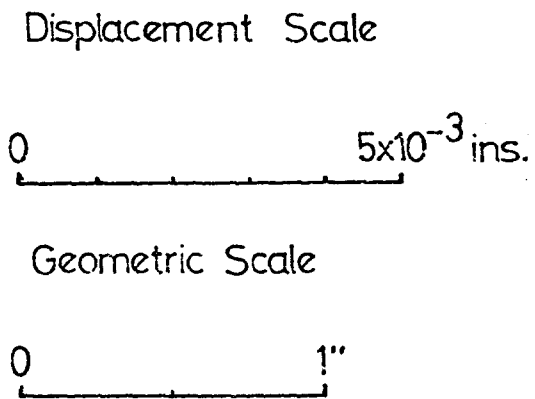
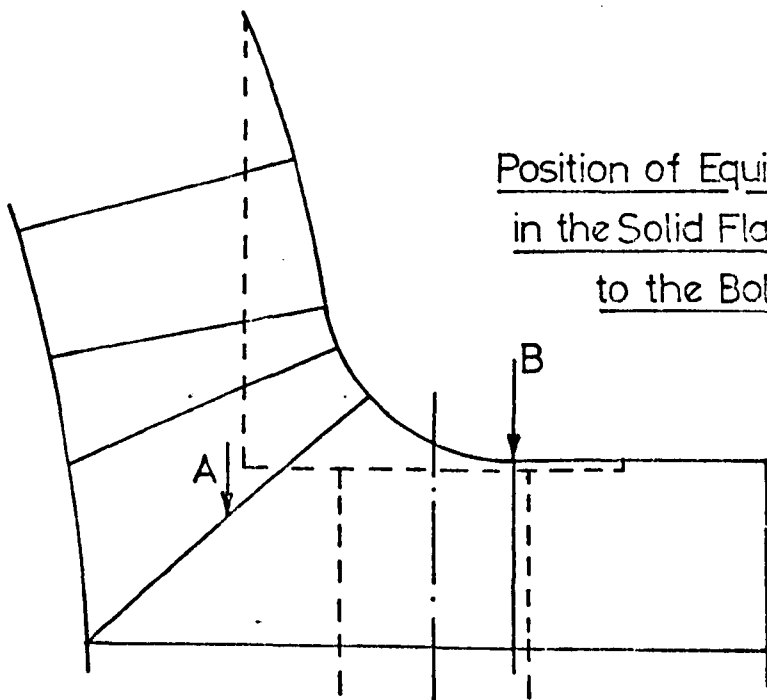
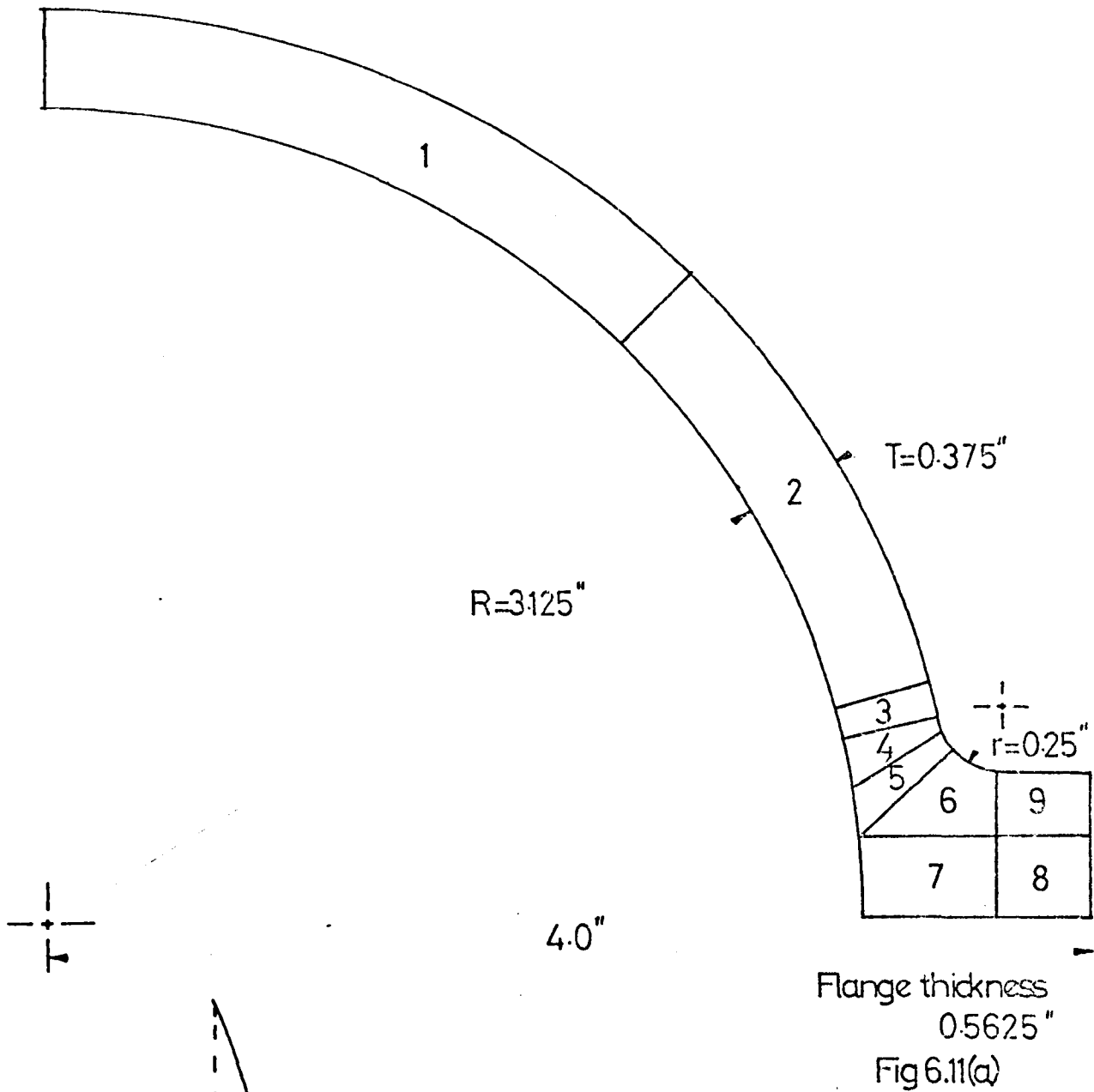


Fig 6.10(z)

9 Element Idealisation of Turbine Casing Section (Thinner Flange)



Position of Equivalent Bolt Loads
in the Solid Flange Relative
to the Bolt Holes

Fig 6.11(b)

Hoop Stress Distribution for Turbine Casing Section Subjected to Internal Pressure
and Equivalent Bolt Loads

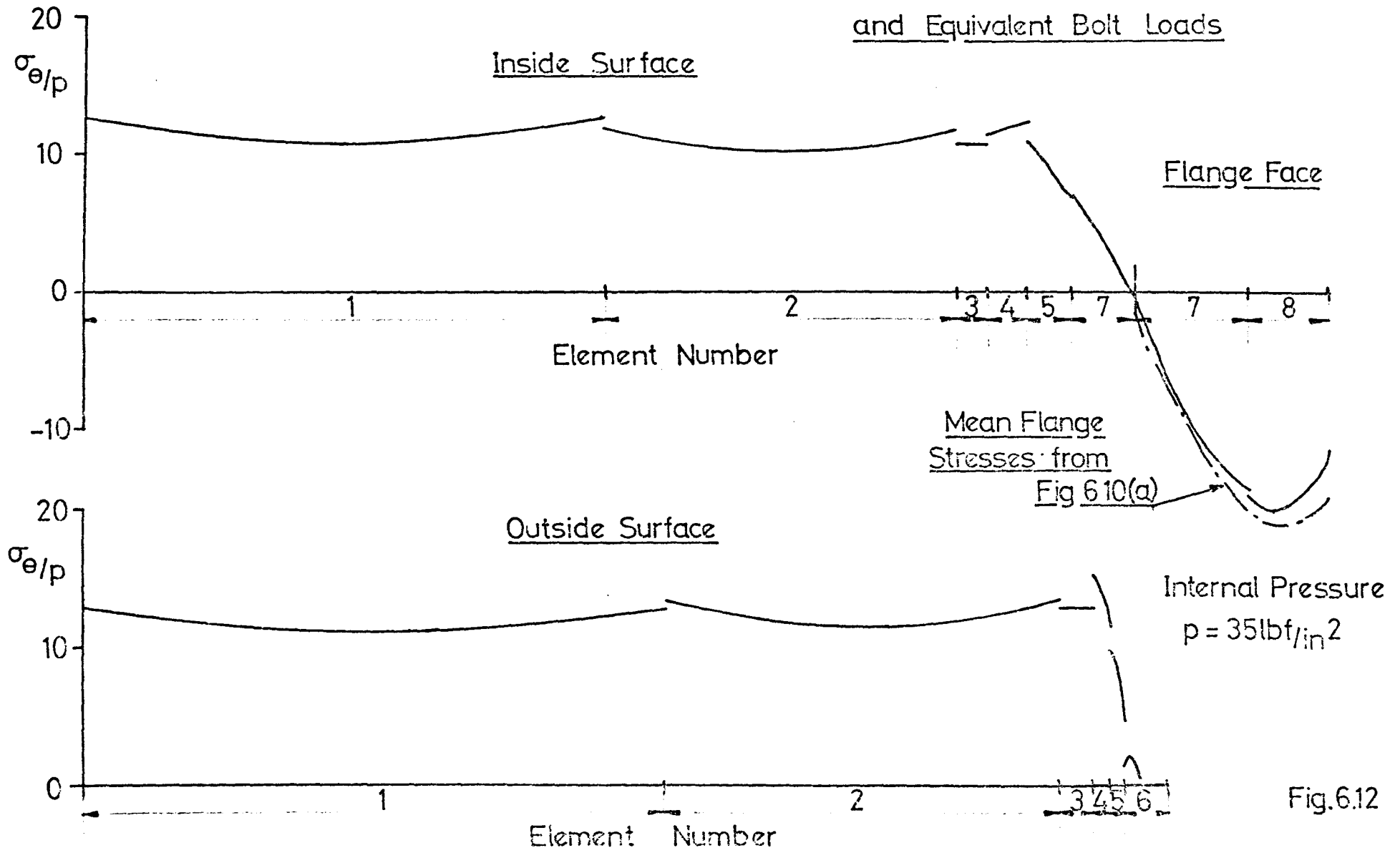


Fig. 6.12

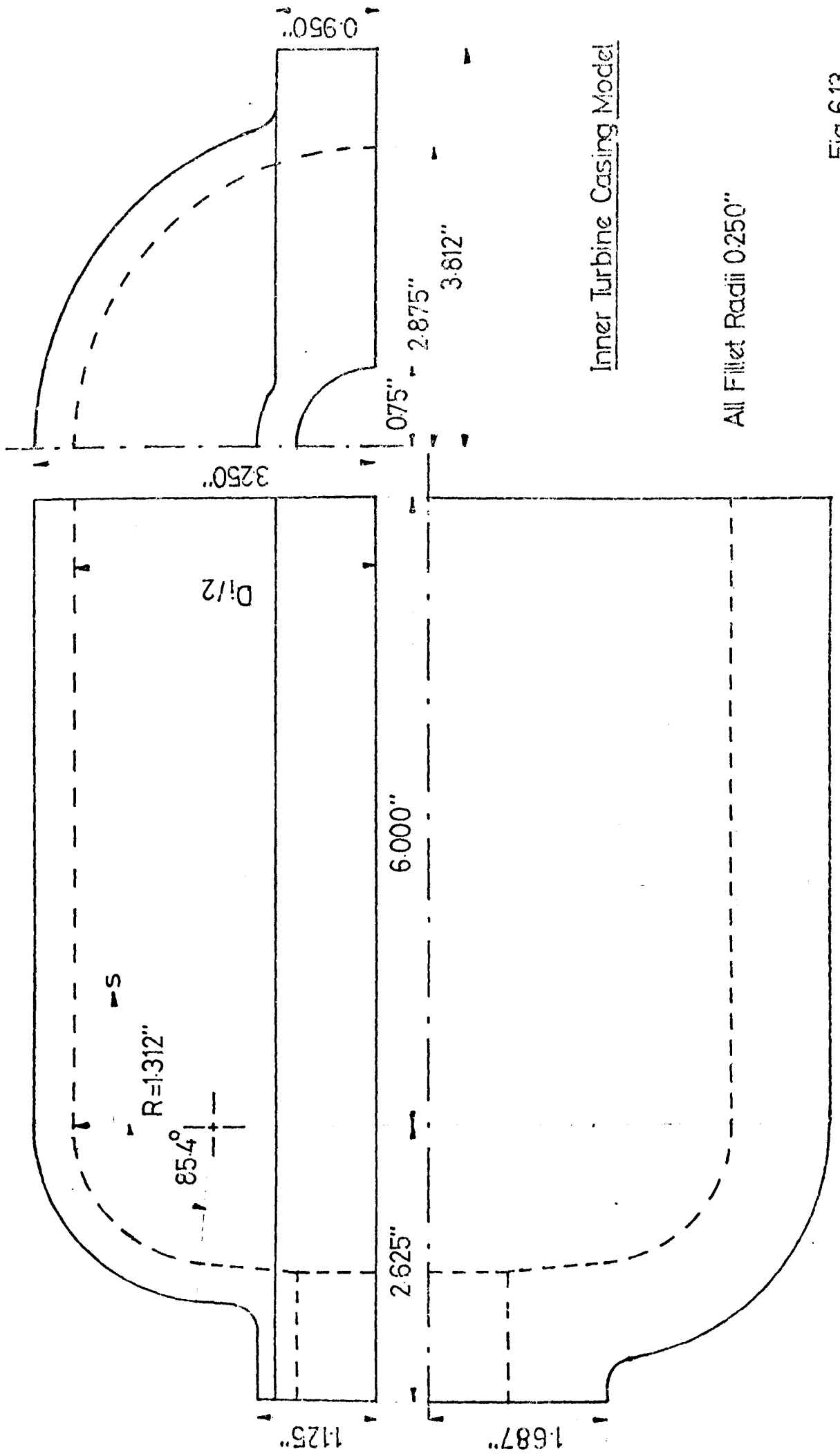
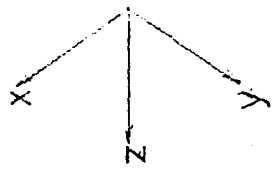


Fig. 6.13



Finite Element Idealisation of Inner Turbine Casing

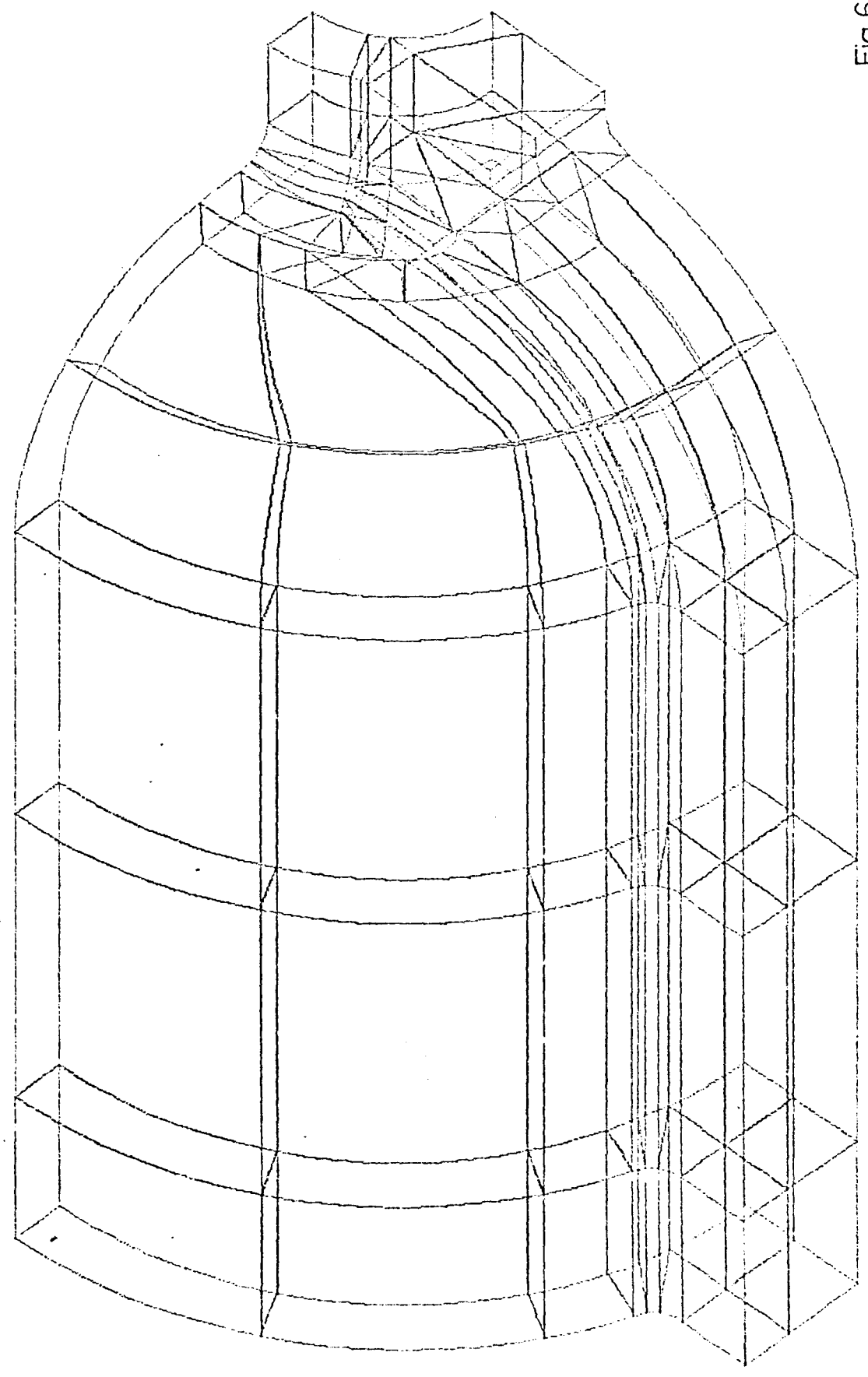


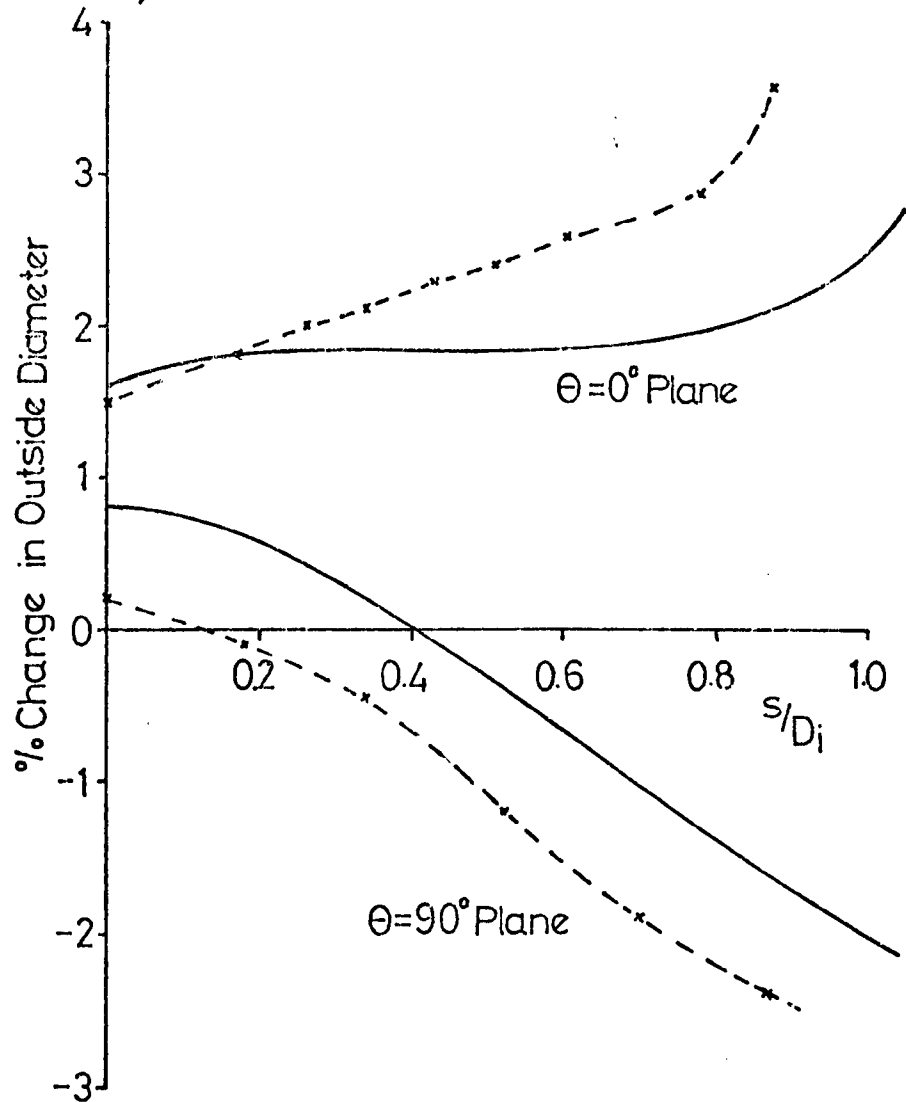
Fig. 6.14

Radial Deformation of the Cylindrical Part
of an Inner Turbine Casing

$$E_{\text{steel}} = 3 \times 10^7 \text{ lbf/in}^2$$

$$E_{\text{araldite}} = 1 \times 10^3 \text{ lbf/in}^2$$

$$\nu_{\text{Hg}} = 7.36$$



— Finite Element Analysis

-*-Photoelastic Analysis(Ref.66)

Fig6.15

Circumferential Stress Index Distributions at the $\theta=0^\circ$ Plane

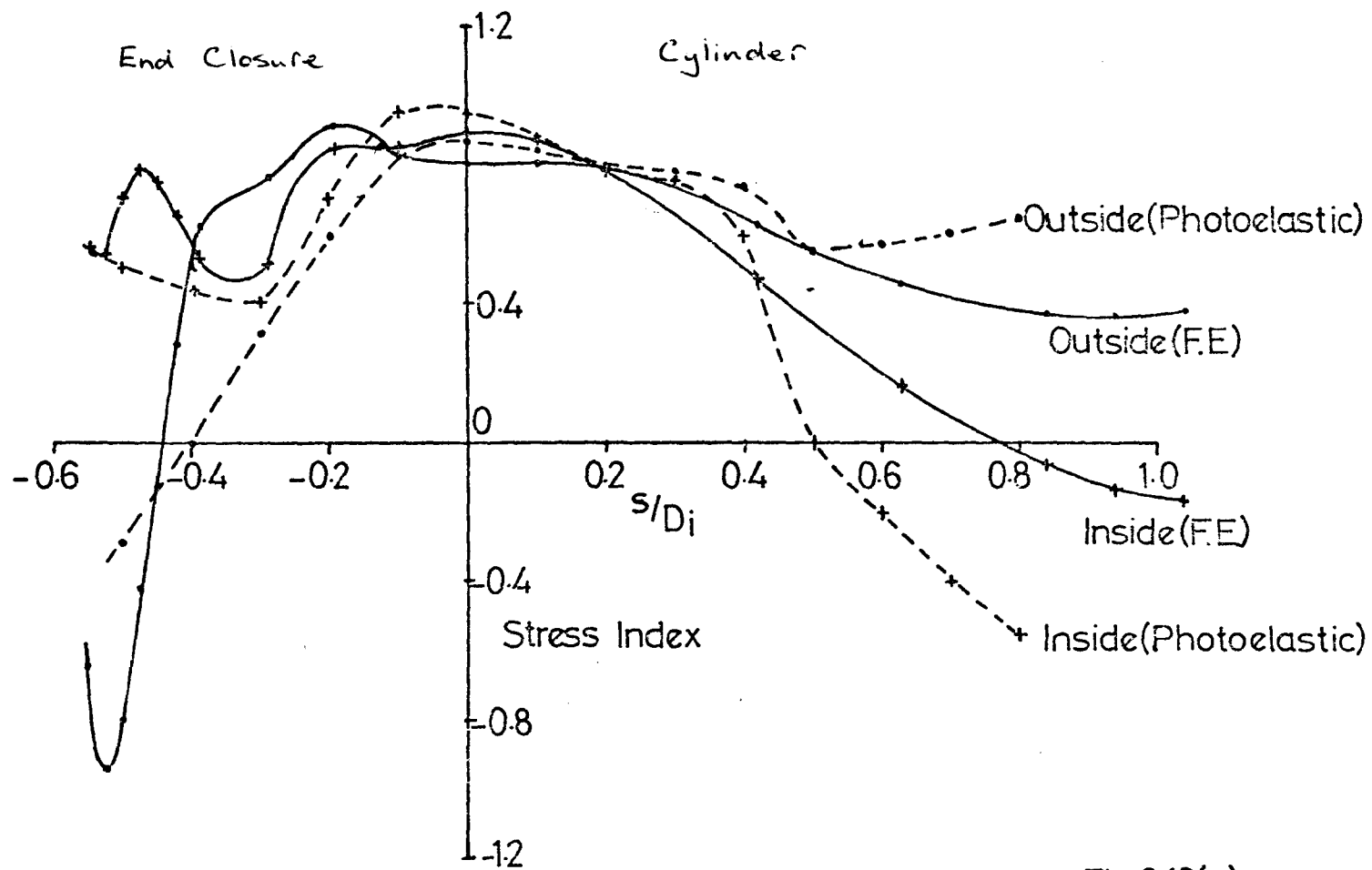


Fig 6.16(a)

Circumferential Stress Index Distributions at the $\theta=90^\circ$ Plane

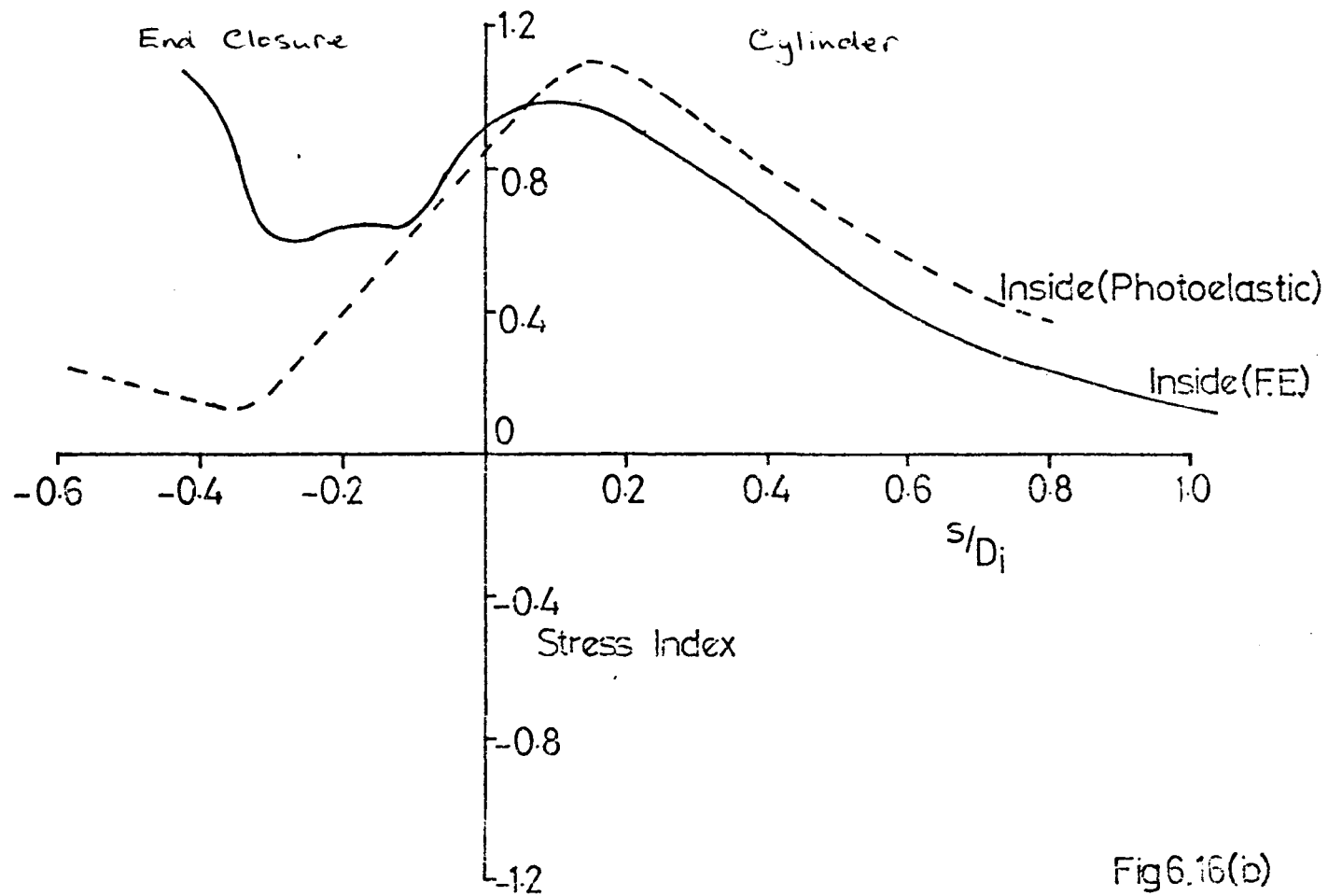


Fig 6.16(b)

Meridional Stress Variation in Inner Turbine Casing

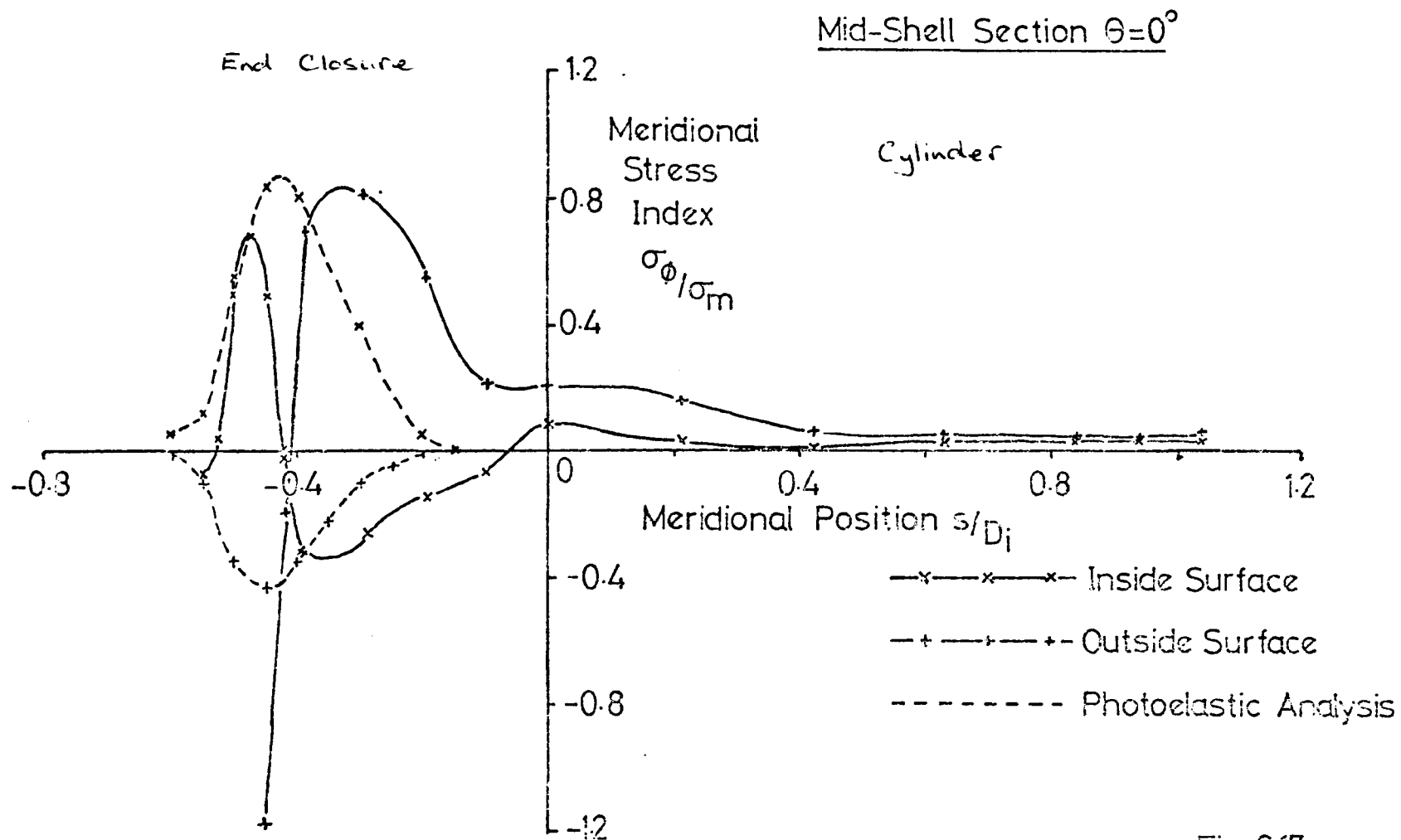
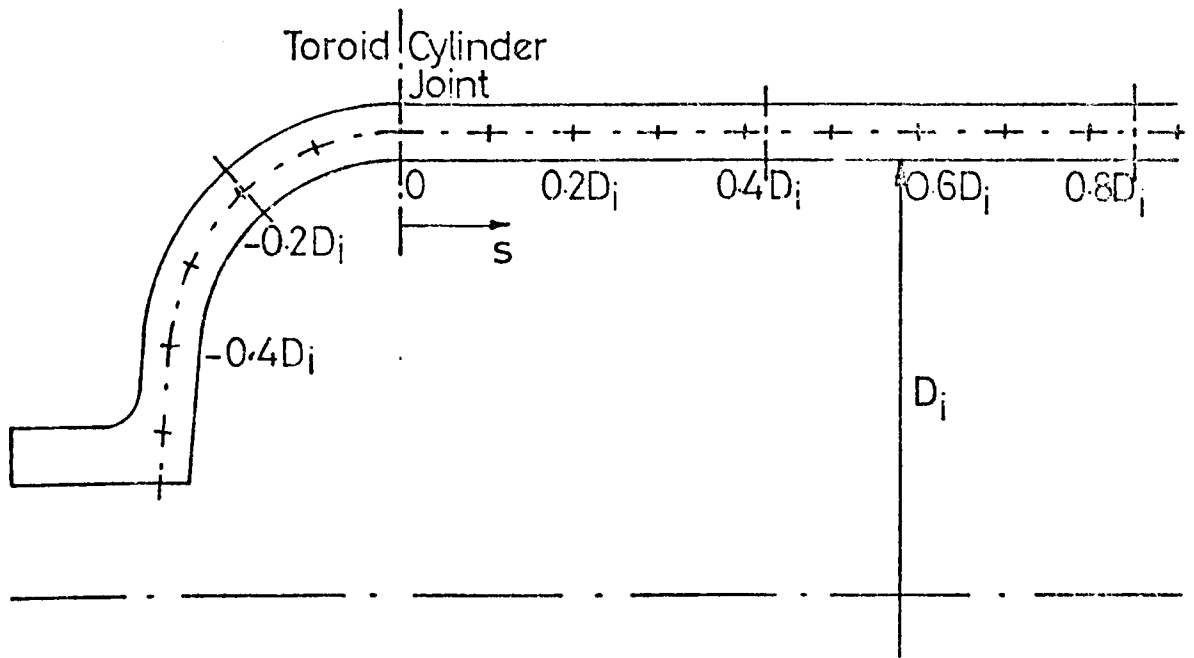


Fig. 6.17

Meridional Positions of Hoop Stress Plots
for Inner Turbine Casing



Circumferential Positions for Hoop Stresses

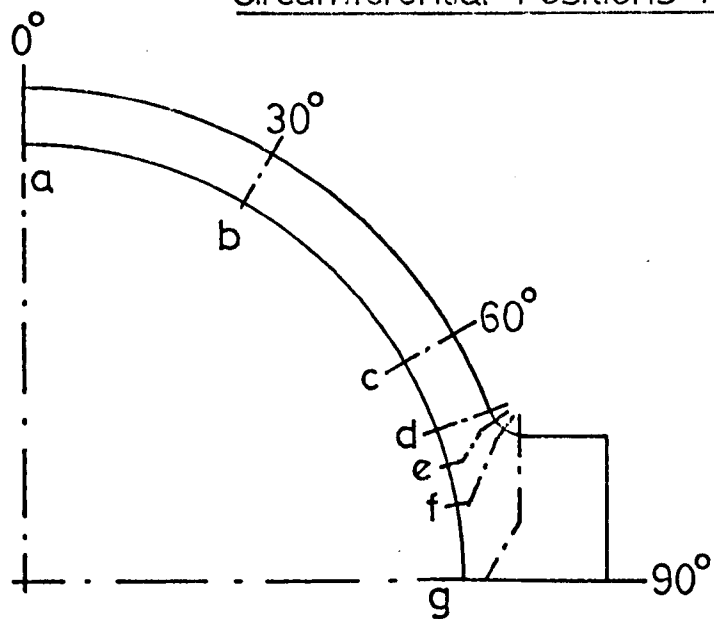


Fig 6.18

Hoop Stress Distribution Due to Axially Varying Pressure Loading

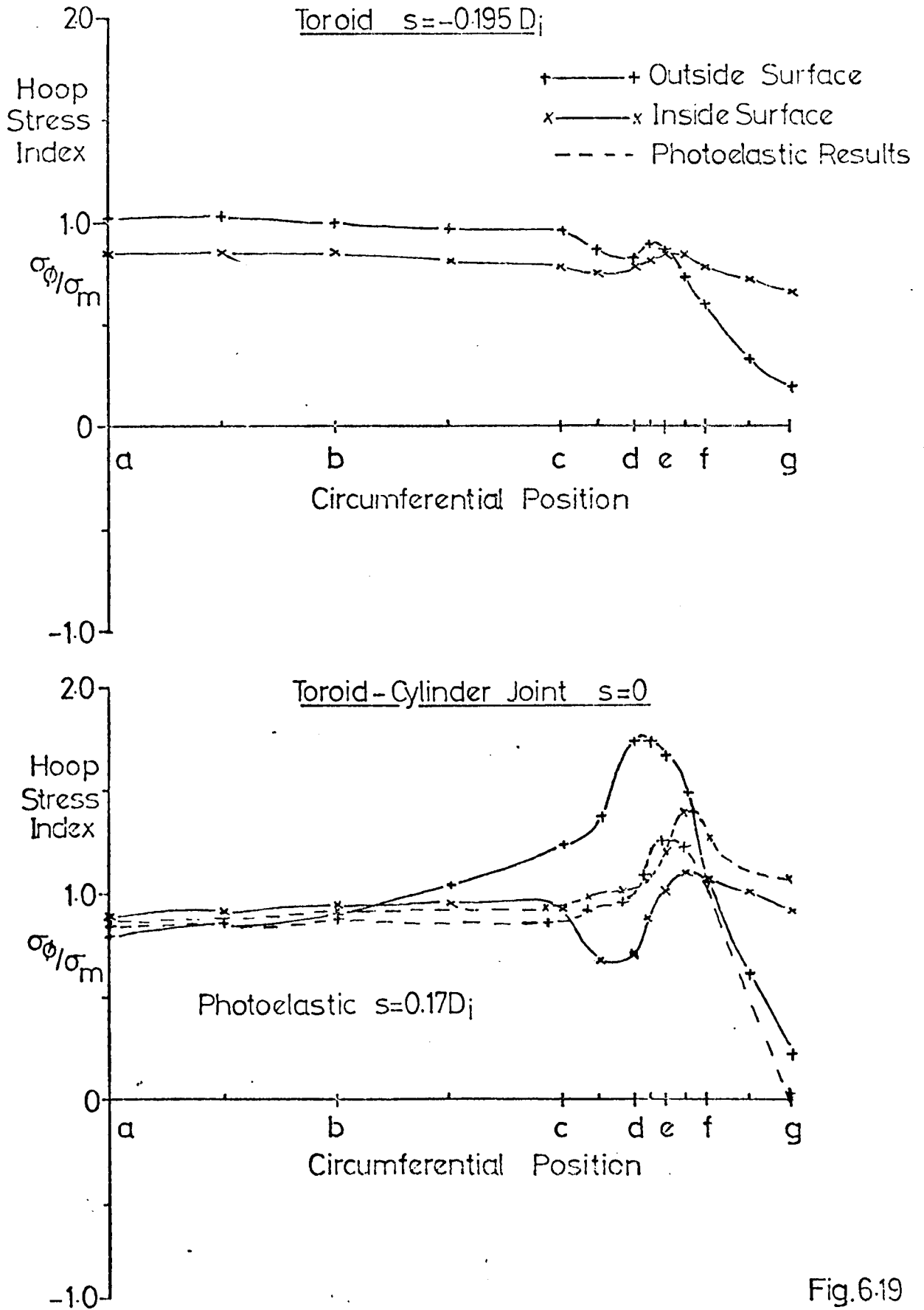


Fig.6.19

Hoop Stress Distribution Due to Axially Varying Pressure Loading

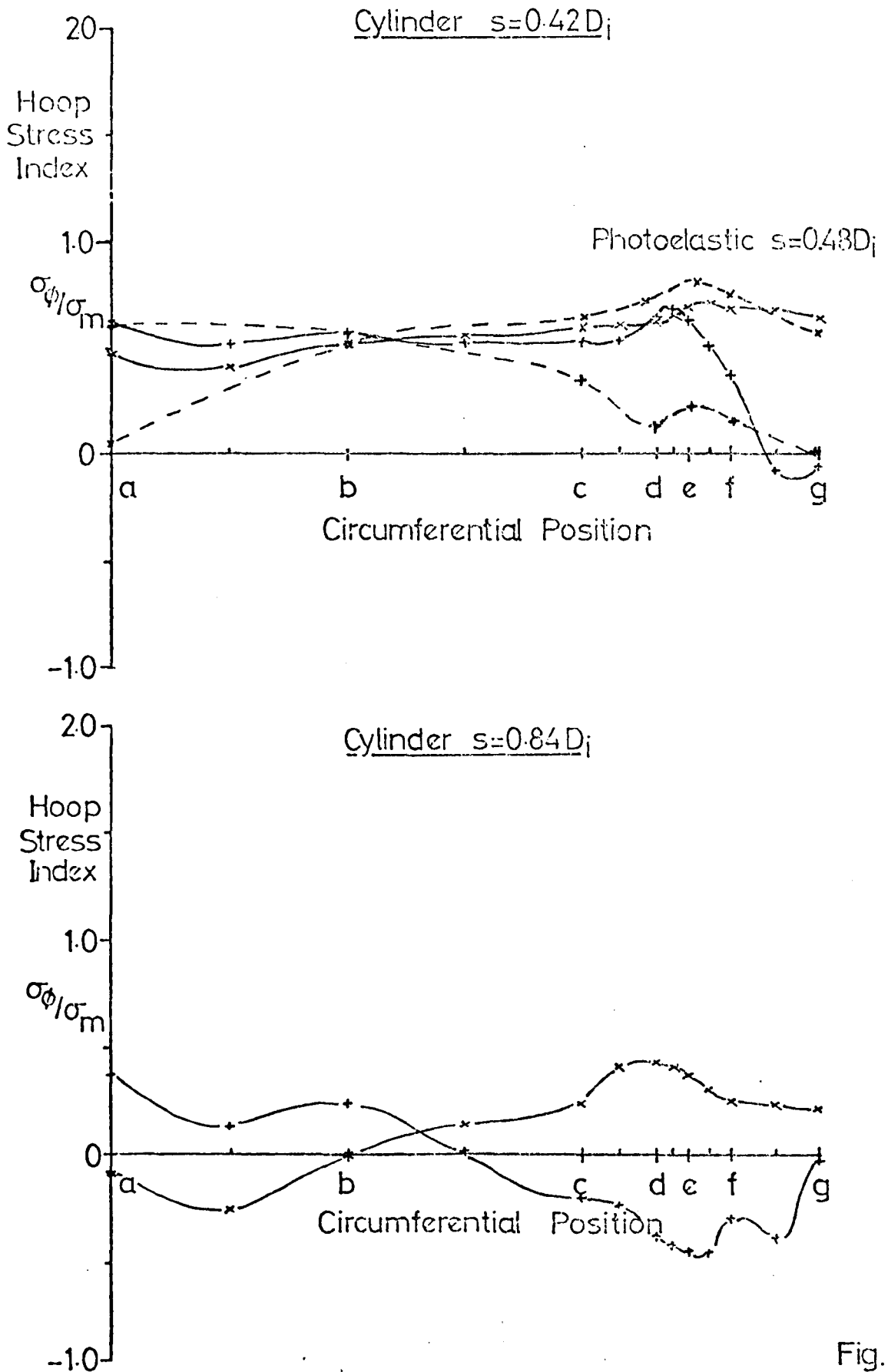


Fig.6.19

Turbine Casing Model

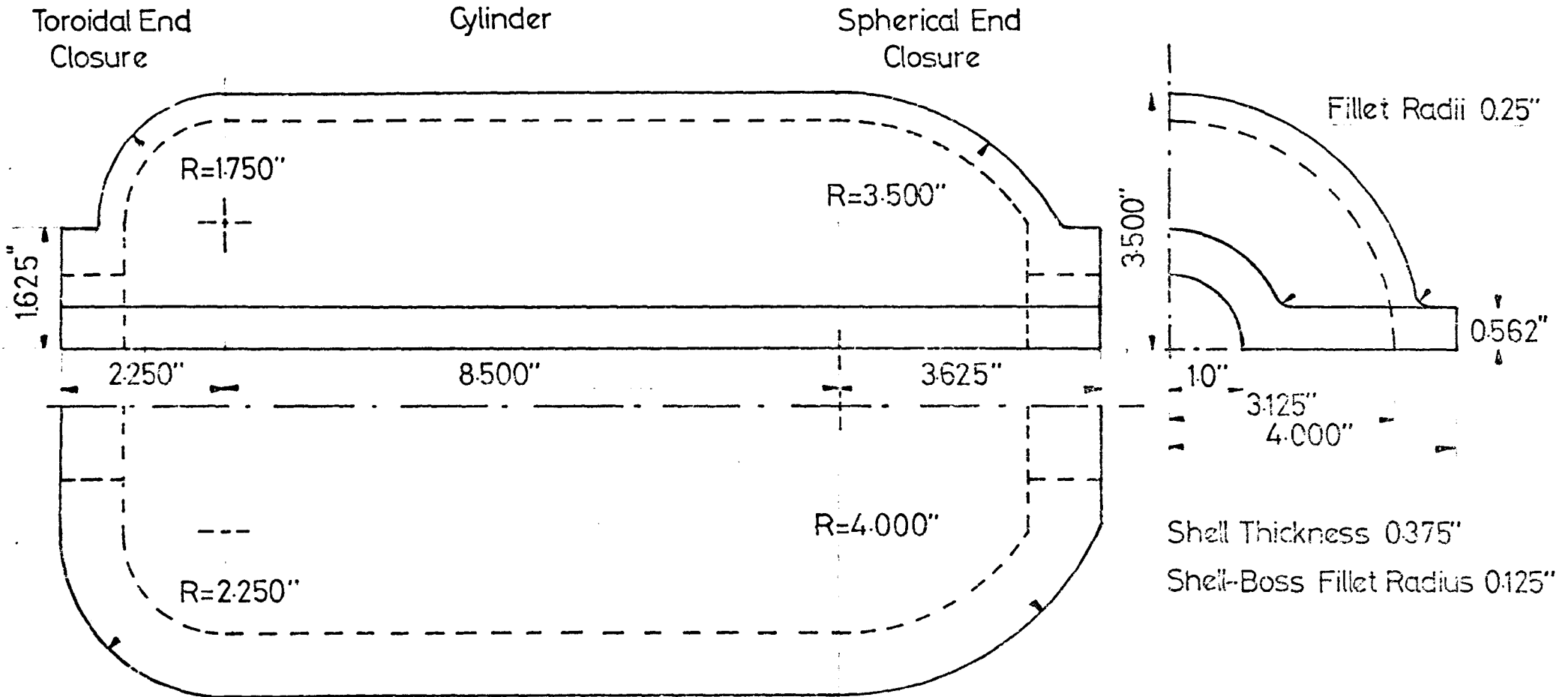
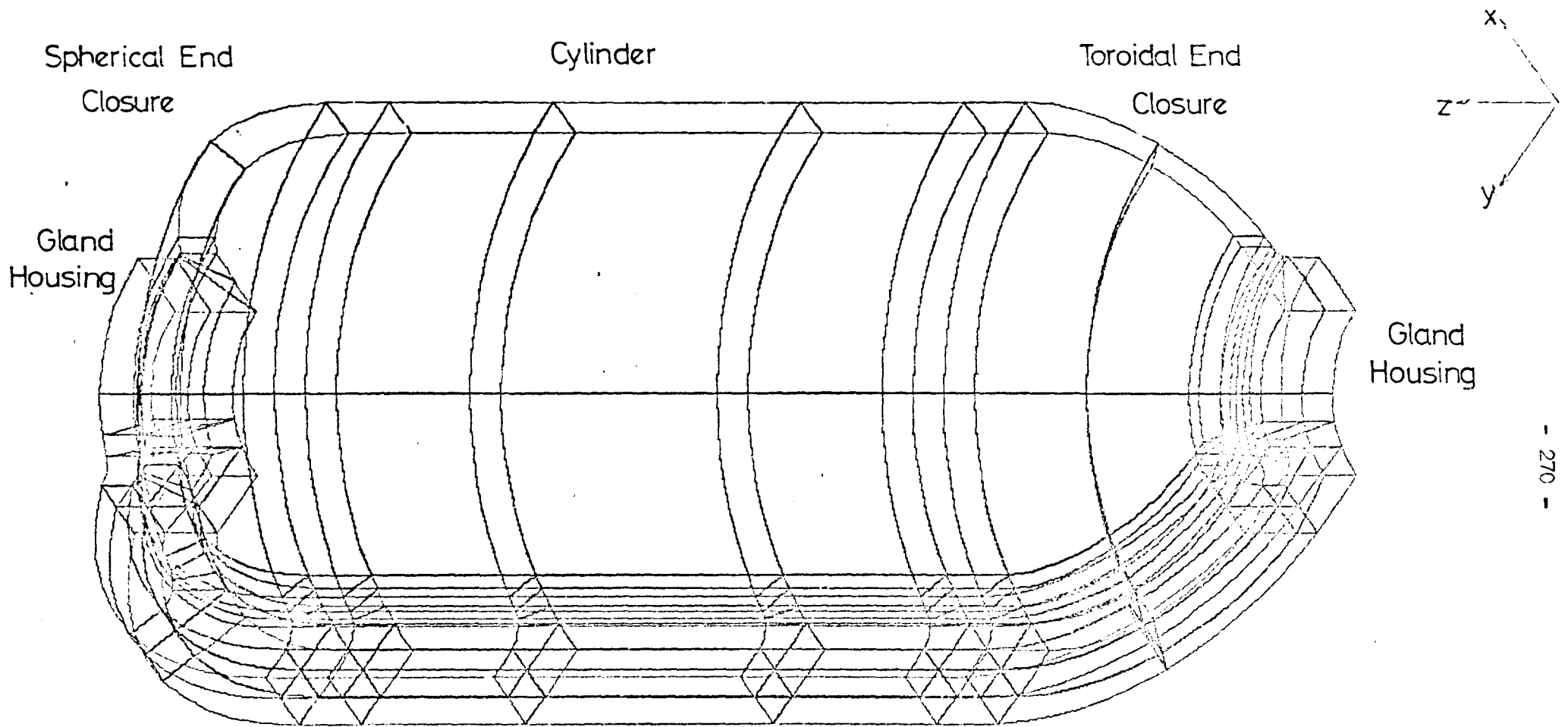
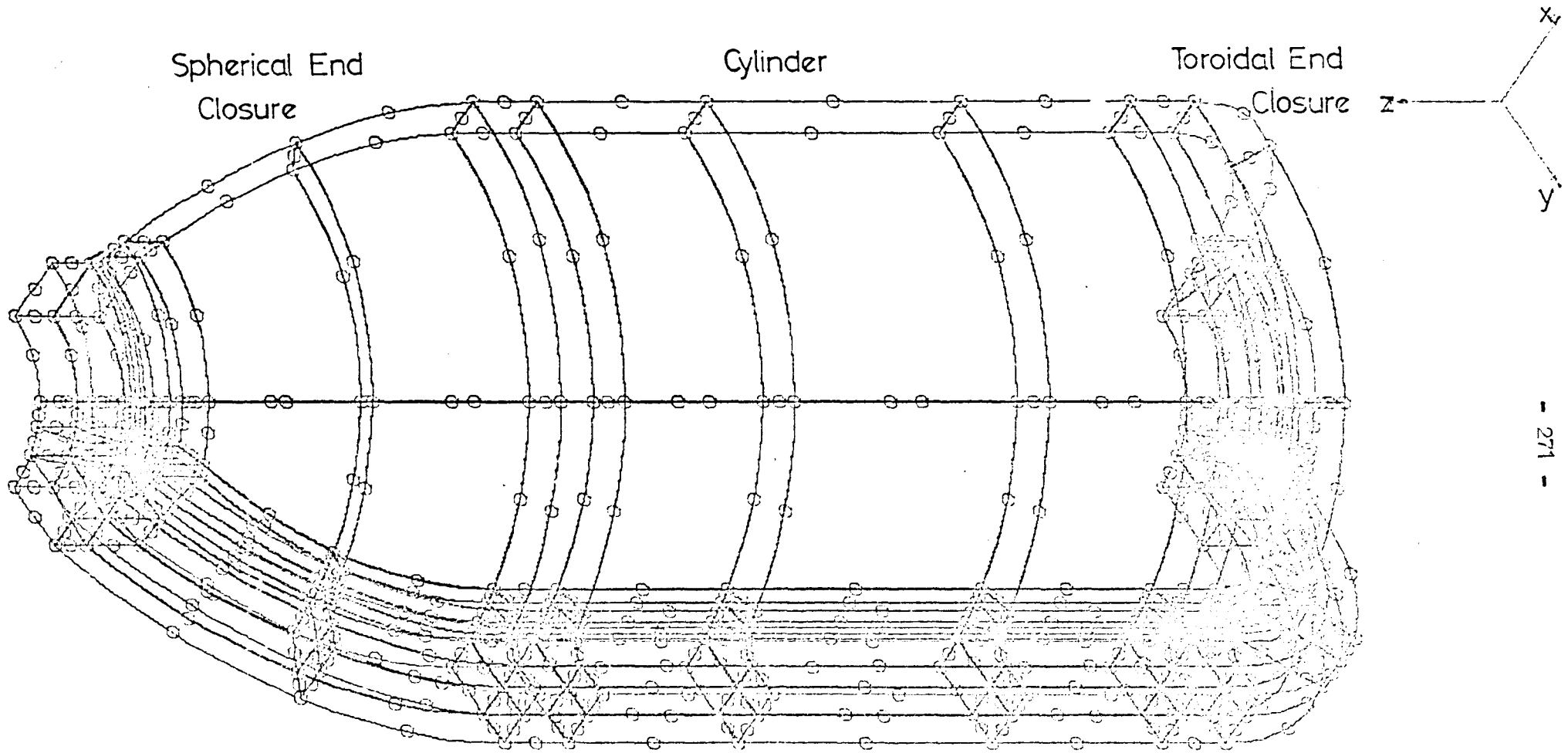


Fig.6.20



Finite Element Idealisation of Split Turbine Casing

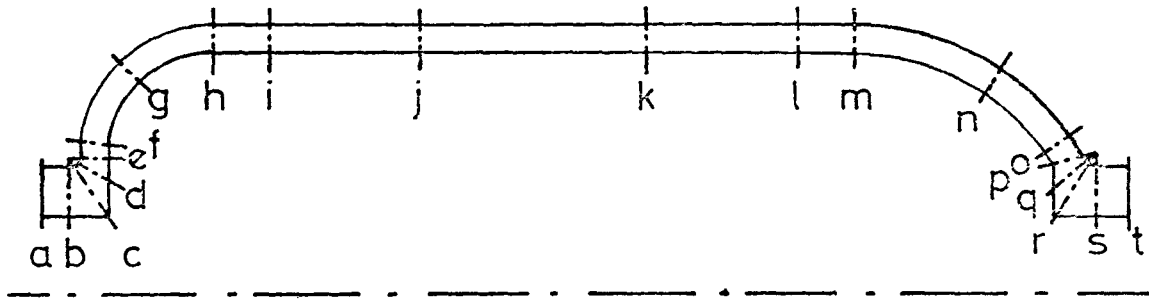
Fig. 6.21(a)



Finite Element Idealisation with Nodes of Split Turbine Casing

Fig.6.21(b)

Meridional Positions in Shell Sections - $\theta=0^\circ, 30^\circ, 60^\circ$



Meridional Positions in Flange Face - $\theta=90^\circ$

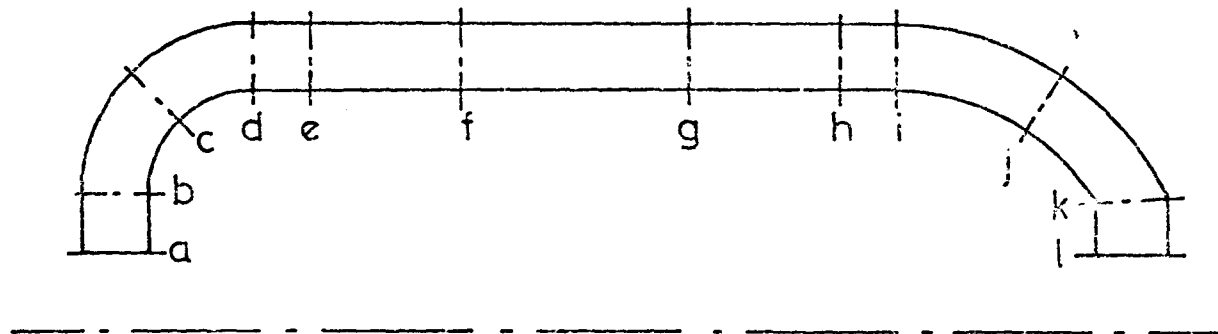


Fig.6.22

Meridional Variation in the Hoop Stresses in the Shell
Portion of a Turbine Casing
Internal Pressure Loading

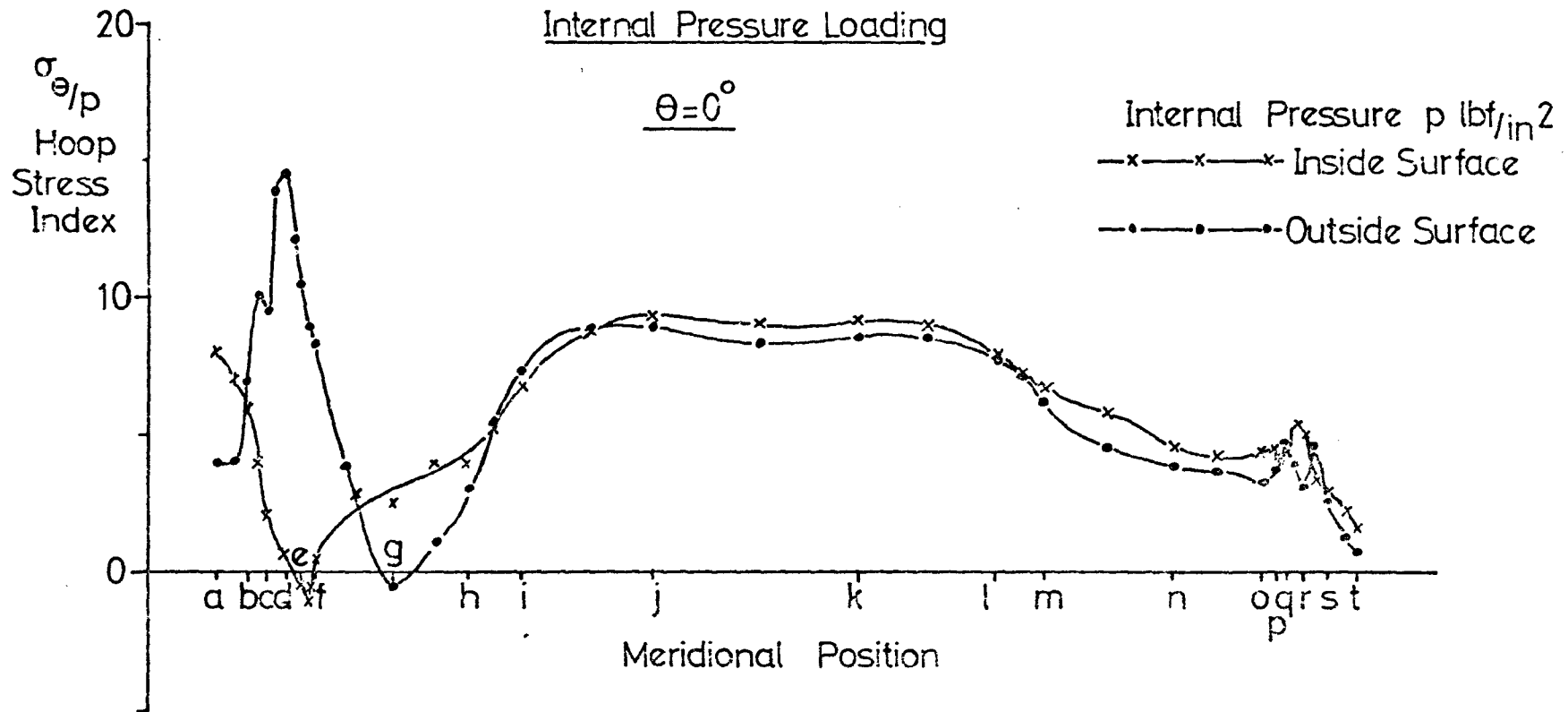


Fig. 6.23

Meridional Stresses in Turbine Casing

Internal Pressure Loading

$$\theta = 0^\circ$$

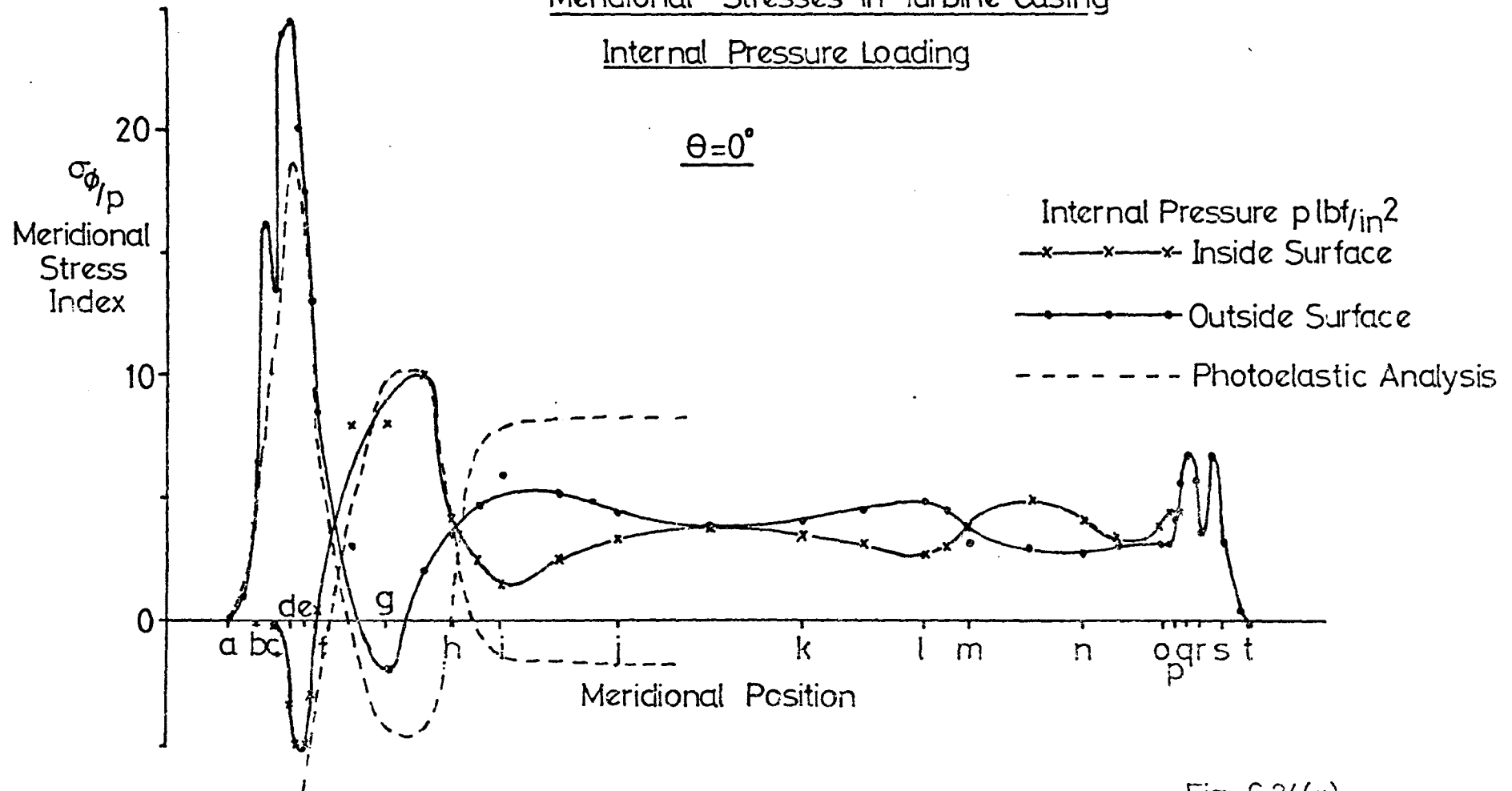


Fig 6.24(a)

Meridional Stresses in Turbine Casing

Internal Pressure Loading

$\theta = 30^\circ$

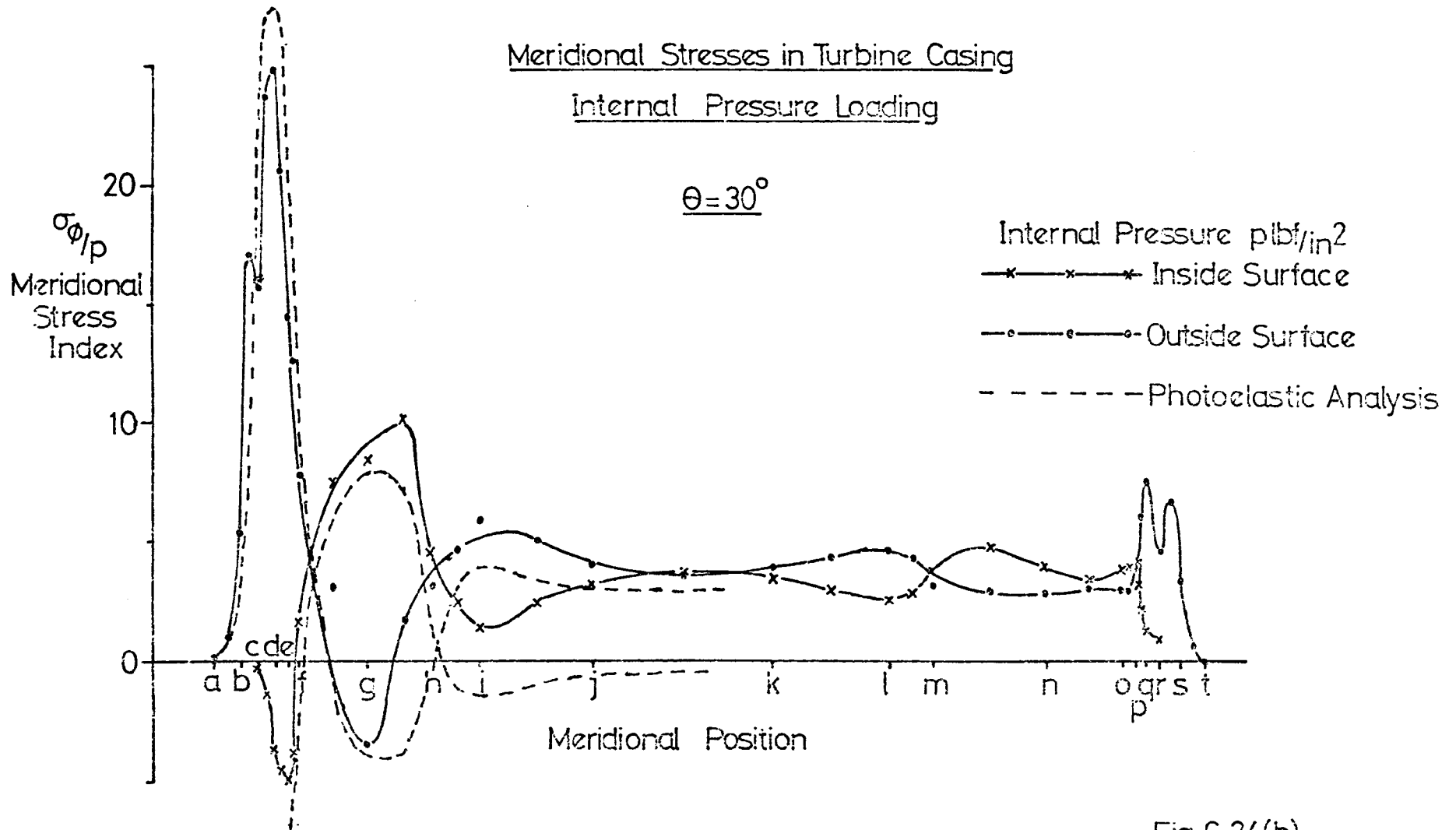


Fig.6.24(b)

Meridional Stresses in Turbine Casing
Internal Pressure Loading

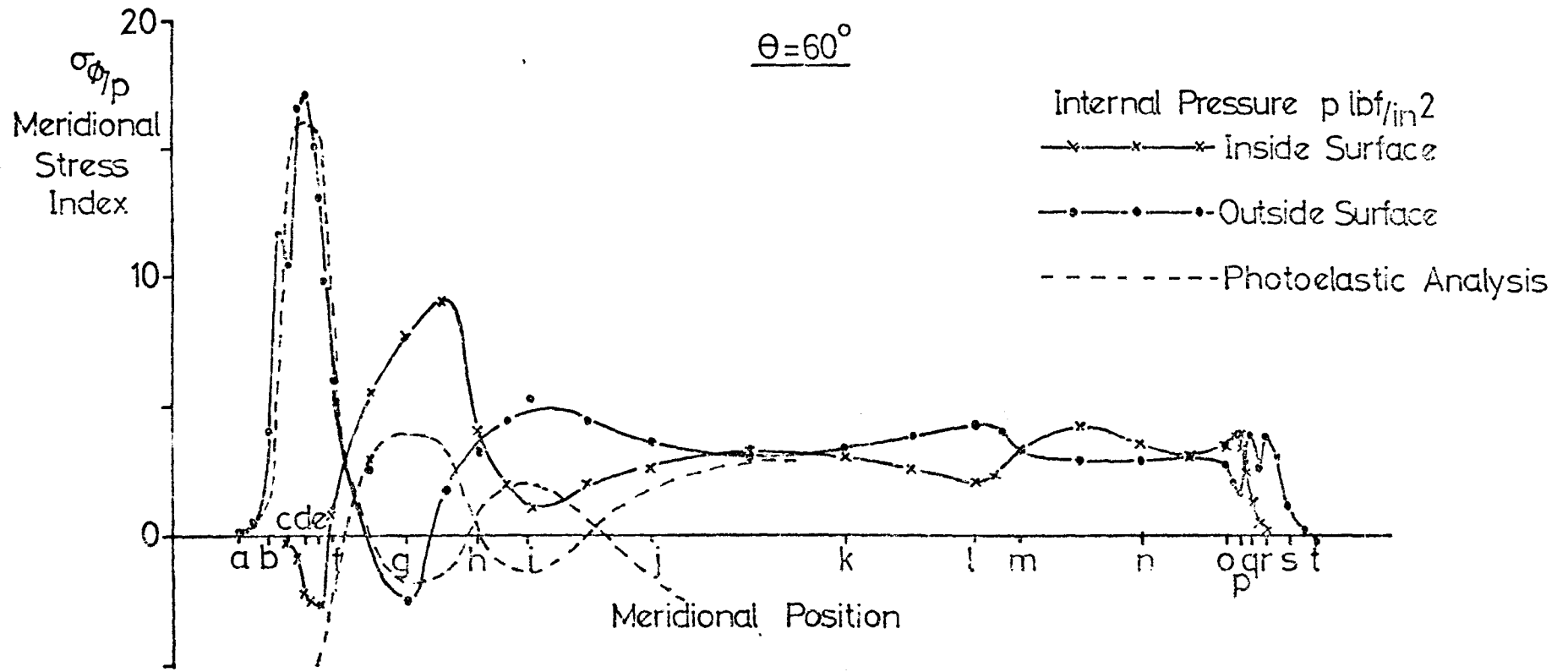


Fig. 6.24(c)

Meridional Stresses in Turbine Casing

Internal Pressure Loading

$\theta = 90^\circ$ (Flange Face)

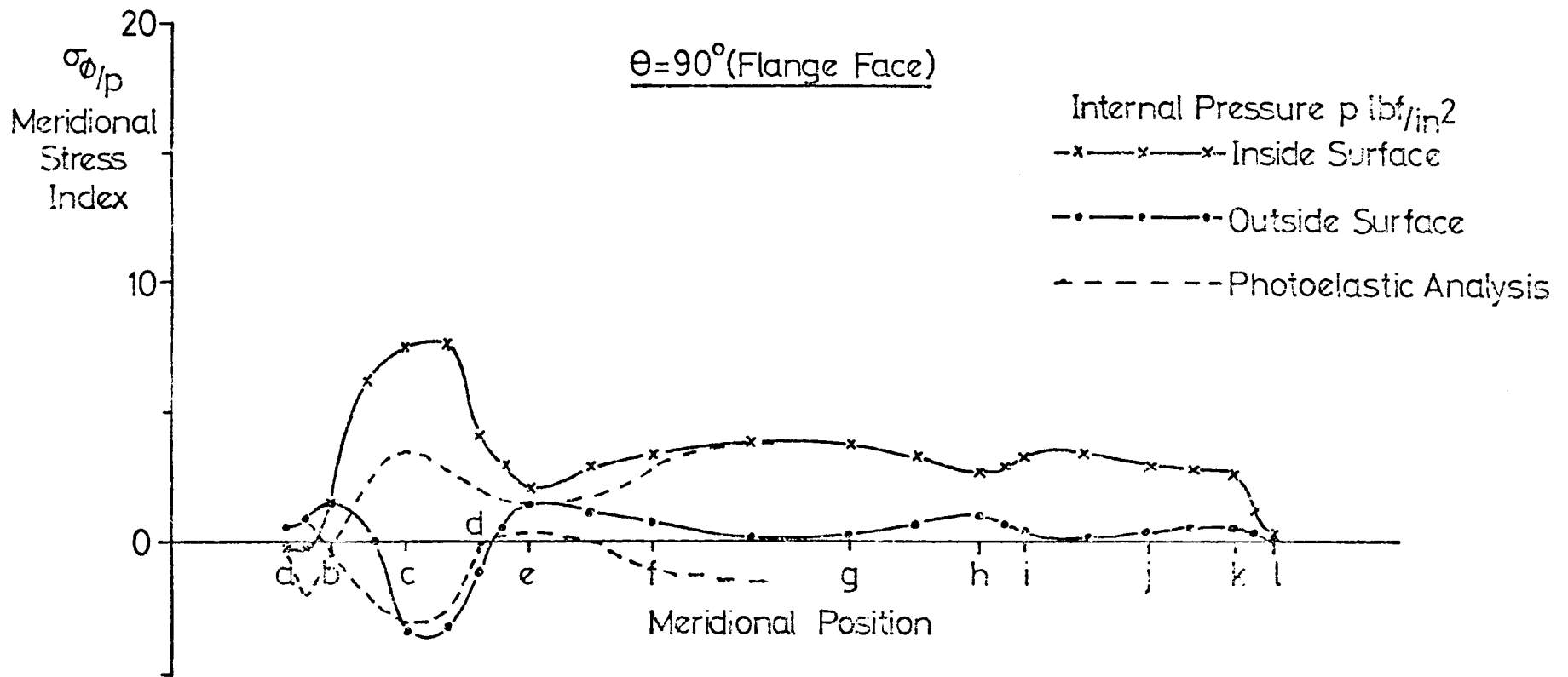
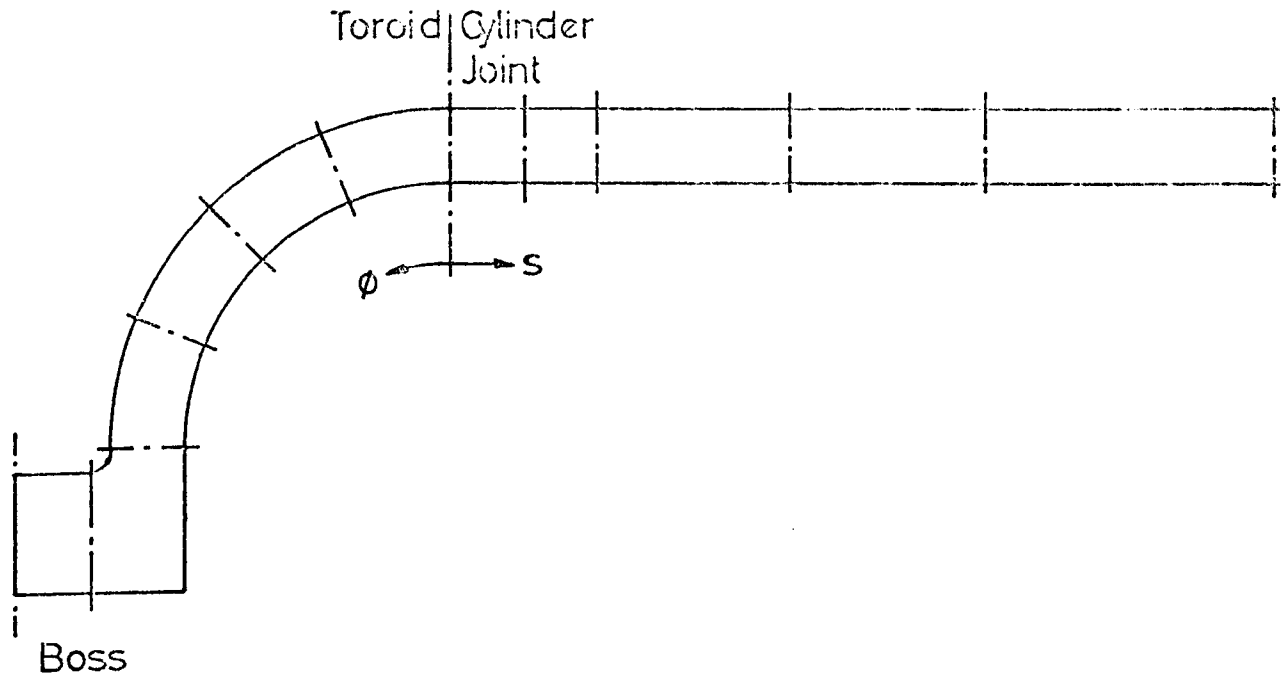


Fig. 6.24(d)

Meridional Positions of Hoop Stress Plots



Circumferential Positions for Hoop Stresses

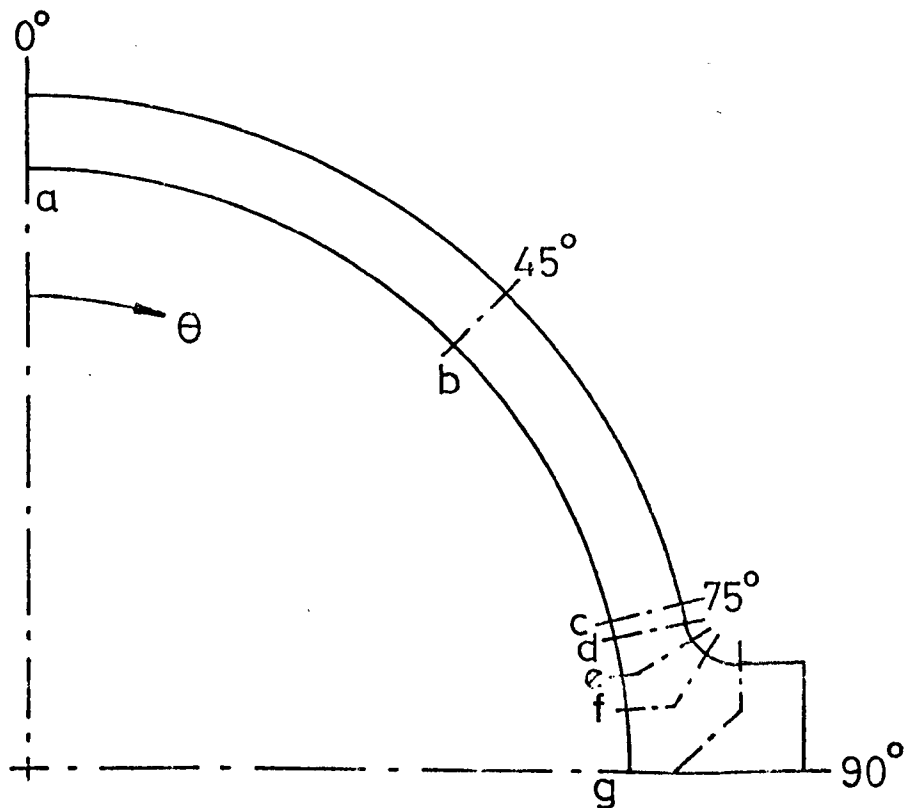


Fig.6.25

Hoop Stress Distributions Due to Internal Pressure Loading Only

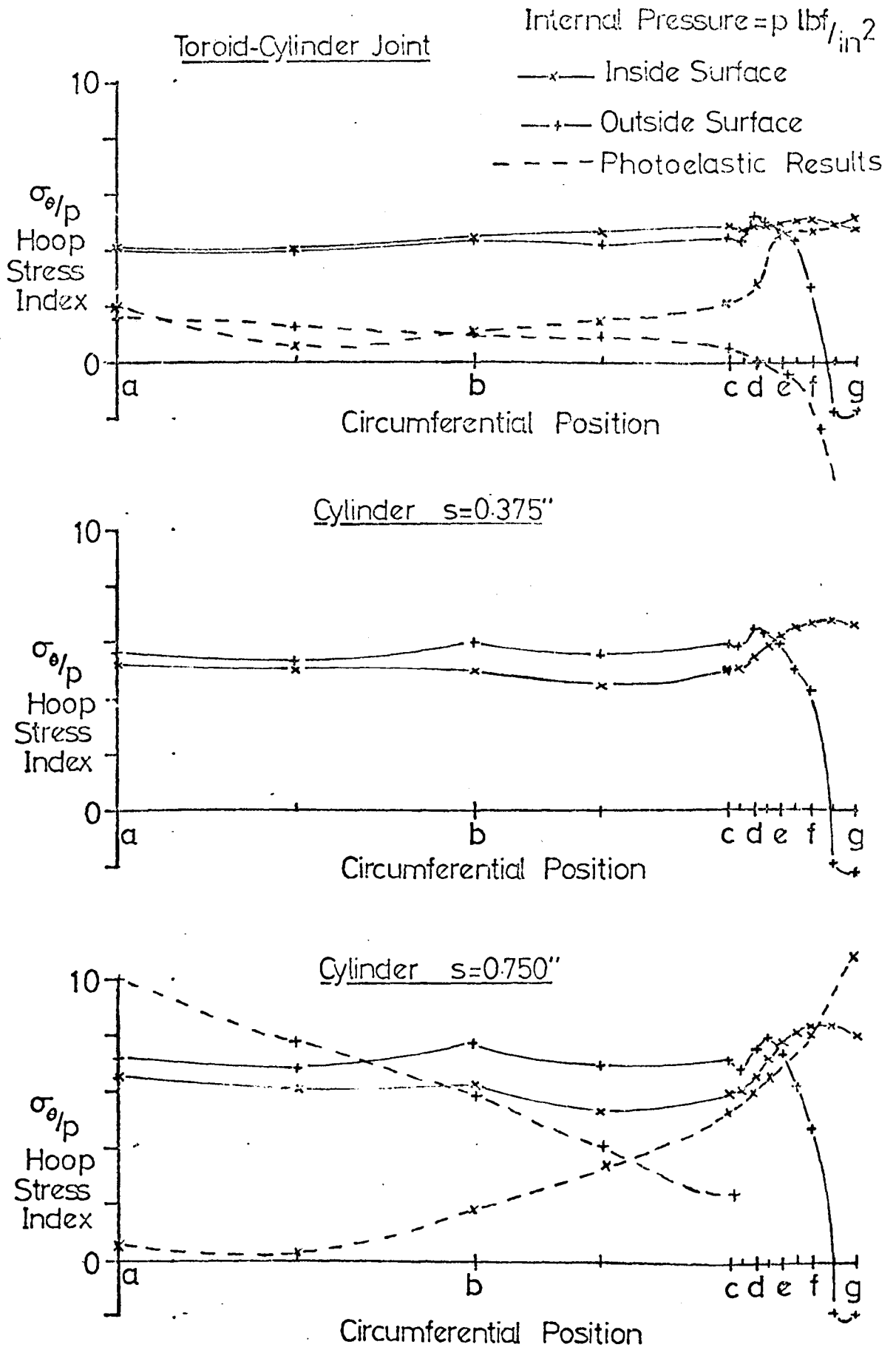


Fig.6.26

Hoop Stress Distributions Due to Internal Pressure Loading Only

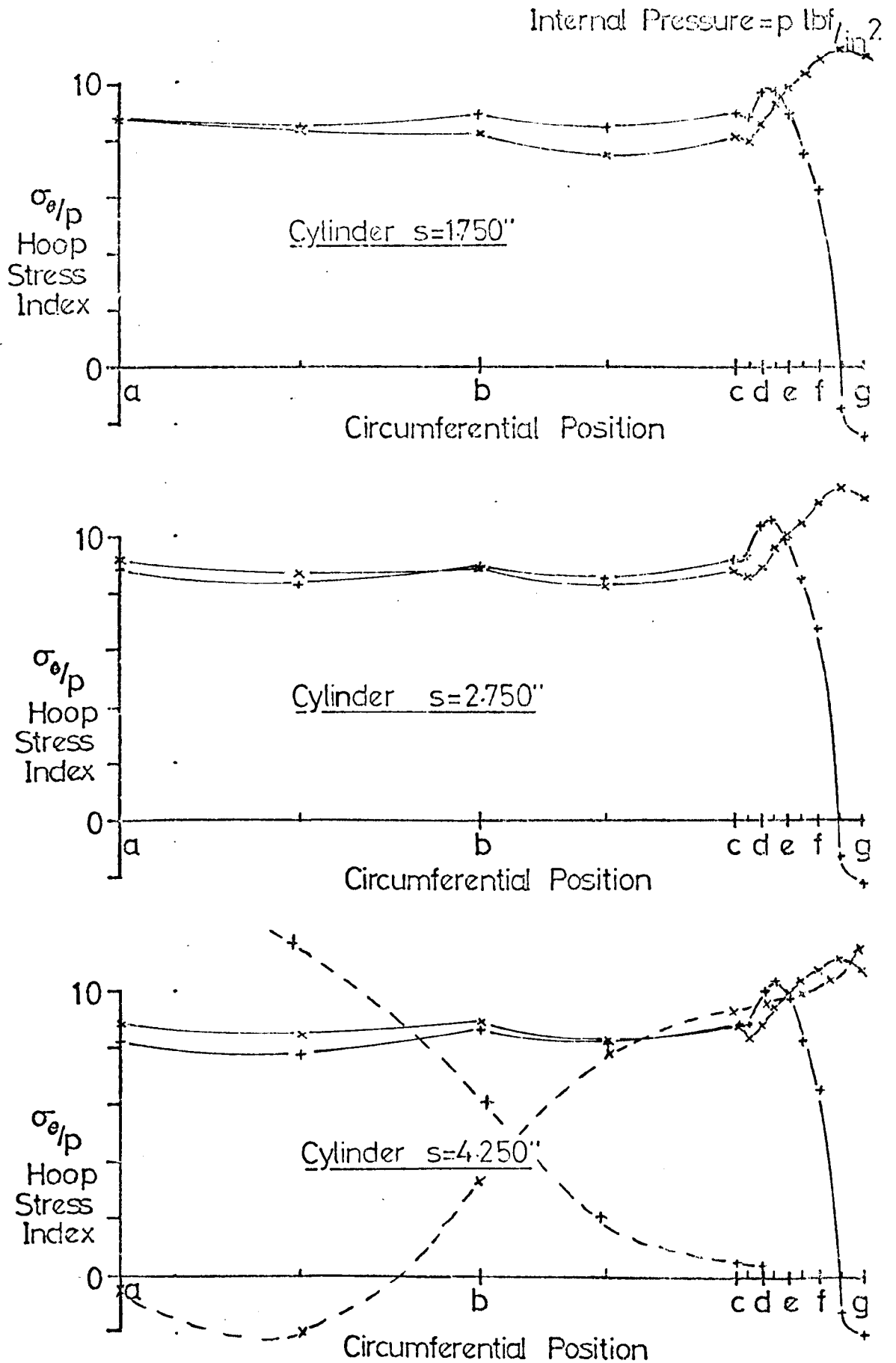


Fig.6.26

Hoop Stress Distributions Due to Internal Pressure Loading Only

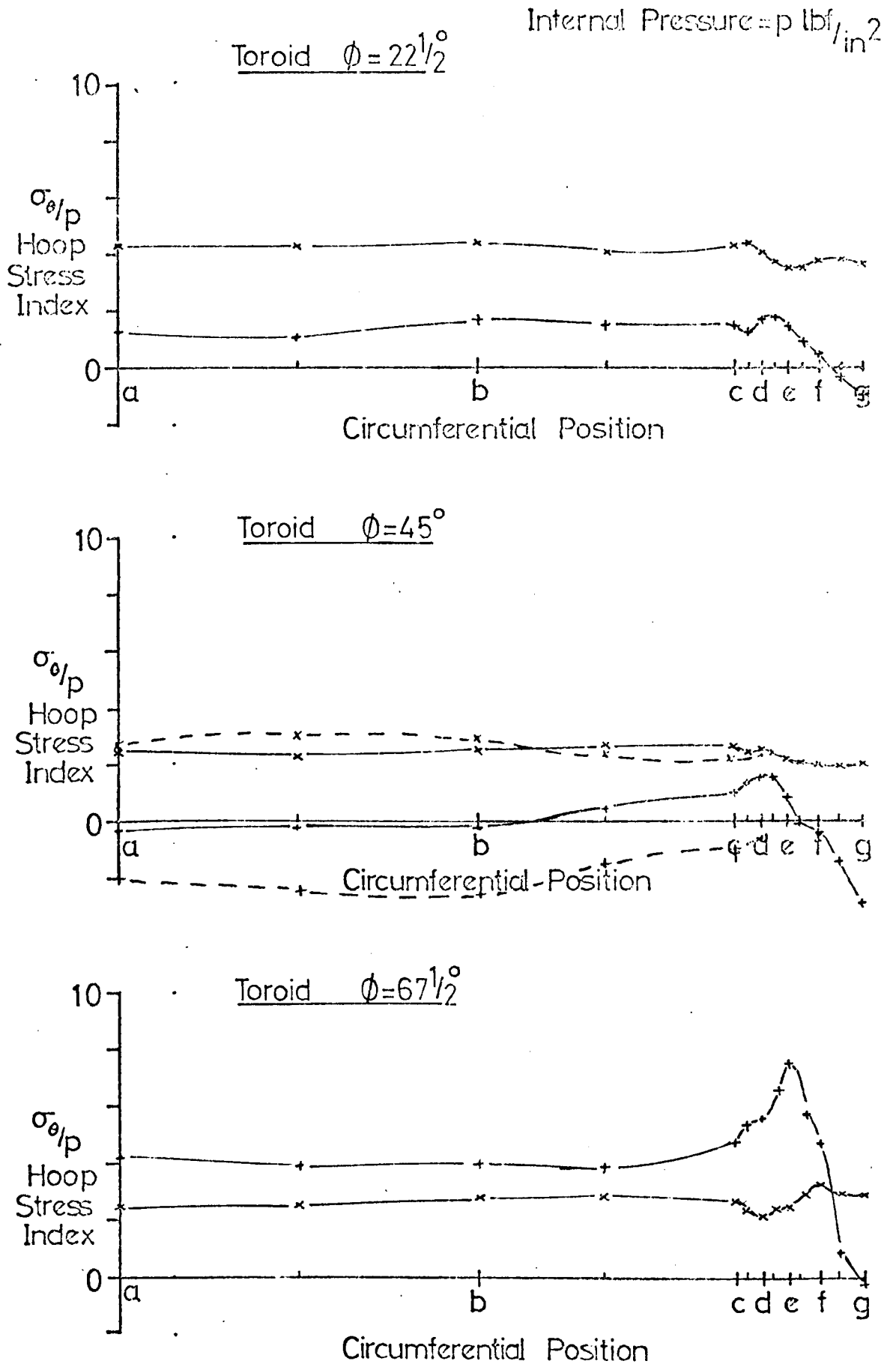


Fig.6.26

Hoop Stress Distributions Due to Internal Pressure Loading Only

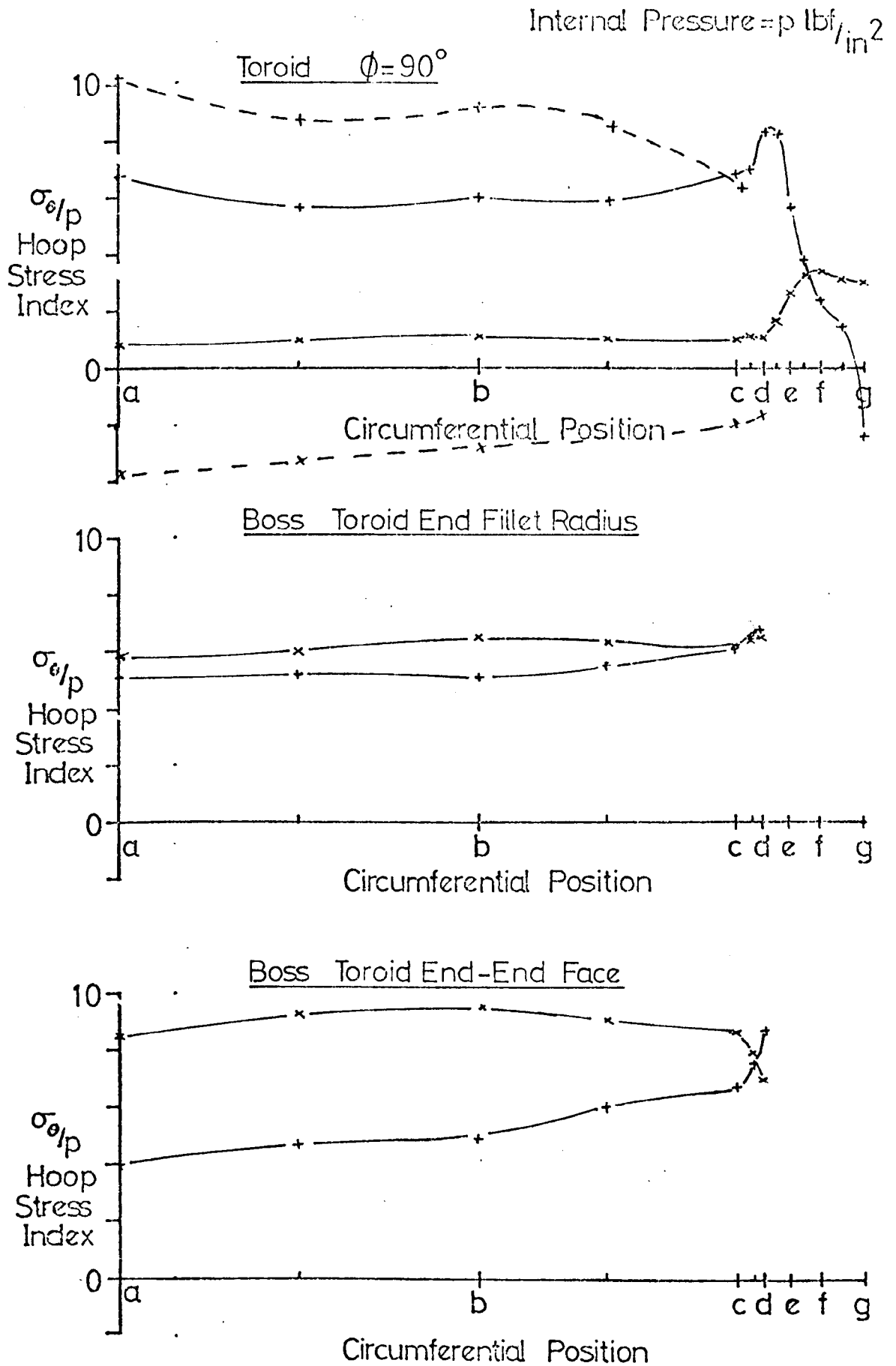


Fig.6.26

Meridional Variation in the Hoop Stresses in the Shell

Portion of a Turbine Casing

Internal Pressure and Bolt Loading

$\theta = 0^\circ$

Internal Pressure 35lb/in²

-x-x-x- Inside Surface

-o-o-o- Outside Surface

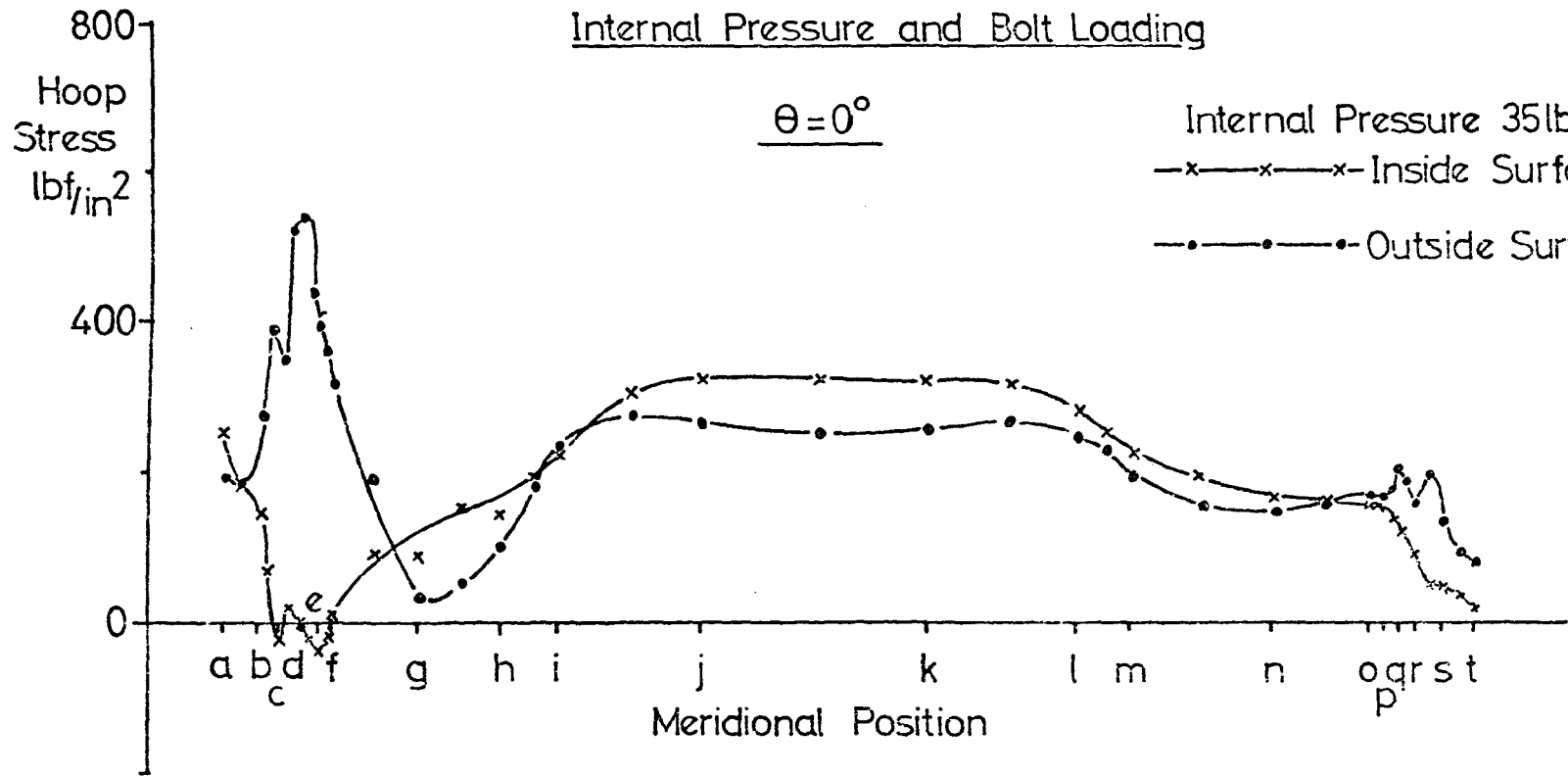


Fig. 6.27

Meridional Stresses in Turbine Casing

Internal Pressure and Bolt Loading

$\theta = 30^\circ$

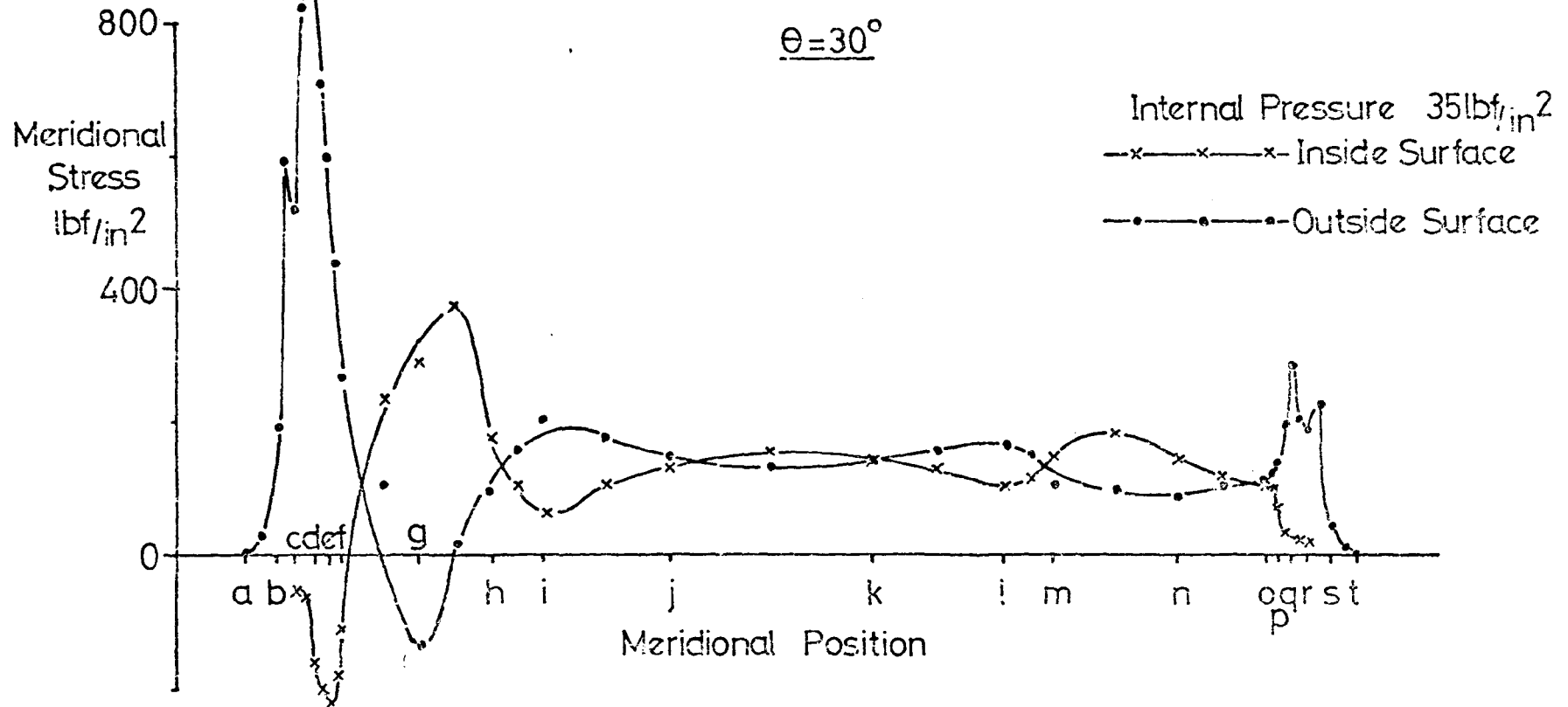


Fig. 6.28(b)

Meridional Stresses in Turbine Casing

Internal Pressure and Bolt Loading

$\theta = 30^\circ$

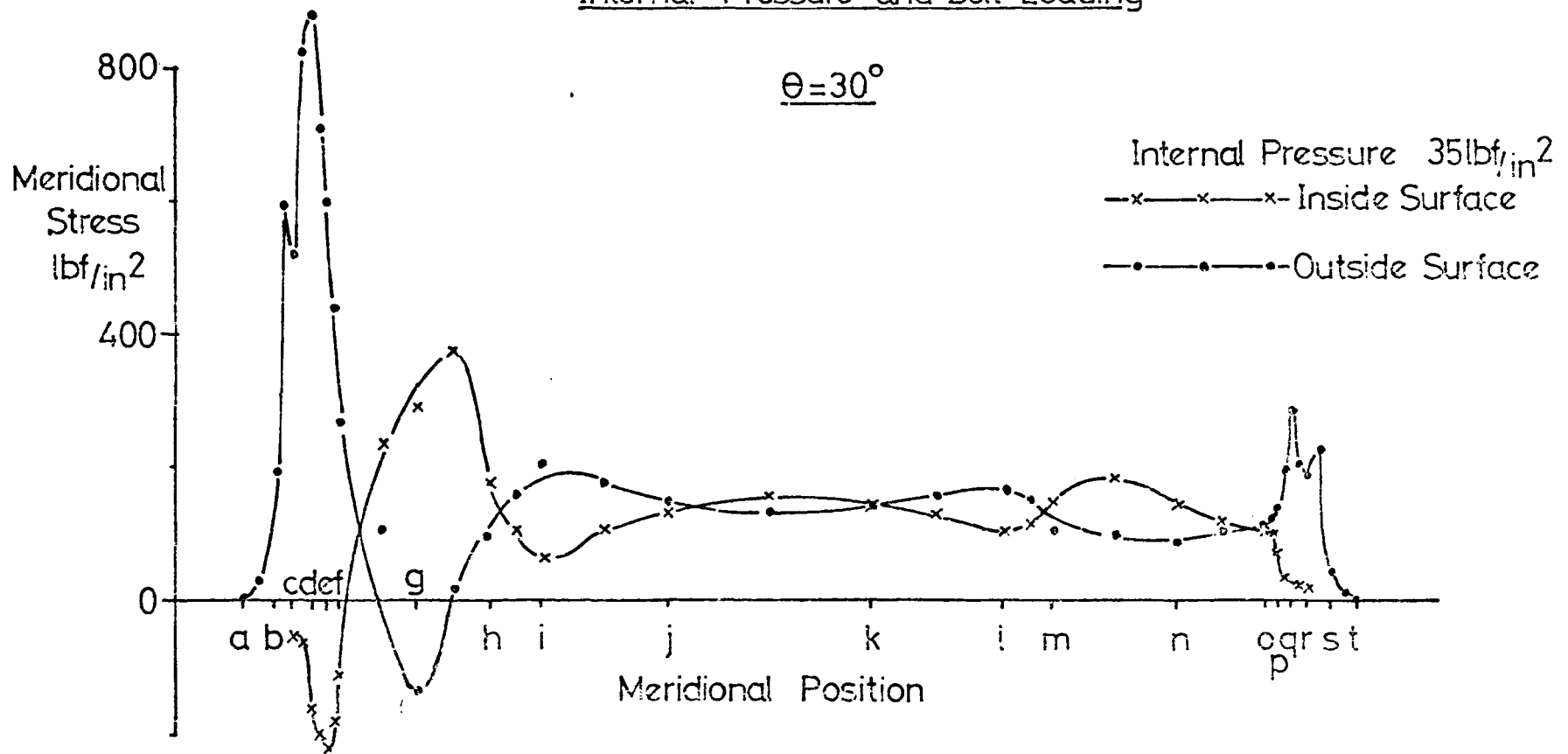


Fig.6.28(b)

Meridional Stresses in Turbine Casing

Internal Pressure and Bolt Loading

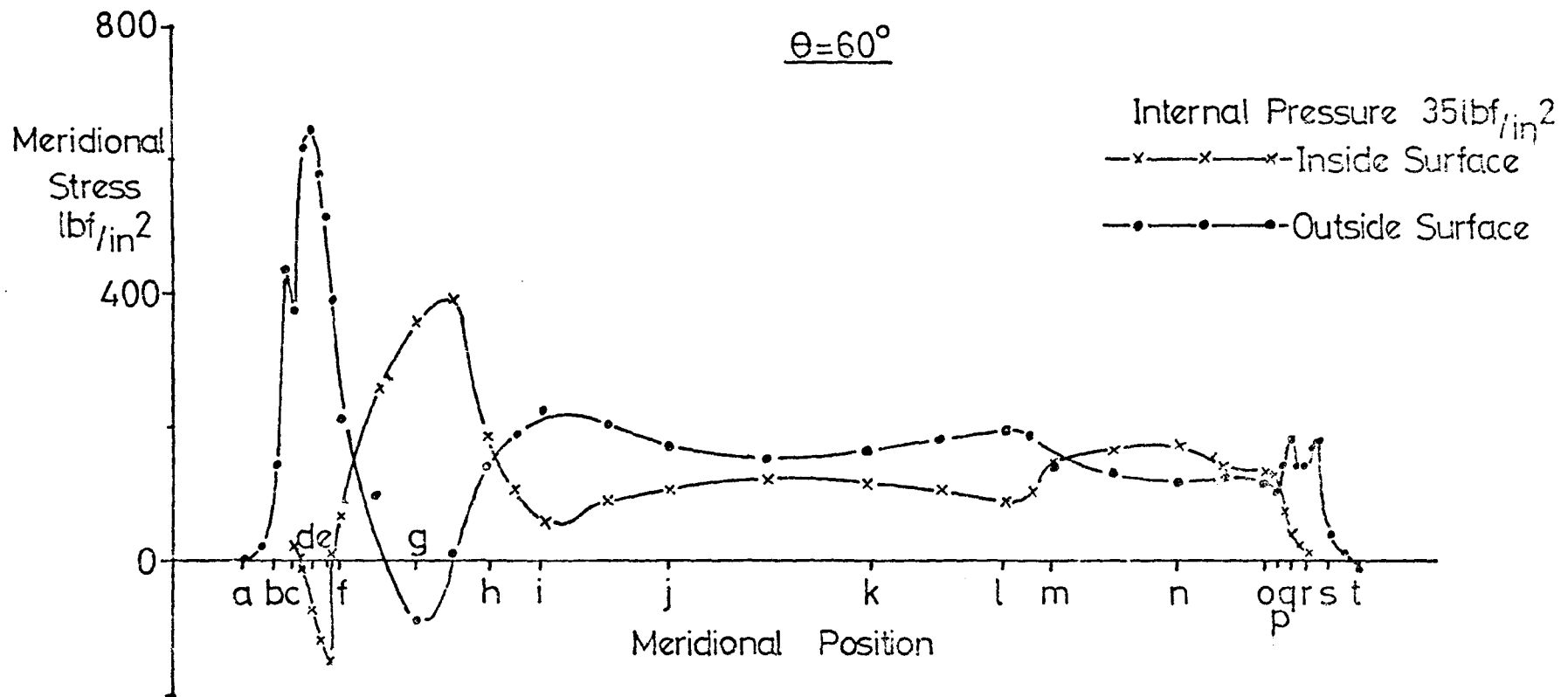


Fig. 6.28(c)

Meridional Stresses in Turbine Casing

Internal Pressure and Bolt Loading

$\theta = 90^\circ$ (Flange Face)

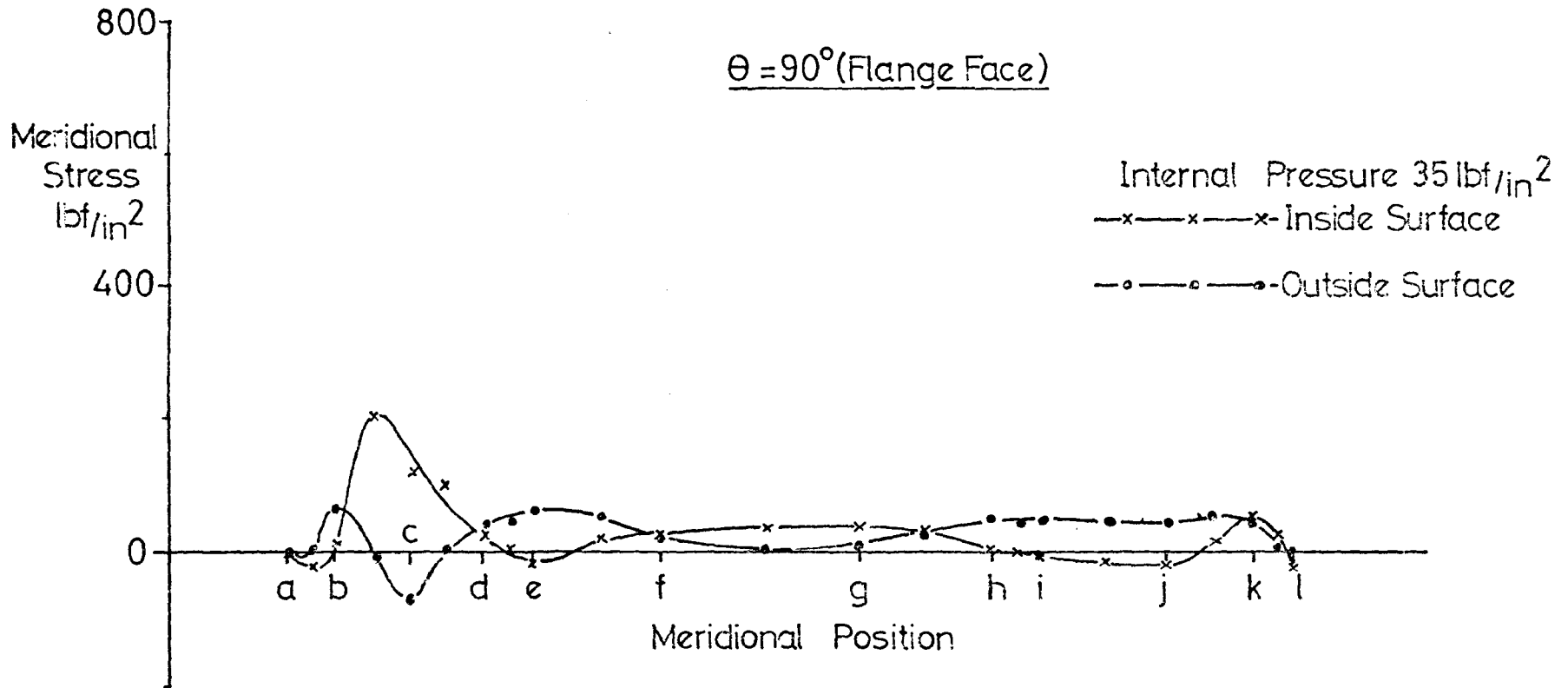


Fig.6.28(d)

Hoop Stress Distributions Due to Internal Pressure and Bolt Loading

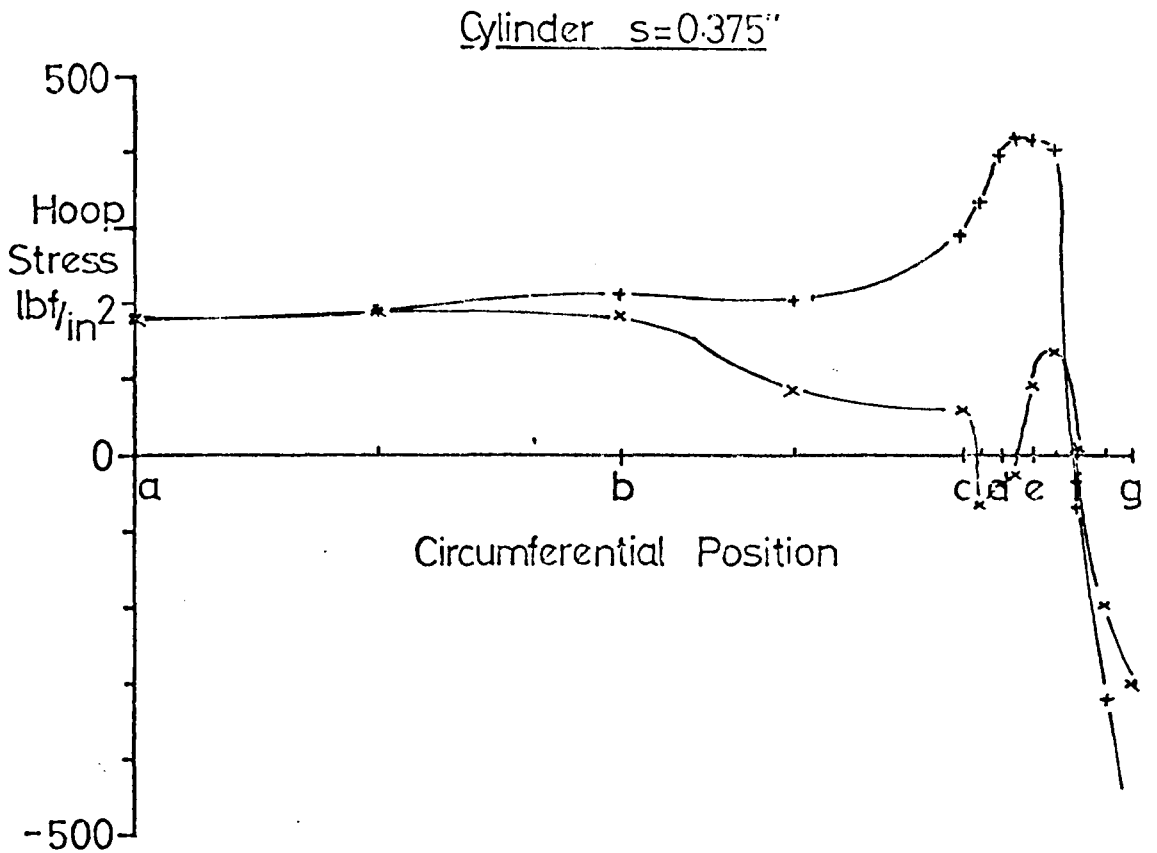
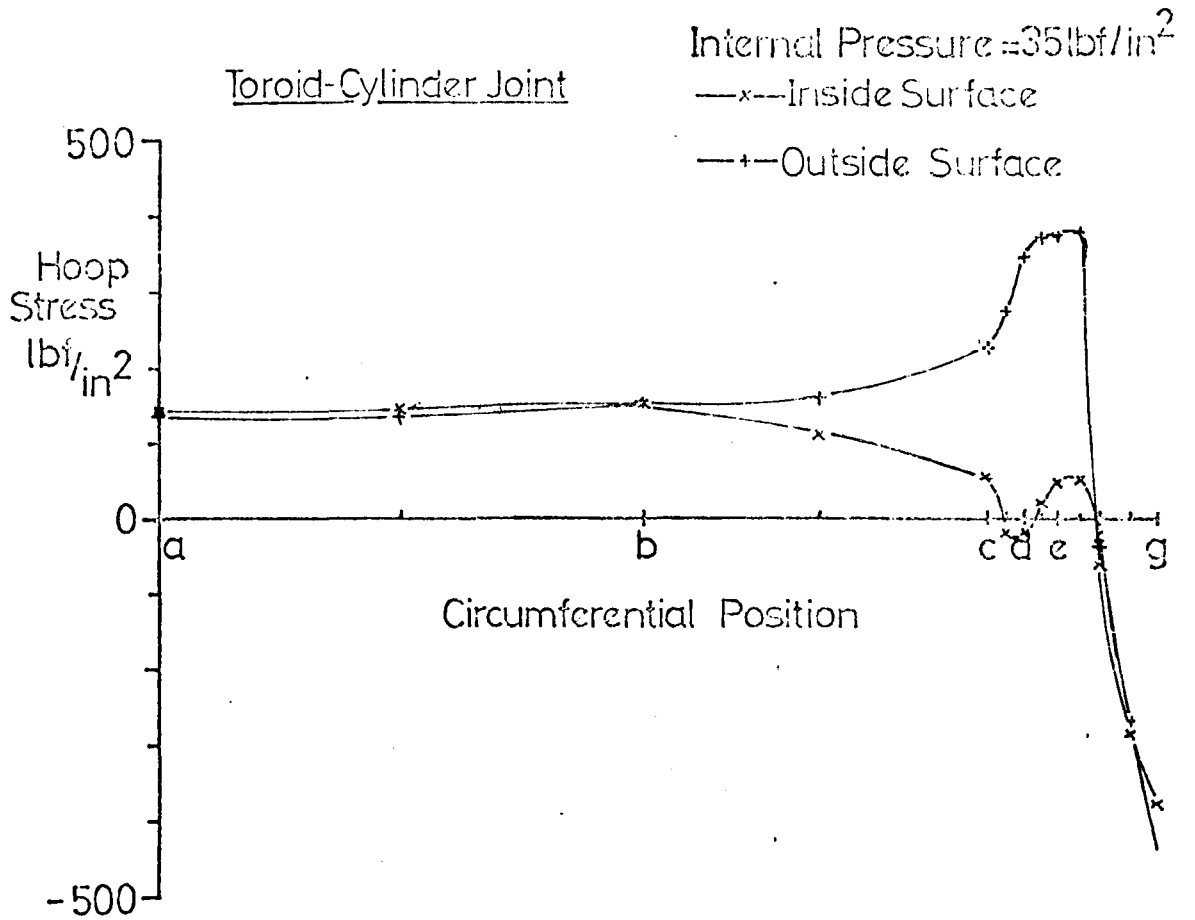


Fig.6.29

Hoop Stress Distributions Due to Internal Pressure and Bolt Loading

Internal Pressure = 35 lbf/in²

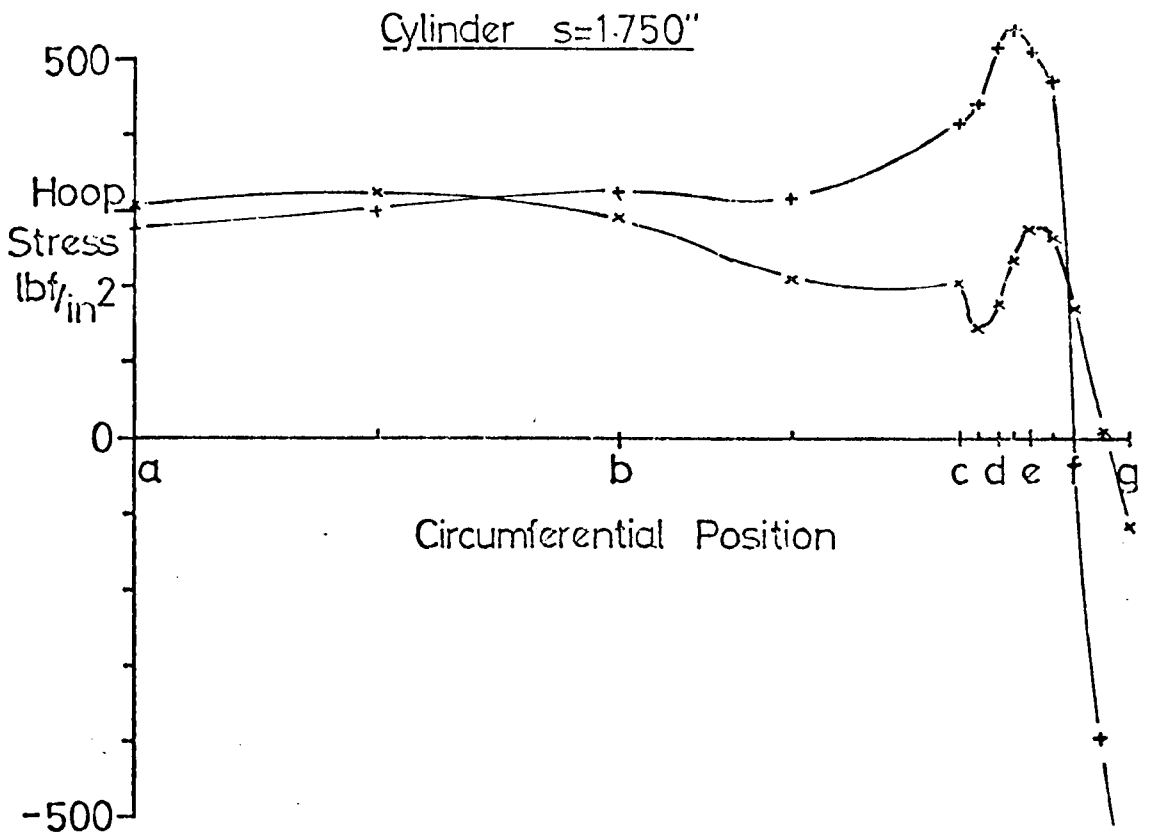
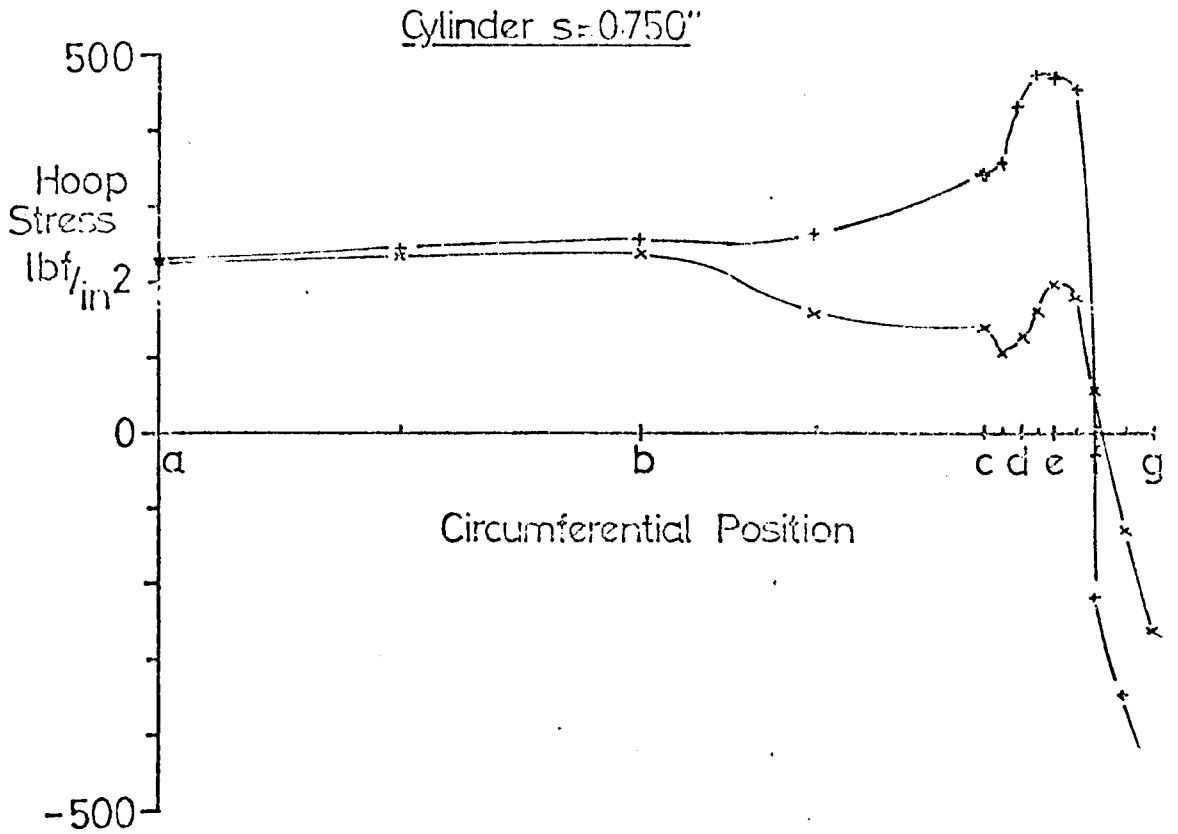


Fig.6.29

Hoop Stress Distributions Due to Internal Pressure and Bolt Loading

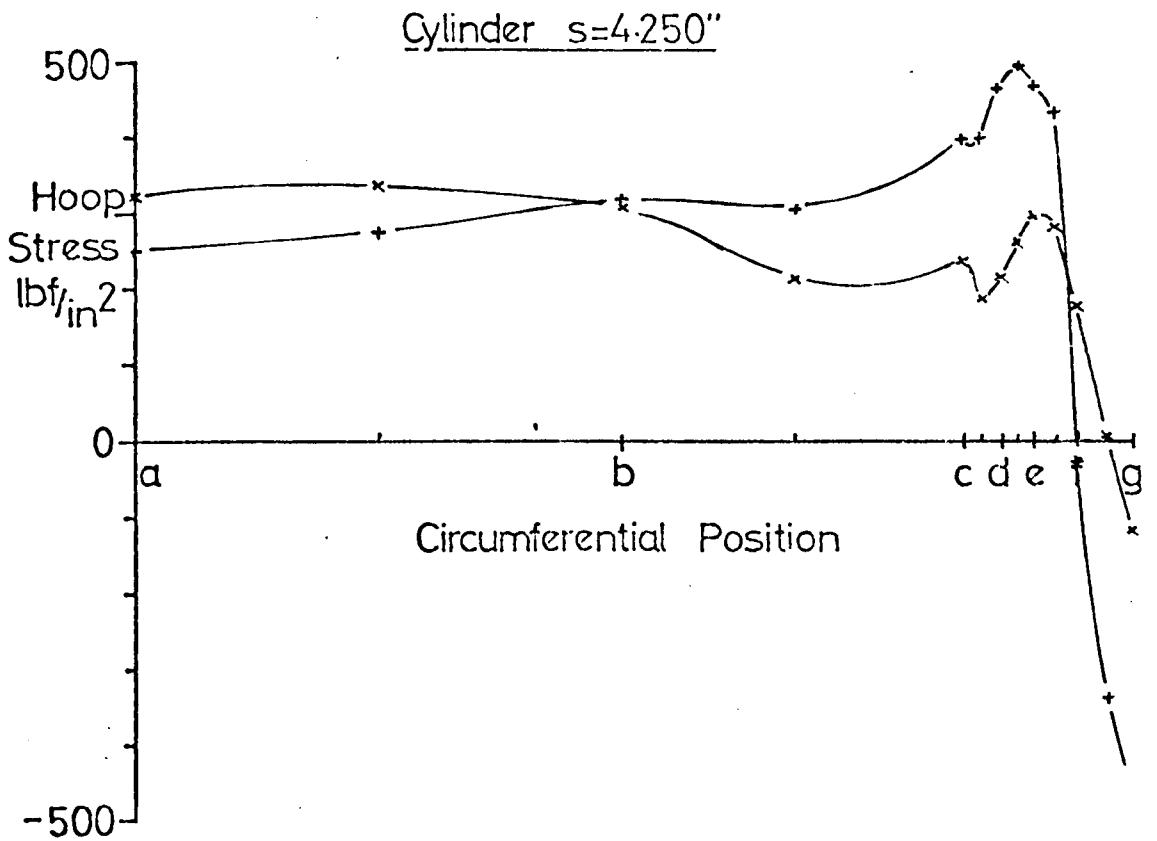
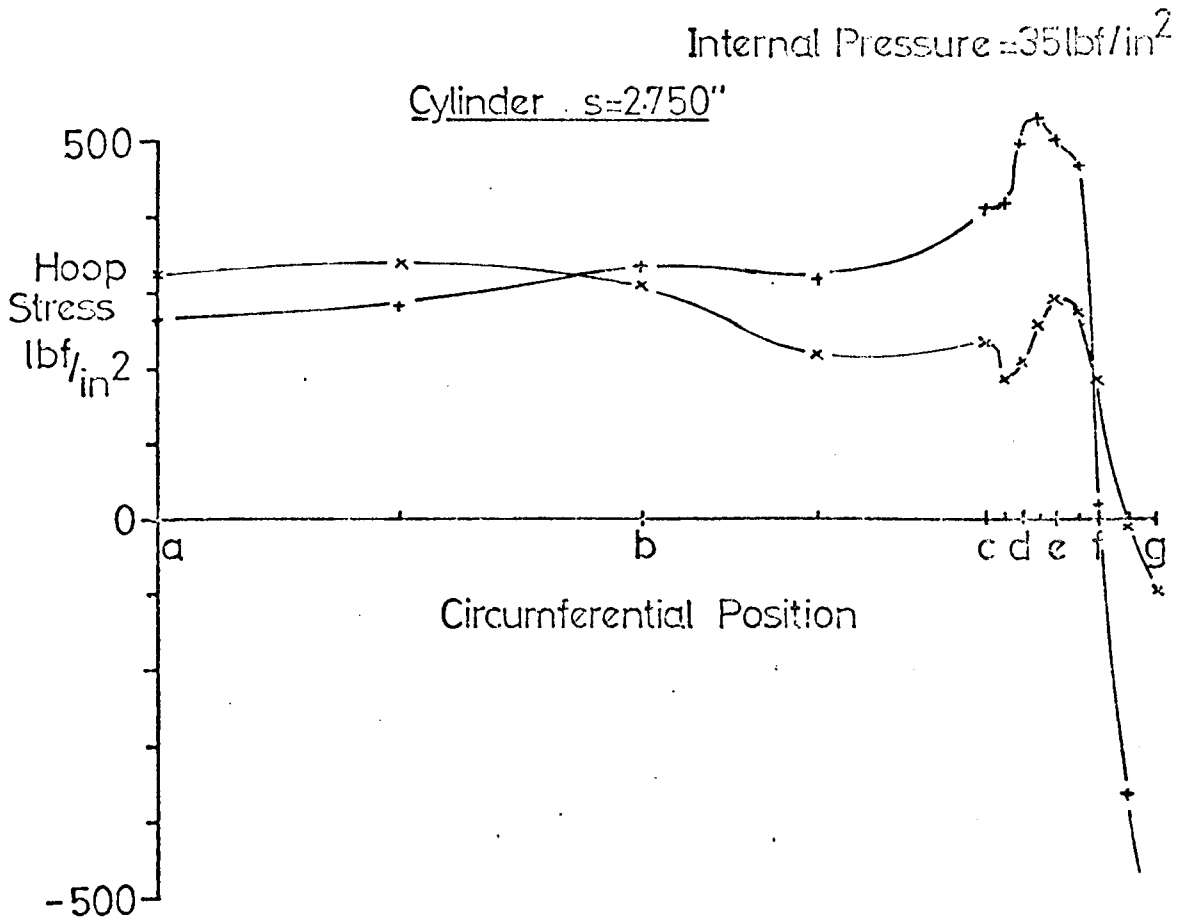
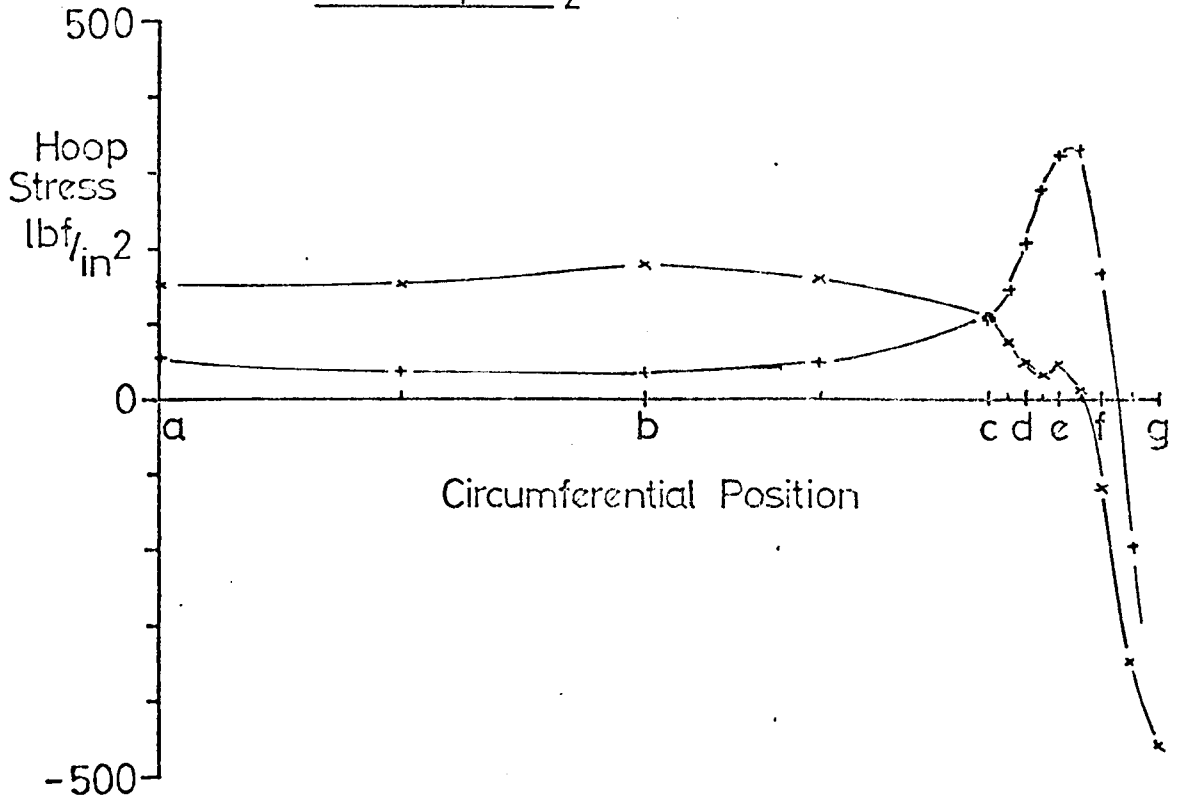


Fig.6.29

Hoop Stress Distributions Due to Internal Pressure and Bolt Loading

Internal Pressure = 35 lbf/in²

Toroid $\phi = 22\frac{1}{2}^\circ$



Toroid $\phi = 45^\circ$

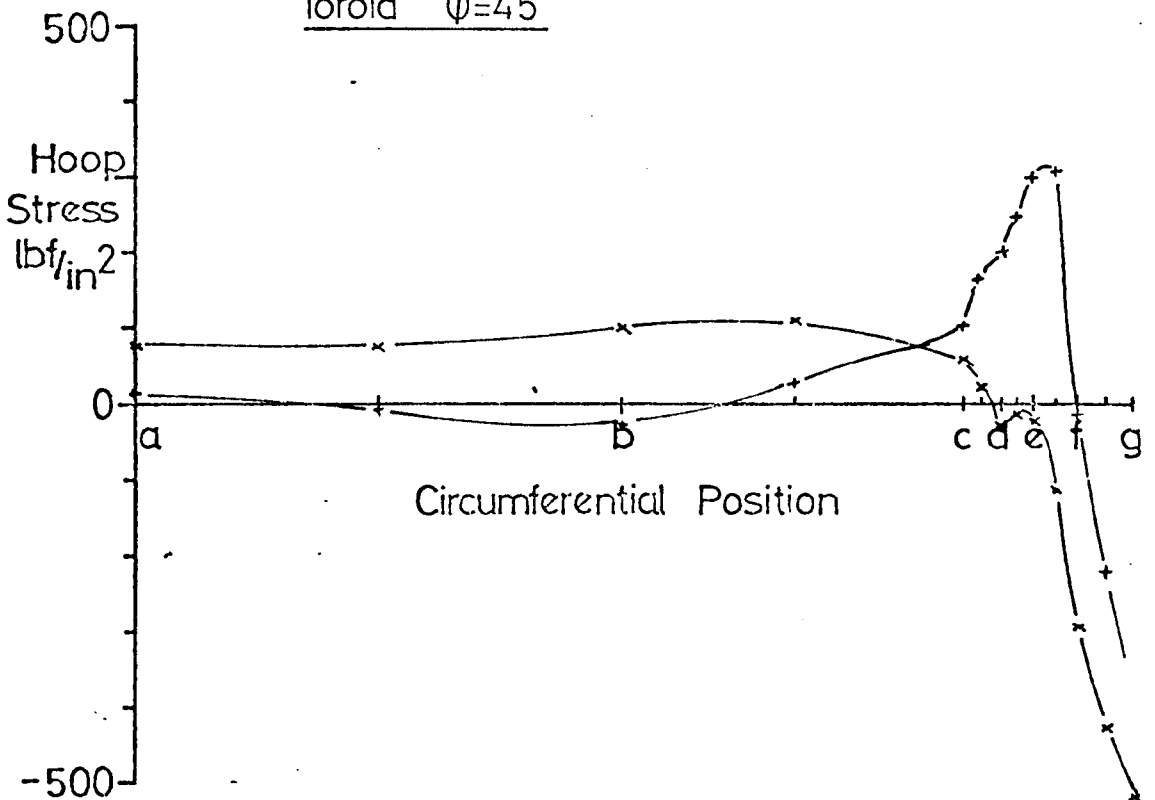


Fig.6.29

Hoop Stress Distributions Due to Internal Pressure and Bolt Loading

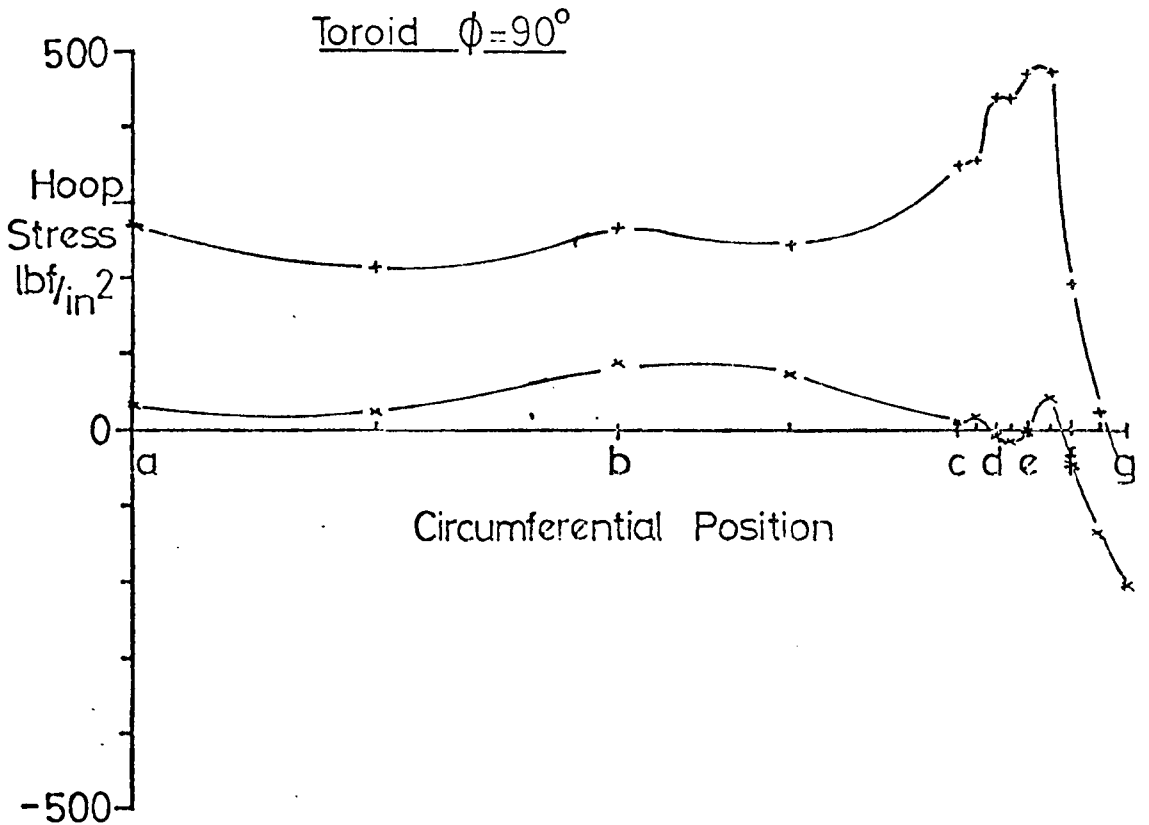
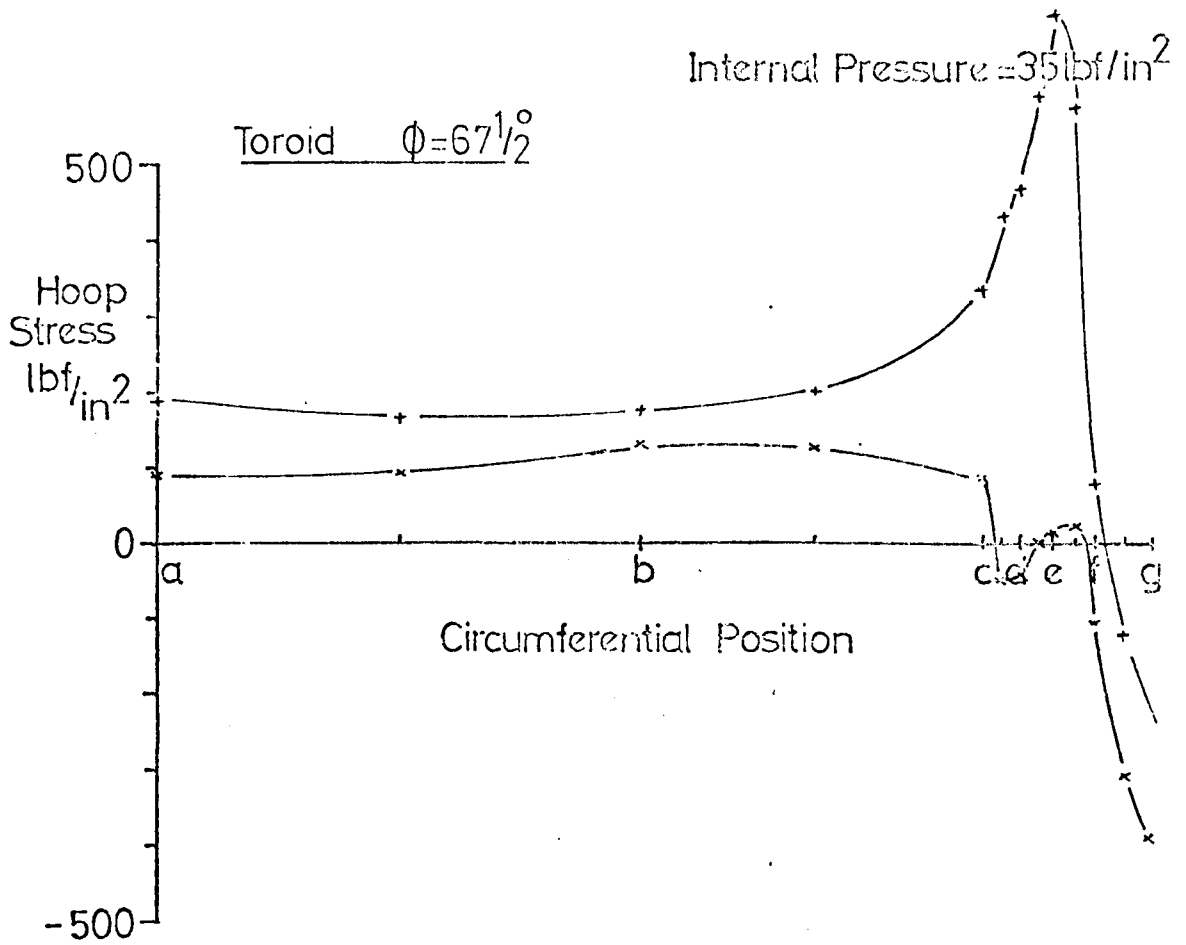


Fig.6.29

Hoop Stress Distributions Due to Internal Pressure and Bolt Loading

Internal Pressure = 35 lbf/in^2

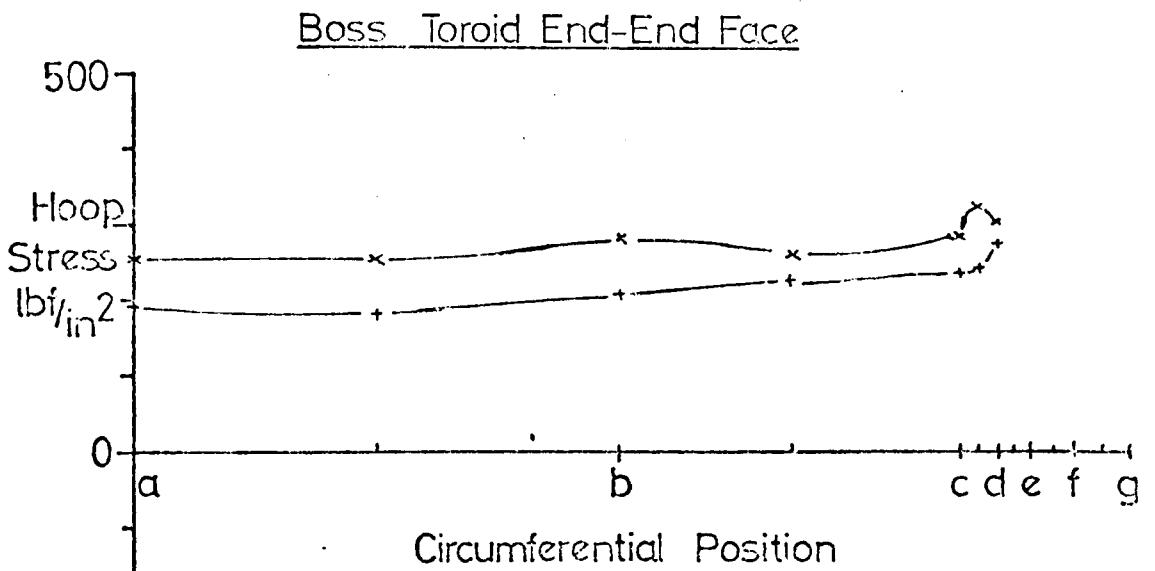
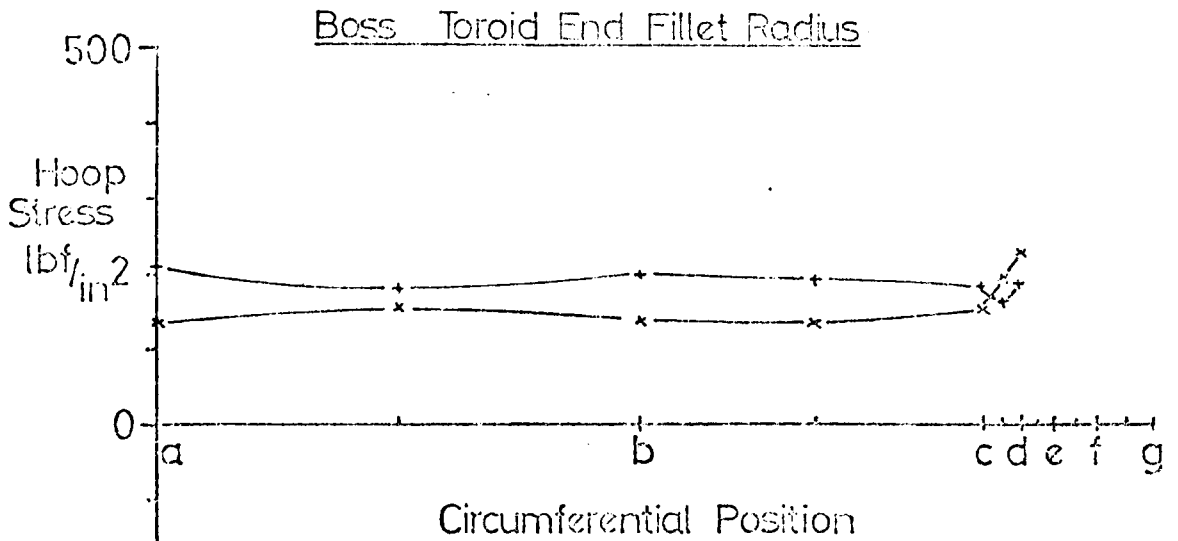


Fig.6.29

Meridional Positions in Axisymmetric Approximation
of Flanged Turbine Casing

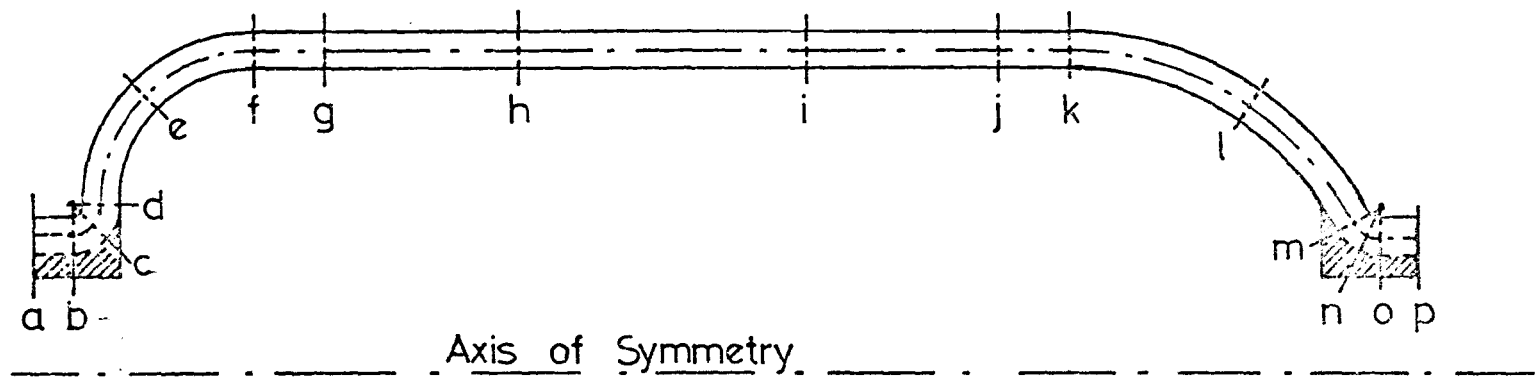


Fig. 6.30

Meridional Variation of Hoop Stresses for Axisymmetric

Approximation of Flanged Turbine Casing

Internal Pressure Loading

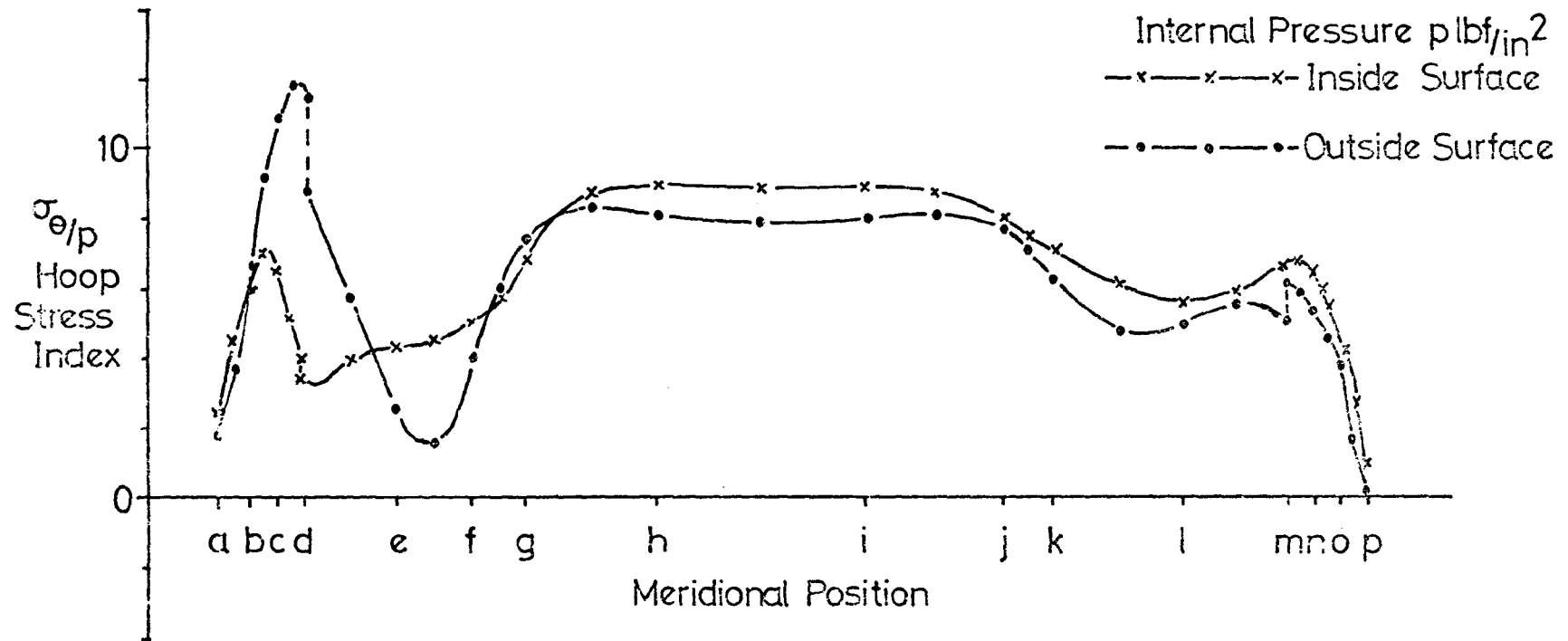


Fig.6.31

Meridional Stresses in Axisymmetric Approximation
to Flanged Turbine Casing
Internal Pressure Loading

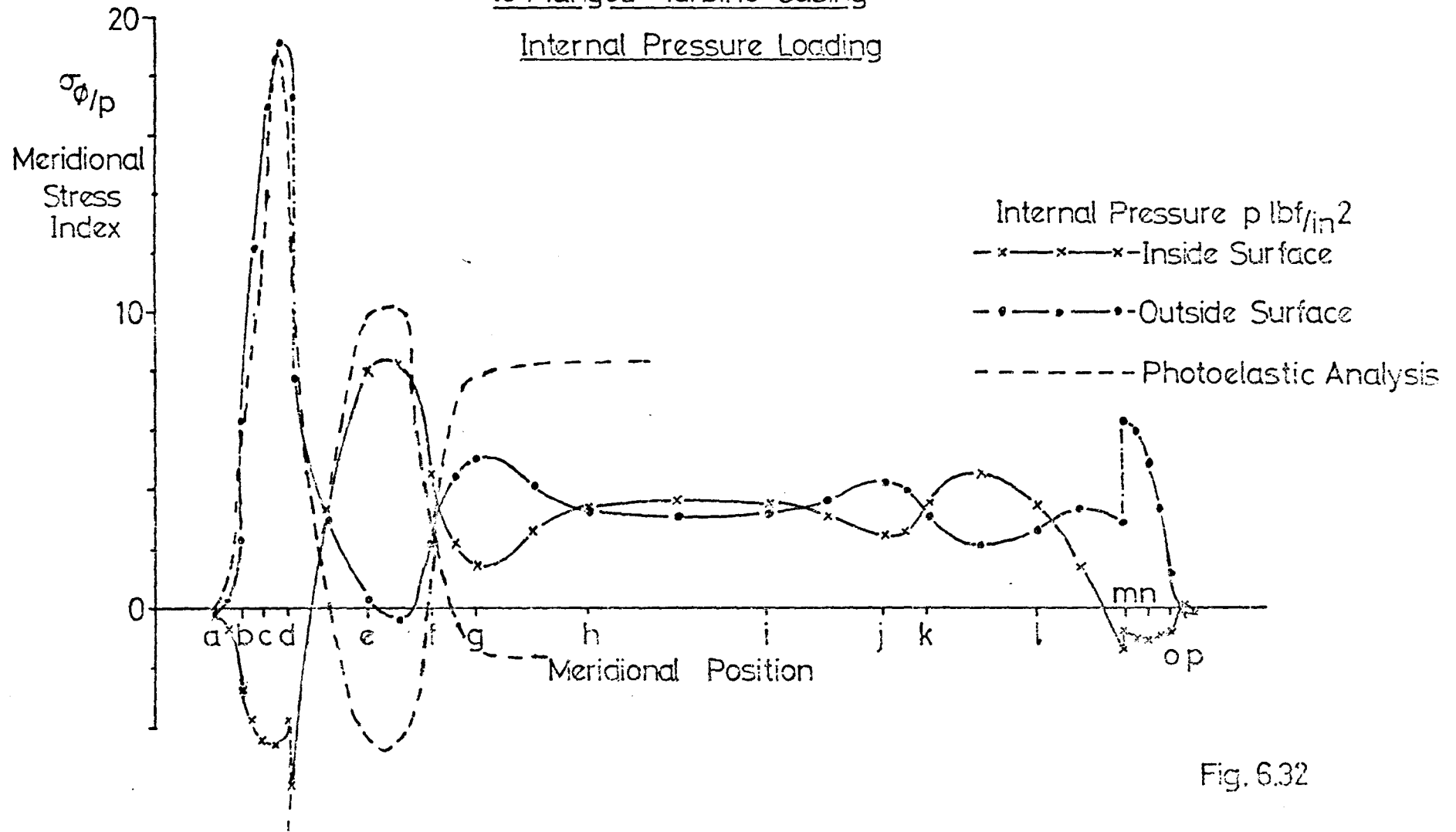


Fig. 6.32

Axial Deformation of Lead Turbine Casing Model with Time due to Creep

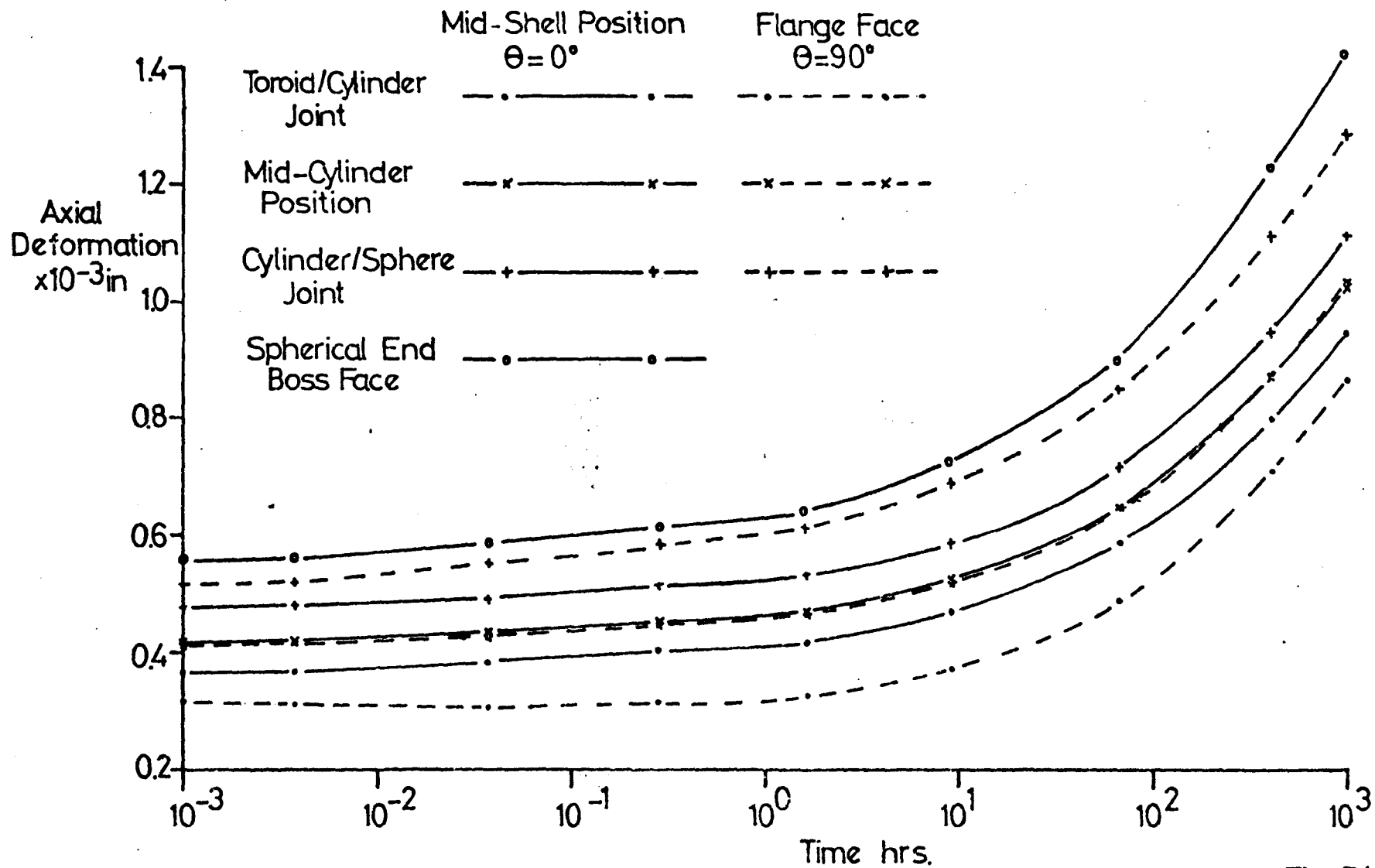


Fig. 7.1(a)

Deformation of Cylindrical Sections of Lead Turbine Casing

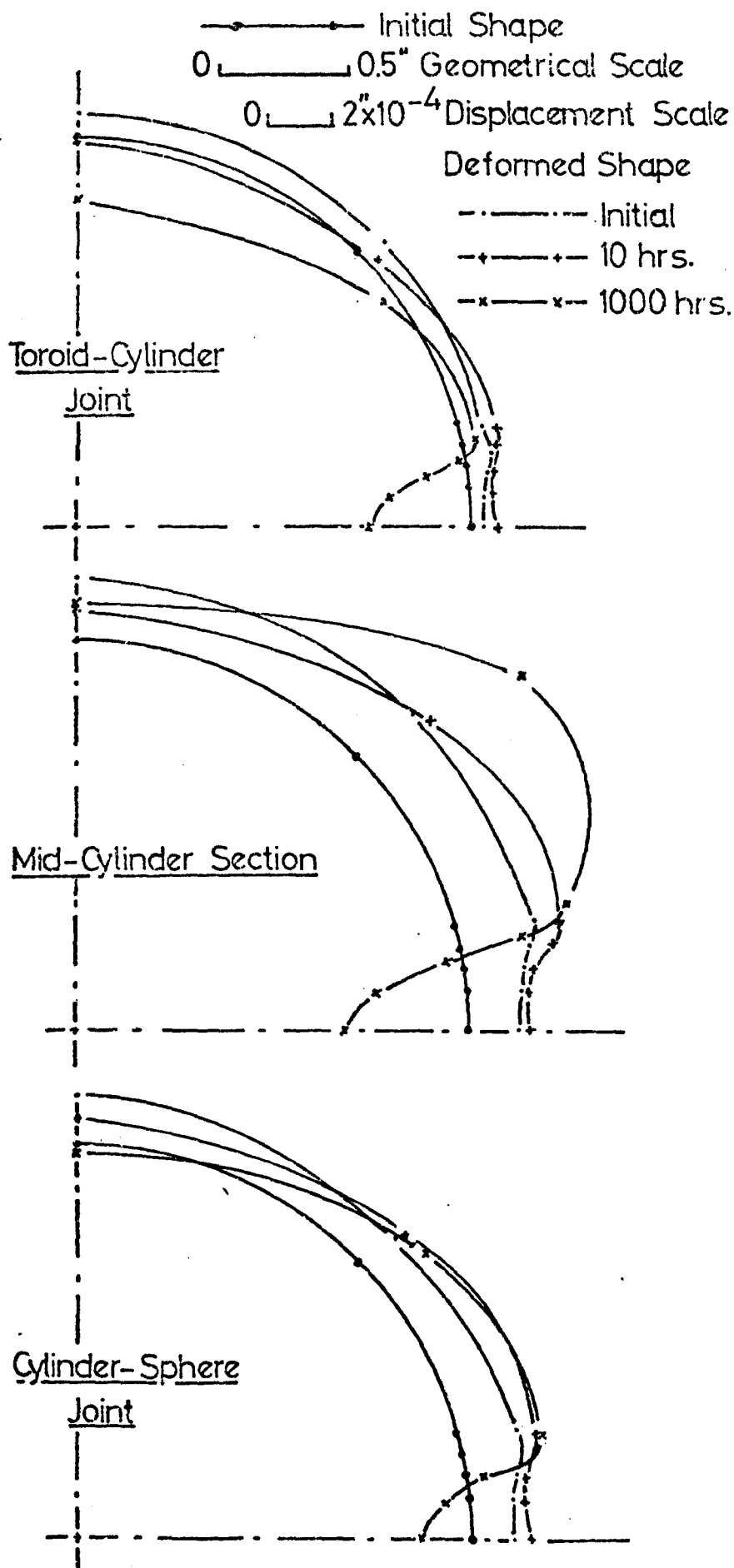
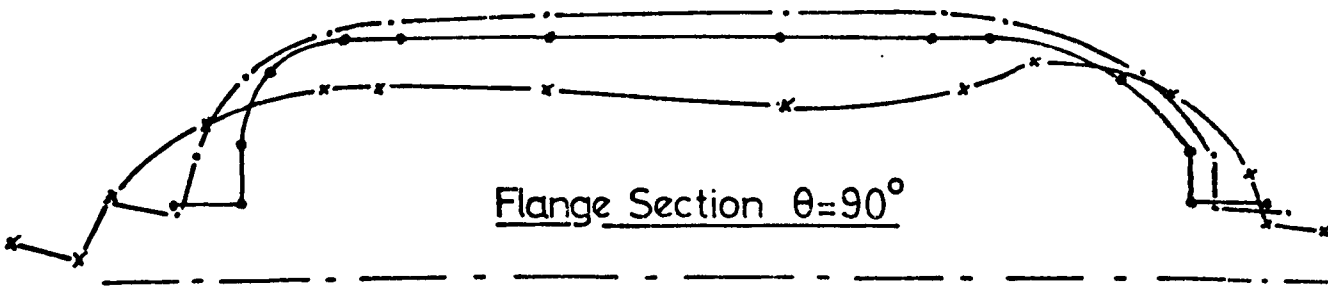
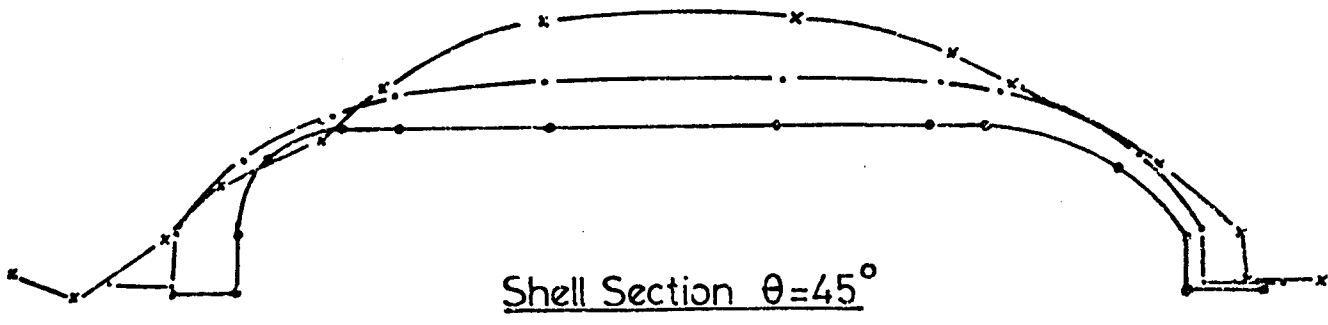
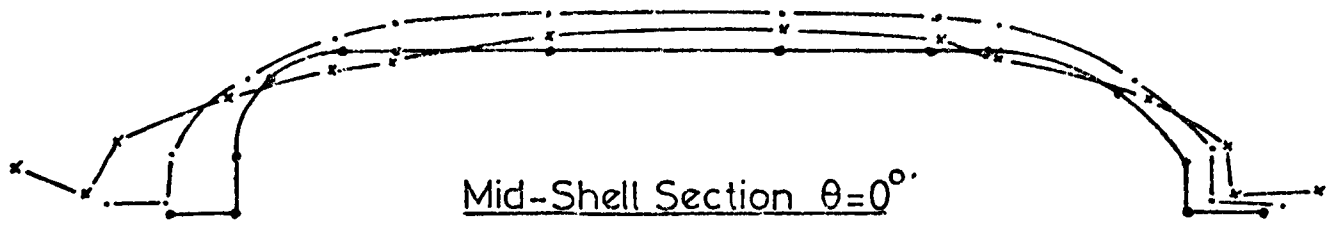


Fig.7.1(c)

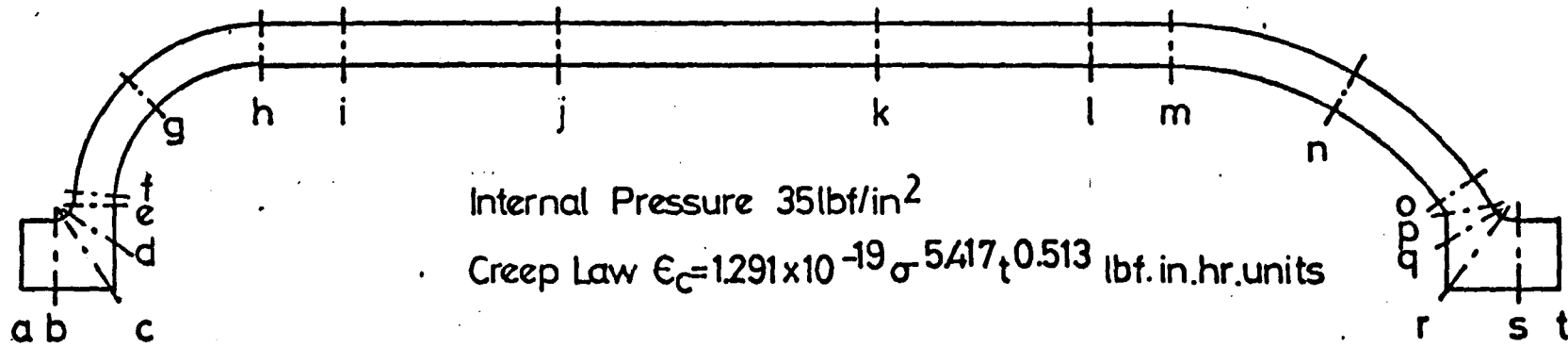
Radial Deformation of Axial Sections of Lead Turbine Casing



—●— Initial Shape
0  2" Geometrical Scale
0  1×10^{-3} Displacement Scale
Deformed Shape
- - - - - Initial
-x-x-x- 1000 hrs.

Fig.7.1(d)

Lead Turbine Casing Model-Meridional Positions at Mid-Shell Section $\theta=0^\circ$



Convention used in Creep Plots

	Time 0hrs.	Time 10hrs.	Time 1000hrs.
Inside Gauss Point	---o---o---o---	-x-x-x-	-+ -+ -+ -
Outside Gauss Point	---o---o---o---	-x-x-x-	-+ -+ -+ -

Fig.7.2

Total Circumferential Strain Distribution due to Creep Deformation
of Lead Turbine Casing

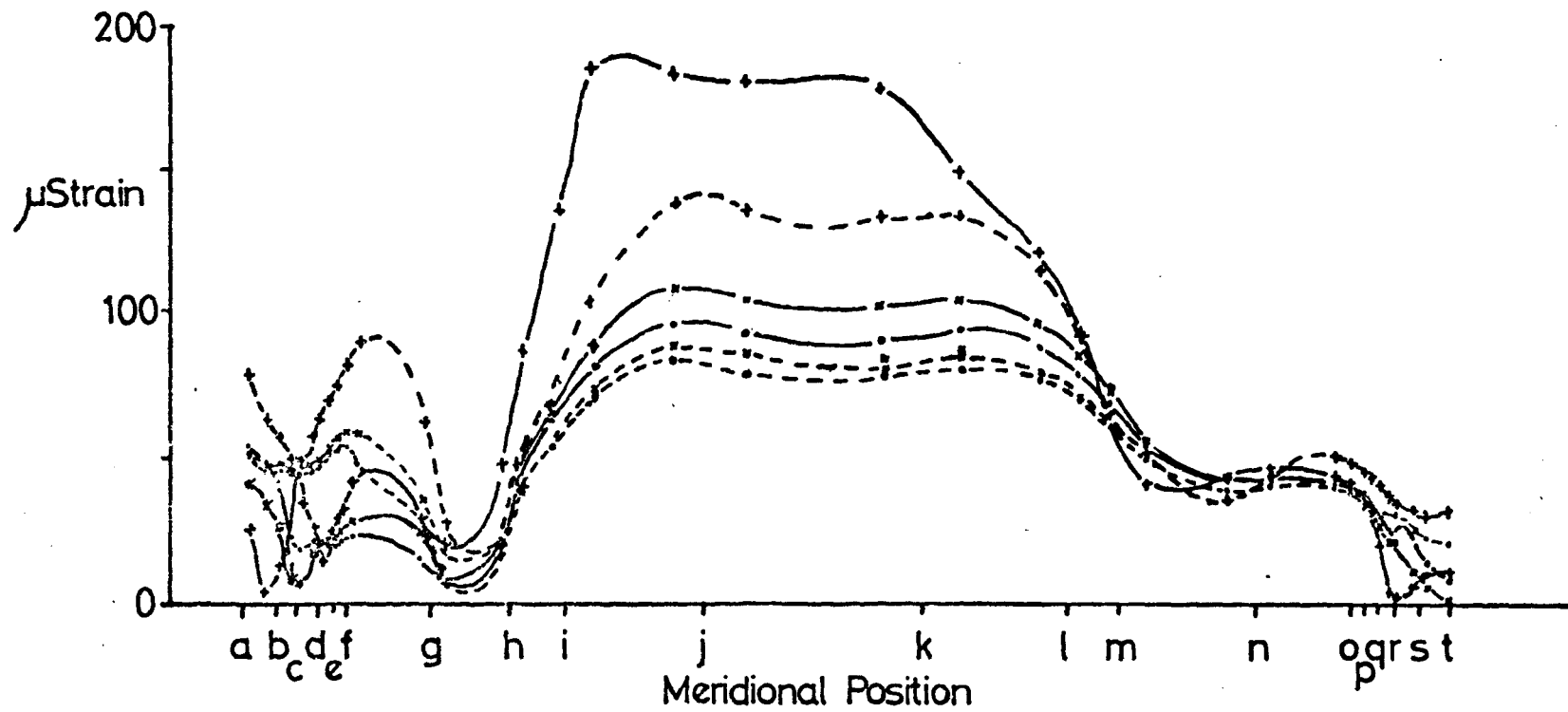


Fig.73(a)

Total Meridional Strain Distribution due to Creep Deformation
of Lead Turbine Casing

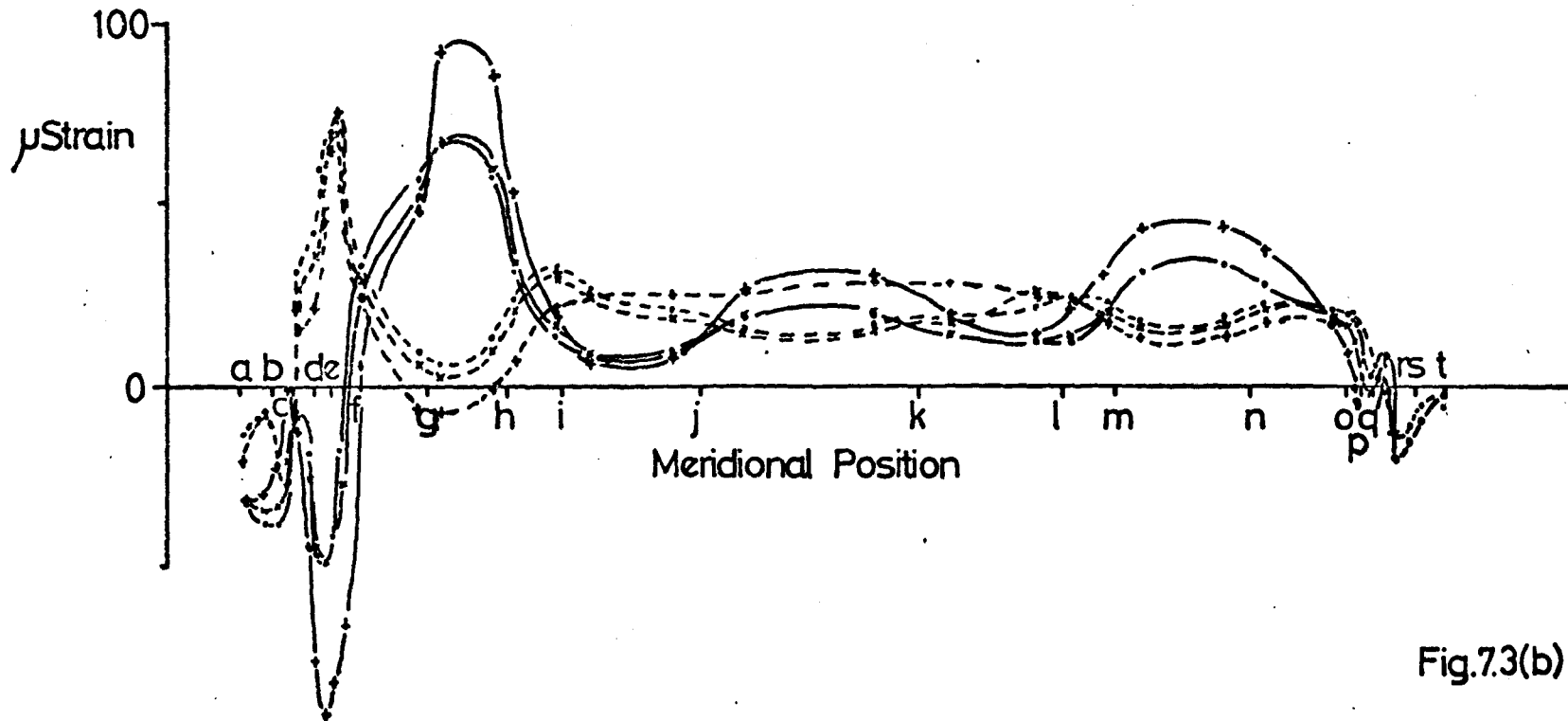


Fig.7.3(b)

Circumferential Stress Redistribution due to Creep Deformation
of Lead Turbine Casing

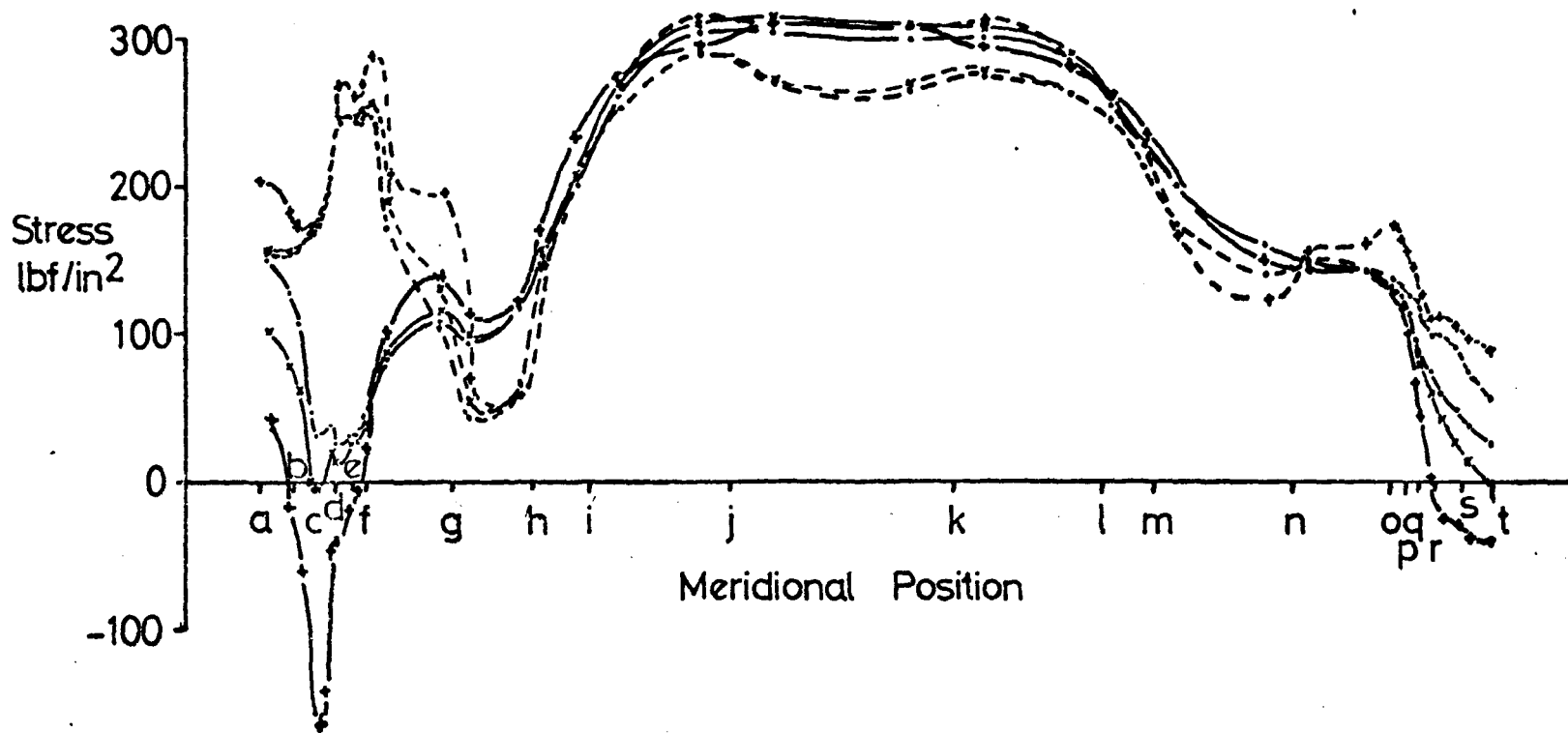


Fig.7.3(c)

Meridional Stress Redistribution due to Creep Deformation
of Lead Turbine Casing

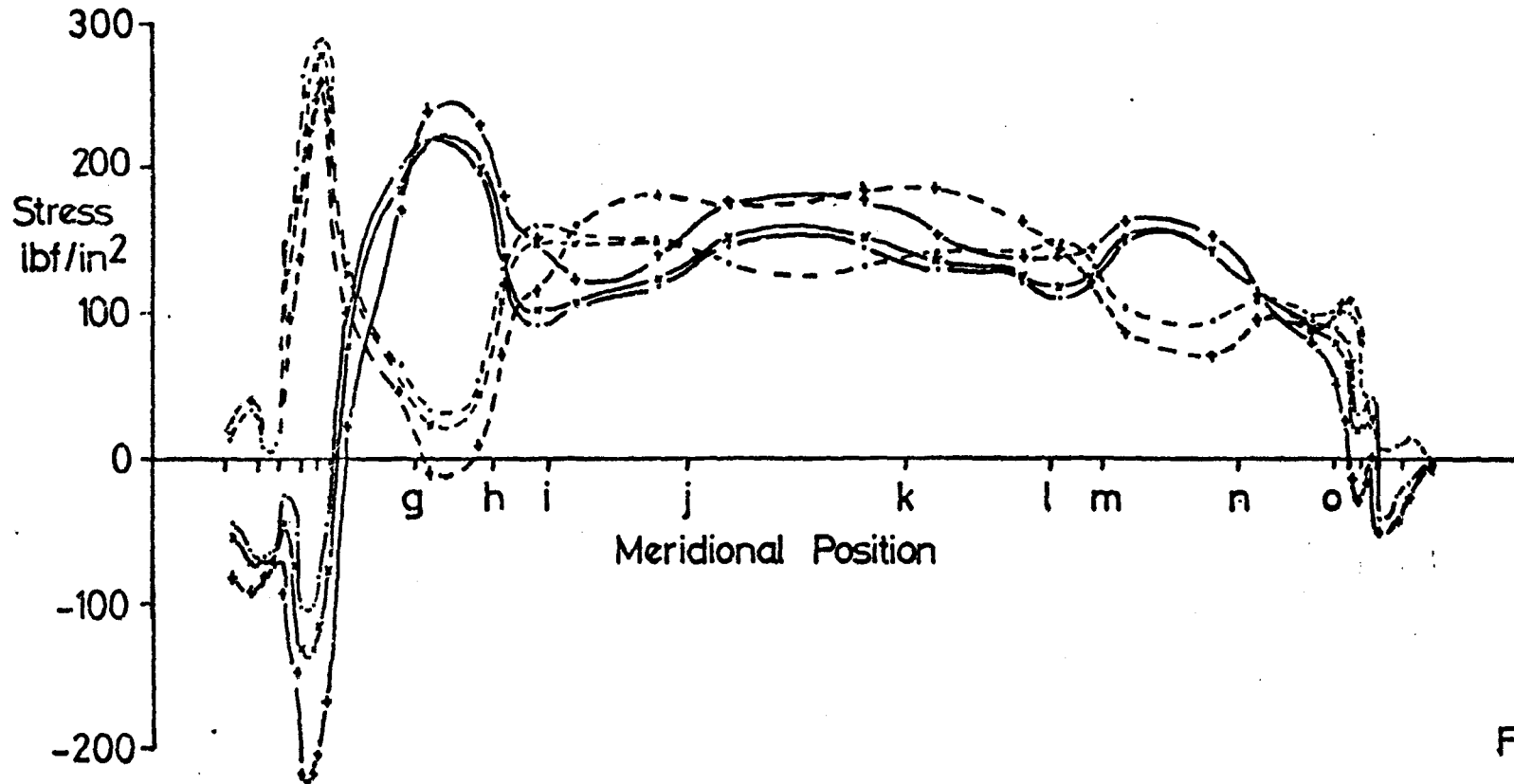


Fig. 7.3(d)

Effective Stress Redistribution due to Creep Deformation
of Lead Turbine Casing

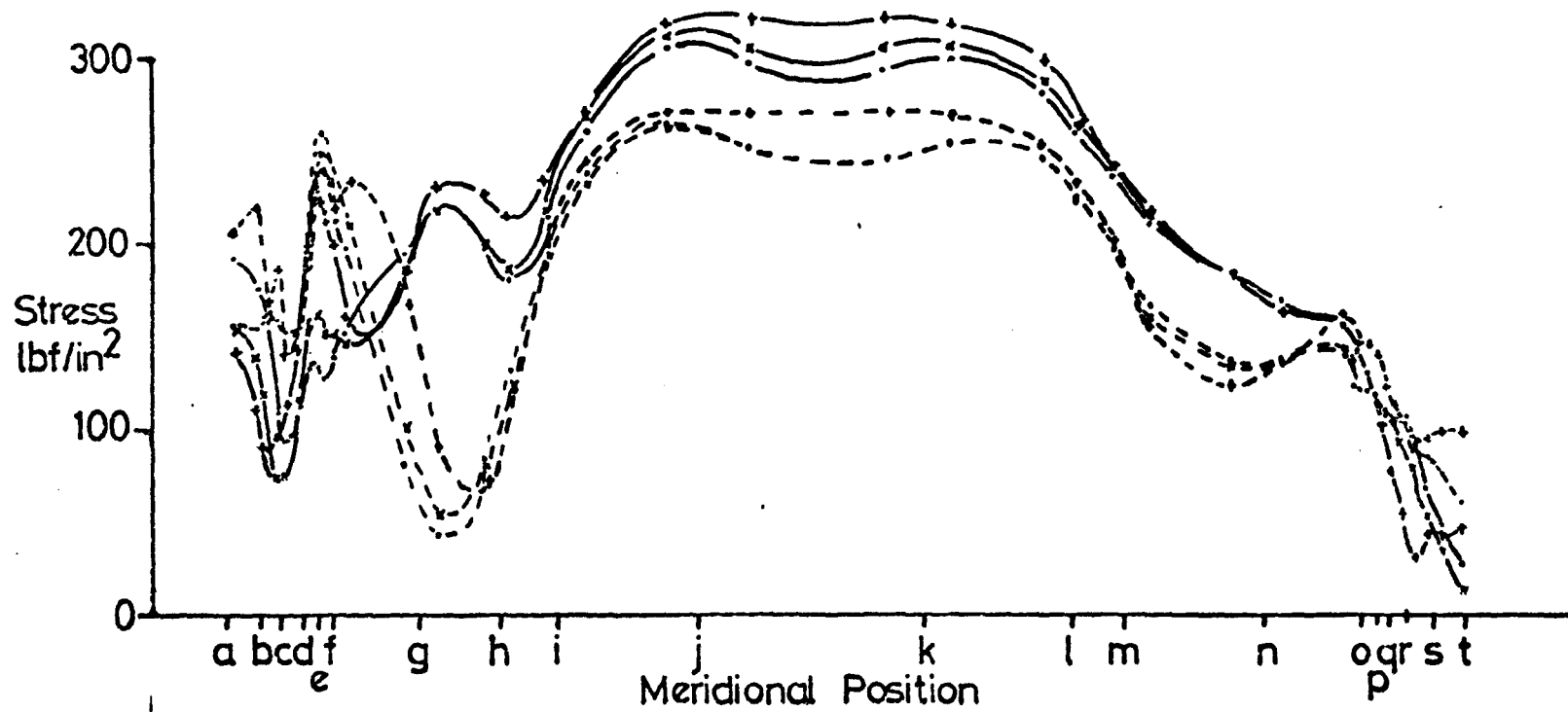
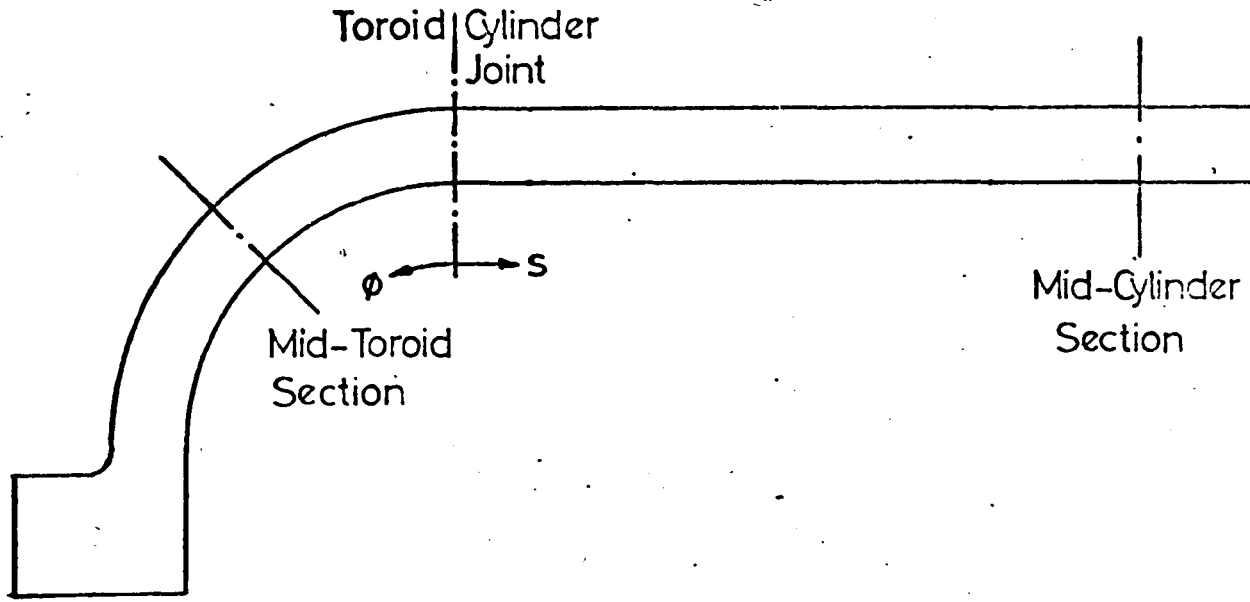


Fig. 7.3(e)

Meridional Positions of Hoop Stress Plots



Circumferential Positions for Hoop Stresses

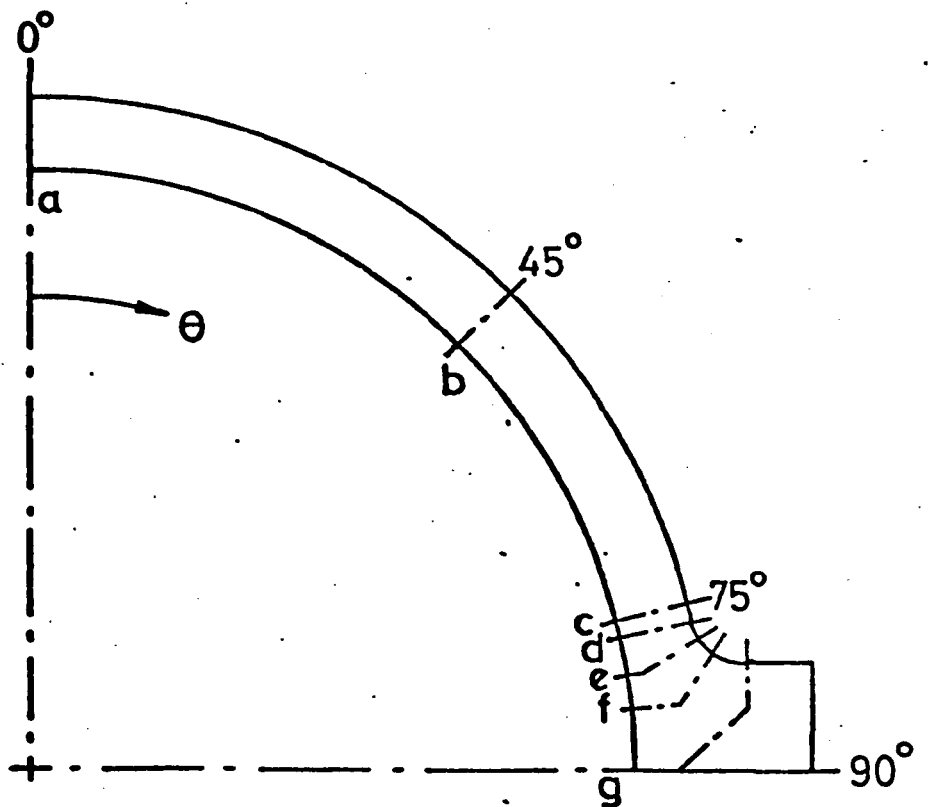


Fig.7.4

Deformation of Lead Turbine Casing

Mid-Cylinder Section s=3.5ins

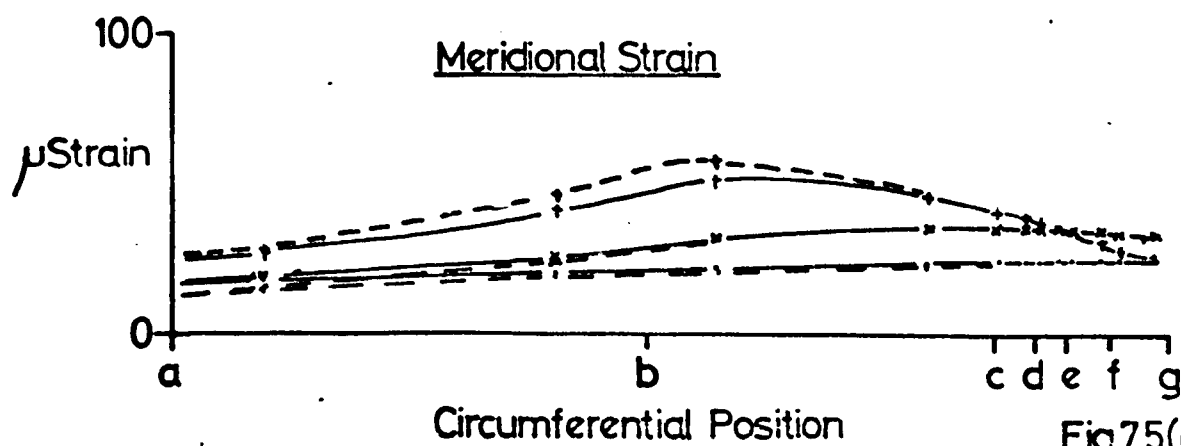
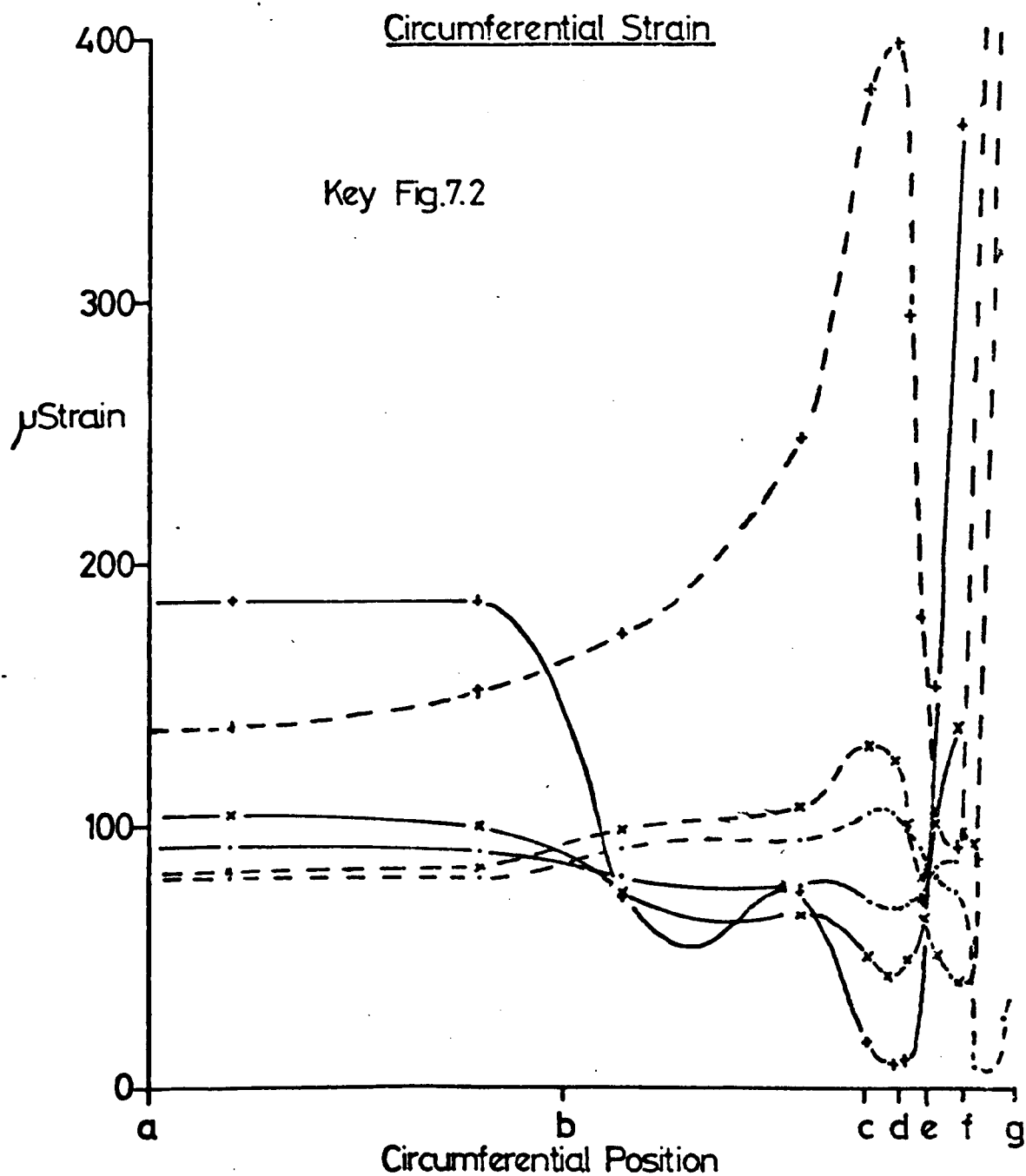


Fig.7.5(a)

Stress Distribution with Time due to Creep

Deformation of Lead Turbine Casing

Mid Cylinder Section $s=3.5$ ins

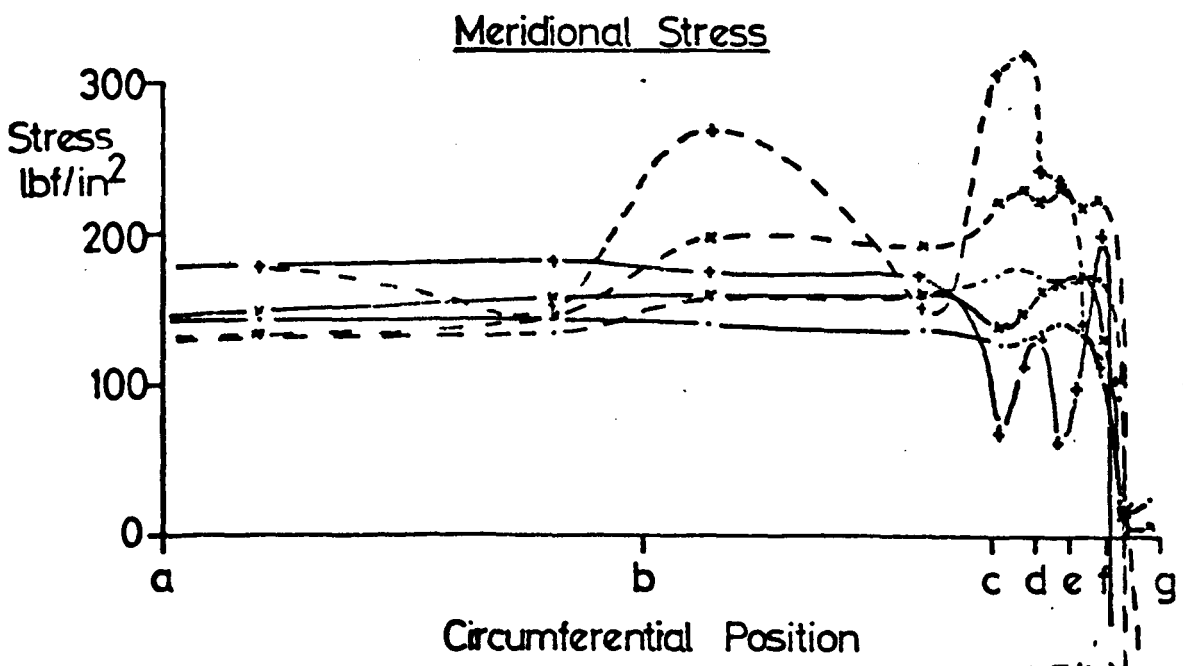
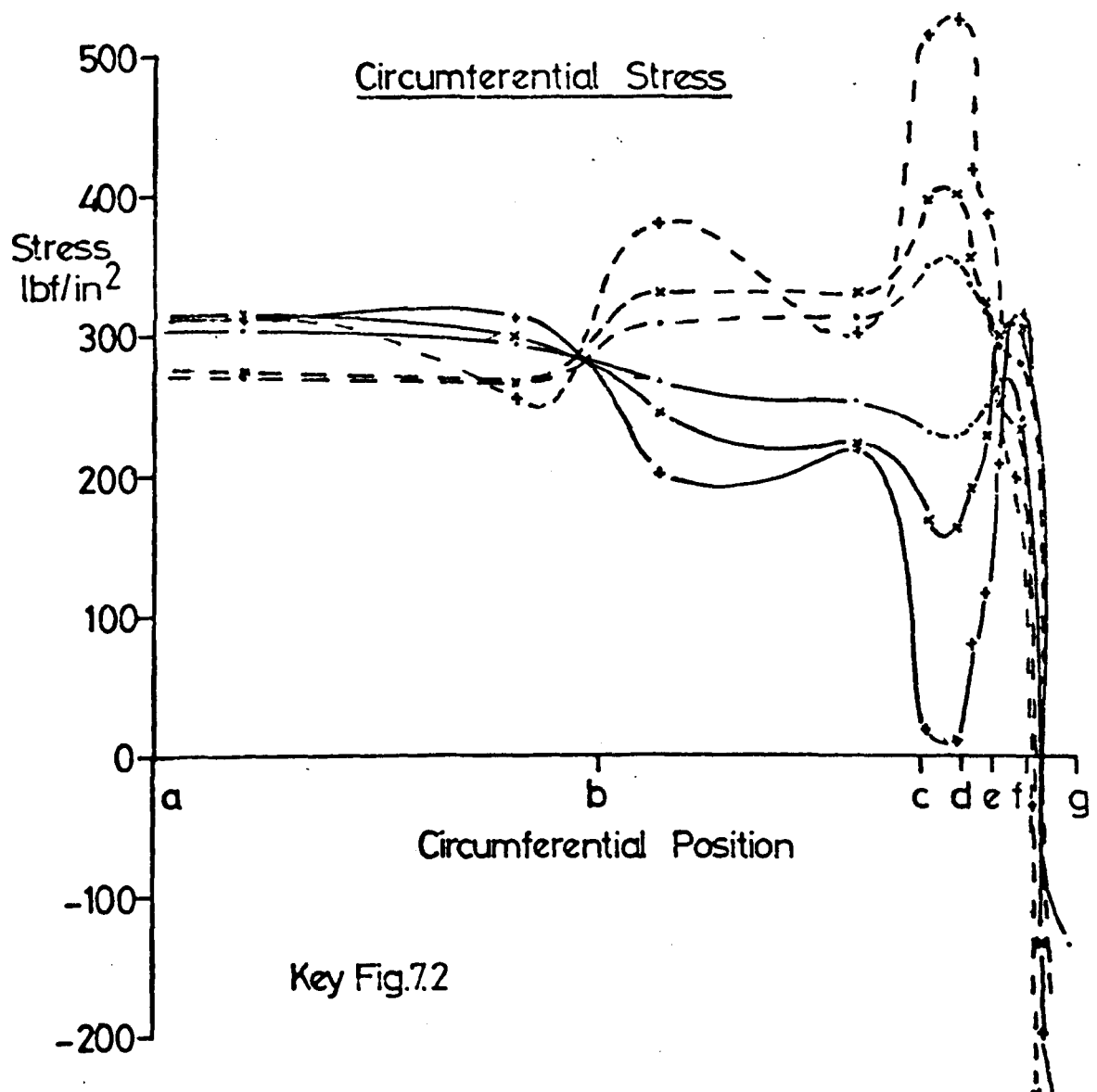
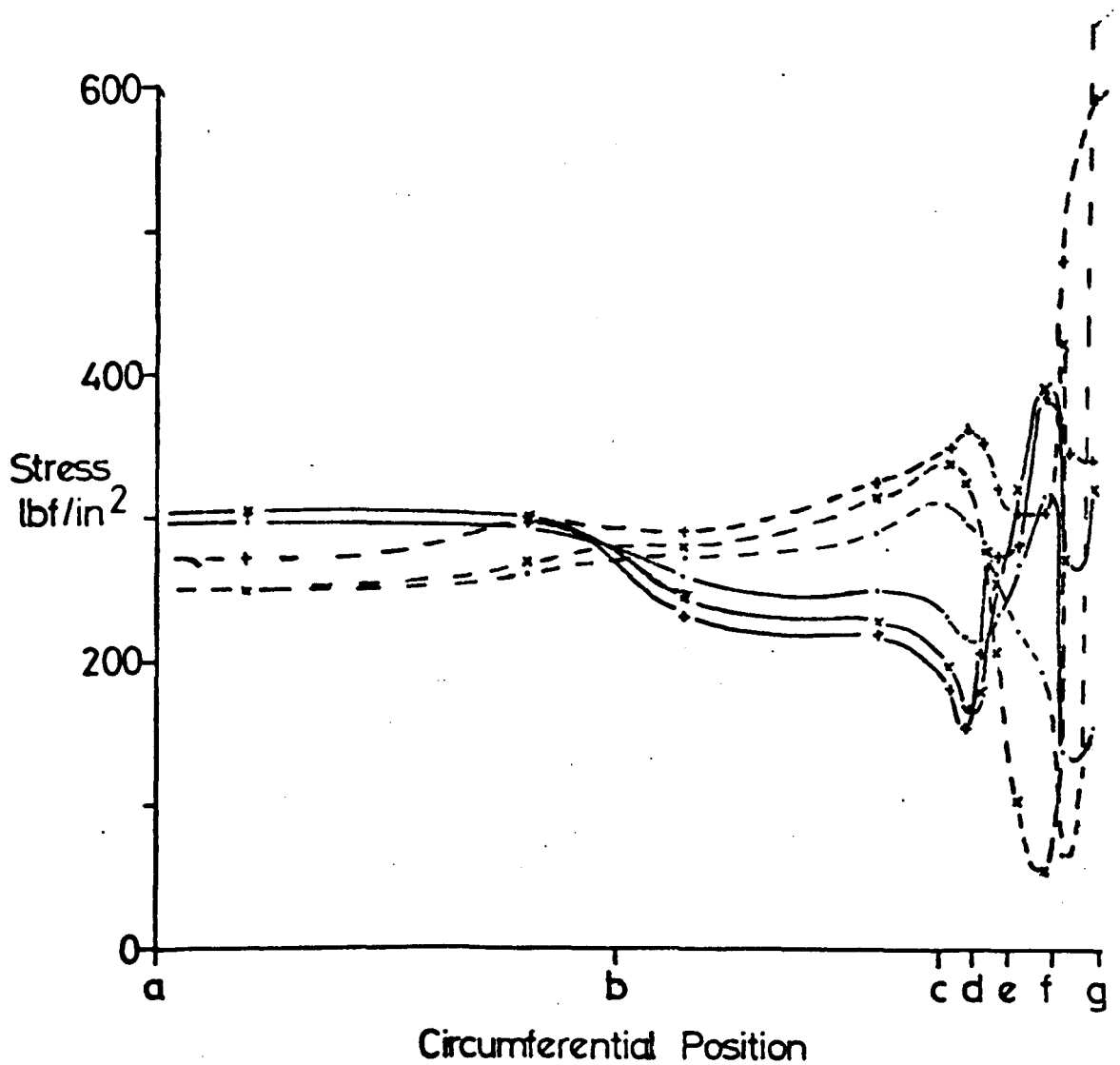


Fig.75(b)

Effective Stress Distribution with Time due to Creep
Deformation of Lead Turbine Casing

Mid-Cylinder Section s=3.5ins.



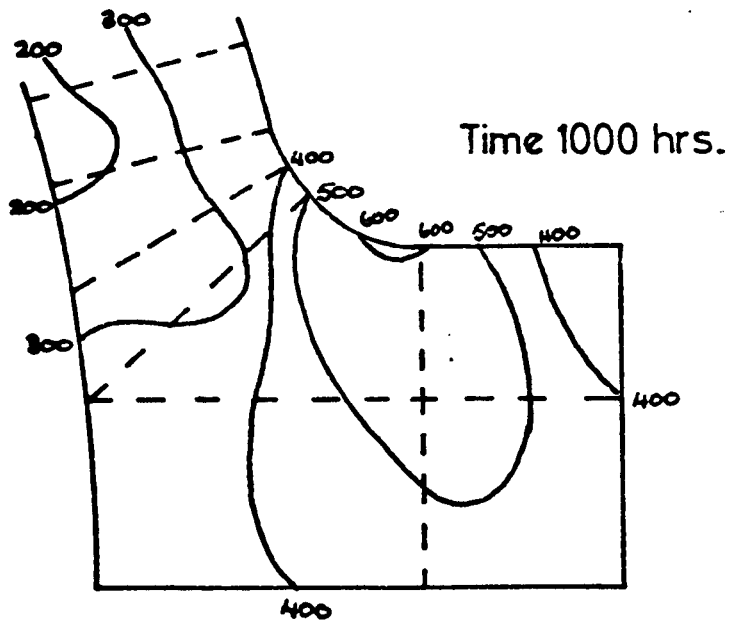
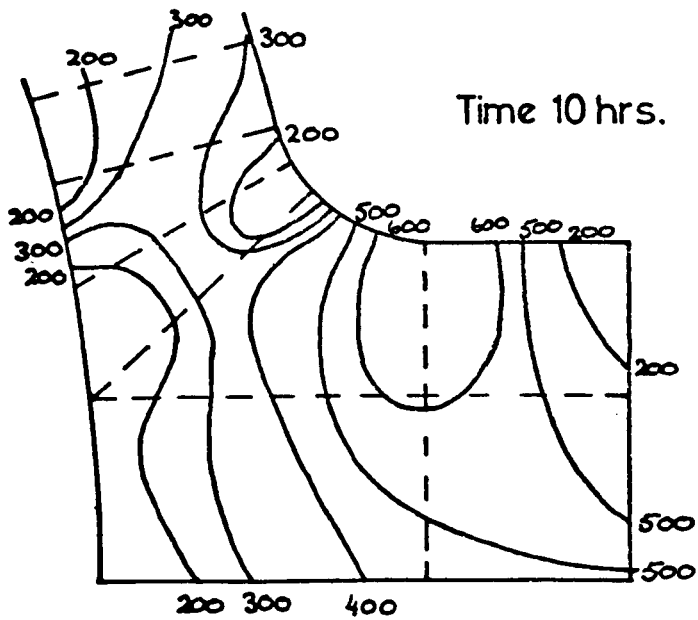
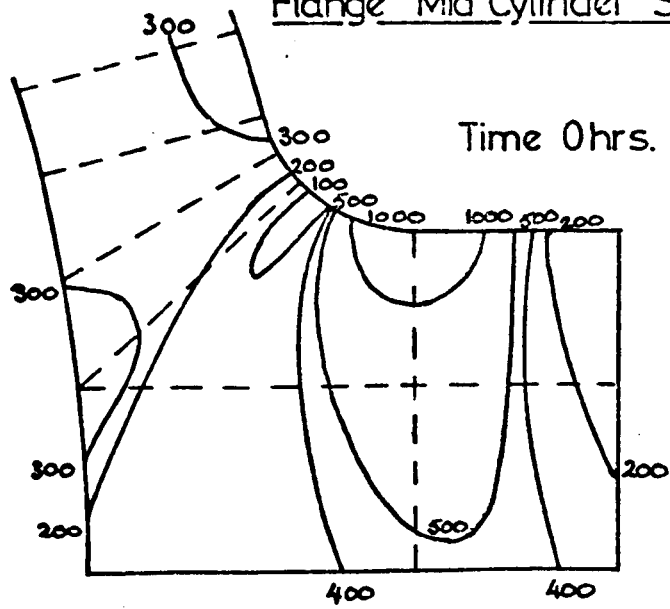
Key Fig.7.2

Fig.7.5(c)

Effective Stress Redistribution due to Creep

Deformation of Lead Turbine Casing

Flange Mid Cylinder Section $s=3.5$ ins.



Stresses lb/in^2

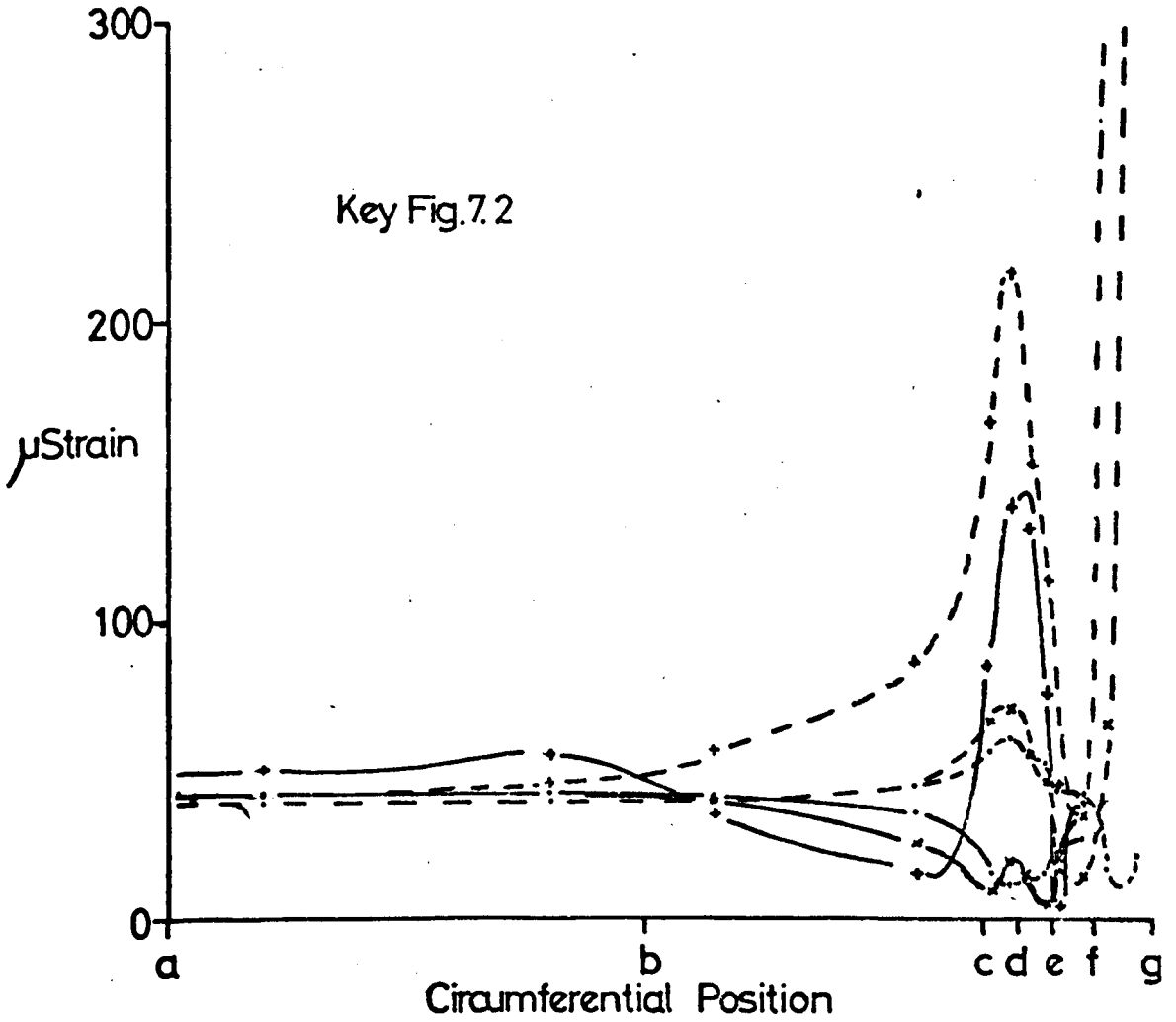
Fig.7.5(d)

Strain Distribution with Time due to Creep Deformation

of Lead Turbine Casing

Toroid-Cylinder Joint $\phi=0^\circ$ $s=0$ ins

Circumferential Strain



Meridional Strain

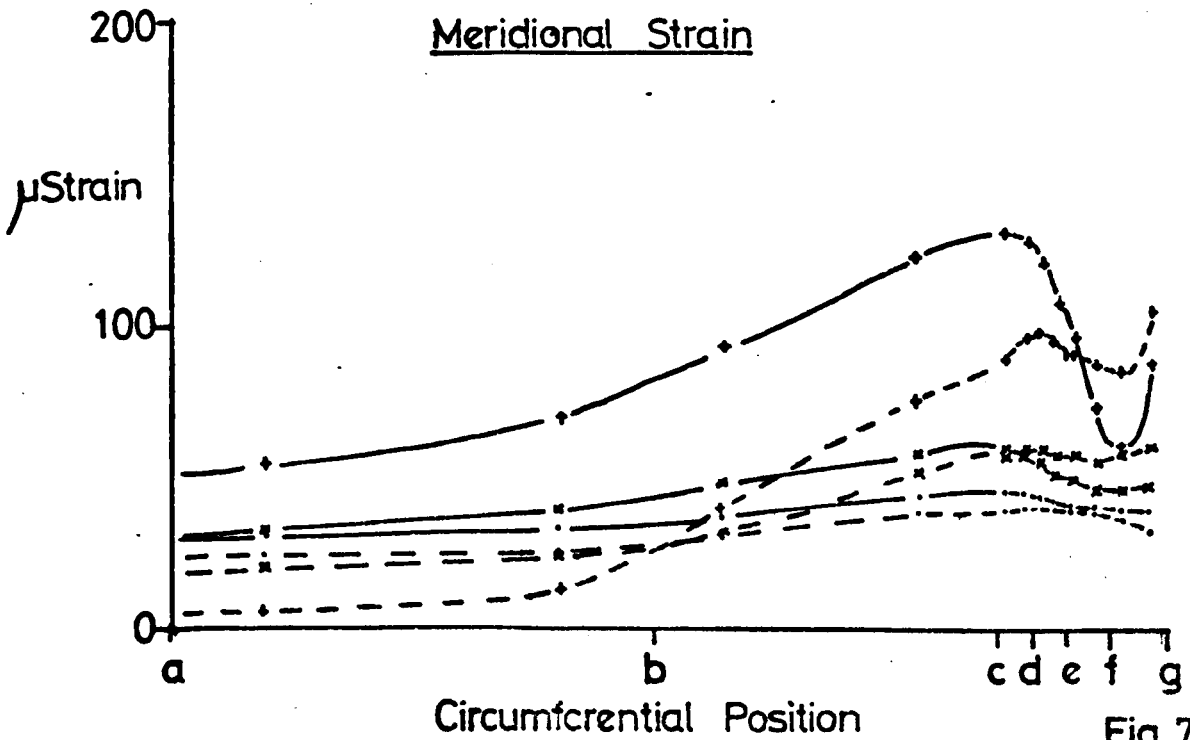


Fig.7.6(a)

Stress Distribution with Time due to Creep Deformation

of Lead Turbine Casing

Toroid-Cylinder Joint $\phi=0^\circ$ $s=0$ ins

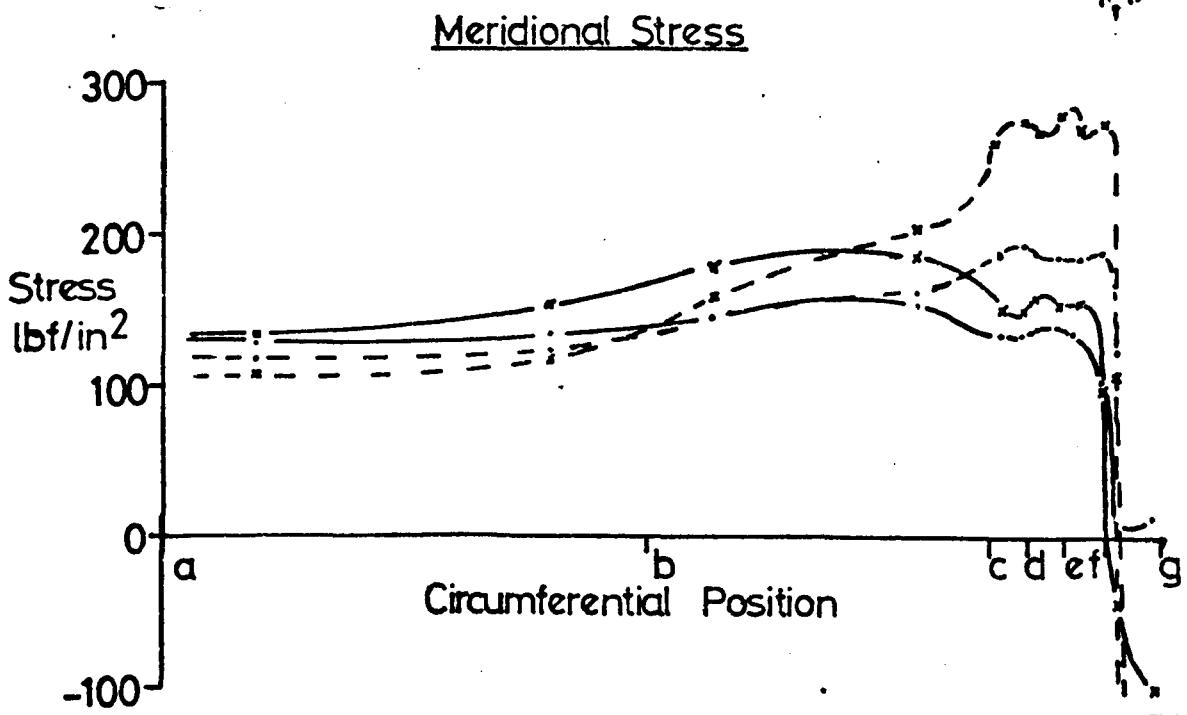
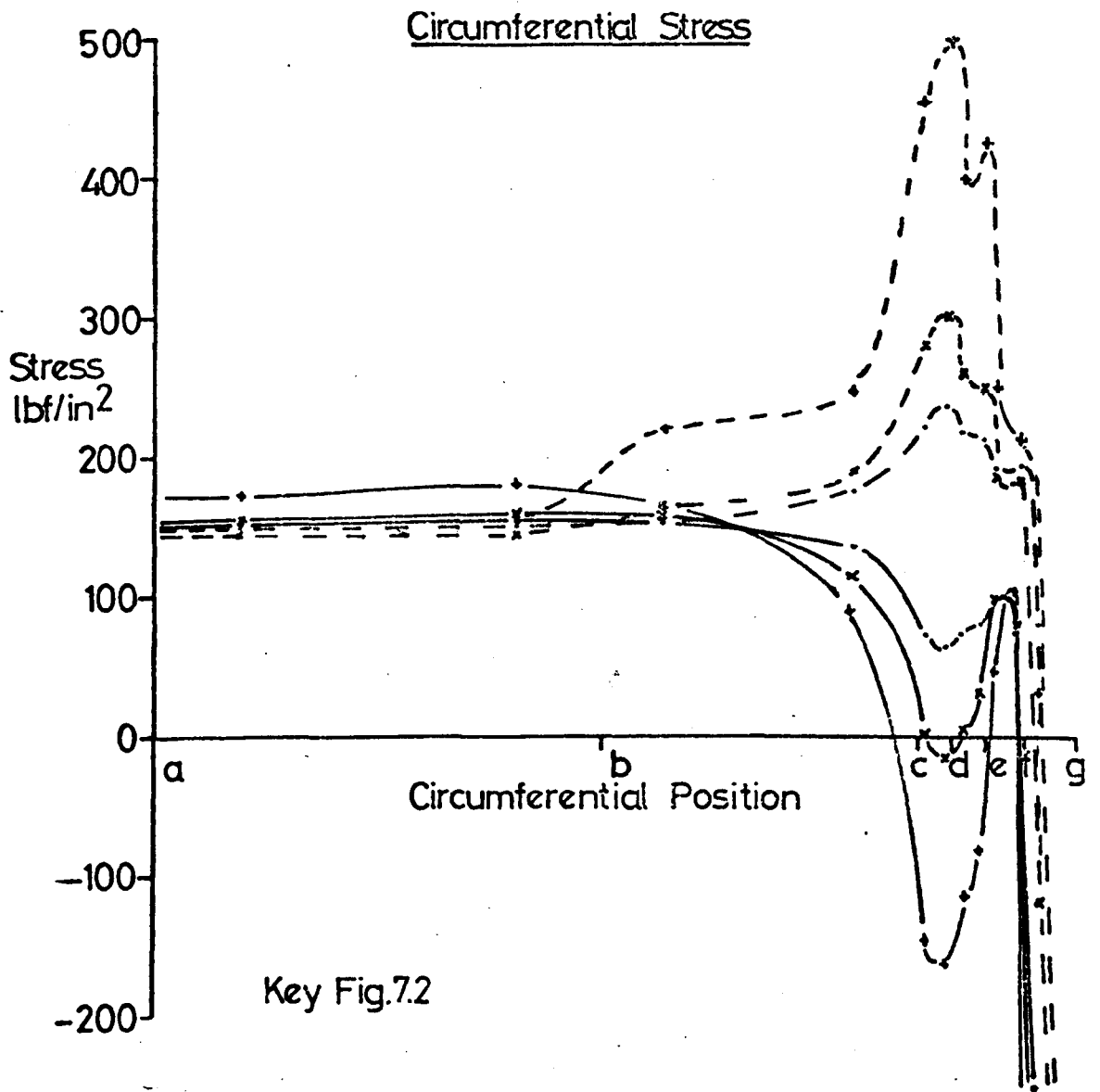
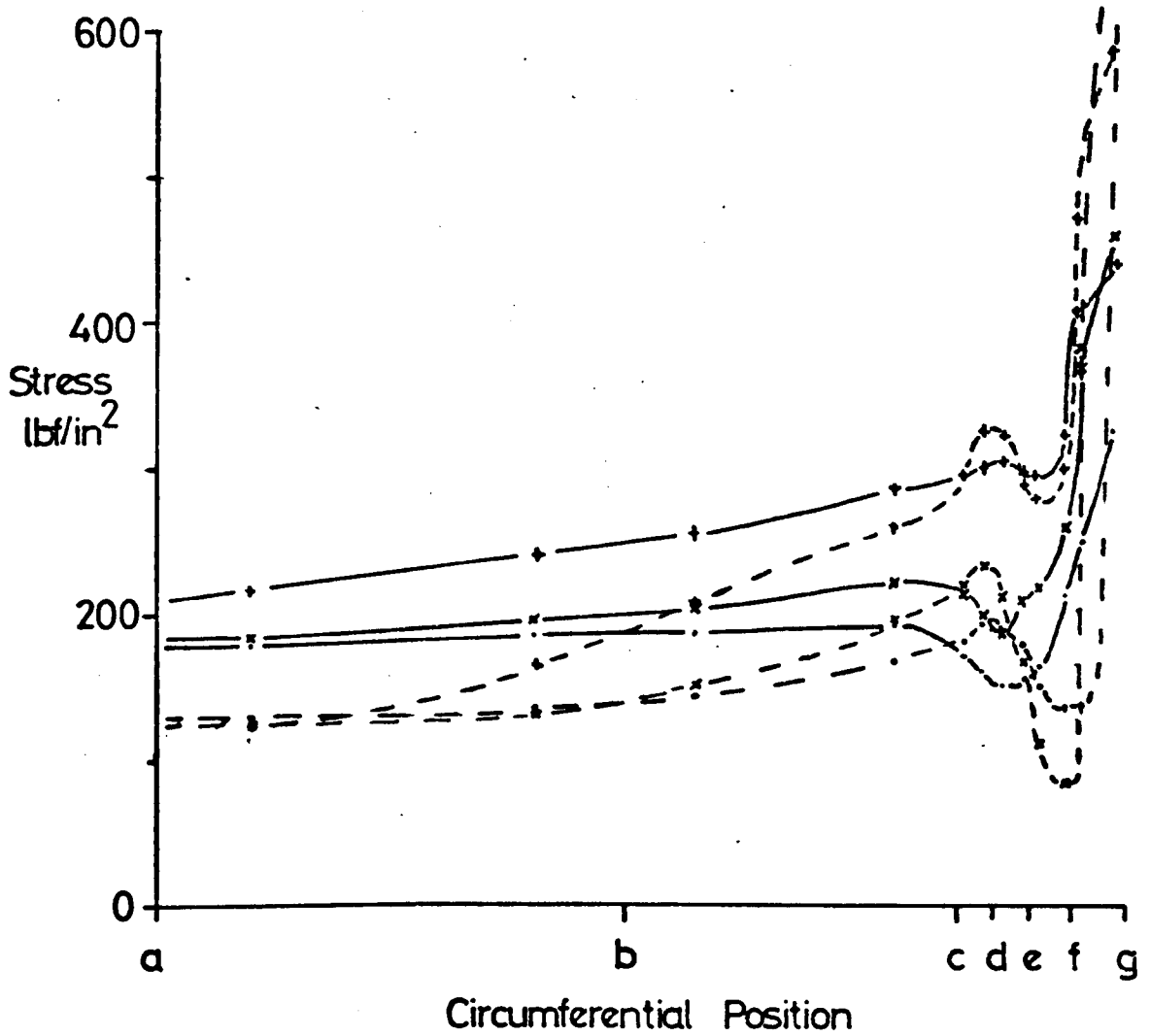


Fig.7.6(b)

Effective Stress Distribution with Time due to Creep

Deformation of Lead Turbine Casing

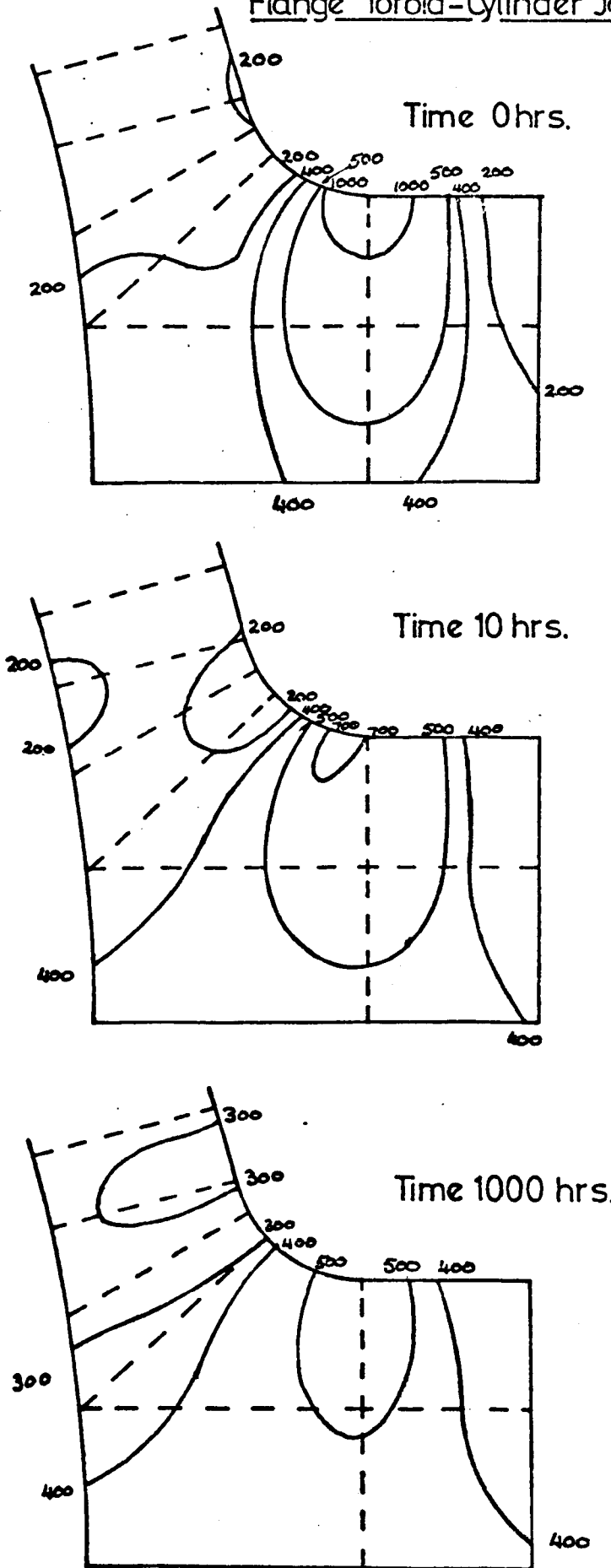
Toroid-Cylinder Joint $\phi=0^\circ$ $s=0$ ins



Key Fig.7.2

Fig.7.6(c)

Effective Stress Redistribution due to Creep
Deformation of Lead Turbine Casing
Flange Toroid-Cylinder Joint



Stresses lb/in^2

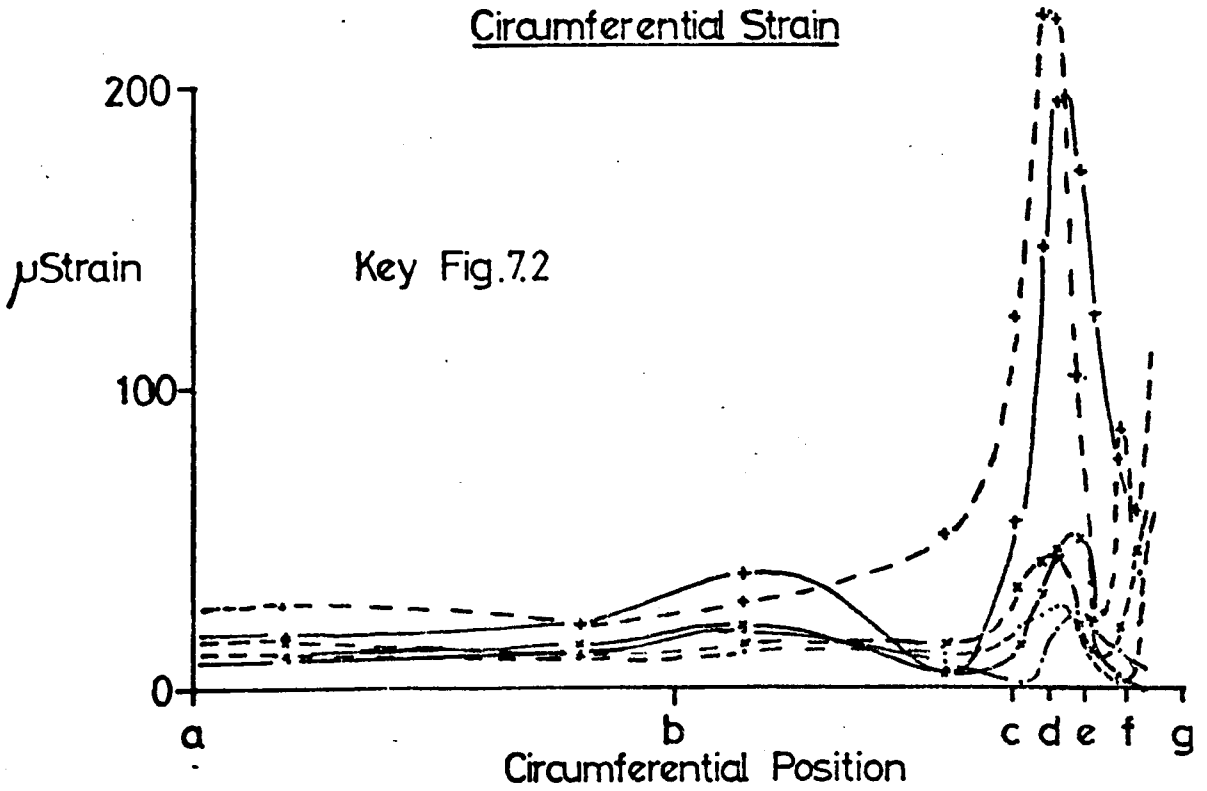
Fig.7.6(d)

Strain Distribution with Time due to Creep Deformation

of Lead Turbine Casing

Mid-Toroid Section $\phi=45^\circ$

Circumferential Strain



Meridional Strain

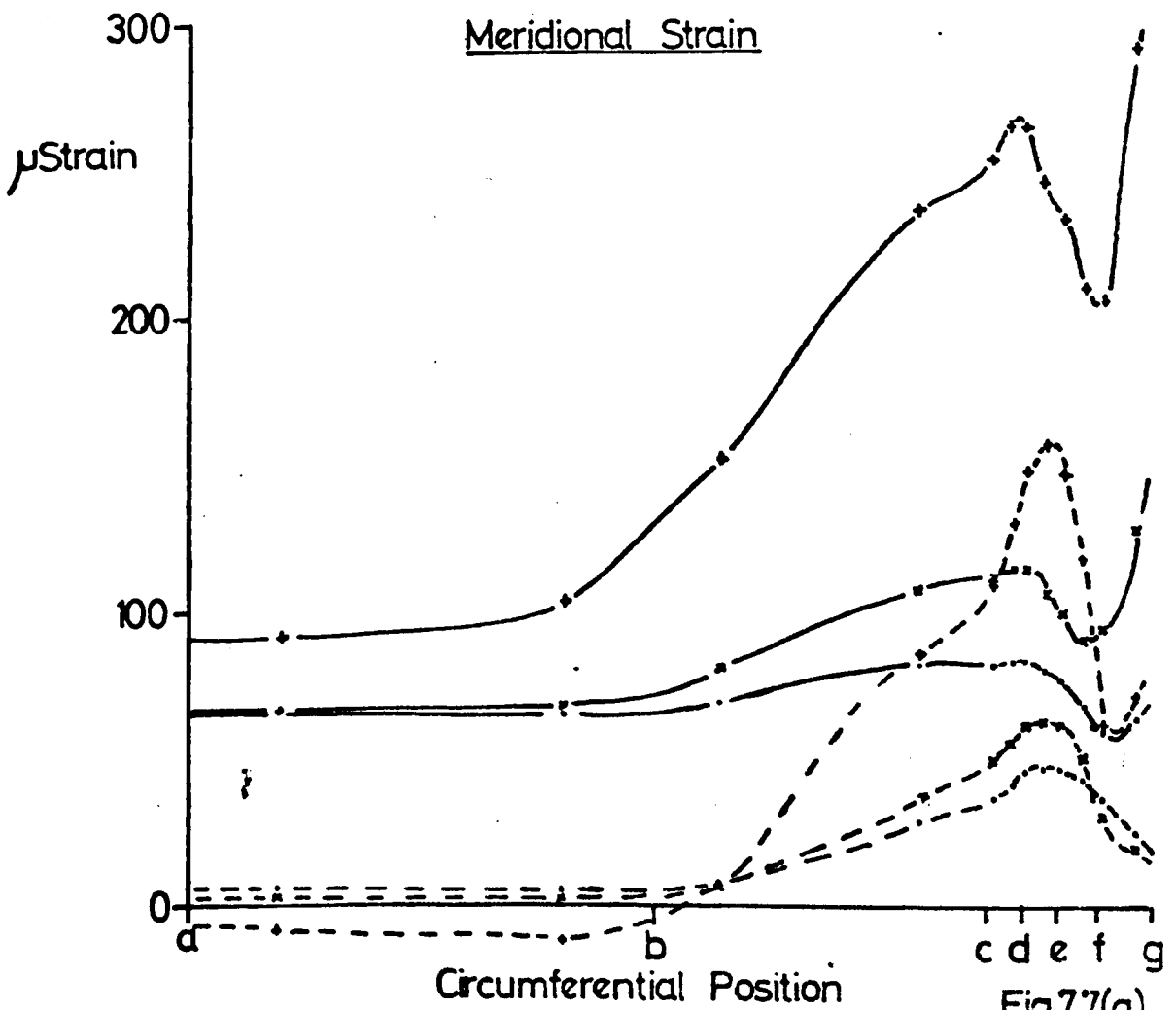


Fig.7.7(a)

Stress Distribution with Time due to Creep Deformation

of Lead Turbine Casing

Mid-Toroid Section $\phi=45^\circ$

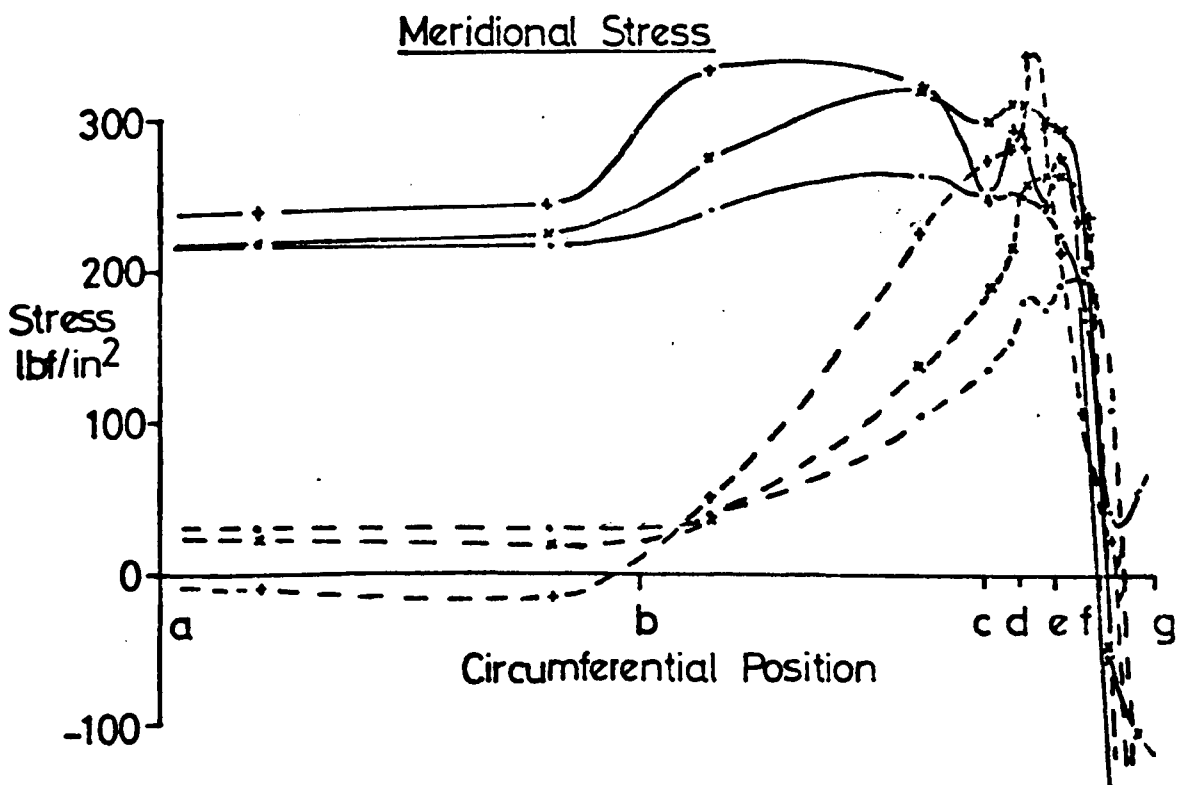
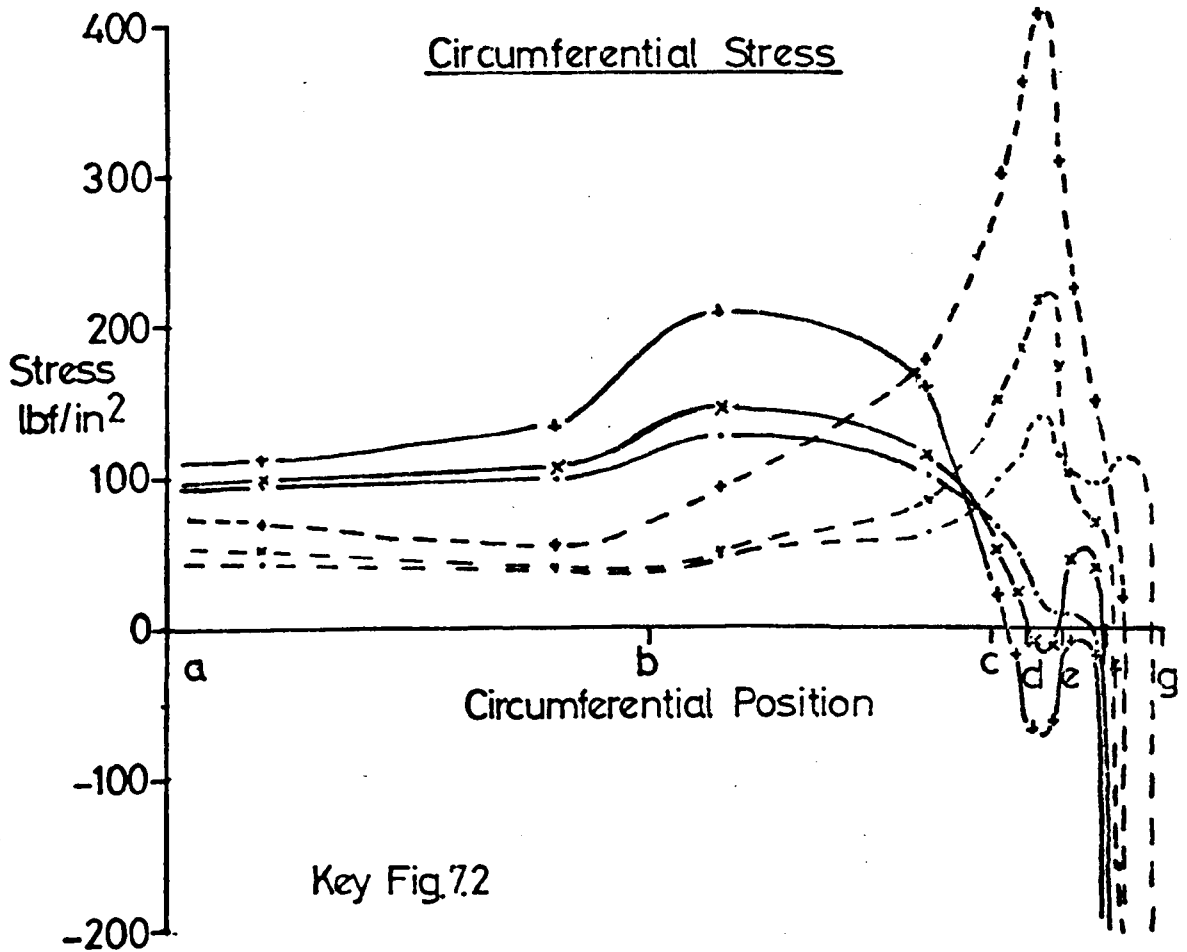
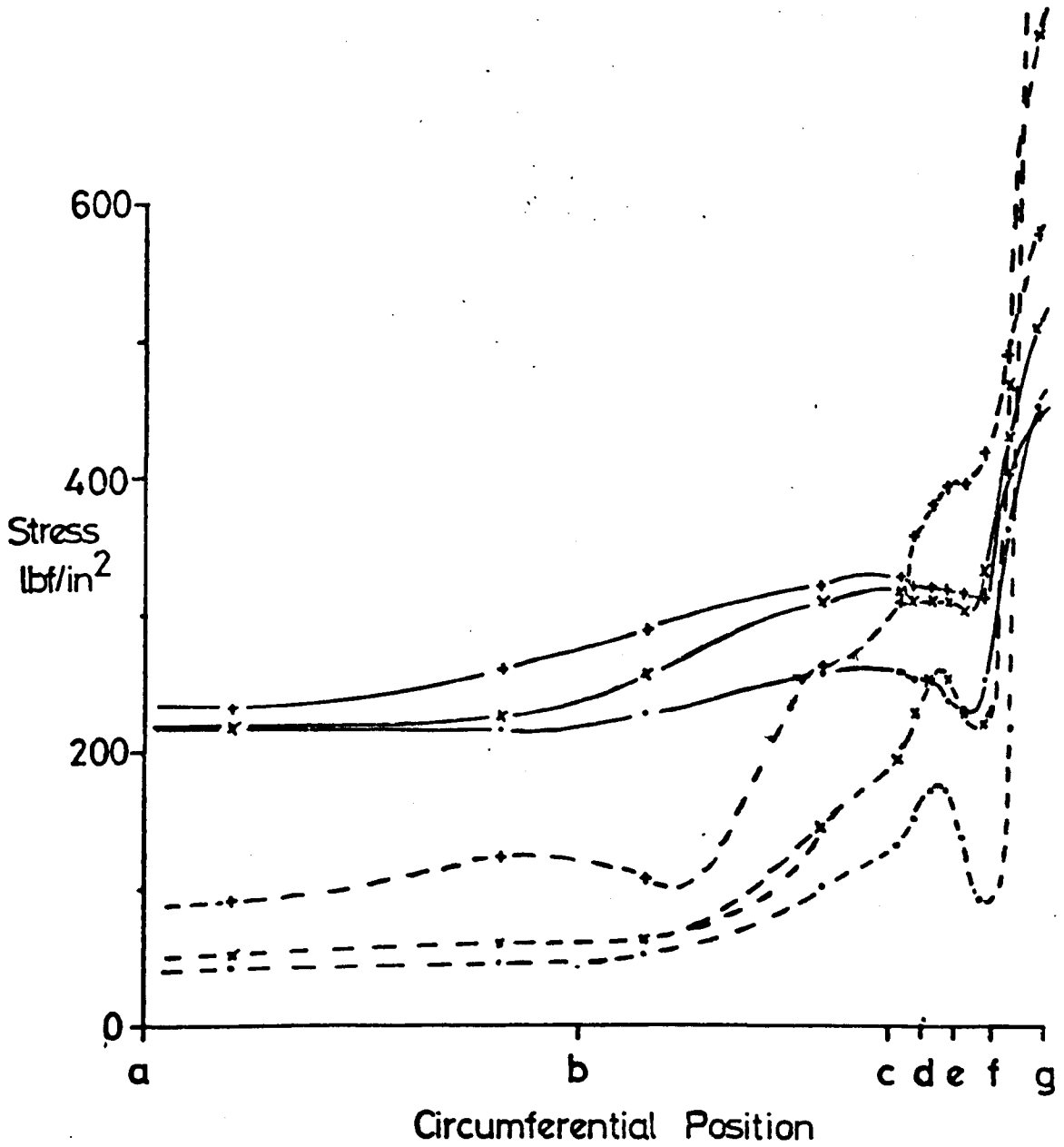


Fig.7.7(b)

Effective Stress Distribution with Time due to Creep
Deformation of Lead Turbine Casing

Mid-Toroid Section $\phi = 45^\circ$



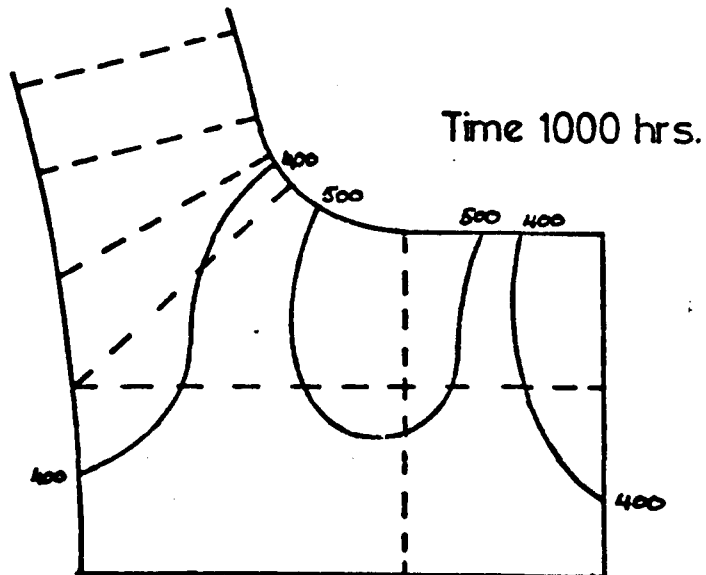
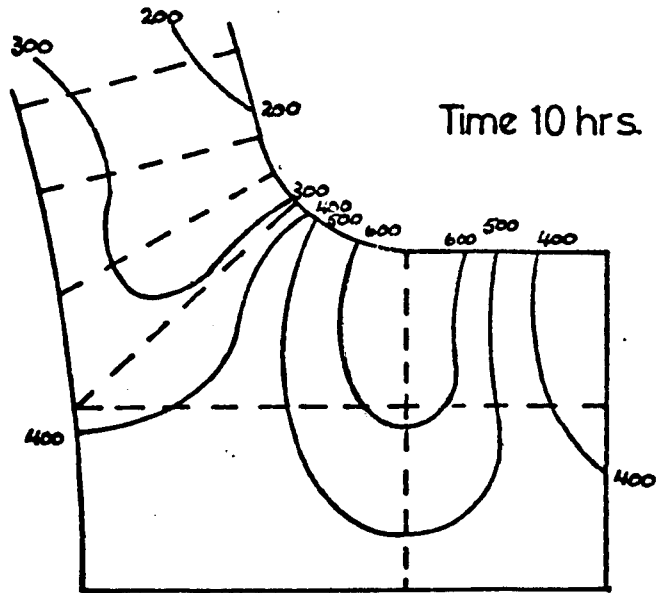
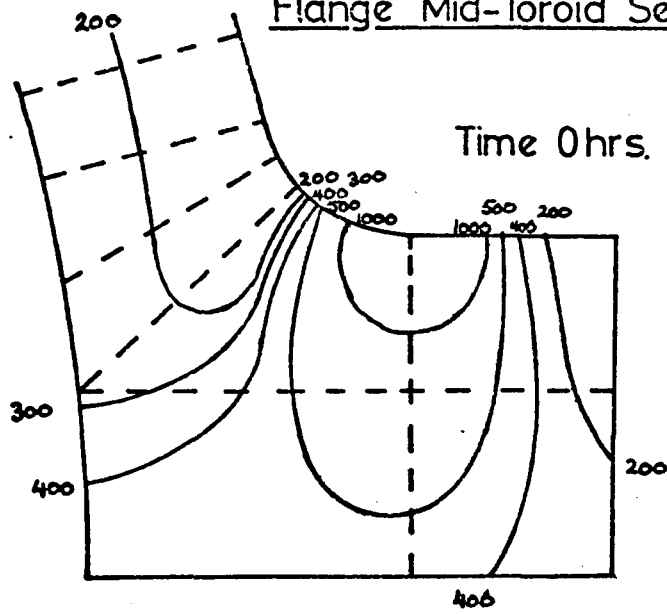
Key Fig.7.2

Fig.7.7(c)

Effective Stress Redistribution due to Creep

Deformation of Lead Turbine Casing

Flange Mid-Toroid Section $\phi=45^\circ$



Stresses lbf/in²

Fig.7.7(d)

Meridional Positions in Axisymmetric Approximation
of Flanged Turbine Casing

Internal Pressure 35 lbf/in^2
Creep Law $\epsilon_c = 1.291 \times 10^{-19} \sigma^{5.417} t^{0.513}$ lbf.in.hr. units

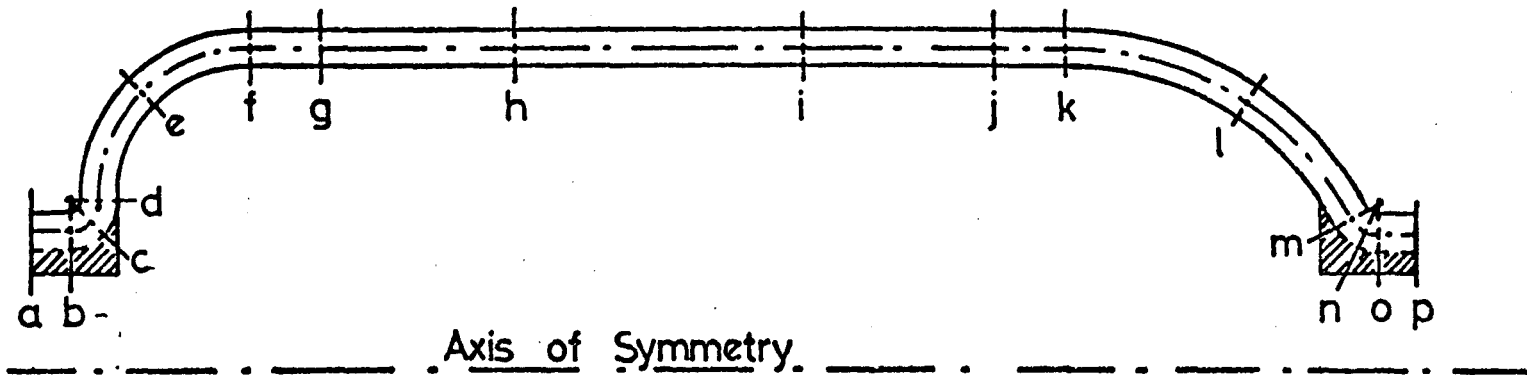


Fig. 7.8

Total Meridional Strain Distribution with Time for Axisymmetric

Approximation of Lead Turbine Casing

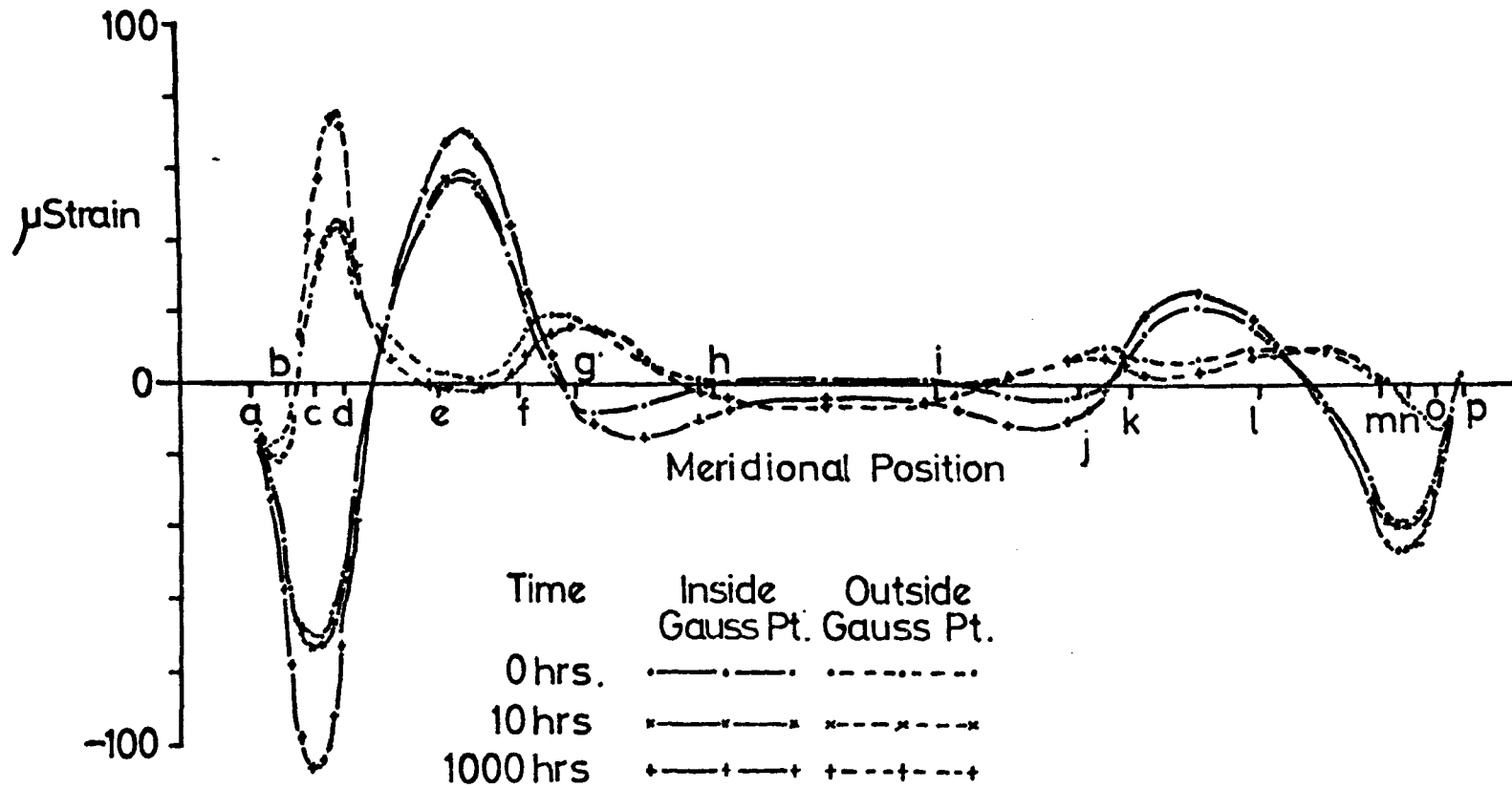


Fig.7.9(b)

References.

1. D. KALDERON "Large Steam Turbines for Nuclear and Conventional Power Stations"
British Engineering Week, Helsinki 12-16, October 1970, EE-AEI Publications.
2. J.M. MITCHELL "Trends in the Design of Highly Rated Steam Turbines"
Proc. I. Mech. E. "Steam Plant for the 1970's"
Vol. 183, Pt. 30, Paper 1, 1968-69.
3. R. BAGLEY "Design Features in Conventional Boiler Plant for the 1970's"
Proc. I. Mech. E. "Steam Plant for the 1970's"
Vol. 183, Pt. 30, Paper 6, 1968-69.
4. L.M. WYATT & M.G. GEMMILL "Experience with Power Generating Steam Plant and its Bearing on Future Developments"
Jnt. Int. Conf. on Creep, Proc. I. Mech. E.,
Vol. 178, Pt. 3A, August 1963.
5. F. DOLLIN "Some Design Problems arising in the Development of Very Large High Speed Turbines"
Proc. I. Mech. E., Vol. 177, No. 9, p 221.
6. W. WRIGHT Reply to Paper by B. Hernan, Proc. I. Mech. E.,
"Steam Plant for the 1970's", Vol. 183, Pt. 30,
p 121, 1968-69.
7. R.A. BELIAMY Ph. D. Thesis, University of Nottingham, 1972.
8. R.D. HENSHELL "PAFEC 70" Users Manual.
9. A. STODOLA "Steam and Gas Turbines" McGraw-Hill, p 507, 1927.
10. C.R. SODERBERG Reply to Paper by C.B. Campbell on "Practical Aspects of Turbine Cylinder Joints"
Jn. Appl. Mech. Trans. ASME Vol 6, March 1939.

11. H. McKENZIE "Design of Steam Turbine Casing Flanges"
M. Sc. Thesis, University of Nottingham, 1970.
12. P.E. GRAFTON & D.R. STROME "Analysis of Axisymmetrical Shells by
the Direct Stiffness Method".
AIAA Journal, Vol. 1, p 2324, 1963.
13. J.H. PERCY, T.H.H. PIAN, S. KLEIN & D.N. NAVARATNA "Application
of Matrix Displacement Method to Linear Elastic
Analysis of Shells of Revolution"
AIAA Journal, Vol. 3, p 2138, 1965.
14. E.G. POPOV, J. PENZIEN & Z. LU "Finite Element Solution for
Axisymmetrical Shells"
Jnl. Eng. Mech. Div. Proc. ASCE EM5, Vol. 90, p 119,
1964.
15. R.E. JONES & D.R. STROME "Direct Stiffness Method Analysis of
Shells of Revolution Utilising Curved Elements"
AIAA Journal, Vol. 4, p 1519, 1966.
16. D.R. NAVARATNA "Natural Vibrations of Deep Spherical Shells"
AIAA Journal, Vol. 4, p 2056, 1966.
17. J.J. WEBSTER "Free Vibrations of Shells of Revolution Using
Ring Finite Elements"
Int. Jnl. Mech. Sci., Vol 9, p 559, 1967.
18. J.J. WEBSTER "The Accuracy of Finite Element Solutions for the
Modal Characteristics of Shells of Revolution"
Int. Jnl. Mech. Sci., Vol. 12, p 157, 1970.
19. W. FLÜGGE "Stresses in Shells", Springer-Verlag, Berlin, p 317,
1960.
20. O.C. ZIENKIEWICZ & Y.K. CHEUNG "The Finite Element Method in
Structural and Continuum Mechanics"
McGraw-Hill, London, 1967.

21. A.H. STROUD & DON SECREST "Gaussian Quadrature Formulas"
Eaglewood Cliffs, Prentice Hall, p 99, 1966.
22. R.S. MARTIN, G. PETERS & J.H. WILKINSON "Symmetric Decomposition
of a Positive Definite Matrix"
Numerische Mathematik, Vol. 7, p 362, 1965.
23. R.S. MARTIN & J.H. WILKINSON "Solution of Symmetric and Unsymmetric
Band Equations and the Calculation of Eigenvectors
of Band Matrices"
Numerische Mathematik, Vol. 9, p 279, 1967.
24. S. TIMOSHENKO & S. WOINOWSKY-KRIEGER "Theory of Plates and Shells"
McGraw-Hill, New York, p 553, 1959.
25. G.E. FINDLEY, D.G. MOFFAT & P. STANLEY "Elastic Stresses in
Torispherical Drumheads: Experimental Verification"
Jnl. of Strain Analysis, Vol. 3, p 219, 1968.
26. R.A. BELLAMY & H. FESSLER "Stepped Cylindrical Pressure Vessel"
1st Report to Science Research Council on Steam
Turbine Casings, Dept. of Mech. Eng., Univ. of
Nottingham, 1969.
27. R.J ROARK "Formulas for Stress and Strain", McGraw-Hill, p334,
1954.
28. K.W. YANG & C.W.LEE "Thermal Stresses in Thick Walled Circular
Cylinders under Axisymmetric Temperature Distribution
ASME Paper, 71-PVP-16, 1971.
29. S. MURAKAMI & S. IWATSUKI "Transient Creep of Circular Cylindrical
Shells"
Int. Jnl. Mech. Sci., Vol. 11, p 897, 1969.
30. J.G. ERGATOUDIS, B.M. IRONS & O.C. ZIENKIEWICZ "Curved, Isoparametric
Quadrilateral Elements for Finite Element Analysis"
Int. Jnl. Solids & Structures, Vol 4, p 31, 1968

31. O.C. ZIENKIEWICZ "The Finite Element Method in Engineering Science"
McGraw-Hill, London, 1971.
32. O.C. ZIENKIEWICZ, B.M. IRONS, J.G. ERGATOUDIS, S AHMAD & F.C. SCOTT
"Isoparametric and Associated Element Families for
Two and Three-Dimensional Analysis"
Proc. Course on Finite Element Methods in Stress
Analysis, Edited I Holand & K. Bell, Tapir, Norway,
1969.
33. T.K. HELLEN & H.A. MONEY "The Application of Three-Dimensional
Finite Elements to a Cylinder-Cylinder Intersection"
Int. Jnl. Num. Methods in Eng., Vol. 2, p 415, 1970
34. S. AHMAD, B.M. IRONS & O.C. ZIENKIEWICZ "Analysis of Thick and Thin
Shell Structures by Curved Finite Elements"
Int. Jnl. Num. Methods in Eng., Vol. 2, p 419, 1970.
35. L.B. BENNY "Mathematics for Students of Engineering and Applied
Science"
Oxford University Press, London, p 491, 1958.
36. B.M. IRONS "Economical Computer Techniques for Numerically
Integrated Finite Elements"
Int. Jnl. Num. Methods in Eng., Vol. 1, p 201, 1969.
37. B.M. IRONS "A Frontal Solution Program for Finite Element
Analysis"
Int. Jnl. Num. Methods in Eng., Vol. 2, p 5, 1970.
38. G. CANTIN "An Equation Solver of Very Large Capacity"
Int. Jnl. Num. Methods in Eng., Vol. 3, p 379, 1971.
39. J.R. WESTLAKE "A Handbook of Numerical Matrix Inversion and
Solution of Linear Equations"
John Wiley & Sons, New York, 1968.

40. Y.R. RASHID "Three-Dimensional Analysis of Elastic Solids"
Pt. 1 "Analysis Procedure" Int. Jnl. Solids &
Structures, Vol. 5, p 1311, 1969.
Pt. 2 "The Computational Problem" Int. Jnl. Solids
& Structures, Vol. 6, p 195, 1970.
41. B.M. IRONS & D.K.Y. KAN "Equation-Solving Algorithms for the Finite
Element Method", Dept. of Civil Eng., Univ. College
of Wales (Swansea).
42. B.M. IRONS "Roundoff Criteria in Direct Stiffness Solutions"
AIAA Jnl., Vol. 6, No. 7, p 1308, 1968.
43. T.J. BOND "Some Considerations of the Finite Element Method
in Stress Analysis"
Ph. D. Thesis, University of Nottingham, 1972.
44. F.K.G. ODCVIST "Engineering Theories of Creep"
Proc. of 5th Congress on Theoretical & Applied
Mechanics, Symposium on Non-Linear Physical Problems,
Roorkee,
45. I. FINNIE "Steady Creep of a Tube Under Combined Bending and
Internal Pressure"
Jnl. of Basic Eng. (Trans. ASME), p 462, June 1960.
46. I. FINNIE "Steady- State Creep of a Thick-Walled Cylinder
Under Combined Axial Load and Internal Pressure"
Jnl. of Basic Eng. (Trans. ASME), p 689, Sept. 1960.
47. E.M. SMITH "Analysis of Creep in Cylinders, Spheres and Thin
Discs"
Jnl. Mech. Eng. Sci., Vol. 7, p 82, 1965.
48. J. FAIRBURN & W.W. MACKIE "A Simple Method of Obtaining Creep Rates
of a Thick-Walled Cylinder under Internal Pressure"
Jnl. Mech. Eng. Sci., Vol. 10, p 286, 1968.

49. R.K. PENNY "The Creep of Pressurised Cylindrical Shells"
Aeronautical Journal, Vol. 73, p 514, June 1969.
50. A. MENDELSON, M.H. HIRSCHBERG & S.S. MANSON "A General Approach
to the Practical Solution of Creep Problems"
Jnl. of Basic Eng. (ASME Trans.), p 585, Dec. 1959.
51. O.C. ZIENKIEWICZ, M. WATSON & I.P. KING "A Numerical Method of
Visco-Elastic Stress Analysis"
Int. Jnl. Mech. Sci., Vol. 10, p 807, 1968.
52. R.K. PENNY "Axisymmetric Bending of the General Shell of
Revolution during Creep"
Jnl. Mech. Eng. Sci., Vol. 6, 1964.
53. R.K. PENNY "The Creep of Spherical Shells Containing
Discontinuities"
Int. Jnl. Mech. Sci., Vol. 9, 1967.
54. A.E. JOHNSON "Creep under Complex Stress Systems at Elevated
Temperatures"
Proc. I. Mech. E., vol. 164, p 432, 1951.
55. A.E. JOHNSON & B. KHAN "Creep under Changing Complex-Stress Systems
in Copper at 250°C"
Int. Jnl. Mech. Sci., Vol. 7, p 791, 1965.
56. F.K.G. ODQVIST "Engineering Theories of Metallic Creep"
Symposium su la Plastica Nella Scienza delle
Costruzioni, Varenna, p 204, 1956.
57. E.M. SMITH "Estimation of the Useful Life and Strain History
of a Thick Tube Creeping under Non-Steady Conditions"
Jnl. of Strain Analysis, Vol. 1, p 44, 1965.
58. G.A. GREENBAUM & M.F. RUBINSTEIN "Creep Analysis of Axisymmetric
Bodies Using Finite Elements"
Nuclear Eng. & Design, Vol. 7, p 379, 1968

59. C.C. SHULTZ & D.B. VAN FOSSEN "Combined Elastic-Plastic-Creep Analysis of Two-Dimensional Bodies"
ASME Publication 71-PVP-30, 1971.
60. J.D. LUBAHN & R.P. FELGAR "Plasticity and Creep of Metals"
John Wiley & Son, New York, 1961.
61. R. HILL "The Mathematical Theory of Plasticity"
Clarendon Press, Oxford, 1950.
62. J.C. JAEGER "Elasticity, Fracture and Flow"
Methuen (Science Paperbacks), p 89, 1971.
63. O.C. ZIENKIEWICZ, J. TOO & R.L. TAYLOR "Reduced Integration Technique in General Analysis of Plates and Shells"
Int. Jnl. Num. Methods Eng., Vol. 3, p 275, 1971.
64. E.P. POPOV "Bending of Beams with Creep"
Jnl. of Applied Physics, Vol. 20, p 251, March 1949.
65. H. FESSLER, P.A.T. GILL & P. STANLEY "Creep Strains in Thick Rings Subjected to Internal Pressure"
Advances in Creep Design (The A.E. Johnson Memorial Volume), Edited by A.I. Smith & A.M. Nicholson,
Applied Science Publishers Ltd., London, 1970.
66. V. KUZELKA & H. FESSLER "Elastic Stresses in a Simplified Turbine Inner Casing subjected to Internal Pressure"
1st Report to Science Research Council on Steam Turbine Casings, Dept. of Mech. Eng., University of Nottingham, Dec. 1969.
67. J. SWANNELL, T.J. BOND, R.D. HENSHELL & G.B. WARBURTON "Curved Two-Dimensional Finite Elements with Displacement Assumptions", to be published.

68. F. SAFAVI "Automatic Data Checking for Structural Analysis using Graphical Techniques"
M. Sc. Thesis, University of Nottingham, 1971.
69. S. TIMOSHENKO & J. GOODIER "Theory of Elasticity"
2nd. Edition, McGraw-Hill, 1951.
70. A. NADAI "Theory of Flow and Fracture of Solids", Vol. 1,
2nd. Edition, McGraw-Hill, 1950.
71. Boley & Weiner "Theory of Thermal Stresses" Columbia
University Institute of Flight Structures.
p. 263